



HAL
open science

Estimation des gradients de température pendant le remplissage d'un réservoir d'hydrogène gazeux.

Rémi Gonin

► **To cite this version:**

Rémi Gonin. Estimation des gradients de température pendant le remplissage d'un réservoir d'hydrogène gazeux.. Dynamique des Fluides [physics.flu-dyn]. Institut National Polytechnique de Toulouse - INPT, 2022. Français. NNT: 2022INPT0096 . tel-04248242

HAL Id: tel-04248242

<https://theses.hal.science/tel-04248242>

Submitted on 18 Oct 2023

HAL is a multi-disciplinary open access archive for the deposit and dissemination of scientific research documents, whether they are published or not. The documents may come from teaching and research institutions in France or abroad, or from public or private research centers.

L'archive ouverte pluridisciplinaire **HAL**, est destinée au dépôt et à la diffusion de documents scientifiques de niveau recherche, publiés ou non, émanant des établissements d'enseignement et de recherche français ou étrangers, des laboratoires publics ou privés.



Université
de Toulouse

THÈSE

En vue de l'obtention du

DOCTORAT DE L'UNIVERSITÉ DE TOULOUSE

Délivré par :

Institut National Polytechnique de Toulouse (Toulouse INP)

Discipline ou spécialité :

Dynamique des fluides

Présentée et soutenue par :

M. REMI GONIN

le mardi 20 septembre 2022

Titre :

Estimation des gradients de température pendant le remplissage d'un réservoir d'hydrogène gazeux.

Ecole doctorale :

Mécanique, Energétique, Génie civil, Procédés (MEGeP)

Unité de recherche :

Institut de Mécanique des Fluides de Toulouse (IMFT)

Directeur(s) de Thèse :

M. DAVID FABRE

M. RÉMI BOURGUET

Rapporteurs :

MME ANNE SERGENT, UNIVERSITE PARIS-SACLAY

M. PIETRO SALIZZONI, ECOLE CENTRALE DE LYON

Membre(s) du jury :

M. LAURENT JOLY, ISAE-SUPAERO, Président

M. DAVID FABRE, UNIVERSITE TOULOUSE 3, Membre

M. FOUAD AMMOURI, AIR LIQUIDE, Membre

M. MARCELLO MELDI, ENSAM LILLE, Membre

MME ELENA VYAZMINA, AIR LIQUIDE, Invité(e)

M. RÉMI BOURGUET, UNIVERSITE TOULOUSE 3, Invité(e)

À ma famille et mes amis,

C'est avec beaucoup de gratitude que je remercie mes encadrants de thèse de m'avoir accordé leur confiance tout au long de cette thèse. C'est grâce à leur soutien que j'ai pu m'investir pleinement. Je remercie donc très chaleureusement, Rémi Bourguet, David Fabre, Fouad Ammouri. Je souhaite également remercier Elena Viazmina pour s'être autant investie dans l'accompagnement de ma thèse. J'adresse pareillement un grand merci à Pierre Horgue et Romain Guibert pour leur aide précieuse et leur disponibilité. Je souhaite remercier David Lo Jacono pour avoir impulsé cette thèse. Je remercie bien sûr tous les membres du jury, Mme. Anne Sergent, M. Pietro Salizzoni, M. Laurent Joly et M. Marcello Meldi pour leur participation.

Si mon passage à l'IMFT a été si agréable, c'est bien grâce à Paul, Nabil et Javier. Je remercie également Nadine, Patricia et Véronique pour nos nombreuses conversations en salle commune Camichel. Je remercie également tous les autres membres de l'IMFT dont je ne pourrais citer ici tous les noms mais à qui je dois plein de bon souvenir.

Je profite de cette occasion pour remercier ma famille pour leur soutien, toujours indéfectible, et également Manon sans qui sûrement ces dernières années auraient été moins joyeuses.

Abstract

Hydrogen can be employed to power a fuel-cell vehicle (FCV). In order to gather 5 kg of gaseous hydrogen in a 125 L tank to reach a 500 km range, it must be stored at high-pressure, 700 bar. For a filling time ranging from 3 to 5 min, the rapid compression of gaseous hydrogen, from 20 bar to 700 bar, induces an increase of gas temperature in the tank. According to safety recommendations, the temperature must not exceed 85°C for composite tanks. To restrain the rising averaged temperature in the tank, the injected hydrogen is cooled down to -40°C depending on the ambient temperature and tank initial pressure. Assuming a uniform temperature in the tank, 0 dimension (0D) models were developed in order to predict the averaged gas temperature during the filling process. Depending on the injected gas temperature and mass flowrate, a final filling temperature is estimated. An optimization process can then be carried out in order to limit the energetic cost of a filling, while keeping the final averaged temperature below 85°C. However, experimental observations reveal the existence of thermal gradients for some filling scenarios of horizontally tank leading to local peaks exceeding 85°C while the averaged temperature remains below the limits. These thermal heterogeneities cannot be predicted by 0D models and question their relevance for the optimization of the filling process. The link between the thermal stratification and the filling scenario has been established but the underlying mechanisms involved still need be clarified. This is the object of the present work, which aims at investigating, through numerical simulations, the fluid dynamics and thermal phenomena at play during the filling process of a hydrogen filled horizontally with an axial injection. As the first step, a numerical model capturing the tridimensional hydrogen flow and the thermal conduction through walls is developed via the open-source software OpenFOAM. The accuracy of the numerical approach is assessed by comparison with different experimental measurements and previous results, for two thermally contrasted filling scenarios, i.e. homogeneous versus heterogeneous. The homogeneous scenario is well predicted while the thermal gradient is underestimated for the heterogeneous scenario. This is consistent with the results from previous numerical studies. As the second step, focus is placed on the improvement of thermal gradient prediction by analyzing the impact of turbulence modeling approach, especially on thermal diffusivity. A turbulence model leading to an improved prediction of the thermal behavior is identified and implemented. Finally, the physical mechanisms of thermal stratification are more specifically examined in order to improve 0D models. As shown by tridimensional simulations, the stratification results from a deflection of the cold injected jet towards the lower hemisphere of the tank, due to buoyancy forces. A model of buoyant jet is suggested to predict the jet deflection and provide insights into thermal stratification. This is expected to enhance the reliability of the optimization procedure of filling scenarios based on 0D models.

Keywords — fluid mechanics; experimental validation; hydrogen gas; numerical simulation; turbulence modeling; heat transfer.

Résumé

L'hydrogène peut générer l'électricité nécessaire à la propulsion des véhicules à pile à combustible. Pour réunir dans 125 L la quantité d'hydrogène nécessaire pour parcourir 500 km pour un véhicule léger (voiture), soit 5 kg, il doit être comprimé à 700 bar. Pour un remplissage de 3 à 5 min, la compression rapide de l'hydrogène de 20 bar à 700 bar produit une élévation de la température dans le réservoir. Selon les recommandations de sécurité, la température ne doit pas excéder 85°C pour un réservoir en matériau composite. Pour contrer l'élévation de la température moyenne du gaz dans le réservoir, l'hydrogène injecté est alors pré-refroidi jusqu'à -40°C selon la température ambiante et la pression initiale du réservoir, ce qui constitue une dépense énergétique. Sous l'hypothèse d'une température homogène du gaz dans le réservoir, des modèles 0 dimension (0D) ont été développés pour prédire la température moyenne du fluide. Selon la température du gaz injecté et le débit massique d'injection, une température finale de remplissage peut être estimée. Un travail d'optimisation est alors possible pour limiter les coûts énergétiques d'un remplissage tout en maintenant la température finale sous les 85°C. Cependant, des résultats expérimentaux montrent qu'une stratification thermique peut apparaître pour les réservoirs horizontaux sous certaines conditions avec des températures dépassant localement 85°C alors que la température moyenne est largement inférieure. Cette hétérogénéité remet en question la pertinence des modèles 0D et l'optimisation du remplissage qu'ils permettent. Le lien entre la stratification thermique et le scénario de remplissage a été établi mais les mécanismes sous-jacents restent à éclaircir. C'est l'objet de cette thèse, qui vise à explorer les couplages entre dynamique des fluides et thermique pendant les remplissages de réservoir d'hydrogène par des méthodes numériques. Dans un premier temps, un modèle numérique simulant les écoulements tridimensionnels de l'hydrogène et la conduction thermique dans les parois du réservoir est développé via le logiciel OpenFOAM. Les capacités prédictives de ce modèle sont évaluées par comparaison avec des résultats expérimentaux et numériques antérieurs, pour des scénarios de remplissage caractérisés par des comportements thermiques contrastés: homogène et hétérogène. Il apparaît que les cas peu stratifiés sont rigoureusement prédits mais que les gradients thermiques sont sous-estimés dans les cas hétérogènes, en accord avec les résultats des simulations numériques antérieures. Dans un deuxième temps, afin d'améliorer la prédiction des gradients thermiques, l'influence du modèle de turbulence sur la diffusivité thermique est analysée et l'approche retenue conduit à sélectionner un modèle de turbulence avancé produisant des résultats plus fidèles aux résultats expérimentaux. Enfin, dans un troisième temps, l'étude se focalise sur la phénoménologie de la stratification thermique et l'amélioration des modèles 0D pour un réservoir horizontal. Comme le montrent les simulations tridimensionnelles, la stratification résulte de la déflexion de l'hydrogène froid injecté dans un réservoir de plus en plus chaud. Une modélisation de cette déflexion est proposée via un modèle de jet pesant pour une injection axiale. Elle est ensuite reliée aux gradients thermiques puis implantée dans un modèle 0D, afin d'enrichir les capacités prédictives de cette approche.

Mots-Clés — simulation numérique; mécanique des fluides; hydrogène gazeux; validation expérimentale; modèle de turbulence; transfert thermique.

Contents

Abstract	iii
Résumé	v
General introduction	1
Nomenclature	9
1 Literature review	17
1.1 Occurrence of the thermal heterogeneity during a filling of compressed-gas tank	17
1.2 Numerical approaches	20
1.2.1 0D models	21
1.2.2 CFD models	23
2 Resources and methods	25
2.1 Resources	25
2.1.1 Experimental measurements from the HyTransfer project	25
2.1.2 OpenFOAM and Paraview	28
2.1.3 3D model	28
2.1.4 Calmip and TGCC	33
2.2 Methods	33
2.2.1 Equation of state of the Hydrogen	33
2.2.2 SOFIL: 0D model from Air Liquide	36
2.2.3 Governing equations for the 3D model	37
2.2.4 Meshing	43
2.2.5 Numerical Schemes	46
2.2.6 Numerical Algorithm and solver	46
2.2.7 Boundary Conditions	48
3 First CFD results	53
3.1 A computational fluid dynamic study of the filling of a gaseous hydrogen tank under two contrasted scenarios	53
3.2 Additional results	81
3.2.1 Gas temperatures	81
3.2.2 Heat exchanged between the gas and the walls	83
3.2.3 Comparison between OpenFOAM results and experimental measurements for the temperatures located between the liner and the composite	84

4	Improvement of CFD approach	93
4.1	Advanced turbulence modeling improves thermal gradient prediction during compressed hydrogen tank filling	94
4.2	Additional results	121
4.2.1	Gas temperatures	121
4.2.2	Heat exchanged between the gas and the walls	121
4.2.3	Comparison between OpenFOAM results and experimental measurements for the temperatures between the liner and the composite	121
5	Simplified model to predict the thermal stratification	127
5.1	Reference data	128
5.1.1	Experimental data	128
5.1.2	CFD Results	129
5.2	The buoyant round jet model	129
5.2.1	Model development	129
5.2.2	Thermal gradient correction	135
5.2.3	Numerical method	137
5.3	CFD post-process	137
5.4	Results and discussion	140
5.4.1	Comparison between the CFD results and the buoyant round jet model results	140
5.4.2	Influence of the physical parameters α , λ and ρ_{grad} on the modeling	141
5.4.3	Comparison between the experimental data and the buoyant round jet model results	147
5.4.4	Discussion on the 5 m/s	149
6	Complementary studies	155
6.1	Full 3D CFD simulation of scenario D3Q8	155
6.2	Jet oscillation frequency	156
6.3	Steady-state like method	165
6.3.1	Numerical method	165
6.3.2	Application	167
6.4	Emptying case	170
6.5	Inverse model to estimate the temperature at the gas-liner interface	176
6.5.1	Direct problem	180
6.5.2	Inverse problem	184
	Conclusion and perspectives	191

General introduction

Hydrogen, the smallest existing molecule, harbors great hopes for the energy transition. The reaction of hydrogen with oxygen generates water and quantities of energy are released without carbon based elements. This reaction can be achieved by combustion, inducing heat which can be converted, partly (around 30% for a classic vehicle), in mechanical work, or via a fuel cell converting the energy with the efficiency of 60 % in electrical power [1]. Benefiting from this propriety, hydrogen is an interesting energy carrier to reduce CO_2 emissions. As urged by the Cop26 [2], avoiding an increase of 2 °C of the global temperature above pre-industrial levels requires to reduce the global CO_2 emission by 45 % by 2030. Its potential fueled numerous large-scale projects, like NorthH₂ [3], a project of production, storage and transmission of green hydrogen. Often breaking records on the size, giant electrolyzers [4] are created around the world to supply the increasing hydrogen demand. The field of applications for hydrogen is large. It goes from energy buffer for intermittent renewable energy sources or large scale storage in underground salt caverns [5] to transport applications: from light duty vehicles (< 10 kg of hydrogen on board) to heavy duty vehicles (> 10 kg of hydrogen on board), see figure 1.

Pure hydrogen, or under its molecule name dihydrogen, is more energetically dense than standard fuels. For example, in term of energy, 1 kg of hydrogen is equivalent to 2.84 kg of gasoline or 2.25 kg of natural gas [12]. This advantage is however diminished by its very low density at normal temperature and pressure, i.e. 20 °C and 1.01325 bar, about 0.08375 kg/m³. Consequently, maintaining some kilograms of hydrogen in a compact storage is a challenging constraint. The main solutions are based on the dilution of hydrogen into a solid material, like the metal hydrides, or using the pressure and the temperature to increase the density, like liquid hydrogen and compressed hydrogen. Table 1, adapted from [13], presents the different solutions along with their advantages and disadvantages.

For light duty vehicles, hydrogen in gaseous form is the best option. Compressed hydrogen can be stored during a long period of time [14], provides a decent range (up to 650 km for the Toyota Mirai [10]), is less energetically costly than liquid hydrogen (40 % of the internal potential energy is required for the liquefaction against 20 % for compressing at 700 bar [15]). As summarized in figure 2, the density of hydrogen is an important limitation when compared with other standard fuels. Therefore, improving the competitiveness of gaseous hydrogen goes by compressing the hydrogen as much

Method	Temperature [K]	Pressure [bar]	Volumetric energy density [MJ/L]	Remarks
Compressed	293	700	4.9	Current industry standard
Liquid	20	1	6.4	Boil-off constitutes major disadvantage
Cold/cryo compressed	40-80	300	4.0	Boil-off constitutes major disadvantage
Metal hydrides	260-425	20	13.2	Requires thermal management system

Table 1 – Storage methods overview, adapted from [13].

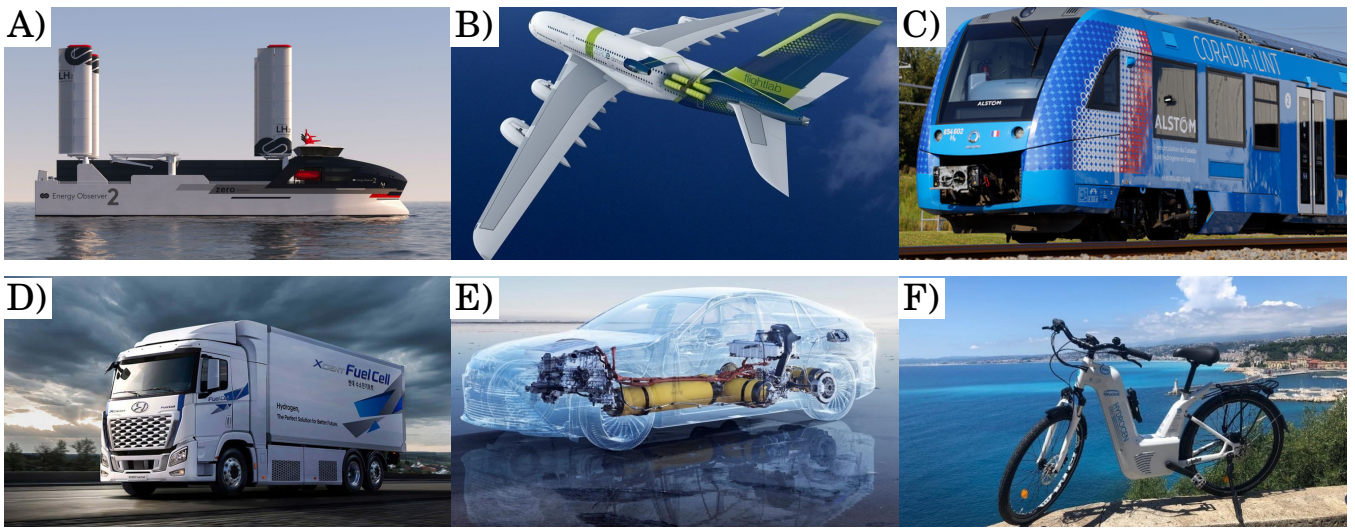


Figure 1 – Hydrogen applications for transportation. A), the Energy Observer 2 [6], a demonstrator vessel that runs on liquid H₂. B), Airbus [7] have the ambition to develop the world first zero-emission commercial aircraft by 2035, using hydrogen combustion technology to power the aircraft. C) Alstom released Coradia iLint™ [8], the world's 1st hydrogen powered train. D), Hyundai develops XCIENT Fuel Cell [9], a hydrogen powered truck. They expected 1 600 hydrogen trucks will be operated in Switzerland by 2025. E), the Toyota Mirai [10], a hydrogen car, released in December 2014 and sold until December 2021 at 17 940 units. F), the Alpha bike, a product from Pragma Industries [11]. It is the first commercially available electrically assisted bike with a fuel cell.

as possible.

The admissible pressure for a tank depends on the material used. The weight of the tank matters for embedded application. The specific energy, i.e. gravimetric density, changes dramatically if the tank weight is taken into account, as in figure 3.

Due to its small size, hydrogen can cross solid walls by diffusion and a liner is needed to limit this phenomenon. The improvement of hydrogen tank over years, using lighter, stronger and less permeable materials led to different types of hydrogen tank, as detailed in table 2.

From a user perspective, the filling time of a hydrogen light duty vehicle is close to the filling time of fossil-fuel based vehicle, between 3 to 5 min, which is a serious advantage on battery-based electric vehicle. During a filling, as the tank is a closed volume, injecting a mass induces a compression of the gas. The inner pressure rises from 20 bar to the target, 700 bar. This compression induces, as thermodynamics can explain, an elevation of the temperature in the tank. The temperature shall be controlled to not exceed the limit recommended by the J2601 standard of the Society of Automobile Engineers (SAE) organism [18]. This standard requests to keep the inner temperature between $-40\text{ }^{\circ}\text{C}$ and $85\text{ }^{\circ}\text{C}$. This is achieved by pre-cooling the injected gas, until $-40\text{ }^{\circ}\text{C}$, and implies an additional energetic cost for the filling. Numerous studies [19–22] highlight the link between the temperature in the tank and the pre-cooling temperature. In figure 4 issued from [19], it is demonstrated that the final temperature in the tank can be reduced in order to stay below the recommended $85\text{ }^{\circ}\text{C}$ by changing the injected temperature. The influence of the initial temperature on the final temperature has been studied in [23]. The exterior environment plays also a role on the thermal equilibrium. Generally colder than inside the tank, it participates to cool the tank but its effect depends on the filling time [24] and the materials used. A faster filling, i.e. higher mass flowrate, does not let sufficient time for the gas to exchange its heat with the walls as studied in [25–27], see figure 5.

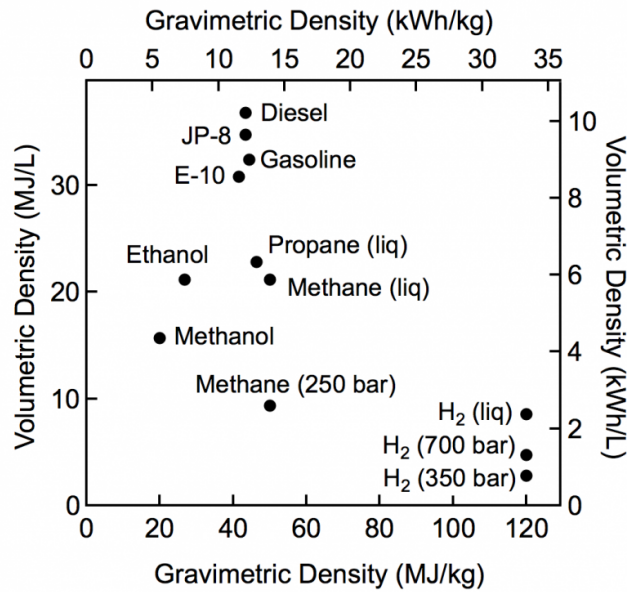


Figure 2 – Comparison of specific energy and energy density for several fuels. The tank weight is not taking into account, issued from [16].

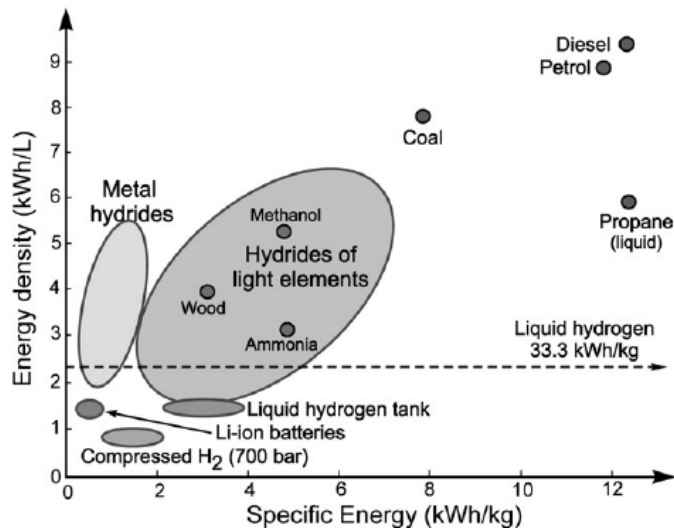


Figure 3 – Comparison of specific energy and energy density for several fuels based on tank weight. The tank weight is taking into account, issued from [15].

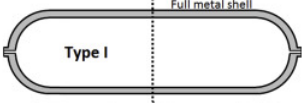
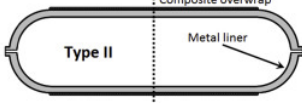
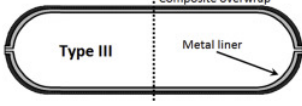
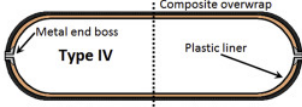
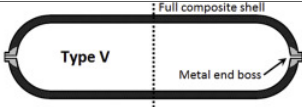
Type	Materials	Typical pressure [bar]	Schematic
I	Metal tank	200	
II	Metal tank with composite over-wrapped	200-300	
III	Metal liner with composite over-wrapped	350-700	
IV	Plastic liner with composite over-wrapped	700	
V	Liner-less tank all composite over-wrapped	700	

Table 2 – Tank illustrations are adapted from [17]. Type IV tank is in bold to highlight it is the only type of tank considered in this study.

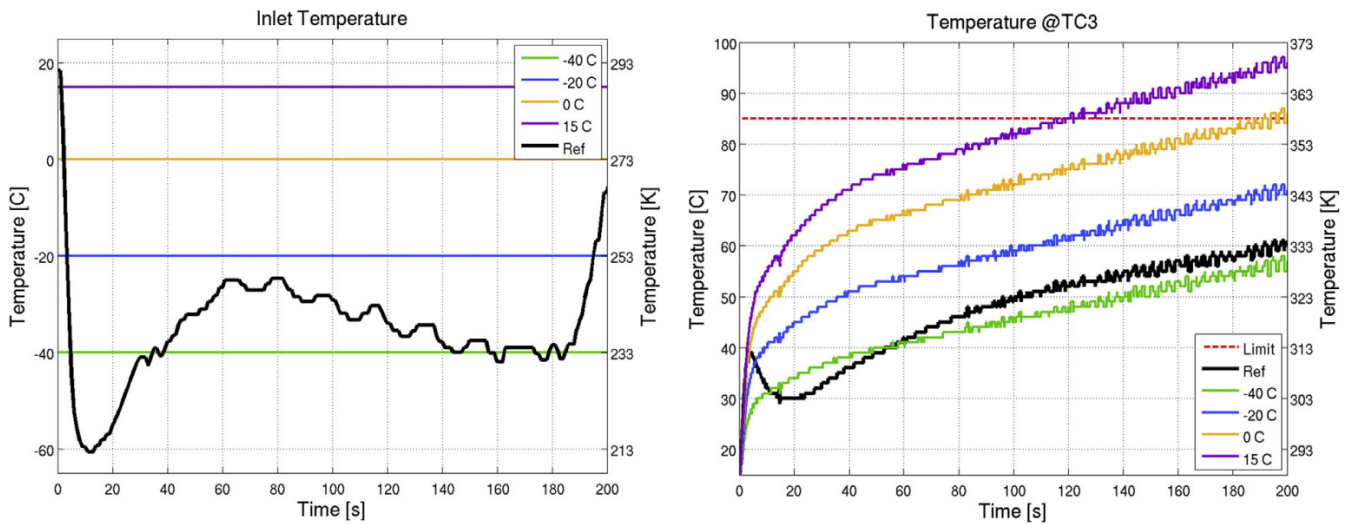


Figure 4 – Injection temperature versus time (left-hand side). Tank gas temperature history during filling (right-hand side), issued from [19].

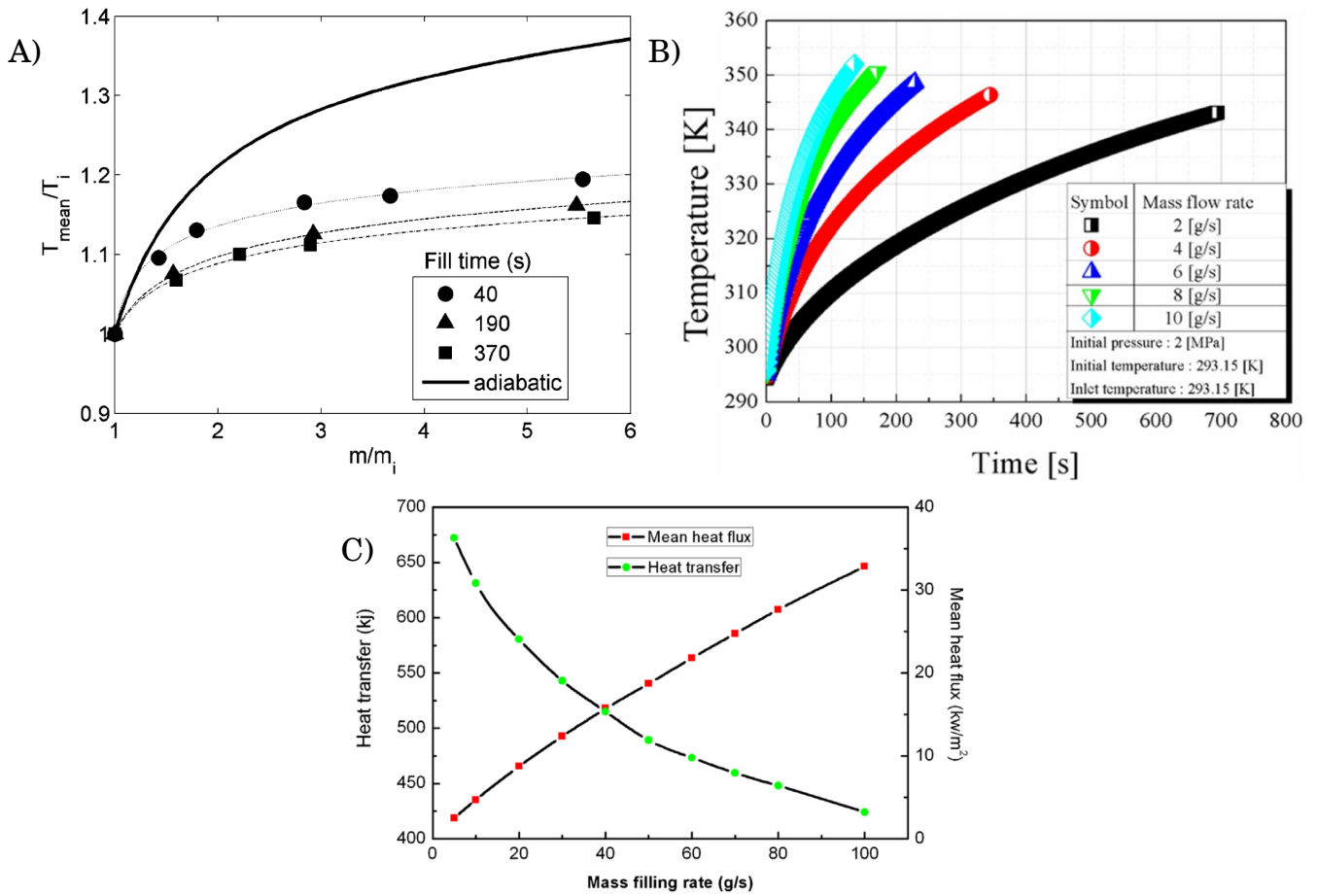


Figure 5 – A), from [25]: Temperature rate between the averaged temperature T_{mean} over the initial temperature T_i as a function of the mass filling ratio in the tank (m over the initial mass m_i). The different filling time are reported using markers. B), from [26]: left hand axis, heat transfer [kJ] as a function of the mass flowrate. C), from [27]: Averaged temperature in the tank as a function of time for different mass flowrate. .

The thermal properties of the solid regions are an important factor on the gas temperature. Due to the plastic liner and the carbon wrap, two materials considered as thermal insulator, type IV tank tends to limit the heat exchange between the gas and the walls.

To avoid the gas temperature exceeding the 85 °C limit, a possible solution is to increase the filling time. However, this solution raises other issues. Longer filling time implies a smaller mass flowrate. The mass flowrate, highlighted in the work of Dickens et al. [28] and reported in figure 6, was identified as a factor of thermal heterogeneity. In [28], among three filling time scenarios (40 s, 190 s, 370 s), the longest one induced the highest vertical stratification for a tank filled horizontally with an axial injection. This effect was attributed to a decrease in thermal mixing between the injected gas and gas in the tank when the mass flowrate is reduced.

Terada et al. [29] precised the importance of the injection velocity on the thermal gradient. To avoid the thermal gradient occurrences on a type IV 65 L tank (0.832 m length and 0.4 m diameter), a velocity of 5 m/s for the injected gaseous hydrogen should be maintained a good mixing and to avoid thermal heterogeneity.

The thermal heterogeneities are challenging when designing a hydrogen filling protocol. Indeed, an important tool to

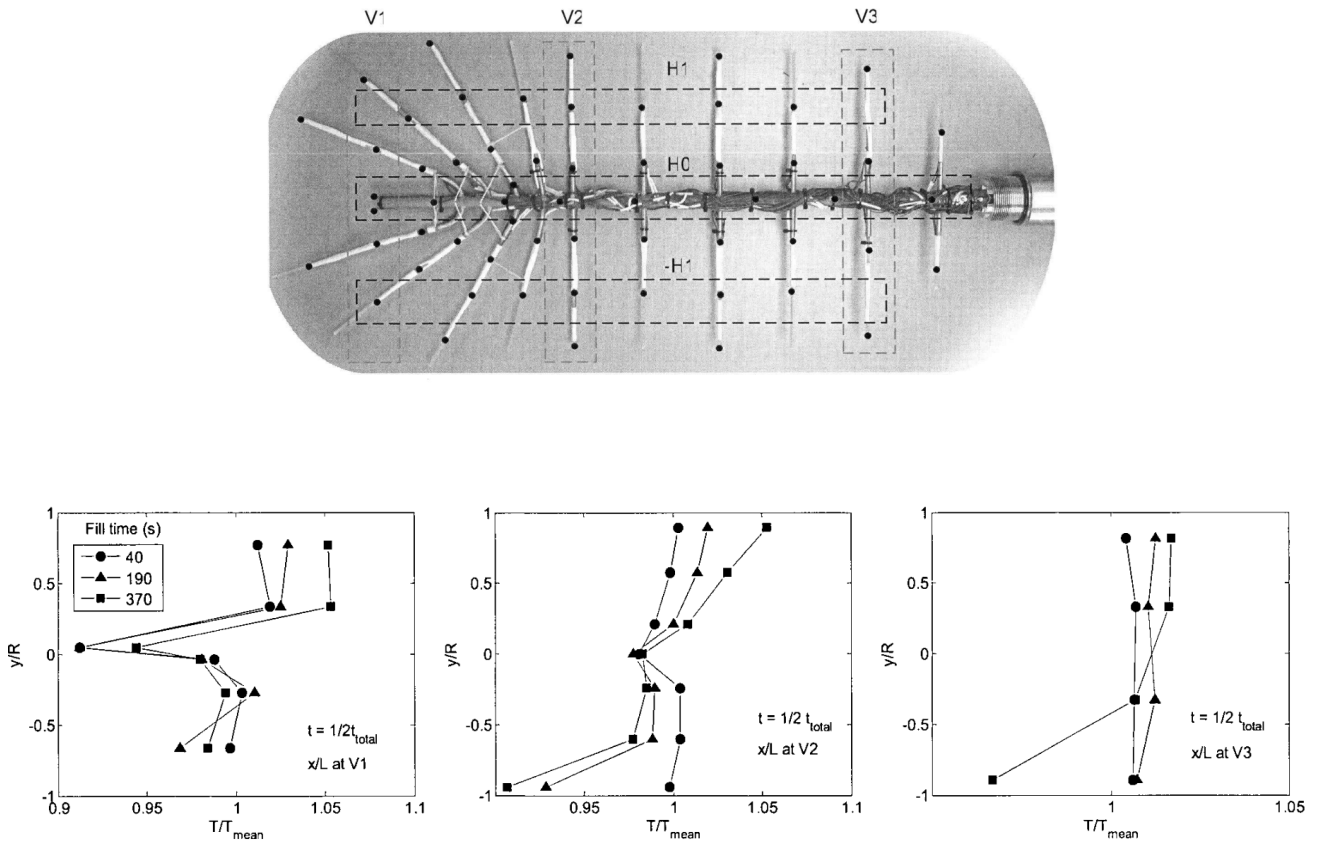


Figure 6 – Issued from [28]: The upper panel shows the tree of thermal probes located inside the tank for the measurements and allows to see the vertical planes V1, V2, V3. The lower panel shows the plot of the measured temperatures along the vertical planes V1, V2, V3 (left, middle, right, respectively) at $t = t_{\text{total}}/2$ for three fills. .

select the optimal injection temperature and mass flowrate, in order to remain in the limits of the J2601 standard, is 0 dimension (0D) model of tank filling. This type of model considers the tank as a unique isothermal volume in which a mass and energy balance is applied. By nature, only estimation of the volume-averaged gas temperature in the tank can be obtained for all filling scenarios, i.e. homogeneous and heterogeneous cases. By construction, occurrence of thermal heterogeneities and therefore local hot spots cannot be captured by 0D models (2.2.2).

To access the complete temperature map inside the tank, 3 dimensions (3D) calculations are required. These calculations are based on computational fluid dynamics (CFD): a numerical tool which expressed the Navier-Stokes equation set, i.e. conservation of the mass, the momentum and the energy on elementary control volumes, i.e. the cells from a mesh describing the 3D geometry studied (2.2.3). The CFD takes into account the complex physics involved in the tank: (i) the numerical problem is unsteady; (ii) the flow is turbulent; (iii) walls are present; (iv) different geometrical scales are considered; (v) the fluid dynamics and thermal behavior interaction. The complexity of the problem raises issues on the capture of thermal gradients by CFD and improvement of the CFD approach is needed. Although CFD remains the proper tool to better understand the thermal gradient mechanism, it requires significant cputime (from weeks to months) to complete one filling scenario. Consequently, it does not allow to do parametric study to optimize the filling process. 0D models are still the best solution for this purpose. Adding to 0D models a knowledge of the heterogeneity generation in the tank would be a valuable new functionality.

Physical System

The object of the study is a type IV 37 L hydrogen tank provided by @Hexagon (0.643 m inner length and 0.269 m inner diameter). During the experiments, the tank is laying along its main axis, the x-axis, in a horizontal position and the incoming gas is injected along the x-axis. The gravity vector \vec{g} is acting vertically along the y-axis. The tank geometry has a circular symmetry around the x-axis. In figure 7, the tank is represented in the plane (x,y). It is composed of 4 or 5 solid regions, depending on the presence of an injection pipe: (i) a composite wrap which undergoes the mechanical constraint due to gas pressure, (ii) a plastic liner which limits the molecular diffusion of hydrogen through the wall, (iii) metallic bosses, (iv) plugs at each tank extremities and (v) a metallic injection pipe (depending on the case). The fluid region is the volume enclosed by the solid regions. The tank is surrounded by air at atmospheric pressure and temperature.

The hydrogen tank is a closed volume. At the beginning of a filling, a hydrogen mass is present and for the current studies the initial pressure is 20 bar. During the filling, gaseous hydrogen from the filling station is injected via an injector pipe in the tank. The mass in the tank then gradually rise. As the volume remains constant, simple thermodynamic considerations can predict an elevation of the pressure and the temperature. The warm gas transfers its heat to the interior walls of the tank, which is conducted through the solid regions until the exterior wall of the tank in contact with the open environment. The physical system is consequently neither closed, neither isolated as the total mass and energy of system are changing through time. Typically, time scale for a small tank filling is about the minute (between 3 min to 10 min in the following considered cases). The temperatures range from $-20\text{ }^{\circ}\text{C}$ to $100\text{ }^{\circ}\text{C}$ and the pressures range from 20 bar to 800 bar. The pressures in bar are absolute pressures for all parts of this document.

Objectives of the thesis and outline

Experimental results from the HyTransfer project [30], detailed in section 2.1.1, revealed important thermal gradients during tank filling. The present work focuses on these thermal gradients. The link between the thermal gradients and

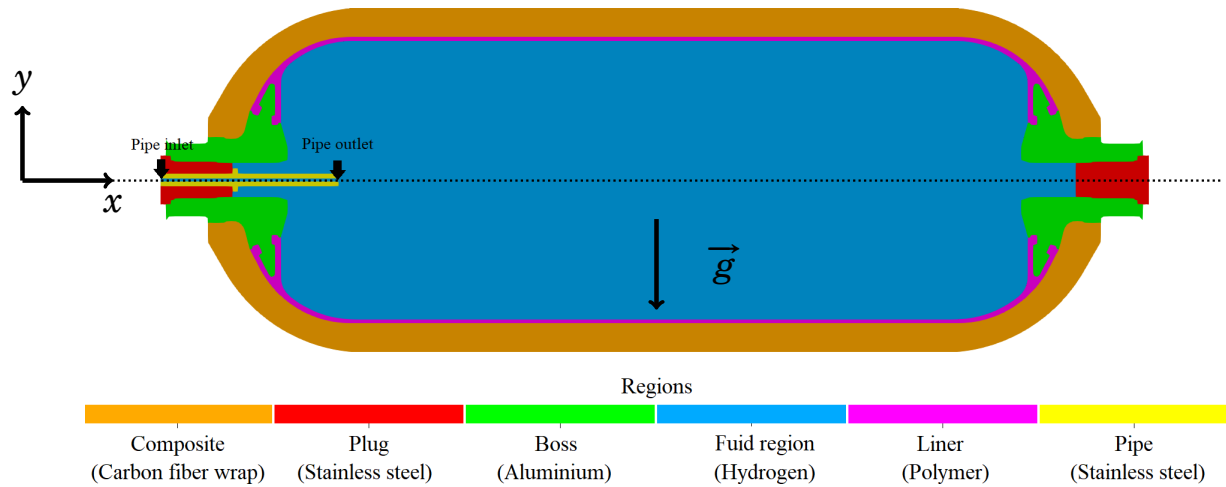


Figure 7 – Type IV 37 L tank with a 3 mm injection cut through the plane (x,y) . The tank geometry has a circular symmetry around the x -axis.

the filling scenario has been established but the underlying mechanisms involved still need be clarified. The purpose of the thesis is to investigate, using 3D CFD simulations, how the vertical thermal gradients are generated. The present study also aims at developing a simple modeling approach, suitable for engineering applications, to predict the vertical thermal gradients.

The present work is structured as follows:

- In chapter 1, a review of literature is carried out to set the state of the art on the problematic of the filling of hydrogen gaseous tank.
- In chapter 2, the resources used in the study concerning the experimental data, the 3D models and the software are detailed. The numerical methods and physical model used in the study are precised.
- In chapter 3, CFD simulations are performed with OpenFOAM, an open-source software. The validation of the solver, mesh and physical models is conducted by comparison with experimental measurements and prior CFD results. The 3D nature of the physical mechanisms is investigated by comparison between 2D-axisymmetric and 3D simulation results.
- In chapter 4, considering the limitations for thermal gradient predictions by CFD simulations identified in chapter 3, an improvement of the turbulent modeling is proposed.
- In chapter 5, based on the insights obtained from CFD results, a reduced model to predict the thermal stratification is developed using a buoyant round jet theory and 0D model.
- In chapter 6, complementary studies have been carried out to develop new approaches and to improve the general comprehension of the subject.

Nomenclature

General variable

β	Isothermal compressibility of the gas	1/K
Δt	Time step	s
$\delta_{i,j}$	Kronecker delta	1/s
\dot{m}_{inj}	Mass flowrate	kg/s
ϵ	Thermal radiation emissivity of the exterior tank wall	1
λ	Thermal conductivity of the gas	W/m/K
λ_w	Thermal conductivity of the wall	W/m/K
μ	Dynamic viscosity of the gas	kg/m/s
Φ	Generic variable name for mathematical application	
Φ_{ext}	Total heat flux at the exterior wall	W
ϕ_i	Face volumetric flux of a mesh cell	m ³ /s
Φ_{rad}	Radiative heat flux at the exterior wall	W
π	Mathematical constant Pi	1
ρ	Density	kg/m ³
ρ_i	Density of a cell in the mesh	kg/m ³
ρ_w	Density of the wall	kg/m ³
ρ_{inj}	Density of the gas at the pipe outlet	kg/m ³
σ	Stefan–Boltzmann constant	W/m ² /K ⁴
τ_{ij}	Viscous stress tensor	kg/m/s ²
c_p	Specific thermal capacity of the gas	J/kg/K
$c_{p,inj}$	Specific thermal capacity of the gas at the pipe outlet	J/kg/K

NOMENCLATURE

$c_{p,i}$	Specific thermal capacity of a cell in the mesh	J/kg/K
$c_{p,w}$	Specific thermal capacity of the wall	J/kg/K
Fr	Froude number	1
g	Gravitational acceleration	m/s ²
g_i	Gravitational acceleration vector	m/s ²
h	Specific enthalpy of the gas	J/kg
k_a	Heat transfer coefficient between the tank and exterior environment	W/m ² /K
k_g	Heat transfer coefficient between the gas and the walls	W/m ² /K
m	Mass of gas in the tank	kg
M_ρ	Matrix form of the density in function the temperature and the pressure	kg/m ³
Nu	Nusselt number	1
p	Pressure	Pa
Pr	Prandtl number	1
q_i	Conductive heat flux of the gas	W/m ²
r	Radial axis	m
Ra	Rayleigh number	1
Re	Reynolds number	1
Ri	Richardson number	1
S_{ij}	Strain rate tensor	1/s
T	Temperature	K
t	Time	s
T_w	Temperature of the wall	K
T_{av}	Averaged temperature of the gas	K
T_{ext}	Temperature of the exterior environment	K
$T_{g,w}$	Temperature at the wall in contact with the gas	K
T_{inj}	Temperature of the gas at the pipe outlet	K
T_{max}	Maximal temperature of the gas	K
T_{min}	Minimal temperature of the gas	K

$T_{w,ext}$	Temperature of the exterior surface of the tank wall, in contact with the exterior environment	K
U	Generic velocity of the gas	m/s^2
u_i	Velocity vector	m/s
u_{inj}	Velocity of the gas at the pipe outlet	m/s
x	Cartesian axis	m
x_i	Generic cartesian coordinate written	m
y	Cartesian axis or the distance from a wall when specified	m
Turbulence variable		
λ_t	Turbulent thermal conductivity	W/m/K
μ_t	Turbulent dynamic viscosity	kg/m/s
ω	Specific rate of dissipation of the turbulence kinetic energy	1/s
τ_w	Wall shear stress	$kg/m/s^2$
ε	Rate of dissipation of turbulent kinetic energy	m^2/s^3
C_f	Skin friction coefficient	1
k	Turbulence kinetic energy	J/kg
L_t	Turbulent length scale	m
L_{vK}	Von Karman length scale	m
Pr_t	Turbulent Prandtl number	1
u^+	Friction velocity	1
U_i	Reynolds averaged velocity vector	m/s
u_{tau}	Friction velocity	m/s
y^+	Dimensionless distance from the wall	1
Geometrical parameter		
$\frac{L}{D}$	Geometrical ratio of the tank	1
D	Internal tank diameter in the context $\frac{L}{D}$, diameter of the pipe in the context of a scenario name, e.g. $D3Q8$	m
D_{ext}	External tank diameter	m
d_{inj}	diameter of the pipe section	m
D_{int}	Internal tank diameter	m

NOMENCLATURE

L	Internal tank length	m
r_{inj}	Radius of the pipe section	m
S_w	Interior surface of the tank, i.e. interior surface in contact with the gas	m ²
S_{ext}	Exterior surface of the tank	m ²
V	Volume of the tank	m ³
v_i	Volume of a cell in the mesh	m ³
Buoyant round jet model		
α	Entrainment rate	1
λ	Difference of variance between the velocity and density Gaussian profile	1
ρ_{av}	Averaged gas density	kg/m ³
ρ_{grad}	Density gradient,	kg/m ³
ρ_m	Median density of the density gradient, i.e. $\rho_m = \rho_{grad}(0)$	kg/m ³
ρ_{ref}	Reference density	kg/m ³
ρ_s	Density on the jet centerline	kg/m ³
θ	Angle between the jet centerline and the x-axis	rad
b	Radius of the jet	m
g'	Reduced gravity	m/s ²
g_c	Reduced gravity on the jet centerline	m/s ²
J	Buoyancy flux divided by a reference density	m ⁴ /s ²
L_{pipe}	Pipe length inside the tank	m
L_{tank}	Internal tank length	m
L_{ZFE}	length of the zone of flow establishment	m
M	Mass flux divided by a reference density	m ⁴ /s ²
p_{tank}	Averaged gas pressure	Pa
Q	Mass flux divided by a reference density	m ³ /s
r_{inj}	Radius of the pipe section	m
R_{int}	Internal tank radius	m
s	Curvilinear abscissa of the jet trajectory	m

T_{inj}	Temperature at the injector	K
T_{tank}	Averaged gas temperature	K
u_0	Velocity at the pipe outlet	m/s
u_r	Radial velocity on the jet centerline	m/s
u_s	Axial velocity on the jet centerline	m/s
u_{critic}	Critical velocity below which the thermal stratification occurs	m/s
Complementary studies		
α	Parameter to fix, used in the Tikhonov regularization method	1
λ_c	Thermal conductivity of the composite	W/m/K
λ_l	Thermal conductivity of the liner	W/m/K
ϕ_{ext}	Temperature on the exterior composite wall	W/m ²
ϕ_{f-l}	Heat flux at the interface between the gas and the liner	W/m ²
ϕ_{l-c}	Heat flux at the interface between the liner and the composite	W/m ²
ρ_c	Density of the composite	kg/m ³
ρ_l	Density of the liner	kg/m ³
$\sigma_{T_{av}}$	Standard deviation around the gas temperature	K
$\tau_{diffusion}$	Characteristic time of the thermal diffusion	s
Θ	Laplace transform of a temperature θ	
θ_{f-l}	Different of temperatures $T_{f-l} - T_{f-l}(0)$	K
θ_{l-c}	Different of temperatures $T_{l-c} - T_{f-l}(0)$	K
θ_{l-c}^*	Different of temperatures from the experimental data	K
A	Matrix	1
c_{p_c}	Specific thermal capacity of the composite	J/kg/K
c_{p_l}	Specific thermal capacity of the liner	J/kg/K
f	Frequency of the jet oscillation	1/s
H	Total enthalpy of a tank region	J
$H(p)$	Transfer function	
$h(t)$	Transfer function in time domain	

NOMENCLATURE

n	Number of value measured	1
p	Complex variable used in the Laplace transform	
R	Tikhonov regularization matrix	1
T_{ext}	Temperature on the exterior composite wall	K
T_{f-l}	Temperature at the interface between the gas and the liner	K
T_i	Temperature at the center of a cell in the mesh	K
T_{l-c}	Temperature at the interface between the liner and the composite	K
v_i	Volume of a cell in the mesh	m ³

Acronym

0D	Zero Dimension
1D	One Dimension
2D	Two Dimensions
3D	Three Dimensions
ALAT	Air Liquide Advanced Technologies
AMI	Arbitrary Mesh Interface
CAD	Computer-aided design
CALMIP	CALcul en MIIdi Pyrénées (French)
cDNS	coarse Direct Numerical Simulation
CFD	Computational Fluid Dynamics
CFL	Courant, Friedrichs and Lewy number
CPU	Central Processing Unit
DNS	Direct Numerical Simulation
EOS	Equation Of State
ET	Energie Technologie
IJHE	International Journal of Hydrogen Energy
JRC	Joint Research Centre of the european commission
NIST	National Institute of Standards and Technology
OpenFOAM	Open-source Field Operation And Manipulation

PIMPLE PISO + SIMPLE

PISO Pressure-Implicit with Splitting of Operators

SAE Society of Automotive Engineers

SAS Scale-Adaptive Simulation

SDFT Sliding Discrete Fourier Transform

SIMPLE Semi-Implicit Method for Pressure Linked Equations

SST Shear-Stress Transport

TGCC Très Grand Centre de Calcul (French)

URANS Unsteady Reynolds-Averaged Navier–Stokes

ZFE Zone of Flow Establishment

Dimensionless numbers

The dimensionless numbers are the proper tool to highlight which phenomenon is dominant in a study. They are built using characteristic values as a velocity or a length, selected regarding the study case.

The Reynolds number Re , characterizes the ratio of the inertia forces over the viscous forces:

$$Re = \frac{\rho UL}{\mu}, \quad (1)$$

where ρ [kg/m^3] is a density, U [m/s] a velocity, L [m] a length and μ [$kg/m/s$] a dynamic viscosity.

The Froude number Fr , characterizes the ratio of the inertia forces over the buoyancy forces:

$$Fr = \frac{U}{\sqrt{g \frac{\rho_1 - \rho_2}{\rho_1} L}}, \quad (2)$$

where U [m/s] is a velocity, L [m] a length, ρ_1 [kg/m^3] a reference density, ρ_2 [kg/m^3] a secondary density, and g [m/s^2] the gravity acceleration. It is related to the Richardson number Ri , as

$$\begin{aligned} Ri &= \frac{g \frac{\rho_1 - \rho_2}{\rho_1} L}{U^2} \\ &= \frac{1}{Fr^2}. \end{aligned} \quad (3)$$

The Rayleigh number Ra , characterizes the ratio of the buoyancy forces over the viscous forces:

$$Ra = \frac{g \rho \beta}{\mu \alpha} (T_w - T_f) L^3, \quad (4)$$

where g [m/s^2] is the gravity acceleration, ρ [kg/m^3] the gas density, β [$1/K$] the thermal expansion coefficient of the gas, α [m^2/s] the thermal gas diffusivity, μ [$kg/m/s$] the dynamic gas viscosity, T_w [K] the temperature at a wall, T_f [K] the temperature in the fluid bulk and L [m] a length.

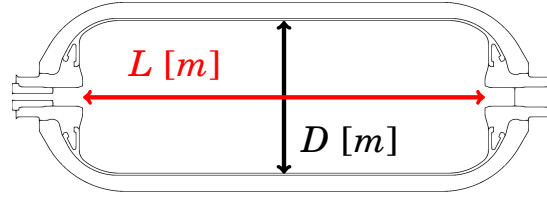


Figure 8 – The tank geometry main length is L and the inner diameter is D .

The Prandtl number Pr , characterizes the ratio of the thermal diffusion rate over the viscous diffusion rate:

$$Pr = \frac{c_p \mu}{\lambda}, \quad (5)$$

where c_p [$J/kg/K$] is a specific heat capacity, μ [$kg/m/s$] a dynamic viscosity and λ [$W/m/K$] a thermal conductivity.

The Nusselt number Nu , characterizes the ratio of a forced convection heat flux over a conduction heat flux:

$$Nu = \frac{hL}{\lambda}, \quad (6)$$

where h [$W/m^2/K$] is a convective heat transfer, L [m] a length and λ [$W/m/K$] a thermal conductivity.

The Strouhal number St , characterizes the ratio between an oscillation time period and the time of flow transport:

$$St = \frac{fL}{U}, \quad (7)$$

where f [s^{-1}] is a frequency, L [m] a length and U [m/s] a velocity.

The geometrical ratio $\frac{L}{D}$ is a dimensionless value used in order to characterize the shape of a tank. It is based on dimensions in the fluid region corresponding to the ratio between the main tank length over the tank inner diameter (figure 8).

The Courant, Friedrichs and Lewy (CFL) number is a limiting factor for the performance of numerical schemes. Depending on the method used to solve a discretised equation, a different maximum value of this number can be tolerated. It is defined as

$$CFL = \frac{\Delta t}{2v_i} \sum_{faces} |\phi_i|, \quad (8)$$

where v_i [m^3] is the cell volume and ϕ_i [m^3/s] is volume flux crossing a cell face.

Chapter 1

Literature review

This section is dedicated to a literature on the filling of compressed-gas tank for hydrogen applications. The first section is dedicated to the understanding of thermal heterogeneities occurring during the filling stage. The second section is dedicated to the numerical approaches related to the prediction of the physics involved. Unless it is specified, the tanks are filled with hydrogen, horizontally and with an axial injector. Connected to the following content, two review articles [31, 32] are available in the literature. In [31] the focus was on the different solutions found in the literature for the modeling of tank filling. They listed heat transfer coefficients for 0D model, the turbulence models for computational fluid dynamics (CFD) and equations of state (EOS) for the hydrogen. In [32] the focus was on the impact on the gas temperature in the tank of the tank dimension, the material properties, the initial pressure, the filling rate and the inlet temperature.

1.1 Occurrence of the thermal heterogeneity during a filling of compressed-gas tank

For first time the appearance of a vertical gradient during the filling stage of hydrogen tank was mentioned in Dicken et al. [25]. They carried out experimental measurements on a type III 74 L tank with a geometrical ratio $\frac{L}{D} = 2.49$. In the range [100 bar; 350 bar], they used different pressure ramp rates corresponding to filling times (40 s, 190 s, 370 s). They found a link between the mass flowrate and the vertical thermal stratification. They explained that the phenomenon by a consequence of the buoyancy forces on the thermal distribution for longer filling time, i.e. smaller mass flowrate, which corresponds to lower gas injection velocities. To investigate the inner temperature disparity due to the pre-cooling gas injected into the warm tank, a 2D axis-symmetric CFD study was carried out. A conical temperature gradient at the injection was highlighted. They used the CFD software Fluent 6.2 and the standard $k - \epsilon$ turbulence model [33]. The Redlich-Kwong EOS [34] is used in this study.

Terada et al. [29] investigated the effect of the velocity injection on a type IV 65 L tank with as geometrical ratio $\frac{L}{D} = 2.04$. It was filled from 20 bar to 350 bar. Using different pressure ramp rates (2.5 MPa/min, 6.6 MPa/min, 12.5 MPa/min) and different injection diameters (4.5 mm, 5.2 mm, 7 mm, 8.5 mm, 10 mm). They found that the injection velocity must be maintained at above 5 m/s to keep a homogeneous temperature in the tank. The injection velocity u_{inj} was calculated using the mass flowrate Q , the injected gas density ρ_{inj} was calculated using the pre-cooling

gas temperature and the tank pressure and the injection radius r via the relationship:

$$u_{inj} = \frac{\dot{m}_{inj}}{\rho_{inj} \pi r_{inj}^2} \quad (1.1)$$

They also investigated the effect on the thermal heterogeneity of the injection orientation. They kept the same injection diameter and filling rate as a scenario leading to a homogeneous thermal state but they injected radially (90° upward, 90° downward, 90° sideways). They found no remarkable differences, the thermal state remained homogeneous.

Kim et al. [35] carried out 3D CFD studies on a type IV 72 L tank, loaded until 350 bar and compared with experimental measurements. They used the CFD software Fluent 6.2 and the standard $k-\varepsilon$ turbulence model. Their hybrid (tetrahedral and hexahedral) mesh included 300 000 cells. The Redlich-Kwong EOS [34] was used. They pointed out the occurrence of vertical thermal gradients. They found a temperature gradient of 10°C between the upper part and the lower part of the tank by CFD whereas experimentally the gradient was 6°C . The effects of the buoyancy on the thermal fields was clearly visible, with a deflection of the cold gas jet toward the lower part of the tank, due to the negative buoyancy.

Immel et al. [36] carried out 3D CFD studies on a type IV 129 L tank, loaded until 700 bar and compared with experimental measurements. They used the CFD software Fluent 12 and the standard $k-\varepsilon$ turbulence model. Their mesh contained a total of 2.4 million cells in the solid regions and 1.4 million cells in the fluid region. The Aungier-Redlich-Kwong EOS [37] was used. The deflection of the injected cold gas is visible at 177.8 s of the filling. It is not possible to estimate the thermal gradient due to the saturation of the color map used for the temperature field displayed. After the filling, at 252 s, the difference in temperature between the upper part and the lower part was approximately 15°C .

Takagi et al. [38] carried out 3D CFD studies on a type III 34 L tank, loaded until 350 bar and compared with experimental measurements. They used the CFD software OpenFOAM and the standard $k-\omega$ Shear-Stress Transport (SST) turbulence model. Their mesh contained approximately 20 000 cells in the fluid region. The conduction into the wall was not considered; i.e. an adiabatic condition was set. The ideal gas law was used. The inlet diameter was 14 mm. The CFD gave temperature largely higher than for the experimental measurements, approximately 40°C . This is probably due to the adiabatic condition set at the inner tank wall. The vertical thermal gradient found experimentally was at the end of the filling, i.e. $t = 80\text{s}$, approximately 10°C . The vertical thermal gradient found numerically was at the end of the filling approximately 20°C . The overestimation of the vertical gradient can be explained by an averaged temperature 40°C higher for the CFD inducing a more important effect of the buoyancy force. The injected cold gas is be more deflected toward the lower part of the tank. The vertical thermal gradient is consequently more important.

Setoguchi et al. [39] carried out 3D CFD studies on a type III 74 L tank, loaded until 350 bar and compared with experimental measurements from Dicken et al. [25]. They used the CFD software Fluent 13.0 and the $k-\omega$ SST turbulence model. Their mesh contained a total of 96 772 hexahedral cells in the solid regions and 209 360 hexahedral cells in the fluid region. The Redlich-Kwong EOS [34] is used. Their work was completed in study [40] where the conical cold jet was displayed and a jet oscillation in the tank can be identified.

During the HyTransfer project [30], different tank types and geometries were investigated [41]. A vertical thermal gradient was observed in a type IV 37 L tank ($\frac{L}{D} = 2.4$) and type IV 531 L tank ($\frac{L}{D} = 5.6$). Different inlet diameters (3 mm, 6 mm, 10 mm) as well as different mass flowrates (8 g/s and 2 g/s) were used to investigate the injection velocity influence. The rise of the thermal heterogeneity with the decrease of the injection velocity was observed and the criterion of Terada et al. [29] of 5 m/s for the injection velocity to keep a thermal homogeneous behavior in the tank was confirmed for the different tanks involved in the studies [42–44].

Yamada et al. [45] carried out experimental measurements on a type IV 11 L tank, loaded until 700 bar developed for

motorcycles. They used an injector oriented at 45° upward in order to improve the homogeneity of the gas in the tank. They measured temperature at three locations arranged vertically inside the gas to capture vertical thermal gradients. They investigated the influence of intermittent filling scenarios on the final temperature. The filling is stopped during a waiting phase before being continued. After a filling phase, i.e. at the beginning of a waiting phase, they observed a thermal vertical stratification appearing. During the stratification process, the maximum temperature did not increase: the stratification grew due to the decrease of the temperature of the lowermost probe. This showed as soon as the injection stops, the natural convection tends to vertically stratify the thermal distribution in the tank. For their 3 min filling scenario, they concluded that the intermittent filling was not efficient to reduce the final temperature if executed after 10 s. The influence of an intermittent filling was also investigated by Wu et al. [46]. They carried out 3D CFD studies on a type III 134 L tank, loaded until 700 bar. They used the CFD software Fluent 2019 and the standard $k - \epsilon$ model. Their mesh contained a total of 505 286 cells (no precision on the region concerned but figure 4 let suggest it is in the fluid region). The National Institute of Standards and Technology (NIST) gas property data was used for hydrogen EOS. They used an injector oriented 30° upward. They investigated intermittent filling scenario based on fixed filling time but using different pressure rates and waiting phases leading to the same total mass injected. They found little effects on the final gas temperature depending on the intermittent filling scenario. It can be seen their thermal distribution in the fluid region is unusual. The cold gas injected upward impacts the upper wall of the tank and seems to be absorbed instead of being deflected by the wall. This could be explained by the use of the standard $k - \epsilon$ turbulence model which produces coarser prediction than the $k - \omega$ SST model for near wall fluid dynamics. More investigations of the accuracy of the CFD would be valuable to confirm the validity of the thermal distribution obtained by Wu et al. [46].

The Joint Research Centre (JRC) of the European Commission, gave many contributions on the topic of hydrogen tank filling [19, 20, 23, 44, 47–56]. In particular, they investigated, using 3D CFD studies on the half of geometrical domain, the effect of the injector orientation on the thermal stratification in a conference article [54] completed with a journal article [55]. In [54] and [55], they worked on a type IV 37 L tank issued from HyTransfer. They used the CFD software CFX V15.0 and the $k - \omega$ SST $\gamma - Re_\theta$ turbulence model [57, 58]. This turbulence model is designed to capture the turbulent transition toward a laminar regime and to improve the simulation in flow stagnation area. The comparison between the CFD result and the experimental data demonstrated the capture of the thermal gradient was underestimated in [54]. They found at the end of the filling, between the top and the bottom of the tank, 26°C for the CFD calculation and 31°C for the experimental measurements. They judged the overall CFD model satisfactory to investigate the effects of other injector orientations where no experimental data were available. For a 6 mm diameter injector at 45° upward, the thermal gradient in the tank was reduced. They found at the end of the filling, between the top and the bottom of the tank, 7°C instead of the 26°C with the axial injector. In [55] the work was extended for 3 mm diameter injector. The tendency was confirmed: the upward injection produced less thermal stratification. For different initial temperatures, the study demonstrated a linear link between the initial gas temperature and the magnitude of the thermal gradient. The linear line slope was dependent on the injector orientation. Injecting upward reduced the line slope.

On the type IV 37 L issued from the HyTransfer project [30], Zaepffel et al. [59] carried out 3D CFD studies on the half of geometrical domain. They used the CFD software Fluent 16 and the $k - \omega$ SST turbulence model. They obtained similar results as the JRC in [54], i.e. good agreement with the experimental measurements for the temperature probe in the gas until the onset of stratification. The vertical thermal gradient was underestimated after.

Li et al. [60] carried out 3D CFD studies on a type III 70.6 L tank with geometrical ratio $\frac{L}{D} = 3.6$. They used the CFD software Fluent 17.0 and the Realizable $k - \epsilon$ turbulence model. The Redlich-Kwong EOS is used. They used 277 072 cells for the mesh. They aimed at investigating during a 180 s tank filling until 700 bar the effects of using different porous infills inside the tank volume. Four cases with different infill properties were simulated and compared. The presence of the porous infill reduced the convective heat transfer and resulted in a lower wall temperature and higher gas

temperature. The porous infill reduced the thermal mixing allowed by the turbulence and the convection, and the vertical thermal gradient increased. A comparison between 2D and 3D CFD approaches was carried out. As the tank was filled horizontally, a 2D-axisymmetric CFD cannot capture the buoyancy effects and the vertical thermal gradient cannot be predicted.

Concerning another kind of heterogeneity, an interesting note can be found in the work of Muto et al. [61] about the mixing consideration in the tank. Muto reminds that a 0D model is based on the assumption that the gas temperature is uniform in the tank, i.e. the incoming gas expands and diffuses instantaneously throughout the gas in the tank. He did not find thermal heterogeneity (not greater than 0.28 °C). However, He reported that W. C. Reynolds [62] found considerable temperature gradients throughout the filling stage. Muto assumed the difference could be explained by the difference of tank geometry used by W. C. Reynolds, inducing a piston effect which could occur when the inner jet width becomes larger than the tank diameter. This would create a horizontal gradient. In the final public report [42] from the HyTransfer project [30] was reported for a 531 L tank ($\frac{L}{D} = 5.6$), the phenomenon appeared when injection velocities are high (above 100 m/s). A hot spot was trapped at the opposite extremity from the injector. The incoming cold jet failed to refresh this remote area. The phenomenon appeared in the work of Qianfeng et al. [63] or in the work Ramasamy et al. [64]. For the latter, using the same filling condition, the temperature elevation in the opposite area from the injector was globally increasing with the length of the tank. The length of the tank was increased from 2.4 times the tank diameter to 8 times. The study was carried out using 2D axis-symmetric CFD approach and cannot include the effect of gravity for horizontally filled tank. For horizontally filled tank, the thermal distribution should be affected by the gravity, especially in remote areas where the buoyancy forces drive the flow. 2D axis-symmetric CFD constrains the flow dynamics to be axis-symmetric, i.e. the incoming jet remains on the main tank axis. The piston effect should be studied using 3D simulations to fully understand the underlying mechanism.

1.2 Numerical approaches

During a filling of a gaseous tank, the inner thermal behavior is affected by different parameters. Their nature can be (i) geometric: the length and diameter of the tank, the injection diameter, the tank volume etc; (ii) related to the materials involved: type I to V tank, material of the bosses etc; (iii) based on the filling conditions: injection temperature, exterior temperature, mass flowrate, initial pressure and temperature in the tank etc. To test these different parameters, two different approaches exist: the experiment approach and the simulation approach. The advantage of experiment measurements is to avoid modeling the complex physic to extract insightful values. The disadvantages are:

- (i) The information extracted is partial with no information on the gas velocities and limited number of temperature values into the tank.
- (ii) The probes are generally located on a thermocouple tree, see figure 1.1, which is an intrusive device for the inner flow, consequently an experimental set up biases the real filling condition.
- (iii) The temperatures at the liner inner wall, in contact with the gas, are difficult to measure.
- (iv) Probes are affected by measurement uncertainties such as the probe accuracy, the thermal inertia of the probe, etc.
- (v) High-pressure hydrogen represents a hazard risk, consequently safety measures are required and complicates the experimental set-up [56].

Due to these experimental obstacles, numerical approaches are advantageous even though they need experimental data to be validated first. Among different types of approaches, the simplest and the fastest (some minutes) is 0D model.

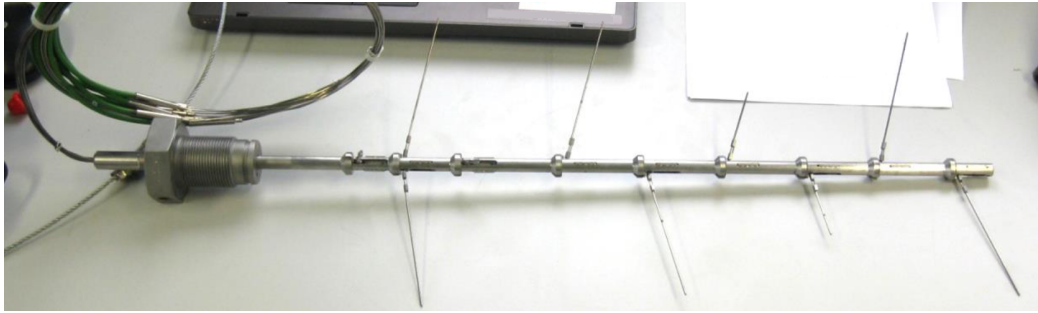


Figure 1.1 – Thermocouple tree used in the HyTransfer project [41].

Based on the mass and the energy balance equations, these models can predict rapidly the averaged temperature and pressure in the tank. They can be used in parametric studies investigating all filling parameter listed above and detecting if the averaged temperature exceeds the recommended $85\text{ }^{\circ}\text{C}$. They need a heat transfer coefficient between the gas and the wall which must be extracted from experiment or CFD.

The CFD approach is based on the mass, the momentum and the energy balance equations. The CFD approach can be 2D-axisymmetric, i.e. round symmetry around the main tank axis. A 2D-axisymmetric simulation takes from several days to several weeks. It cannot include the gravity for horizontal filling. This approach allows to obtain the heat transfer between the gas and the fluid. However, the approach is not able to represent the thermal stratification for horizontal filling. This approach is also not suitable for other than axial injection direction. The CFD approach can be 3D, i.e. the full geometrical domain can be selected. A symmetry assumption can be applied in the plane containing the gravity, to select the half of geometrical domain to reduce the computational cost. A 3D CFD simulation takes from weeks to months to model a complete filling.

1.2.1 0D models

A 0D approach for modeling the filling of a tank can be found in the work of W. C. Reynolds [62]. The document was not accessible. Although, comments on the document can be found in the work of Muto et al. [61]. Muto et al. [61] compared a 0D model to experimental data for a 676.8 L tank loaded with air from 2 bar to 8 bar with 4 temperature probes in the fluid region. They used a correlation of forced convection [65] for the heat transfer coefficient to model the heat exchanged between the gas and the wall. They found a good agreement between the averaged temperature predicted by the 0D model and the experimental measurement at the end of the filling. At the initial stage of the filling, the prediction is coarser.

The first application of a 0D model on hydrogen tank has been found in the work of Perret et al. [66]. The wall was considered to be one dimensional (1D), i.e. conduction was allowed in the radial direction, assuming the tank geometry to be a cylinder. The hydrogen cannot be considered as a perfect gas at high pressure and the Redlich-Kwong equation (EOS) [34] was selected.

Melideo et al. [19] compared different real gas EOS for hydrogen (standard Redlich-Kwong [34], Aungier Redlich-Kwong [37], Soave Redlich-Kwong [67] and Peng-Robinson [68]) and the ideal gas law using 2D simulations. Using the Aungier Redlich-Kwong EOS, they found less than $5\text{ }^{\circ}\text{C}$ of difference on the final temperature with experimental data. The other real gas EOS gave similar good results. For the ideal gas law, they found more than $10\text{ }^{\circ}\text{C}$ of difference on the final temperature with the experiment. This demonstrated the importance of using real gas EOS in numerical method related to high pressure hydrogen.

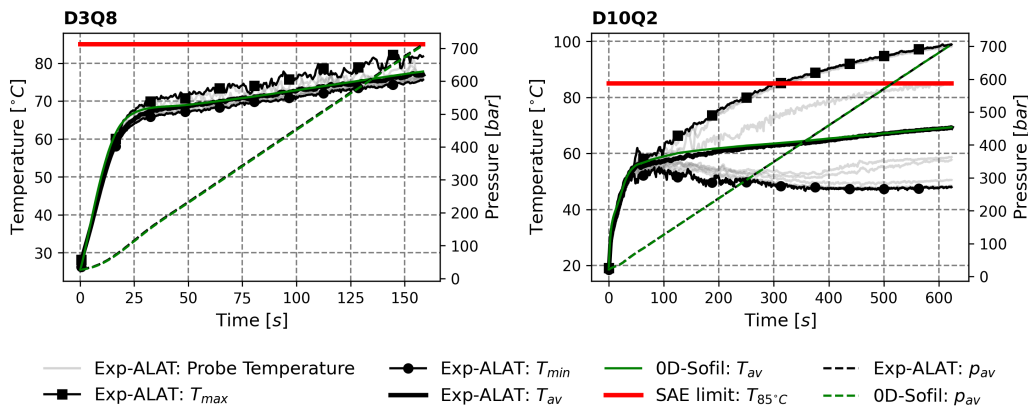


Figure 1.2 – Comparison between SOFIL [43, 70] modeling results and experimental results on two filling scenarios from HyTransfer project [41]. The D3Q8 scenario (injection diameter 3 mm and averaged mass flowrate 8 g/s) leads to a homogeneous thermal behavior and the D10Q2 scenario (injection diameter 10 mm and averaged mass flowrate 2 g/s) leads to vertical thermal gradient which locally exceeds the SAE [18] recommendation of 85 °C.

The heat transfer coefficient needed to close the equation system of 0D model for tank filling is a subject of improvement. Perret et al. [66], used the maximum between the heat exchange coefficient issued from a forced convection correlation and the one issued from a natural convection correlation, which is an improvement compared to Muto et al. where only a forced convection correlation was used. Advanced investigation on the competition between forced convection and the natural convection in the tank was carried out by Woodfield et al. [69]. They used an experimental set-up where a 1.4 L test chamber ($\frac{L}{D} = 2.8$) could be loaded until 400 bar using different gases (hydrogen, nitrogen and argon). The test chamber was filled vertically from the top with an axial injector. They deduced a mixed convection correlation to evaluate a heat transfer coefficient for charging vessel. The effect of the Prandtl number on the heat transfer was excluded because the different gas involved in the study had a similar Prandtl number value.

Air Liquide developed its own 0D model [43, 70], SOFIL, for **soft** for **filling**, which is able to simulate filling stage, waiting stage and emptying stage of gaseous tank. The walls are modeled using a 1D model, i.e. they are considered 1D in the radial direction (walls width) and discretized along the radial direction. A reading table method of the hydrogen thermo-properties from NIST is used as EOS. A modified heat transfer coefficient from Woodfield et al. [69] is used. This tool is used in this work, therefore more details will be given in a dedicated section. It shows a good agreement with the experimental measurements for the averaged values. For example, for the 37 L tank provided by ©Hexagon issued from the HyTransfer project [41], for the D3Q8 scenario (injection diameter 3 mm and averaged mass flowrate 8 g/s) and the D10Q2 scenario (injection diameter 10 mm and averaged mass flowrate 2 g/s) the averaged gas temperature and pressure are well predicted, see figure 1.2. When vertical thermal gradient occurs, the maximum temperature can largely exceed 85 °C, see figure 1.2 left view, and the knowledge of the averaged temperature is not sufficient. Consequently, CFD needs to be carried out to predict the local maximal temperature.

To conclude this section, recent publications [22, 71–76] are still using a 0D model approach, mostly to design a more efficient filling protocol. The general principle of the model remains the same, as well as its limitation.

1.2.2 CFD models

The tank is generally round symmetric, i.e. symmetrical around its main axis. In order to limit the computational cost required to run the CFD simulation, the assumption of a 2D axis-symmetric flow in the tank was used for the earlier CFD studies [77, 78]. This approach was recently employed by Ramasamy et al. [64] to perform parametric studies within a small parameter range.

The flow in the tank is turbulent and requires an adequate turbulence model. The Unsteady Reynolds-Averaged Navier–Stokes (URANS) approach is selected to limit the computational cost. Initially the $k - \varepsilon$ Realizable model was designated by Suryan et al. [78] as the most efficient turbulence model for the filling of hydrogen tank. It showed the best execution time and gave reasonable accuracy. The influence of the different models on temperature distribution is not investigated in [78]. The $k - \varepsilon$ Realizable model was recently used for the study of temperature distribution during filling stage of hydrogen tank in [46, 64, 79]. This model captures correctly the round jet physic [80] which is an important part of the fluid dynamics at play in the tank. On walls, the $k - \varepsilon$ Realizable turbulence model needs a wall function to reproduce the effect of the boundary layer. This could lead to coarser predictions of the heat transfer between the gas and the walls. In [81], it is recommended to use the $k - \omega$ SST turbulence model to improve this aspect.

The 2D axis-symmetric CFD approach allows to extract a heat transfer coefficient between the gas and the wall, as done in [77]. The heat transfer coefficient can be used to close the equation system implemented in 0D models. The main disadvantage of the 2D axis-symmetric simulation is the impossibility to capture gravity effects for horizontally filled tank. It is also impossible to use a non axial injector. When compared with 3D simulations, the 2D axis-symmetric simulations gave valid insights on the physic while the simulation case lead to a homogeneous thermal behavior [19] but cannot capture the physic when thermal heterogeneities occurred [60, 82].

Gravity effects for horizontally filled tank, need 3D simulations: as the cold injection jet is deflected toward the lower part of the tank, due to negative buoyancy forces, the phenomenon requires 3D simulations to be captured. In figure 1.3 issued by ALAT [59], the cold injection jet can be seen on the right panel thanks to velocity stream-lines. The stream-lines are deflected toward the lower part of the tank. This breaks the horizontal symmetry and a vertical stratification appears on the left panel where the thermal field is displayed. The 3D CFD approach captures well the onset of the stratification [54, 55, 59]. The thermal stratification magnitude, i.e. the upper part maximum temperature and the lower part minimum temperature prediction, is however underestimated in [54, 55, 59]. This means the lower part minimum temperature is predicted warmer and the upper part maximum temperature is predicted colder. The averaged temperature is correctly predicted when compared with experimental measurements. This is problematic when the purpose of the CFD is to detect if locally the temperature exceeds $85\text{ }^{\circ}\text{C}$. Advanced turbulence model, i.e. $k - \omega$ SST $\gamma - Re_{\theta}$ turbulence model [57, 58], was used to improve this aspect in [54, 55] but led to an underestimation of the thermal gradient (between the top and the bottom of the tank at the end of the filling $26\text{ }^{\circ}\text{C}$ for the CFD results and $31\text{ }^{\circ}\text{C}$ for the experimental measurements). As no comparisons with previous turbulence models, such as the $k - \omega$ SST or the $k - \varepsilon$ Realizable are available, the improvement potential given by the $k - \omega$ SST $\gamma - Re_{\theta}$ turbulence model cannot be evaluated. Finally, the improvement potential for thermal gradient capture of advanced turbulence model requires additional investigations.

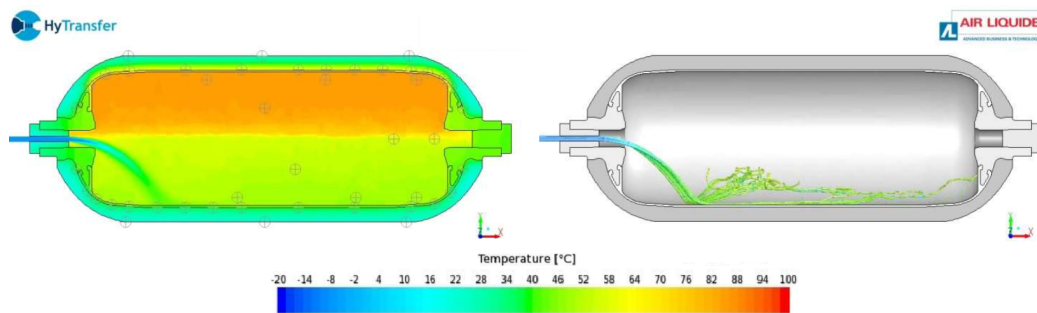


Figure 1.3 – CFD results from ALAT [59]. On the left panel, the temperature field is displayed in the symmetry plane. The upper part of the tank is warmer than the lower part. The cold jet is deflected toward the lower part. On the right panel, the streamlines are displayed through the symmetry plane and mapped with the temperature field.

Chapter 2

Resources and methods

2.1 Resources

2.1.1 Experimental measurements from the HyTransfer project

During this study, experimental results are used to validate the numerical methods. These data come from the HyTransfer project [30], started in June 2013 and concluded in December 2016. The HyTransfer project addresses theme SP1-JTI-FCH.2012.2.6 from the European Fuel Cells & Hydrogen Joint Undertaking Annual Implementation Plan (AIP 2012). It aims, in part, at investigating the temperature behavior during the fast filling of compressed-hydrogen tank in order to optimize the pre-cooling temperature and limit the energetic cost of a filling process. Three different actors took part in the experimental campaigns: Air Liquide Advanced Technologies (ALAT), the Joint Research Centre to the European Commission [83] (JRC) and the Energie Technologie (ET). During the project, three tanks were selected. Table 2.1 lists the different tanks with their main specificities. For these three tanks, about 40 filling scenarios at horizontal in were conducted using different filling rates, initial pressures and injector diameters. The data issued from the experimental campaign are available in the public report [41].

All scenarios cannot be considered for the Computational Fluid Dynamics (CFD) study. The type IV 37 L provided by Hexagon with the data provided by the experimental measurements from ALAT has been selected. The following content explains this choice.

The type IV 37 L tank led to more contrasted results in term of vertical thermal gradient than the type III 40 L tank. This can be explained by the use of a polymer for liner in type IV tank which has a smaller thermal diffusivity, $2.52e^{-7} m^2/s$, compared with the metallic liner $7.15e^{-5} m^2/s$ used in type III tank. Consequently the heat exchanged between the gas and the walls is reduced for type IV and more thermal heterogeneities are expected. Temperature probes were located in the gaseous volume of tanks via tree of termocouples. The temperature probes inside the type IV 531 L tank were not well specially distributed, see figure 2.1. The probes are located in the rear region far from the injector.

Type	Volume [L]	Ratio L/D	Provider	Experimenter
III	40	2.7	Dynetek	JRC;ET
IV	36.7	2.4	Hexagon	JRC;ALAT
IV	531	5.6	Hexagon	ALAT

Table 2.1 – The different tanks used during the HyTransfer project [30] with their specificities.

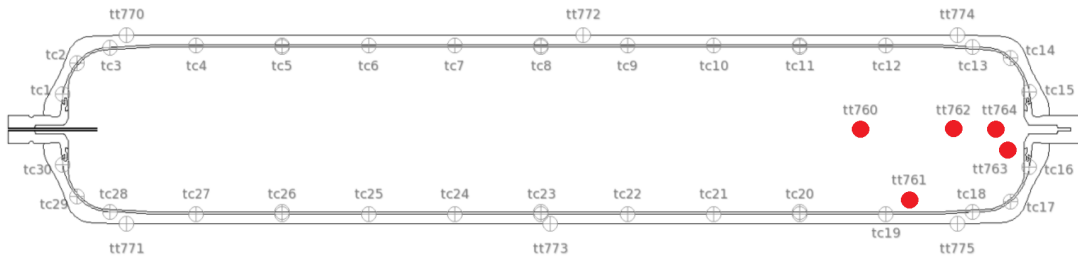


Figure 2.1 – Cutting view through the plane (x,y) of the type IV 531 L tank. Probe locations are indicated by circles. Probes located in the fluid region are filled in red.

	Hexagon 37 L					
Scenario name	D3Q2	D3Q8	D6Q2	D6Q8	D10Q2	D10Q8
Injection diameter (mm)	3	3	6	6	10	10
Averaged mass flow rate (g/s)	2	8	2	8	2	8
ALAT : $T_{max} - T_{av}$ (K)	8.36	6.35	26.76	11.28	30.03	24.39
JRC : $T_{max} - T_{av}$ (K)	3.72	2.74	17.18	3.69	29.97	23.12

Table 2.2 – Thermal gradient measurements for the type IV 37 L tank from ALAT and JRC.

The averaged temperature calculated with the temperatures from probes might not be representative of the averaged temperature of the gas in the tank. This is problematic for CFD validation. Accordingly, the type IV 37 L appeared more relevant to carry out the CFD study.

Both ALAT and JRC carried out experiments on the type IV 37 L tank. They investigated different filling rates and injection diameters. The thermal gradient issued from the different filling conditions can be estimated using the difference between the maximum temperature from probes, T_{max} , and the averaged temperature resulting from the probes, T_{av} . Table 5.1 presents the results for each scenario for the ALAT measurement set and the JRC measurement set.

An estimation of the injection velocity can be obtained from the measured mass flowrate, the pipe section and the density at injection. The injection velocity resulting from ALAT and JRC are calculated and reported in figure 2.4. The two measurement sets are consistent: a higher injection velocity induces a smaller vertical thermal gradient. During ALAT measurements, more probes (10 probes) were present in the fluid region than in the JRC measurements (6 probes), see figure 2.2. The database from ALAT has been selected. To distinguish the different scenarios, the scenario names are constructed using the injector diameter D [mm], and the time-averaged mass flowrate Q [g/s]. For example, the scenario **D6Q8** means an injector diameter of 6 mm and an averaged mass flowrate of 8 g/s. Two extreme scenarios, leading to opposite thermal behaviors, can be identified in table 5.1: scenario D3Q8, the most homogeneous case and scenario D10Q2, the most heterogeneous case.

Figure 2.3 shows the different temperatures from the experimental measurements in the fluid region for ALAT (black) and the JRC (red). One can observe in this figure that the initial rise of the temperatures with time is higher for ALAT results. This can be explained by a warmer injected temperature during ALAT experiments, see figure 2.4. Also, ALAT results showed more vertical thermal stratification than the JRC results. The injection velocities are similar for the two experimental set-ups and cannot explain the difference in term of temperature reported in figure 2.4. The difference of thermal stratification could be explained by the different locations of the probes. ALAT had its probes closer to walls and might capture a larger gradient amplitude since the hot spot and cold spot are close to walls. Also, the thermocouple tree,

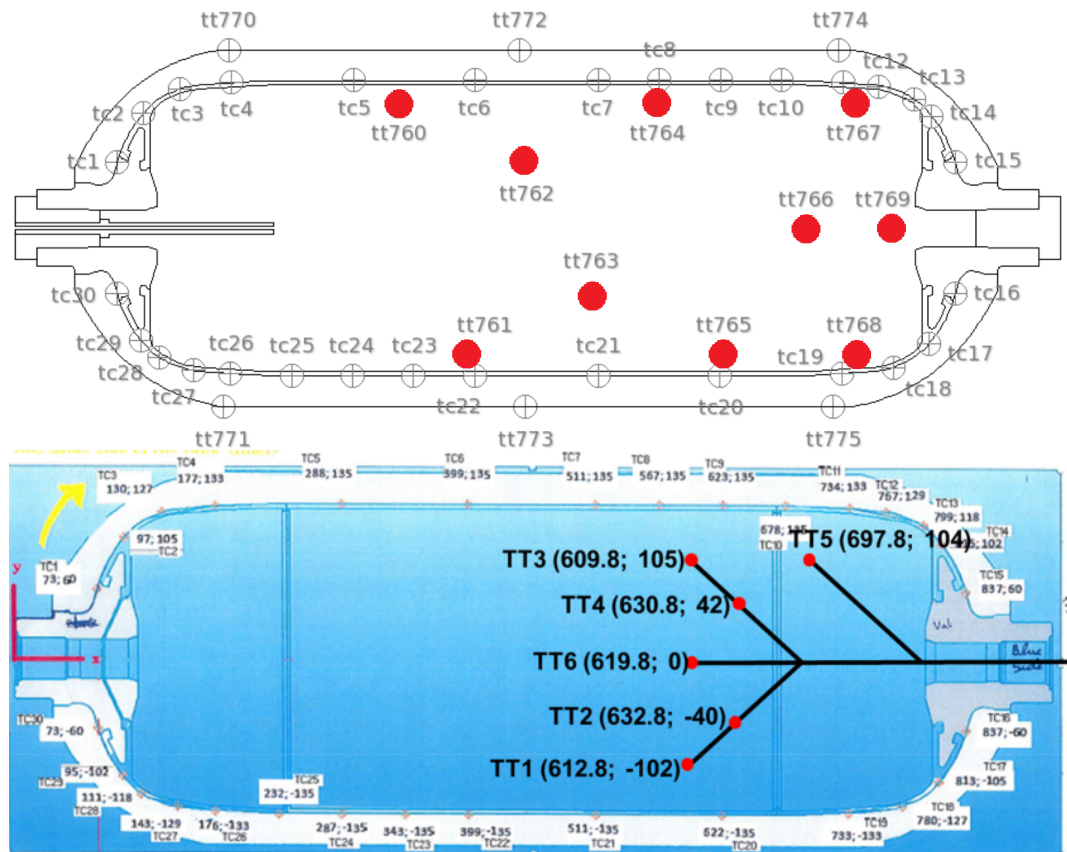


Figure 2.2 – Cutting view through the plane (x,y) of the type IV 37 L tank. Probe locations are indicated by circles: probes located in the fluid region filled in red. Upper panel, schematic for ALAT experimental set-up. Lower panel, schematic for JRC experimental set-up.

might interfere with the flow. The thermocouple tree extremity for the ALAT measurements is closer to the injector outlet than the thermocouple tree extremity for the JRC, see 2.2. The ALAT measurements should be more impacted by the presence of the thermocouple tree than for the JRC measurements. The flow could lose its momentum when it hits the thermocouple tree and this could lead to a larger thermal stratification due to less flow mixing.

2.1.2 OpenFOAM and Paraview

OpenFOAM® [84, 85] has been chosen to carry out the CFD simulation during this study. OpenFOAM, for **Open**-source **F**ield **O**peration **A**nd **M**anipulation, is a C++ toolbox for the development of customized numerical solvers. Its main purpose is to solve continuum mechanics problems in particular CFD, using finite-volume method to solve partial differential equations. The use of OpenFOAM has been motivated by the access to the source code allowing to implement custom boundary condition, custom solver or custom post-processing. Also, for parallel computations, the number of processors is not limited by licenses.

The OpenFOAM 6 version maintained by the OpenFOAM Foundation has been selected for this work. Documentation for this version is available online [86]. The software does not provide a graphical user interface. The configuration of a case goes through files located in the case folder, as illustrated in figure 2.5. The solutions are written in the root case folder and, for an unsteady simulation, named after the time reached by the simulation. A solution folder has the same structure as the folder 0, which can be considered as the solution at $t = 0$ s. Once the case well configured, the solver is called from a console of the operating system, and the calculation starts.

The results issued from OpenFOAM can be displayed via a third-party software, ParaView [88], included within the OpenFOAM set-up package. ParaView is open-source and allows to implement customized function coded in Python via a programmable filter. All visualization of CFD field present in this study have been realized with ParaView.

2.1.3 3D model

An incomplete 3D model of the 37 L Hexagon tank has been obtained from the HyTransfer project database. In a .step format, the real geometry of the bosses, the liner and the composite were accessible. The real geometries include unwanted details. For instance, the liner was composed of three parts with a local junction between parts (see figure 2.6, right panel). The bosses had a complex geometry with protruding edges shared with the liner (see figure 2.6, left panel).

The plugs and the pipe injector 3D models were missing. However, the most important lengths such as the pipe inner diameter or the length of the pipe injector inside the tank were reported in HyTransfer documentations. Several pictures helped in estimating the remaining unknown dimension. In order to complete the 3D geometries and to simplify the existing ones, the tank has been redesigned using Salome [89] as Computer-Aided Design (CAD) software. By intersecting the existing 3D geometries with the plane (x,y) and keeping the lower part of the result, a shape of the 3D model is obtained, see figure 2.7 at the upper panel. Then, by leaning on the shape, a simplified and completed slice of the tank is designed, see figure 2.7 at the lower panel.

The shape is extruded around the x-axis and the complete 3D geometry is reconstructed. The fluid region is obtained by extraction of the volume enclosed by solid regions. To use the 3D geometries for the meshing process, the exportation from Salome in .stl format should be issued from a fine mesh performed in the meshing module, as in 2.8, instead of exporting the .stl via the geometry module.

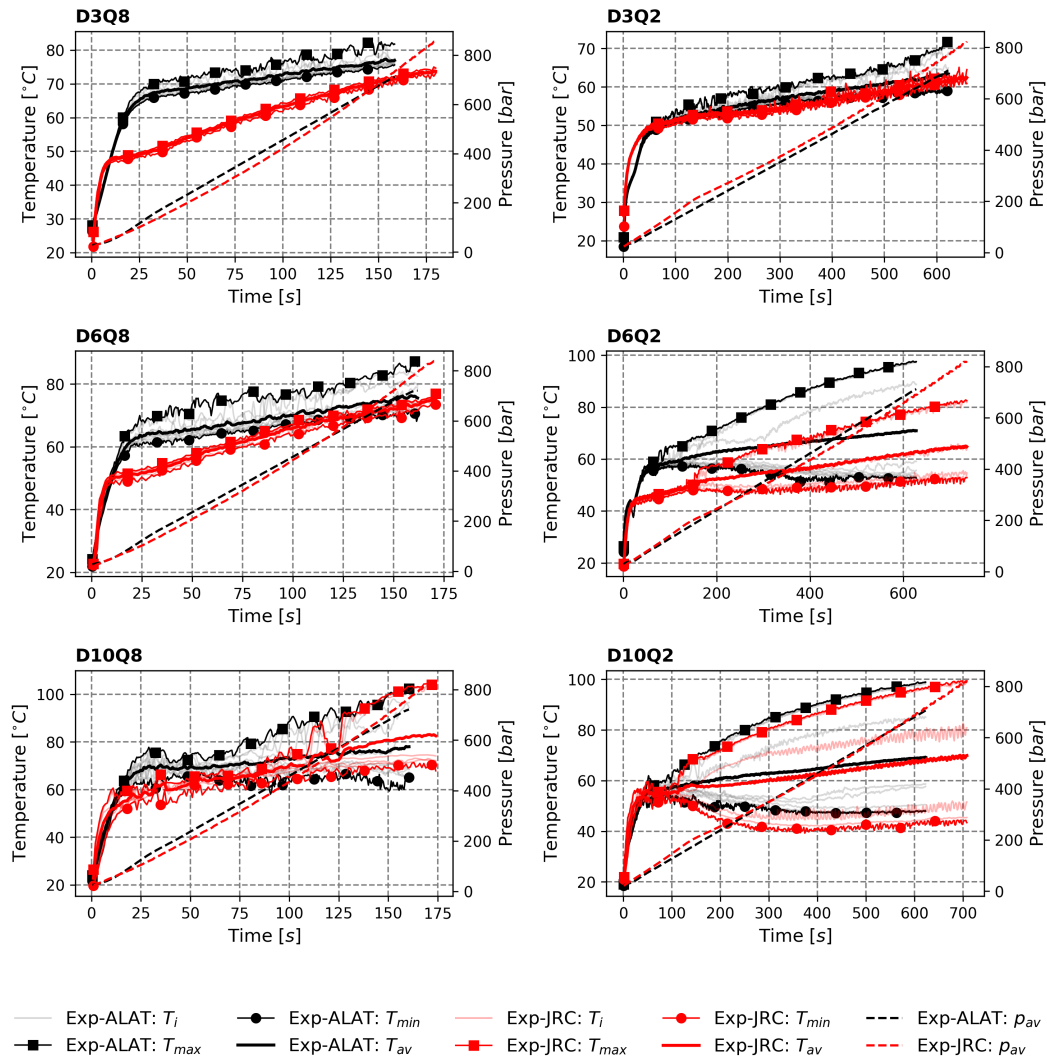


Figure 2.3 – Temperatures and absolute pressures for the fluid region for the type IV 37 L tank issued from measurements from ALAT (in black) and the JRC (in red) [41].

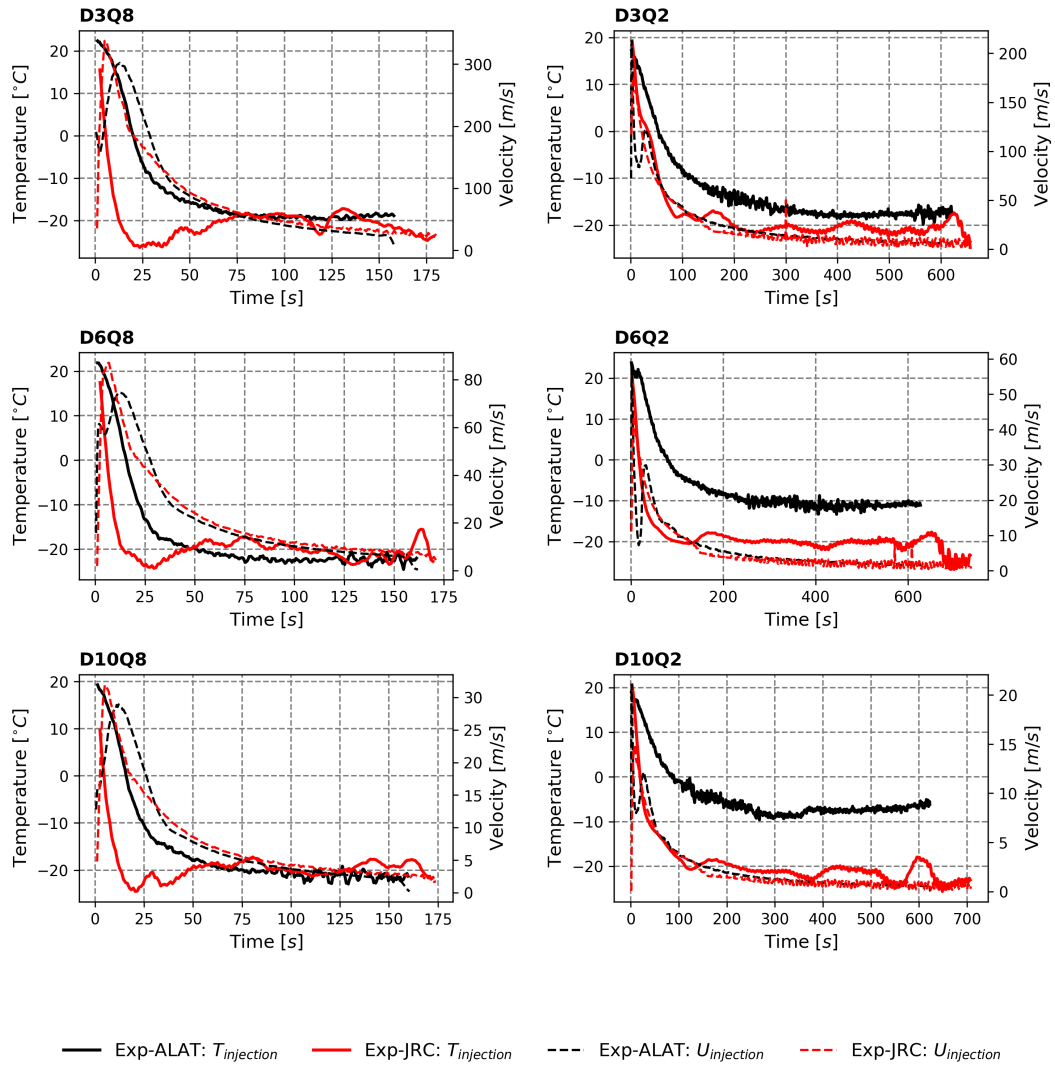


Figure 2.4 – Temperature and velocity at the injection in the fluid region for the type IV 37 L tank for ALAT (in black) and the JRC (in red) [41].

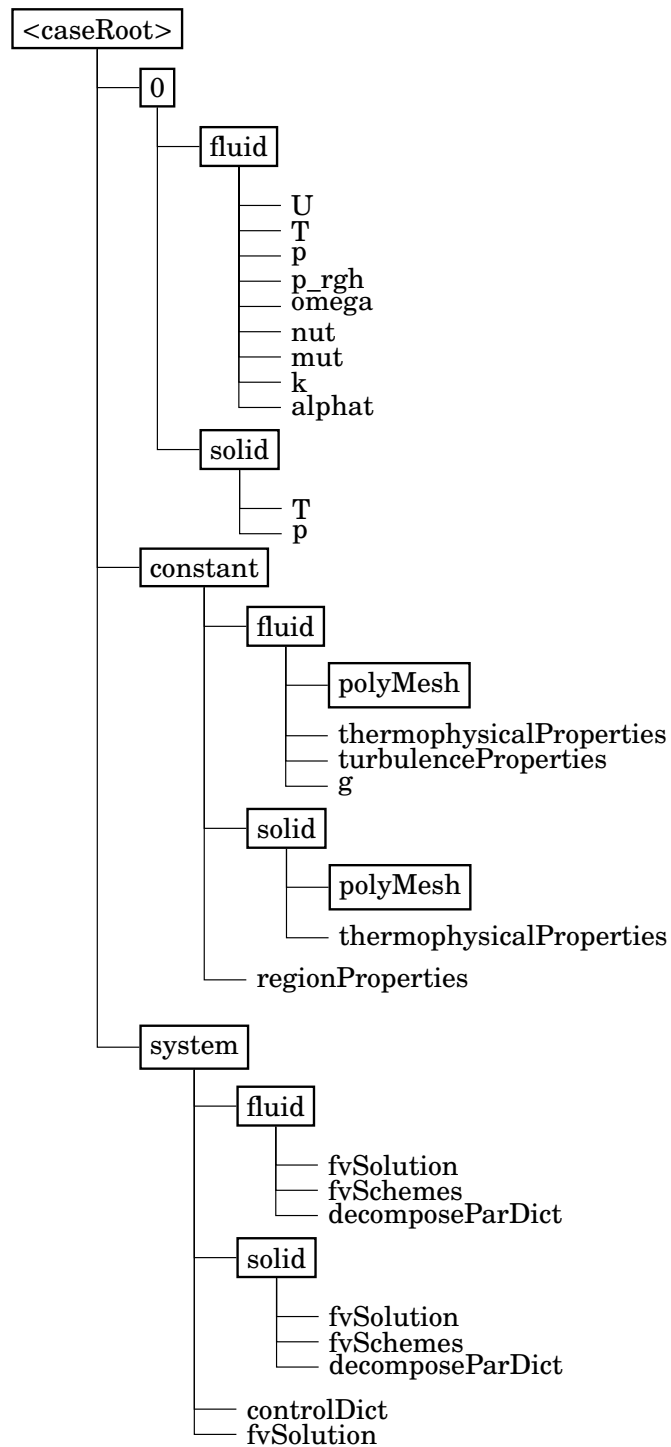


Figure 2.5 – OpenFOAM folders and files tree corresponding to a multi-region simulation case [87] with two regions: fluid and solid. Folder in boxed text and file in unboxed text.

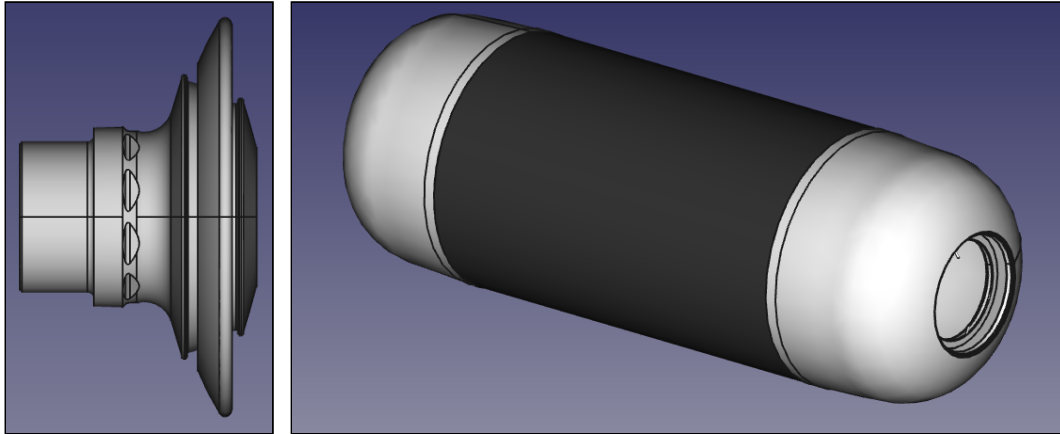


Figure 2.6 – Raw geometry of the 37 L Hexagon tank.

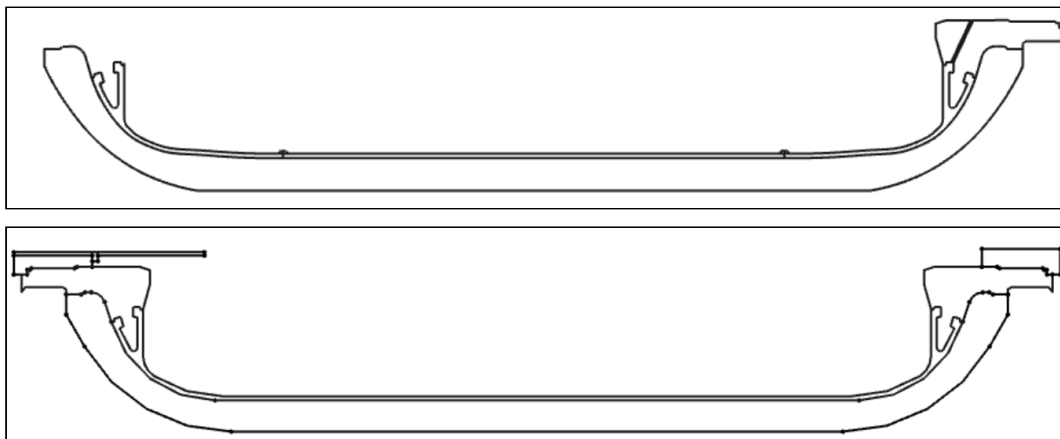


Figure 2.7 – Upper panel: shape of the 37 L Hexagon tank obtained by projection on the plane (x,y) . The upper part is removed. Lower panel: redesigned, simplified and completed shape using Salome.

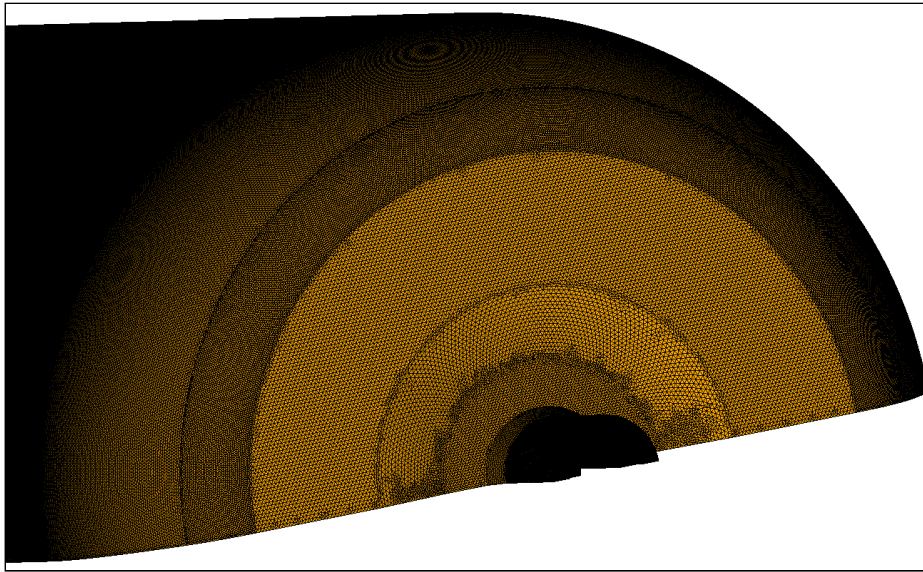


Figure 2.8 – Fine surface mesh of the fluid region exported in `.stl` for the meshing process.

Equation real gas hydrogen	References using the model
Redlich-Kwong and modifications [34, 37, 67]	[19, 28, 91–93]
Able-Noble [94]	[74]
Peng-Robinson [68]	[92]
Reduced Helmholtz free energy [95]	[96]
Van deer Vaal	[90, 97]
Polynomial	[98]
NIST data [99]	[90, 100]

Table 2.3 – Equations of state used in order to model the behavior of gaseous hydrogen.

2.1.4 Calmip and TGCC

During the study, a personal computer could not per High Performance Computing (HPC) stations. For the duration of the PhD, a total of 3 850 000 computation-time hours has been granted by CALMIP (In french, CALcul en MIDI Pyrénées). The supercomputer, named Olympe, has 36 cores of 2.3 *GHz* per node. Typically, for a simulation of 1 200 000 cells, 3 nodes, so 108 cores were allocated. Likewise, a total of 400 000 computation-time hours has been granted by the TGCC (In french, Très Grand Centre de Calcul). The supercomputer, named Irene, has 24 cores of 2.7 *GHz* per node.

2.2 Methods

2.2.1 Equation of state of the Hydrogen

At high pressure, the gaseous hydrogen cannot be considered as a perfect gas [19, 90]. Several equations of state can be chosen in order to reproduce the real gas behavior. They are listed in table 2.3.

In this study, the thermophysical properties for gaseous hydrogen at high pressure have been extracted from REFPROP [101], a software from the National Institute of Standards and Technology (NIST). Instead of using an analytic formula, a

table-reading method has been used. The thermophysical properties depend on temperature and pressure. Their values have been stored in tables where the values are sorted by temperature within the range [170 K 470 K] with a step of [5 K] and by absolute pressure within the range [1 bar 901 bar] with a step of [20 bar]. This can be written in a matrix form. For example, for the density ρ , the matrix M_ρ is

$$M_\rho = \begin{matrix} & 1 & 21 & \dots & 881 & 901 \\ \begin{matrix} 170 \\ 175 \\ \vdots \\ 465 \\ 470 \end{matrix} & \begin{pmatrix} 0.14 & 2.95 & \dots & 63.34 & 64.03 \\ 0.14 & 2.87 & \dots & 62.4 & 63.09 \\ \vdots & \vdots & \vdots & \vdots & \vdots \\ 0.05 & 1.08 & \dots & 33.59 & 34.15 \\ 0.05 & 1.07 & \dots & 33.3 & 33.9 \end{pmatrix} \end{matrix}. \quad (2.1)$$

To access to a value for a given couple of temperature and pressure (T, p), an euclidean division allows to quickly locate the four neighboring matrix cells of the targeted value. A bilinear-interpolation of the four neighboring cells is carried out to estimate the value of the targeted value. To illustrate this with an example, let's select $\rho(T, p)$ and the matrix M_ρ . To ease the writing, $T_{min} = 170 \text{ K}$, $p_{min} = 1 \text{ bar}$, $\Delta T = 5 \text{ K}$, $\Delta p = 20 \text{ bar}$. The values i, j are obtained via the euclidean division (the notation $\lfloor \bullet \rfloor$ for the rounding),

$$i = \lfloor \frac{p - p_{min}}{\Delta p} \rfloor \quad (2.2)$$

$$j = \lfloor \frac{T - T_{min}}{\Delta T} \rfloor. \quad (2.3)$$

The neighboring cells are $M_\rho(i+1, j+1)$, $M_\rho(i+2, j+1)$, $M_\rho(i+1, j+2)$ and $M_\rho(i+2, j+2)$. The remaining part of the euclidean division are named R_T and R_p for the temperature and the pressure respectively,

$$R_p = p - (p_{min} + i\Delta p) \quad (2.4)$$

$$R_T = T - (T_{min} + j\Delta T). \quad (2.5)$$

The bilinear-interpolation becomes:

$$\begin{aligned} \rho(T, p) = & \left(\frac{\Delta p - R_p}{\Delta p} \right) \left(\left(\frac{\Delta T - R_T}{\Delta T} \right) M_\rho(i+1, j+1) + \frac{R_T}{\Delta T} M_\rho(i+1, j+2) \right) \\ & + \left(\frac{R_p}{\Delta p} \right) \left(\left(\frac{\Delta T - R_T}{\Delta T} \right) M_\rho(i+2, j+1) + \frac{R_T}{\Delta T} M_\rho(i+2, j+2) \right). \end{aligned} \quad (2.6)$$

This method was implemented in SOFIL, the 0D model from Air Liquide. It has been implemented in OpenFOAM during this doctoral work using a custom library for transport and thermophysical properties adapted from [102].

Tables of thermophysical properties can be represented in a surface plot, using a colormap to represent the thermophysical value. Figure 2.9 presents the different plots associated with different tables used during this work involving: A) the thermal conductivity, B) the density, C) the specific enthalpy, D) the specific thermal capacity and E) the dynamic viscosity.

The library CoolProp [103] has been used in post-processing script in Python. From this library, functions allow to access the transport and thermophysical properties of hydrogen with a large range of input.

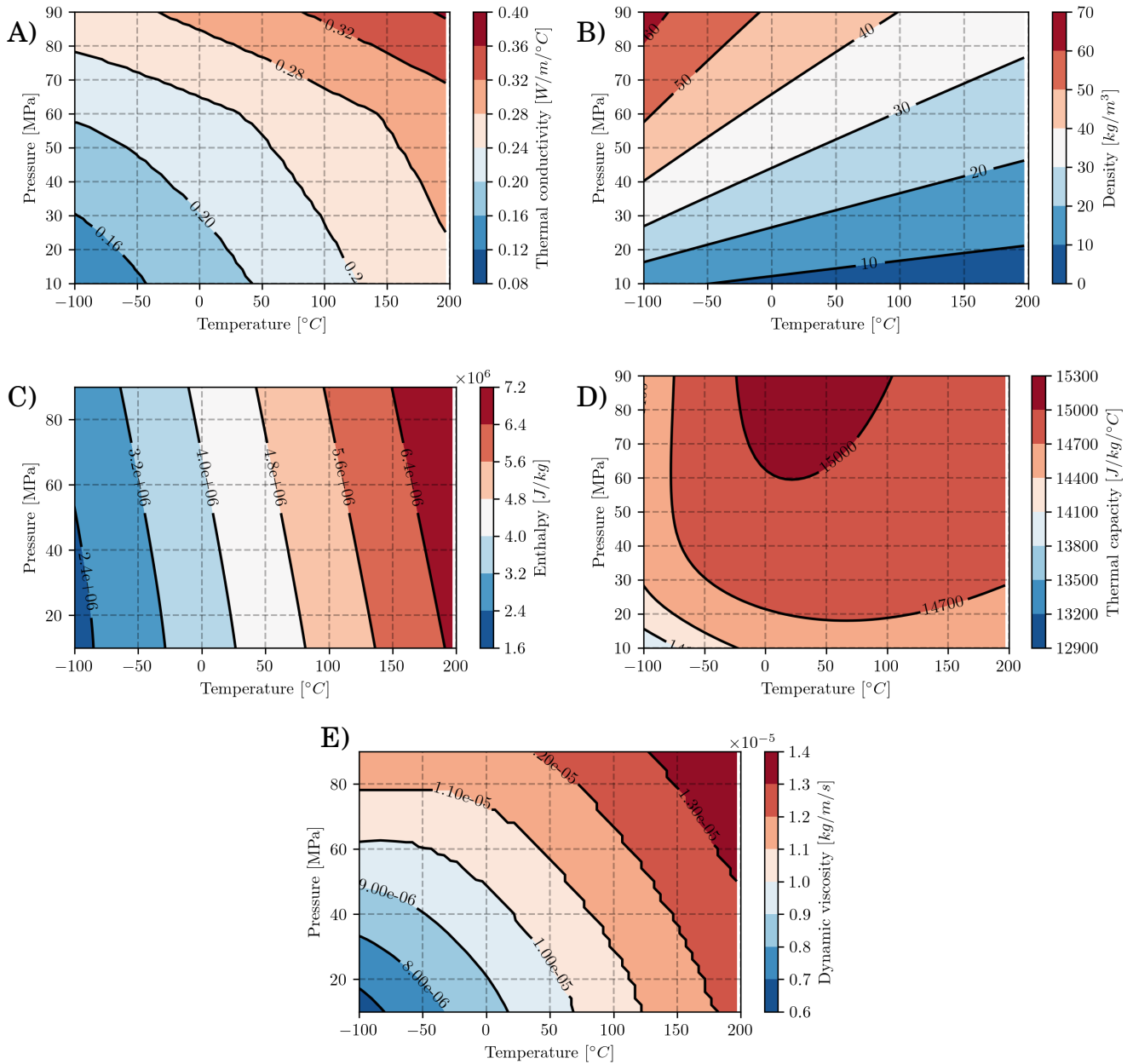


Figure 2.9 – As a function of the pressure and the temperature: panel A), the thermal conductivity; panel B), the density; panel C), the specific enthalpy; panel D), the specific thermal capacity; panel E), the dynamic viscosity.

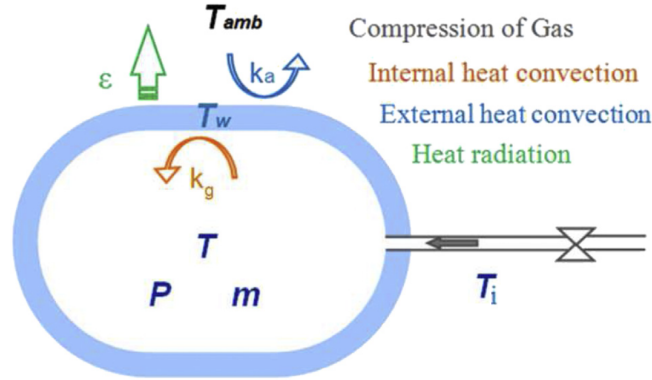


Figure 2.10 – Schematic of the general variables and modeled heat exchanges in SOFIL.

2.2.2 SOFIL: 0D model from Air Liquide

SOFIL, for SOFt for FILLing, is a 0D-1D model for the filling of gas designed by Air Liquide [43, 70]. The gas in the tank is considered as a unique closed volume, i.e. 0D. The surrounding walls are discretized along the radial direction r , i.e. 1D. Figure 2.10 gives a schematic of the general principle of the model.

The governing equations for the gas are the mass (2.7) and energy (2.8) balance equations:

$$\text{mass: } \frac{dm}{dt} = \dot{m}_{inj} \quad (2.7)$$

$$\text{energy: } mc_p \frac{dT}{dt} = V\beta T \frac{dp}{dt} + k_g S_w (T_{g,w} - T) + \dot{m}_{inj} (h_{inj} + \frac{u_{inj}^2}{2} - h(T, p)) \quad (2.8)$$

To close the equation system, thermophysical properties (ρ , c_p , etc) must be evaluated depending on the pressure and the temperature. In this purpose, the table-reading method described in the section 2.2.1 is used.

The heat exchange coefficient k_g is calculated using the correlation (2.9) based on the work of [69].

$$Nu_{D_{int}} = \frac{D_{int} k_g}{\lambda} \quad (2.9)$$

$$= aRa_{D_{int}}^b + cRe_{d_{inj}}^d \quad \text{with} \quad Ra_{D_{int}} = \frac{g|T - T_{g,w}|c_p \rho^2 D_{int}^3}{\mu \lambda} \quad \text{and} \quad Re_{d_{inj}} = \frac{4\dot{m}_{inj}}{\pi d_{inj} \mu} \quad (2.10)$$

The Rayleigh number $Ra_{D_{int}}$ characterizes the importance of the natural convection for heat transfer while Reynolds number $Re_{d_{inj}}$ characterizes the importance of the forced convection. The two dimensionless numbers are weighted in (2.9) using coefficients a , b , c and d . The coefficients are assumed constant and are related only to the tank geometry and orientation (filled horizontally or vertically). Based on experiments, for the type IV 37 L tank filled horizontally, their values are: $a = 0$, $b = 0.352$, $c = 0.17$ and $d = 0.67$. It can be noted that, because $a = 0$, the dependance with the Rayleigh number term is neglected. This means that, for small tanks, the natural convection can be neglected in front of the forced convection when the heat transfer between the gas and the walls is estimated.

The walls are considered as 1D, i.e. walls are discretized in the radial direction. The governing equation is the energy

balance equation:

$$\text{energy: } \rho_w c_{p,w} \frac{\partial T_w}{\partial t} = \frac{1}{r} \frac{\partial}{\partial r} [r \lambda_w \frac{\partial T_w}{\partial r}]. \quad (2.11)$$

The thermophysical properties ($\rho_w, c_{p,w}, \lambda_w$) depend on the material considered (liner or composite). At the interface between the liner and the composite, a continuity of flux and temperature is imposed. On exterior walls, a heat exchange coefficient designed for natural convection for a cylinder in a uniform environment is used [104].

$$\begin{aligned} Nu_a &= \frac{D_{ext} k_a}{\lambda_a} \\ &= 0.125 Ra_{D_{ext}}^{0.33}, \text{ for } Ra_{D_{ext}} > 10^7, \end{aligned} \quad (2.12)$$

and a radiative heat power is modeled between the ambient environment (blackbody) and the tank via

$$\Phi_{rad} = \epsilon \sigma S_{ext} (T_{ext}^4 - T_{w,ext}^4). \quad (2.13)$$

The total heat power at the external surface will be

$$\begin{aligned} \Phi_{ext} &= \lambda_w S_{ext} \left. \frac{\partial T_w}{\partial r} \right|_{r_{ext}} \\ &= k_a S_{ext} (T_{ext} - T_{w,ext}) + \Phi_{rad}. \end{aligned} \quad (2.14)$$

2.2.3 Governing equations for the 3D model

Navier-Stokes

The Navier-Stokes equations, based on the mass, the momentum and the energy balance equations, give the partial differential equations describing the fluid dynamics. Using the Einstein summation notation, the equation system for a compressible fluid can be written as:

$$\text{mass: } \frac{\partial \rho}{\partial t} + \frac{\partial \rho u_i}{\partial x_i} = 0 \quad (2.15)$$

$$\text{momentum: } \frac{\partial \rho u_i}{\partial t} + \frac{\partial \rho u_j u_i}{\partial x_j} = -\frac{\partial p}{\partial x_i} + \frac{\partial}{\partial x_j} [\tau_{ij}] + \rho g_i \quad (2.16)$$

$$\text{energy: } \frac{\partial}{\partial t} [\rho h + \frac{1}{2} \rho u_i u_i] + \frac{\partial}{\partial x_j} [\rho u_j (h + \frac{1}{2} u_i u_i)] = \frac{\partial p}{\partial t} + \frac{\partial}{\partial x_j} [u_i \tau_{ij}] + \rho u_i g_i - \frac{\partial q_i}{\partial x_i} \quad (2.17)$$

The viscous stress tensor τ_{ij} is defined as

$$\tau_{ij} = \mu [2S_{ij}], \quad (2.18)$$

with the strain rate tensor S_{ij} defined as

$$S_{ij} = \frac{1}{2} \left(\frac{\partial u_i}{\partial x_j} + \frac{\partial u_j}{\partial x_i} \right). \quad (2.19)$$

The term g_i is the gravity vector and q_i is the heat flux defined as

$$q_i = -\frac{\lambda}{c_p} \frac{\partial h}{\partial x_i}, \quad (2.20)$$

with λ the thermal conductivity and c_p the thermal capacity.

URANS modeling

The turbulence is present during a fast filling of hydrogen tank. Even with the smallest injection velocity issued from the end of the D10Q2 scenario, the Reynolds number based on the injector diameter remains superior than 15 000. For this Reynolds number value [105], the flow is fully turbulent at the pipe outlet. As theorized by Kolmogorov [106] for turbulent flow, the effect of small-scale eddies are important on the macro-scale flow structure. The equation set (2.15) is sufficient to capture the turbulent flow with CFD but a very fine grid and a small time step is required. This CFD approach is called Direct Numerical Simulation (DNS) and requires too much time and numerical resources not available for this study.

To limit the computation cost, the turbulence effects have to be modeled. The unsteady Reynolds-Averaged Navier-Stokes (URANS) approach is selected to model the turbulence. It is a classical modeling approach for engineering application. Within this approach, the instantaneous flow is not directly solved. Using the Reynolds averaging, see (2.21) and the Favre averaging (suitable for compressible flow), see (2.22), a variable Φ is decomposed in a mean component $\bar{\Phi}$ or $\tilde{\Phi}$ respectively, plus a fluctuating component Φ' and Φ'' respectively

$$\text{Reynolds averaging} \begin{cases} \bar{\Phi}(t) = \frac{1}{n} \sum_n \Phi^n(t) \\ \Phi' = \Phi - \bar{\Phi} \end{cases}, \quad (2.21)$$

with n measurements of the quantity Φ at the same time and position from n identical experiments.

$$\text{Favre averaging} \begin{cases} \tilde{\Phi} = \frac{\bar{\rho}\Phi}{\bar{\rho}} \\ \Phi'' = \Phi - \tilde{\Phi} \end{cases}. \quad (2.22)$$

The Reynolds averaging is applied on the density and the pressure and the Favre averaging is applied on the velocity and the enthalpy. The equation set concerning the conservation of the mean variable component can be written:

$$\text{mass: } \frac{\partial \bar{\rho}}{\partial t} + \frac{\partial \bar{\rho} \tilde{u}_i}{\partial x_i} = 0 \quad (2.23)$$

$$\text{momentum: } \frac{\partial \bar{\rho} \tilde{u}_i}{\partial t} + \frac{\partial \bar{\rho} \tilde{u}_j \tilde{u}_i}{\partial x_j} = -\frac{\partial \bar{p}}{\partial x_i} + \frac{\partial}{\partial x_j} [\bar{\tau}_{ij} - \overline{\rho u_j'' u_i''}] + \bar{\rho} g_i \quad (2.24)$$

$$\begin{aligned} \text{energy: } & \frac{\partial}{\partial t} [\bar{\rho} \tilde{h} + \frac{1}{2} \bar{\rho} \tilde{u}_i \tilde{u}_i + \frac{\overline{\rho u_i'' u_i''}}{2}] + \frac{\partial}{\partial x_j} [\bar{\rho} \tilde{u}_j (\tilde{h} + \frac{1}{2} \tilde{u}_i \tilde{u}_i) + \tilde{u}_j \frac{\overline{\rho u_i'' u_i''}}{2}] \\ & = \frac{\partial \bar{p}}{\partial t} + \frac{\partial}{\partial x_j} [\tilde{u}_i (\bar{\tau}_{ij} - \overline{\rho u_j'' u_i''})] + \bar{\rho} \tilde{u}_i g_i \\ & + \frac{\partial}{\partial x_j} [\bar{\tau}_{ij} u_i'' - \overline{\rho u_j'' \frac{1}{2} u_i'' u_i''}] - \frac{\partial}{\partial x_i} [q_i + \overline{\rho u_i'' h''}] \end{aligned} \quad (2.25)$$

To close the equation system, quantities depending on fluctuating components must be modeled. The Reynolds-Stress tensor $-\overline{\rho u_i'' u_j''}$ is modeled using the Boussinesq hypothesis. This evaluate the Reynolds-Stress tensor using the mean component velocity:

$$\begin{aligned} -\overline{\rho u_i'' u_j''} &= \tau_{ij}^{tur} \\ &= \mu_t \left(\frac{\partial \tilde{u}_i}{\partial x_j} + \frac{\partial \tilde{u}_j}{\partial x_i} \right) - \frac{2}{3} \bar{\rho} k \delta_{ij} \end{aligned} \quad (2.26)$$

with δ_{ij} the Kronecker delta and with k the turbulent kinetic energy computed as

$$\bar{\rho}k = \frac{\overline{\rho u_i'' u_i''}}{2} \quad (2.27)$$

and μ_t the turbulent viscosity modeled via a turbulence model discussed further. The turbulent heat flux conduction $\overline{\rho u_j'' h''}$ is modeled as

$$\begin{aligned} \overline{\rho u_j'' h''} &= -\frac{\mu_t c_p}{Pr_t} \frac{\partial \tilde{T}}{\partial x_j} \\ &= -\lambda_t \frac{\partial \tilde{T}}{\partial x_j}, \end{aligned} \quad (2.28)$$

with the turbulent Prandtl number Pr_t taken as a constant fixed at 0.85 in OpenFOAM.

Molecular diffusion and turbulent transport terms $\overline{\tau_{ij} u''} - \overline{\rho u_j'' \frac{1}{2} u_i'' u_i''}$ are not modeled and neglected in OpenFOAM. Likewise, the turbulent kinetic energy is neglected in front of the enthalpy $k \ll h$.

In order to ease the understanding, the mathematical expression of the system can be simplified. For URANS method, only mean components are estimated. The notation $\bar{\bullet}$ and $\tilde{\bullet}$ can be removed. The common notation U for \tilde{u} is adopted. Then (2.23,2.24,2.25) become:

$$\text{mass: } \frac{\partial \rho}{\partial t} + \frac{\partial \rho U_i}{\partial x_i} = 0 \quad (2.29)$$

$$\text{momentum: } \frac{\partial \rho U_i}{\partial t} + \frac{\partial \rho U_j U_i}{\partial x_j} = -\frac{\partial p}{\partial x_i} + \frac{\partial \tau_{ij}^{eff}}{\partial x_j} + \rho g_i \quad (2.30)$$

$$\begin{aligned} \text{energy: } \frac{\partial}{\partial t} [\rho(h + \frac{1}{2} U_i U_i)] + \frac{\partial}{\partial x_j} [\rho U_j (h + \frac{1}{2} U_i U_i)] \\ = \frac{\partial p}{\partial t} + \frac{\partial U_i \tau_{ij}^{eff}}{\partial x_j} + \rho U_i g_i - \frac{\partial q_i^{eff}}{\partial x_i} \end{aligned} \quad (2.31)$$

with the effective viscous stress tensor τ^{eff} defined as

$$\begin{aligned} \tau_{ij}^{eff} &= \tau_{ij}^{lam} + \tau_{ij}^{tur} \\ &= (\mu + \mu_t)(2S_{ij}) - \frac{2}{3} \rho k \delta_{ij}, \end{aligned} \quad (2.32)$$

and the strain rate tensor S_{ij} defined as

$$S_{ij} = \frac{1}{2} \left(\frac{\partial U_i}{\partial x_j} + \frac{\partial U_j}{\partial x_i} \right), \quad (2.33)$$

and with the effective thermal conduction defined as

$$\begin{aligned} q_i^{eff} &= q_i^{lam} + q_i^{tur} \\ &= \left(\frac{\lambda}{c_p} + \frac{\lambda_t}{c_p} \right) \frac{\partial h}{\partial x_i} \\ &= \left(\frac{\lambda}{c_p} + \frac{\mu_t}{Pr_t} \right) \frac{\partial h}{\partial x_i}. \end{aligned} \quad (2.34)$$

$CD_{k\omega} = \max\left(2\rho\sigma_{\omega 2} \frac{1}{\omega} \frac{\partial k}{\partial x_i} \frac{\partial \omega}{\partial x_i}, 10^{-10}\right)$
$P_k = \min\left(\tau_{ij} \frac{\partial U_i}{\partial x_j}, 10\beta^* k\omega\right)$
$F_1 = \tanh\left[\min\left[\max\left(\frac{\sqrt{k}}{\beta^*\omega y}, \frac{500\nu}{y^2\omega}\right), \frac{4\sigma_{\omega 2} k}{CD_{k\omega} y^2}\right]\right]^4$
$F_2 = \tanh\left[\max\left(\frac{2\sqrt{k}}{\beta^*\omega y}, \frac{500\nu}{y^2\omega}\right)\right]^2$
$\Phi = \Phi_1 F_1 + \Phi_2 (1 - F_1)$
$S = \sqrt{2S_{ij}S_{ij}}$

Table 2.4 – Table of the different auxiliary relations for the $k - \omega$ SST turbulence model [107, 108].

State	σ_k	σ_ω	β	γ	β^*	a_1
1	0.85	0.5	0.075	5/9	0.09	0.31
2	1	0.856	0.0828	0.44	0.09	0.31

Table 2.5 – Table of the different closure coefficients for the $k - \omega$ SST turbulence model [107, 108].

Closure of the URANS modelling

In the URANS approach, the turbulence modeling consists in evaluating the terms μ_t and k to close the system. The first turbulence modeling chosen for this study is the $k - \omega$ Shear Stress Transport (SST) [107, 108], belonging to the two-equation eddy-viscosity model category. Its formulation consists in adding two equations to the URANS equation set (2.29, 2.30, 2.31) based on the balance equation for the turbulent kinetic energy k and the specific dissipation rate of the turbulent kinetic energy ω . The $k - \omega$ SST turbulence model can be seen as a model switching between two turbulence models: (i) the $k - \omega$ [109] in near wall area allowing to avoid using a wall function and (ii) the $k - \varepsilon$ [110] involving the dissipation rate ε for second turbulence variable and allowing to improve fluid dynamics prediction in free-stream area. For the $k - \omega$ SST turbulence model, the balance equation for k , see (2.35) and for ω , see (2.36) need auxiliary relations, reported in table 2.4, and closure coefficients, reported in table 2.5. The closure coefficients in table 2.5 are switching from state 1 ($k - \omega$) to state 2 ($k - \varepsilon$) using the transformation Φ defined in table 2.4.

$$\frac{\partial \rho k}{\partial t} + \frac{\partial}{\partial x_j} [\rho U_j k] = P_k - \beta^* k \omega + \frac{\partial}{\partial x_j} \left[(\mu + \sigma_k \mu_t) \frac{\partial k}{\partial x_j} \right] \quad (2.35)$$

$$\begin{aligned} \frac{\partial \rho \omega}{\partial t} + \frac{\partial}{\partial x_j} [\rho U_j \omega] &= \frac{\rho \gamma}{\mu_t} P_k - \beta \rho \omega^2 + \frac{\partial}{\partial x_j} \left[(\mu + \sigma_\omega \mu_t) \frac{\partial \omega}{\partial x_j} \right] \\ &+ 2\rho(1 - F_1)\sigma_{\omega 2} \frac{1}{\omega} \frac{\partial k}{\partial x_i} \frac{\partial \omega}{\partial x_i} \end{aligned} \quad (2.36)$$

The turbulent viscosity μ_t is calculated in (2.37) using (2.35) and (2.36):

$$\mu_t = \frac{\rho a_1 k}{\max(a_1 \omega, SF2)}. \quad (2.37)$$

The $k - \omega$ SST model is overpredicting the turbulence kinetic energy in areas like stagnation regions [111]. The turbulent thermal conductivity is related to the turbulent viscosity, see (2.34). Overpredicting the turbulence kinetic energy implies overpredicting the thermal diffusion in the tank. Advanced turbulence models can limit the production of

Name	ζ_2	σ_Φ	C_{SAS}	C_s	κ	c_μ	α	β
Value	1.47	2/3	2	0.11	0.41	0.09	0.44	0.0828

Table 2.6 – Constants needed to close the SAS equation set.

turbulent kinetic energy and are expected to improve the thermal gradient prediction. The Scale Adaptive Simulation (SAS) concept applied to the $k - \omega$ SST turbulence model has been used in this work to avoid an over-prediction of the eddy-viscosity. The SAS concept consists in comparing the turbulent length-scale L_t (2.38) issued from the $k - \omega$ SST model,

$$L_t = \frac{\sqrt{k}}{c_\mu^{0.25} \omega}, \quad (2.38)$$

with the Von Karman length scale L_{vK} (2.39), a three-dimensional generalization of the boundary layer thickness definition,

$$L_{vK} = \max\left(\kappa \left| \frac{S}{\sqrt{\frac{\partial^2 U_i}{\partial x_k^2} \frac{\partial^2 U_i}{\partial x_j^2}}} \right|, C_s \sqrt{\frac{\kappa \zeta_2}{\beta / c_\mu - \alpha}} \Delta\right), \quad (2.39)$$

where $\Delta = \sqrt[3]{V}$ the cubic root of a mesh cell, giving a characteristic length of the cell.

Depending on the ratio $\frac{L_t}{L_{vK}}$, a source term Q_{SAS} (2.41) is activated in the balance equation for ω (2.36), correcting the production of ω , and consequently impacting the turbulent viscosity μ_t .

$$\begin{aligned} \frac{\partial \rho \omega}{\partial t} + \frac{\partial}{\partial x_j} [\rho U_j \omega] = & \frac{\rho \gamma}{\mu_t} P_k - \beta \rho \omega^2 + \frac{\partial}{\partial x_j} \left[(\mu + \sigma_\omega \mu_T) \frac{\partial \omega}{\partial x_j} \right] \\ & + 2\rho(1 - F_1) \sigma_\omega \omega^2 \frac{1}{\omega} \frac{\partial k}{\partial x_i} \frac{\partial \omega}{\partial x_i} + \mathbf{Q}_{SAS} \end{aligned} \quad (2.40)$$

where

$$Q_{SAS} = \max \left[\rho \zeta_2 k S^2 \left(\frac{L}{L_{vK}} \right)^2 - C \frac{2\rho k}{\sigma_\Phi} \max \left(\frac{|\nabla \omega|^2}{\nabla \omega^2}, \frac{|k|^2}{k^2} \right), 0 \right]. \quad (2.41)$$

The model involves several constants given in table 2.6.

Wall treatment

At walls, the flow velocity can be estimated using a universal law, i.e. the velocity distribution close to a wall is considered independent from the simulation case. A dimensionless distance from the wall y^+ is used. Depending on the value of this dimensionless distance, three regions can be identified in the boundary layer [112]: the viscous sublayer ($y^+ < 5$), the buffer layer ($5 < y^+ < 30$) and the log-law region ($30 < y^+ < 200$), see figure 2.11. Depending on the regions, the dimensionless velocity u^+ is calculated as a function of y^+ .

Here, y is the distance from the wall. The dimensionless distance from the wall,

$$y^+ = \frac{y \rho u_\tau}{\mu}, \quad (2.42)$$

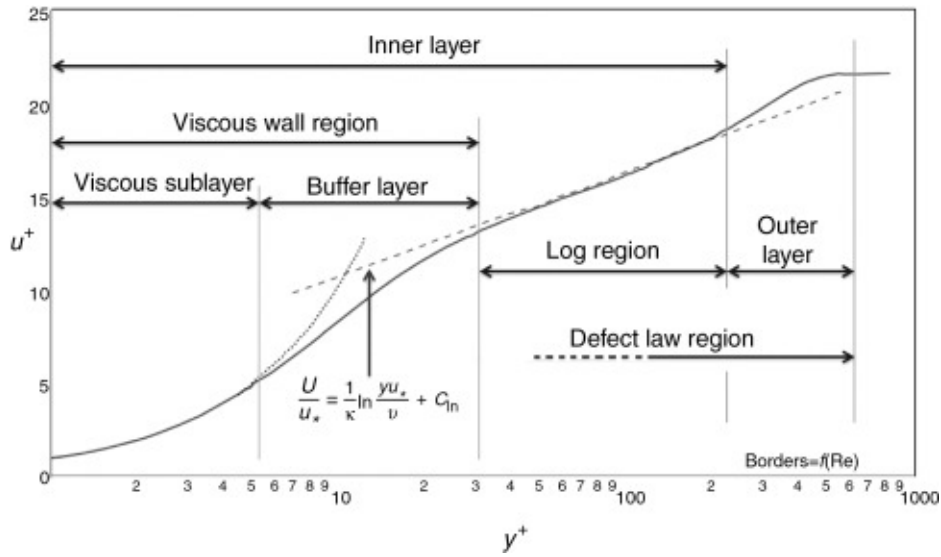


Figure 2.11 – Boundary layer theory for turbulent flow, figure issued from [112].

required the friction velocity u_τ defined as

$$u_\tau = \sqrt{\frac{\tau_w}{\rho}}. \quad (2.43)$$

To be estimated, this quantity requires the wall shear stress τ_w defined as,

$$\tau_w = \mu \frac{\partial U}{\partial y} \Big|_{y=0}. \quad (2.44)$$

The wall shear stress can be linked to the skin friction coefficient C_f ,

$$\tau_w = \frac{1}{2} \rho U_\infty^2 C_f, \quad (2.45)$$

which is evaluated using correlations. These correlations are designed for a flow on a flat plate or a flow within a pipe. The dimensionless velocity is calculated as,

$$u^+ = \frac{u}{u_\tau}. \quad (2.46)$$

If the mesh is fine enough, i.e. $y^+ < 5$ the viscous sublayer can be captured. For coarser mesh $y^+ > 30$, the viscous sublayer and buffer layer must be modeled. During the CFD with OpenFOAM, the criterion $y^+ < 1$ has been targeted for the liner, the plug and the boss walls, no wall function has been required. For the pipe wall, due to higher velocity, the criterion $y^+ < 50$ has been maintained. On this wall, a wall function is selected [113].

Solid regions and Conjugate Heat Transfer

In solid regions, the governing equation is the energy balance (2.47):

$$\text{energy: } \frac{\partial \rho h}{\partial t} = \frac{\partial}{\partial x_i} \left[\frac{\lambda}{c_p} \frac{\partial h}{\partial x_i} \right]. \quad (2.47)$$

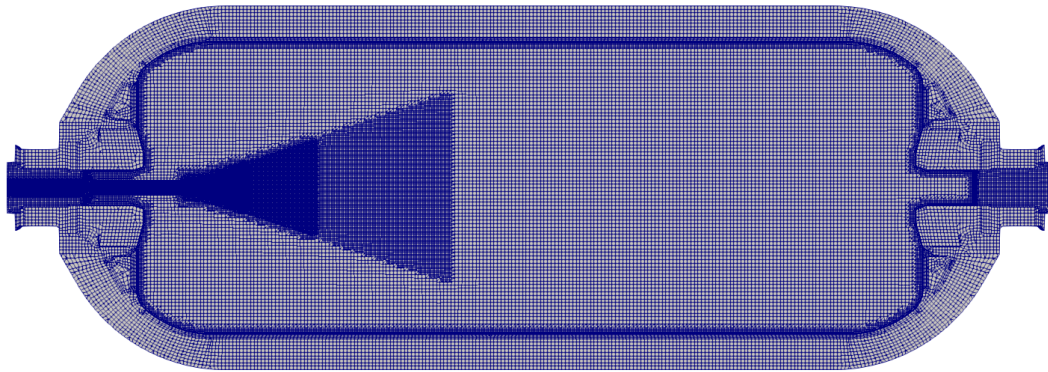


Figure 2.12 – View of the D3Q8 mesh with all the regions from the symmetry plane (x,y).

A multi-regions simulation is carried out with OpenFOAM (fluid region, pipe, liner etc). It captures the fluid dynamics and the thermal behavior in the fluid region and the thermal conduction in the walls. The numerical approach for a coupled analysis between fluids and solids is called Conjugate Heat Transfer (CHT). Its aims at solving the temperature and heat flux distributions at the fluid-solid interfaces as a coupled problem, without assuming a heat transfer coefficient. The solver used in OpenFOAM is the *chtMultiRegionFoam* [114]. It is a partitioned type solver, which means the different regions are solved sequentially, i.e. region after region which required a predictor-corrector loop [115].

At the interface between regions, for example considering regions 1 and 2, a continuity of temperature is assumed (2.48)

$$T_1 = T_2 , \quad (2.48)$$

as well as a continuity of the thermal flux (2.49),

$$\lambda_1 \frac{\partial T_1}{\partial y} |_{1-2} = \lambda_2 \frac{\partial T_2}{\partial y} |_{2-1} , \quad (2.49)$$

where y is the perpendicular direction from the wall.

2.2.4 Meshing

The mesh has been generated using cfMesh [116], an open-source library for automatic 3D meshing available in OpenFOAM v1812. cfMesh uses as input .fms file generated from .stl file via the OpenFOAM tool *FMSToSurface*. As previously said, the process required a good quality .stl file, which could require a first fine surface mesh to be obtained.

For the fluid region, the difference of scale between the region inside the pipe and in the main bulk induces a connection problem between the small cells inside the pipe and the larger cells in the main bulk. A conical refinement method has been chosen to capture the jet dynamic in the fluid region and to gradually increase the cell size, see figure 2.12.

Meshing inside the pipe with the same cell size as the one required at the pipe outlet is generating too many cells. Almost 18 % of the total cells for D3Q8 mesh would be located inside pipe while this region does not represent an area of interest for this study. To reduce the cell number inside the pipe, the main bulk without the inner pipe is meshed using *cfMesh*, see figure 2.13 right panel. Once the mesh obtained, the inner pipe mesh is constructed by an extrusion of the

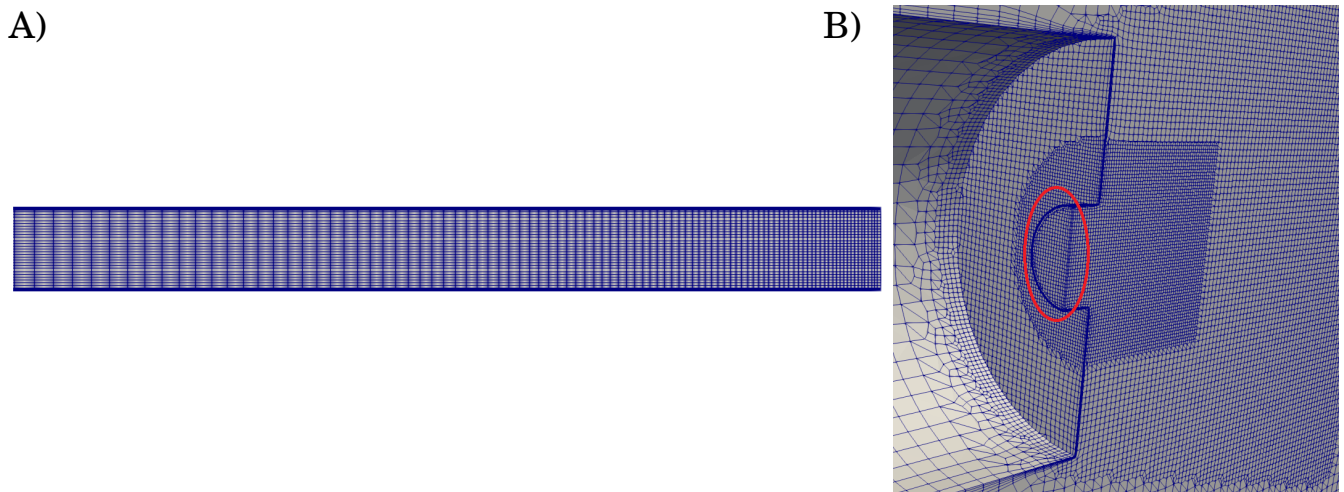


Figure 2.13 – The left panel shows a view of the mesh inside the pipe generated with a constant growth of the aspect ratio between to adjacent cells along the x-axis. The right panel shows a closer view of the pipe outlet. The outlet surface is encircled in red.

		Fluid region	Pipe	Plugs	Bosses	Liner	Composite	Total
D3Q8	2D-axisymmetric	15 605	1 483	269	912	1 034	2 675	21 978
	3D	816 156	43 821	33 532	82 080	93 060	240 750	1 309 399
	full 3D	1 664 904	87 642	67 064	164 160	186120	481 500	2 651 390
D10Q2	2D-axisymmetric	11 273	X	1 252	912	1 034	2 675	17 146
	3D	651 482	X	33 236	82 080	93 060	240 750	1 100 608
	full 3D	1 302 964	X	66 472	164 160	186 120	481 500	2 201 216
D6Q8 & D6Q2	3D	704 209	56 794	33 532	82 080	93 060	240 750	1 210 425
Emptying D3	3D	404 836	43 821	33 532	82 080	93 060	240 750	898 079

Table 2.7 – For each CFD case, the mesh type (2D-axisymmetric, 3D, full 3D), the region and the mesh size corresponding.

pipe outlet surface (encircled in red in figure 2.13) along the x-axis. A constant growth of the aspect ratio between to adjacent cells is used, see figure 2.13 left panel.

In order to test the grid sensitivity, 3 different 2D-axisymmetric meshes issued from 3D meshes have been generated for the fluid region. Due to the computational cost of 3D calculations, the study has been limited to 2D-axisymmetric meshes. The 2D-axisymmetric meshes are obtained by extraction of the surface mesh from the symmetry plane in the plane (x,y) of a 3D mesh. Figure 2.14 shows the 3 different meshes: A) fine 34 378 cells, B) reference 15 605 cells, C) coarse 9 193 cells. The coarse mesh is generated using anisotropic cells.

Figure 2.15 shows that the different meshes gave similar results for the averaged gas temperature. The reference mesh is selected because the anisotropic mesh from the coarse mesh could influence the flow direction for 3D meshes.

A symmetry assumption applied on the plane (x,y) has been used in the majority of 3D CFD cases, i.e. half of the geometry was considered. To avoid confusion, **3D** is associated with this configuration. **Full 3D** is associated with a CFD case where no symmetry assumption is used, i.e. all the geometrical domain is considered. Table 2.7 presents, for each CFD case, the mesh type (2D-axisymmetric, 3D, full 3D), the region and the mesh size corresponding.

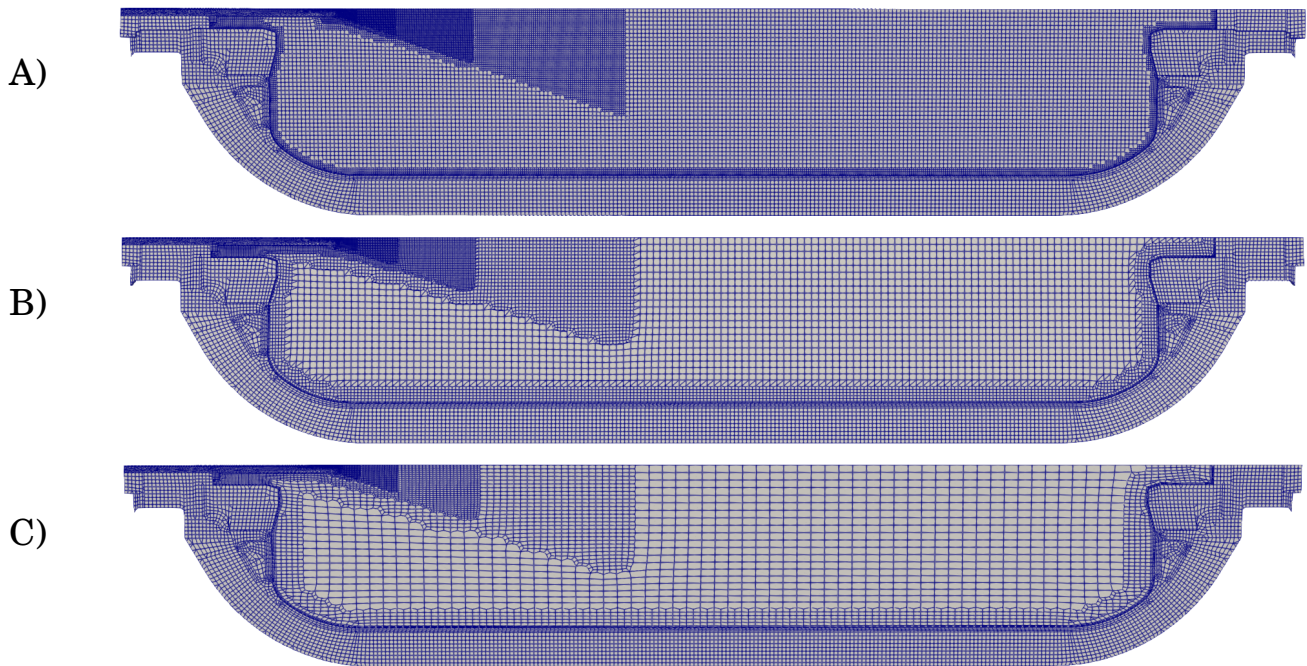


Figure 2.14 – In order to investigate the grid sensitivity, 3 different 2D-axisymmetric meshes issued from 3D meshes, with different grid sizes are obtained: A) fine 34 378 cells, B) reference 15 605 cells, C) coarse 9 193 cells.

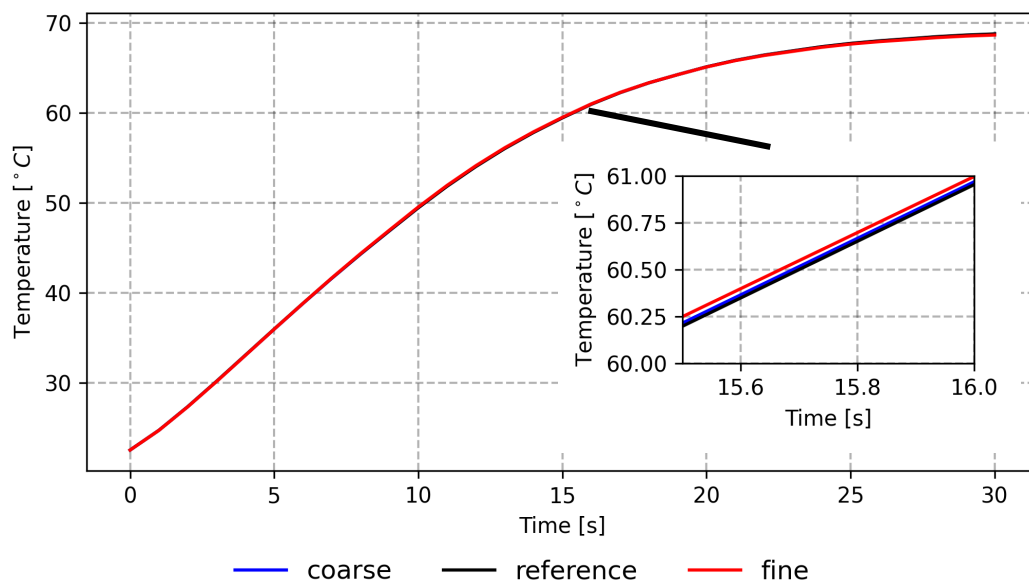


Figure 2.15 – Comparison of the averaged gas temperature on 30 s for the fine, the reference and the coarse case. A closer view on 15.5–16 s shows that the difference is negligible.

Quantity	Numerical Scheme	Order
ddtSchemes		
default	Euler	1
gradSchemes		
default	Gauss linear 1	2
divSchemes		
default	Gauss upwind phi	1
div(((rho*nuEff)*dev2(T(grad(U)))))	Gauss linear 1	2
laplacianSchemes		
default	Gauss linear corrected	2

Table 2.8 – *fvScheme* set-up for the fluid region for the cases D3Q8, D6Q8 and D6Q2.

Quantity	Numerical Scheme	Order
ddtSchemes		
default	backward	2
ddt(rho)	Euler	1
gradSchemes		
default	Gauss linear 1	2
divSchemes		
div(phi,U)	Gauss limitedLinearV 1	1-2 mixed
div(phi,K)	Gauss limitedLinear 1	1-2 mixed
div(phi,h)	Gauss limitedLinear 1	1-2 mixed
div(phi,l)	Gauss limitedLinear 1	1-2 mixed
div(phi,omega)	Gauss limitedLinear 1	1-2 mixed
div(((rho*nuEff)*dev2(T(grad(U)))))	Gauss linear 1	2
laplacianSchemes		
default	Gauss linear corrected	2

Table 2.9 – *fvSolution* set-up for the fluid region for the case D10Q2.

2.2.5 Numerical Schemes

A numerical scheme is the method used to evaluate numerically a mathematical quantity such as a gradient, a divergence or a Laplacian. In OpenFOAM, each numerical scheme can be selected independently in the file *fvScheme*. To avoid numerical instabilities, to evaluate the divergence, less accurate but more stable first-order schemes have been selected for the D3Q8, the D6Q8 and the D6Q2 cases, see table 2.8.

For the D10Q2 case, due to the smaller velocity involved, several second-order schemes for the divergence could be used without inducing numerical instabilities, see table 2.9.

In solid regions, for all cases, the numerical schemes are presented in table 2.10.

2.2.6 Numerical Algorithm and solver

The problem implies a transient buoyant and turbulent flow for the fluid region and heat conduction in solid regions, with conjugate heat transfer between regions. In OpenFOAM the adequate solver is the *ChtMultiRegionFoam* solver. For the fluid, the compressible Navier Stokes equations are solved using a pressure based solver. For every time step, it solves sequentially the energy equation and the momentum and the continuity equation using two predictor-correction steps.

Mathematical quantity	Numerical Scheme	Order
ddtSchemes		
default	Euler	1
gradSchemes		
default	Gauss linear 1	2
divSchemes		
default	none	0
laplacianSchemes		
default	Gauss linear corrected	2

Table 2.10 – *fvSolution* set-up for solid regions for all cases.

Variable	Solver	Preconditioner	Tolerance	Relative Tolerance
p_rgh	PBiCGStab	DIC	1e-8	0
p_rghFinal	PBiCGStab	DIC	1e-8	1e-3
rho rhoFinal	PBiCGStab	DIC	1e-8	0
h hFinal	PBiCGStab	DILU	1e-8	0
k kFinal	PBiCGStab	DILU	1e-8	0
omega omegaFinal	PBiCGStab	DILU	1e-8	0

Table 2.11 – *Linear solver* se-up for the fluid region.

To solve linear systems occurring during the process, linear solvers must be affected to every variable in OpenFOAM, in the file `fvSolution` for the every region. Table 2.11 presents the different linear solvers used for the fluid region and table 2.12 for solid regions.

In OpenFOAM, for unsteady flow, two algorithms are available to solve the continuity and momentum equations. The Pressure-Implicit with Splitting of Operators (PISO) algorithm [117] is an algorithm using a predictor step followed by two corrector steps. The predictor step is using data from the previous time iteration as guess for the pressure field. For the corrector step, the velocity field and the pressure field are corrected to satisfy the continuity equation. It requires a small time step to perform. This time step can be estimated using the convergence condition given by Courant, Friedrichs and Lewy, the CFL number. For PISO algorithm, it should be maintained below 1 for all cells to prevent numerical instabilities. Consequently, the Δt is chosen such as

$$\max(CFL) < 1. \quad (2.50)$$

This could lead to very small Δt and long CFD execution time if the mesh is fine and if the velocities are important (typically inside the pipe). In that event, the PIMPLE algorithm could be used instead. It comes from a congregate of the principle of the PISO algorithm and Semi-Implicit Method for Pressure Linked Equations (SIMPLE) algorithm [118]. Basically, the PIMPLE algorithm includes the PISO algorithm steps in a larger loop called the outer correctors loop. In the outer correctors loop, the PISO algorithm steps are executed with an update of the initial guess using the results

Variable	Solver	Preconditioner	Tolerance	Relative Tolerance
h hFinal	PBiCGStab	DIC	1e-8	0

Table 2.12 – *Linear solver* set-up for solid regions.

	Name	Type
Fluid region	fluid_region_inlet	patch
	fluid_region_to_bosses	mappedWall
	fluid_region_to_plugs	mappedWall
	fluid_region_to_pipe_wall_law_condition	mappedWall
	fluid_region_to_pipe	mappedWall
	fluid_region_to_liner	mappedWall
	fluid_region_symmetry	symmetry
Pipe	pipe_to_fluid_region	mappedWall
	pipe_wall_law_condition_to_fluid_region	mappedWall
	pipe_to_plugs	mappedWall
	pipe_symmetry	symmetry
	pipe_to_ext	wall
Plugs	plugs_to_fluid_region	mappedWall
	plugs_to_bosses	mappedWall
	plugs_to_pipe	mappedWall
	plugs_symmetry	symmetry
	plugs_to_ext	wall
Bosses	bosses_to_fluid_region	mappedWall
	bosses_to_plugs	mappedWall
	bosses_to_liner	mappedWall
	bosses_to_composite	mappedWall
	bosses_symmetry	symmetry
	bosses_to_ext	wall
Liner	liner_to_fluid_region	mappedWall
	liner_to_bosses	mappedWall
	liner_to_composite	mappedWall
	liner_symmetry	symmetry
Composite	composite_to_liner	mappedWall
	composite_to_bosses	mappedWall
	composite_symmetry	symmetry
	composite_to_ext	wall

Table 2.13 – Nature of all surface boundaries for a multi-regions case in OpenFOAM.

of the PISO step. The loop stops when the initial guess on the pressure is converged, i.e. the update does not change significantly the guess. A residual control on the outer correctors loop is required to consider the pressure converged. In OpenFOAM, in the file `fvSolution` for the fluid region, the `outerCorrectorResidualControl` is set at $1e^{-5}$.

2.2.7 Boundary Conditions

In OpenFOAM, the nature of a boundary surface for a region must be defined. It can be a *wall* (for example, the exterior wall of the composite), or a *mappedWall* if the boundary surface is shared between two regions (for example, the wall between the fluid region and the liner). It can be a *patch* if the surface is an inlet or outlet (example, the surface at the inlet of the pipe). Else, it can be a *symmetry* if the surface is virtual due to the symmetry of the construction. For the D3Q8 case, the different natures of boundary surface are informed in the file `boundary` located in the folder `polyMesh` for each region (fluid and solids). It is reported in table 2.13.

As previously said, when the nature of a boundary surface is a *mappedWall*, the boundary surface is shared by two

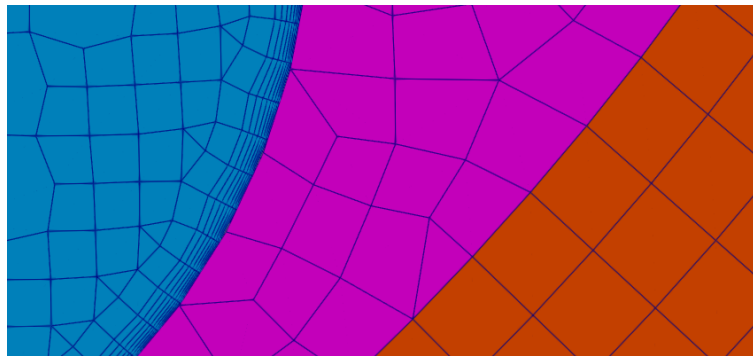


Figure 2.16 – Zoom in the D3Q8 mesh, the fluid region is displayed in blue, the liner is displayed in purple and the composite is displayed in orange. The fluid region mesh is non-conformal with the liner mesh. The liner mesh is conformal with the composite mesh.

regions. These two regions can have an arbitrary mesh interface (AMI), i.e. two adjacent mesh do not share the nodes. For this case, the mesh is called non-conformal. Figure 2.16 shows the fluid region is non-conformal with the liner while it is conformal between the liner and the composite.

In OpenFOAM, an AMI allows to exchange the heat fluxes between two adjacent regions by interpolation using a weighting of the nearest cells. The AMI treatment is set-up in the file boundary as followed.

```
fluid_region_to_plug
{
    type            mappedWall;
    nFaces          786;
    startFace       2497264;
    sampleMode      nearestPatchFaceAMI;
    sampleRegion    plug;
    samplePatch     plug_to_fluid_region;
}
```

In OpenFOAM, the physical boundary condition is defined in the folder named 0. Some implementations of boundary conditions are worth to be detailed. The others are listed in table 2.14.

For the velocity field, a mass flow rate issued from the experimental data is used as boundary condition for the inlet surface of the pipe in the fluid region. Using the surface and the density, a uniform and normal velocity is deduced. The experimental data are stored in table in .txt file. The mass flow rate value at the inlet is read and interpolated from this file at every time.

```
fluid_region_inlet
{
    type            flowRateInletVelocity;
    massFlowRate    tableFile;
    file            "$FOAM_CASE/inlet_data/massFlowRate.txt";
    rho             rho;
    extrapolateProfile    no;
```

```
    value      uniform (0 0 0);  
}
```

On other walls, velocities are imposed null to set a no-slip condition.

```
type      fixedValue;  
value     uniform (0 0 0);
```

For the pressure field, the boundary condition is the *fixedFluxPressure*. It provides a pressure value such as the pressure spatial gradient at the boundary is conditioned by the velocity boundary condition.

The inlet temperature is uniformed at the inlet surface. It issued from experimental data and corresponds to the pre-cooling temperature. Hence, it is function of the time.

```
fluid_domain_inlet  
{  
    type      uniformFixedValue;  
    uniformValue  
    {  
        type      tableFile;  
        file       "$FOAM_CASE/inlet_data/inlet_temperature.txt";  
    }  
}
```

The exchanged heat flux for all parts with the exterior environment is modeled using a local (cell level) heat transfer coefficient:

$$q_i = h_a s_i (T_{ext} - T_{w_i,ext}) \quad (2.51)$$

where h_a is heat transfer coefficient with the exterior, T_{ext} the exterior temperature, $T_{w_i,ext}$ the wall temperature, q_i the heat flux, and s_i the cell surface. The heat transfer coefficient is taken constant, i.e. $h_a = 6 \text{ W/m}^2/\text{K}$, likewise in studies from JRC [19, 55]. The ambient temperature is taken from a time average temperature issued from the experimental data. For small filling time, the heat exchanged with the exterior plays a minor role in the thermal equilibrium for the gas temperature. In OpenFOAM, the boundary condition is implemented as:

```
type      externalWallHeatFluxTemperature;  
mode      coefficient;  
Ta        constant 291.15;  
h         uniform 6;  
kappaMethod solidThermo;  
value     $internalField;
```

Fluid region	p_rgh	T	k	omega	mut	U
Boundary surface	Type	Type	Type	Type	Type	Type
fluid_region_inlet	fixedFluxPressure	uniformFixedValue	turbulentIntensityKineticEnergyInlet	turbulentMixingLengthDissipationRateInlet	calculated	flowRateInletVelocity
fluid_region_to_bosses	fixedFluxPressure	compressible::turbulentTemperatureCoupledBaffleMixed	kLowReWallFunction	omegaWallFunction	mutWallFunction	fixedValue
fluid_region_to_pipe	fixedFluxPressure	compressible::turbulentTemperatureCoupledBaffleMixed	kLowReWallFunction	omegaWallFunction	mutWallFunction	fixedValue
fluid_region_to_pipe_wall_condition	fixedFluxPressure	compressible::turbulentTemperatureCoupledBaffleMixed	kLowReWallFunction	omegaWallFunction	mutWallFunction	fixedValue
fluid_region_to_pipe	fixedFluxPressure	compressible::turbulentTemperatureCoupledBaffleMixed	kLowReWallFunction	omegaWallFunction	mutWallFunction	fixedValue
fluid_region_to_liner	fixedFluxPressure	compressible::turbulentTemperatureCoupledBaffleMixed	kLowReWallFunction	omegaWallFunction	mutWallFunction	fixedValue
fluid_region_symmetry	symmetry	symmetry	symmetry	symmetry	symmetry	symmetry
Pipe						
Boundary surface	p	T				
pipe_to_fluid_region	Type	Type				
pipe_wall_condition_to_fluid_region	calculated	compressible::turbulentTemperatureCoupledBaffleMixed				
pipe_to_plugs	calculated	compressible::turbulentTemperatureCoupledBaffleMixed				
pipe_symmetry	symmetry	symmetry				
pipe_to_ext	calculated	externalWallHeatFluxTemperature				
Plugs						
Boundary surface	p	T				
plugs_to_fluid_region	Type	Type				
plugs_to_bosses	calculated	compressible::turbulentTemperatureCoupledBaffleMixed				
plugs_to_pipe	calculated	compressible::turbulentTemperatureCoupledBaffleMixed				
plugs_symmetry	symmetry	symmetry				
plugs_to_ext	calculated	externalWallHeatFluxTemperature				
Bosses						
Boundary surface	p	T				
bosses_to_fluid_region	Type	Type				
bosses_to_plugs	calculated	compressible::turbulentTemperatureCoupledBaffleMixed				
bosses_to_liner	calculated	compressible::turbulentTemperatureCoupledBaffleMixed				
bosses_to_composite	calculated	compressible::turbulentTemperatureCoupledBaffleMixed				
bosses_symmetry	symmetry	symmetry				
bosses_to_ext	calculated	externalWallHeatFluxTemperature				
Liner						
Boundary surface	p	T				
liner_to_fluid_region	Type	Type				
liner_to_bosses	calculated	compressible::turbulentTemperatureCoupledBaffleMixed				
liner_to_composite	calculated	compressible::turbulentTemperatureCoupledBaffleMixed				
liner_symmetry	symmetry	symmetry				
Composite						
Boundary surface	p	T				
composite_to_liner	Type	Type				
composite_to_bosses	calculated	compressible::turbulentTemperatureCoupledBaffleMixed				
composite_symmetry	symmetry	symmetry				
composite_to_ext	calculated	externalWallHeatFluxTemperature				

Table 2.14 – Table listing the boundary conditions for the different fields and different regions.

Chapter 3

First CFD results

Introduction

OpenFOAM has been used to carry out the CFD simulations. The CFD simulation cases concern fillings with gaseous hydrogen of a type IV 37 L tank loaded until 700 bar with an axial injection. The implementation of a real gas EOS in OpenFOAM has been performed during this work. Numerous tests have been performed to ensure mesh convergence and select the parameters required to execute OpenFOAM multi-region simulations. This CFD modeling is new and must be validated. The most contrasted scenarios in terms of thermal gradients have been selected to perform the validation and to investigate the ability of the CFD modeling to predict the thermal behavior. Scenario D3Q8 led to the most homogeneous thermal behavior and scenario D10Q2 led to the most heterogeneous thermal behavior. The reliability of the 2D-axisymmetric CFD approach versus the 3D CFD approach were also compared. The study is the subject of an article [119] entitled *A computational fluid dynamic study of the filling of a gaseous hydrogen tank under two contrasted scenarios* and published in the International Journal of Hydrogen Energy (IJHE). It is reported in section 3.1. The article does not include a comparison of the CFD results with SOFIL or with the CFD results issued from ALAT. It does not include a comparison between the CFD and the experimental results for the temperatures measured between the liner and the composite. These elements are reported in section 3.2.

3.1 A computational fluid dynamic study of the filling of a gaseous hydrogen tank under two contrasted scenarios

A computational fluid dynamic study of the filling of a gaseous hydrogen tank under two contrasted scenarios

Rémi GONIN^{a,b,*}, Pierre HORGUE^a, Romain GUIBERT^a, David FABRE^a,
Rémi BOURGUET^a, Fouad AMMOURI^b, Elena VYAZMINA^b

^a*Institut de mécanique des fluides de Toulouse (IMFT), Université de Toulouse, CNRS, 2
allée Camille Soula, Toulouse, France*

^b*Air Liquide Innovation Campus Paris, 1 Chemin de la Porte des Loges, Les
Loges-en-Josas, France*

Abstract

The filling of a horizontal hydrogen tank designed for light duty vehicles is investigated by means of multi-physics numerical simulations. The simulation approach, implemented in OpenFOAM, includes compressible Reynolds-Averaged Navier-Stokes (RANS) modeling of the fluid flow and heat transfer in the solid parts. The simulations are carried out for 2D-axisymmetric and 3D configurations. Two filling scenarios of the tank, leading to two distinct thermal behaviors, i.e. homogeneous versus heterogeneous, are simulated and compared to the experimental data issued from the HyTransfer project. In the homogeneous case, where no thermal stratification occurs, the 2D and 3D simulation results are close to the experimental ones. A phenomenon of jet flapping is identified via the 3D simulation. In the heterogeneous case, where thermal stratification occurs, the 3D simulation captures an averaged temperature close to the experimental one, as well as the instant at which the thermal gradients appear. It also captures the deflection of the jet, which is a central element in the emergence of the thermal gradients.

Keywords: compressed hydrogen, tank filling, thermal gradient, CFD
2010 MSC: 00-01, 99-00

Highlights

- 2D axisymmetric and 3D simulations are carried out using free software Open-FOAM.
- Jet deflection and flapping, and onset of stratification are captured.

*Corresponding author

Email address: remi.gonin@toulouse-inp.fr (Rémi GONIN)

- The $k - \omega$ SST turbulence model underestimates the thermal gradients.

1. Introduction

1.1. Context

Hydrogen is currently considered as an alternative source of energy for light and heavy vehicles compared to regular fossil fuel [1]. For practical convenience, the filling time of the hydrogen tank of light duty vehicle should be comparable to that of a standard fuel tank, about 3-5 minutes [2], for a similar operation range, i.e. 500 km. To match these requirements, the internal pressure reaches 70 MPa at a standard temperature. Composite and plastic materials are employed in order to limit tank weight. These materials are characterized by much lower thermal conductivities [3] compared to metallic tanks, leading to reduced heat exchanges with the exterior environment and to a sharp rise of the gas and wall temperatures. The J2601 standard of the Society of Automobile Engineers (SAE) organism [4] advises admissible temperature between $-40\text{ }^{\circ}\text{C}$ and $85\text{ }^{\circ}\text{C}$. Inner temperatures need to be controlled following these specifications.

As shown in previous studies [5, 6, 7], reducing the inlet temperature is a possible way to decrease the maximum temperature reached during the filling. As a result, current filling stations precool the inlet flow down to $-40\text{ }^{\circ}\text{C}$ to reduce the final gas temperature in the tank. However, this solution presents some limitations. It is energetically costly and, considering that the temperature field may be heterogeneous during filling due to buoyancy effects, high temperatures may be reached along the upper walls even with precooling. This heterogeneous thermal field phenomenon has been highlighted during the HyTransfer project [8], funded by the Fuel Cells and Hydrogen Joint Undertaking (FCH JU) partnership. This program involved experiments and computational fluid dynamics (CFD) in two institutions, Air Liquide Advanced Technology (ALAT) and the Joint Research Centre (JRC). With thermal sensors located inside the hydrogen bulk, the thermal behavior of the fluid has been investigated and showed internal thermal gradients for some tank geometries and under some specific filling conditions. However, the limited number of probes within the fluid region did not allow to clarify the mechanism leading to thermal gradients.

Historically, the first attempts to model tank filling were based on thermodynamic zero dimension (0D) models, which consider the fluid bulk as a unique control volume on which mass and energy balance equations are applied (see e.g [9, 10, 11, 12]). These models are suitable to obtain rapid estimations of the averaged temperature of the inner fluid. When reducing the injection velocity, thermal gradients appear in the tank and 0D models cannot capture local temperature variations. Terada et al. [13] observed that this transition occurs below a critical injection velocity of 5 m/s . This criterion was confirmed on HyTransfer cases [14] and gives insights into the occurrence of thermal gradients; however the underlying physical phenomena still need to be explored.

With the increase of computer resources, CFD can now be employed to investigate these configurations. CFD gives access to the entire velocity, pressure

and temperature fields, which are inaccessible via experiments. The HyTransfer experimental database has served as a benchmark for validation of the simulations in both involved teams. On one hand, within JRC team, simulations were carried out with the commercial CFD software Ansys CFX, using a Redlich-Kwong [15] equation of state as real gas equation of hydrogen. For turbulence modeling, in the first study belonging to the HyTransfer project [16], a modified $k - \epsilon$ turbulence model [17] previously used in similar studies from the same team [5, 18, 19, 20] was used. Subsequently, in Refs. [21, 22] a $k - \omega$ shear stress transport (SST) model with a $\Gamma - \Theta$ model transitional turbulent-laminar model described by Langtry et Menter [23] was used to improve the capture of heterogeneities. These simulations captured the onset of thermal stratification but tended to be less reliable to quantify the stratification level. On the other hand, in the ALAT team, simulations were done with the commercial CFD software Ansys Fluent Inc. using a half domain composed of 640 000 cells, a $k - \omega$ SST turbulence model and real gas model data tabulated from REFPROP© v9.1 database. These simulations were able to predict the onset of stratification phenomenon but not the gradient values.

1.2. Case selection from experimental data

To avoid exceeding the temperature limit of 85 °C during the filling, the injected gas is cooled which is energetically costly. The HyTransfer project [8] aimed at optimizing fast filling of compressed hydrogen tank using an experimental setup, to find new filling protocols, limiting the pre-cooling, while guaranteeing safety. In this project, three tanks have been used: (i) a type III tank, i.e. composite material with metal liner, capacity of 40 L, provided by Dynetek Industries Ltd, (ii) a type IV tank, i.e. composite material with plastic liner, capacity of 37 L, and (iii) a type IV tank capacity of 531 L provided by Hexagon. The first two are considered as small tanks with an aspect ratio L/D (tank length over tank inner diameter) about 2.7 and 2.4. The aspect ratio of the third one is about 5.5. All tanks have been placed in horizontal position, the gravity is normal to the tank axis. The main filling parameters are the inlet mass flowrate and the injection diameter.

The present study will only focus on small tanks for light vehicles. Given the reported cases which lead to different results in terms of thermal gradients, the Hexagon 37 L appears to be the best candidate to run CFD validation. For each experimental case, the local temperature has been recorded at selected points. There are 10 probes for ALAT and 6 for JRC. Consequently, local information about the thermal field is limited by the number and location of the probes. To compare the different results, a quantification of the thermal gradients is needed. Based on the available data [24], the maximum difference between the highest probe temperature T_{max} and the averaged probe temperature T_{av} is proposed as an indicator of heterogeneity at each time. Table 1 presents ALAT results. Results from JRC [25] showed the same trend.

For the present study, the best case and the worst case scenarios have been selected: (i) a case with quasi uniform thermal field for 3 mm injection diameter and 8 g/s averaged mass flowrate, which will be named the **homogeneous** case,

	ⓇHexagon 37 L					
Injection diameter [mm]	3	3	6	6	10	10
Averaged mass flowrate [g/s]	2	8	2	8	2	8
Injection velocity* [m/s]	[190;4.2]	[280;17]	[62;1.1]	[73;2.0]	[22;0.41]	[28;1.1]
ALAT: $T_{max} - T_{av}$ [°C]	8.36	6.35	26.76	11.28	30.03	24.39

Table 1: Thermal gradients for the 37 L ⓇHexagon tank from ALAT[24]. Selected cases in bold. *Estimated assuming a uniform velocity profile in the pipe and using the density calculated via the measured inlet temperature and pressure in the tank, the measured mass flowrate and pipe cross section.

and (ii) a case with large thermal gradient for 10 mm injection diameter and 2 g/s averaged mass flowrate, which will be named the **heterogeneous** case. Note that for the heterogeneous case, the 10 mm injection diameter corresponds to filling directly into the plug aperture without an injection pipe, while for the homogeneous case, an injection pipe of 3 mm of diameter and 100 mm length is entering into the hydrogen bulk. As more probes are available, the ALAT experimental data were chosen for the present calculations. The experimental absolute pressure in the bulk and local temperatures will be used to set the initial and boundary conditions and to validate the numerical method.

1.3. Objectives of this work

The main objective of the present study is to capture, numerically, the different thermal behaviors which occur during tank filling. The different injection scenarios involve physical phenomena related to the three-dimensional nature of the problem so three-dimensional (3D) simulations are carried out. Particular attention is paid to the 3D nature of the underlying physical phenomena and to the impact of a 2D-axisymmetric assumption on their prediction. A specificity of the present study is the use of the open-source software OpenFOAM [26]. (version 6.0 from CFD Direct Ltd).

2. Physical system and its modeling

2.1. Physical system

During gas injection in a closed volume, the pressure and temperature gradually rise. Figure 1 represents the physical configuration. The tank is laying along its main axis, the x-axis, in a horizontal position and the incoming gas is injected along the x-direction. The gravity (\mathbf{g}) is acting vertically along the y-axis. The tank is axisymmetric around the x-axis. It is composed of 4 or 5 solid regions, depending on the presence of an injection pipe: (i) a composite wrap which undergoes the mechanical constraint due to gas pressure, (ii) a plastic liner which limits the molecular diffusion of hydrogen through the wall, (iii) metallic bosses and (iv) plugs at each tank extremities and (v) a metallic injection pipe (for the homogeneous case). The fluid region is the volume enclosed by the solid regions. The tank is surrounded by air at atmospheric pressure and temperature.

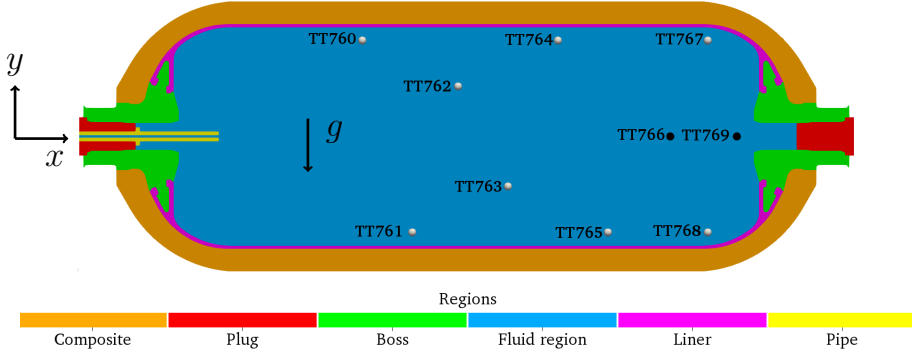


Figure 1: Hexagon 37 *L* tank with a 3 mm injection cut through the (x,y) plane. Probe locations are indicated by circles: probes located in the (x,y) plane in white and probes located outside the (x,y) plane in black.

The simulations are initialized using the pressure and temperature values from the issued experiments. The temperature data come from 10 probes located in the fluid region. Probe locations are given in the HyTransfer project document [24] and shown in figure 1. The inlet temperature and tank pressure were also measured and reported in [24]. Figure 2, adapted from [24], shows plots of all probe measurement for the homogeneous case (plot A) and heterogeneous case (plot B). The results emphasize the contrasted thermal behaviors between the two cases: (i) in the homogeneous case, all probe temperatures remain close to each other for each part; (ii) for the heterogeneous case, the temperatures diverge at $t \approx 100$ s .

2.2. Model

The simulation is based on a coupled fluid dynamics and heat transfer model, called conjugate heat transfer (CHT) [27] method. Depending if the region is fluid or solid, different sets of models and equations are considered.

In solid regions, the governing equation is the energy conservation equation, in order to calculate temperature diffusion across walls. As experiments have been carried out outdoors without control of the environmental conditions, the temperature was not uniform at the beginning of the filling. Assuming a negligible impact of the initial temperature disparity on the final fluid and liner temperatures, all tank regions were initialized at the averaged temperature of the fluid region. Thermophysical properties are constant and can be found in table 2.

On the boundaries, a perfect thermal contact is assumed between the different solid regions, continuity of the heat flux and temperature on walls in contact between solid regions. Heat transfers between the outer faces and the atmosphere are modeled by Newton law,

$$q = hS\Delta T , \quad (1)$$

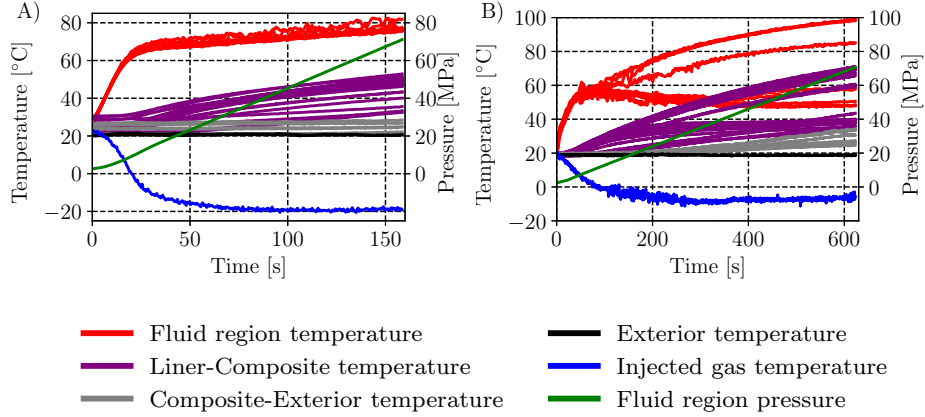


Figure 2: Experimental values from hyTransfer [24]: A) the homogeneous case, B) the heterogeneous case.

Region	Material	Thermal conductivity [W/m/K]	Specific heat capacity [J/kg/K]	Density [kg/m ³]
Composite	Carbon Fiber	0.616	783	1365
Liner	Polymer	0.414	1799	914
Boss	Aluminium 6061	167	896	2700
Plug	Stainless Steel 316L*	16.2	120	7990
Pipe	Stainless Steel 316L*	16.2	120	7990

Table 2: Thermophysical properties of the solid regions. *An erroneous value was used for the specific heat capacity of the stainless steel 316L, which should be close to 500 [J/kg/K]. The plug and the pipe represent a marginal fraction of the solid tank mass and the impact of this error is therefore negligible.

150 with q [W] the thermal flux, h [W/m²/K] the heat transfer coefficient, S [m²] the surface, and ΔT [K] the difference between the solid temperature and the exterior temperature. As set in the JRC work [16, 18, 20], $h = 6$ W/m²/K and the external temperature is set to 18 °C, based on the experimental data values.

155 In the fluid region, the governing equations are the Navier-Stokes equations, i.e. the mass, momentum and energy conservation equation. The Reynolds number based on the pipe diameter, injection velocity and viscosity ranges from 15 000 to 45 000 for the heterogeneous case and from 50 000 to 600 000 for the homogeneous case. At these Reynolds numbers, the flow is turbulent [28] at the pipe outlet. The turbulence is modeled using the Boussinesq assumption with
160 an unsteady Reynolds-averaged Navier–Stokes (URANS) approach and the $k-\omega$ SST equations [29]. This model was shown to be accurate in a fully developed turbulent region like a jet flow [30, 31] and in a pipe flow [32, 33]. Assuming that Prandtl number is close to 1, i.e. the thermal boundary layer and the velocity boundary layer have similar thicknesses, it is expected to capture the
165 thin thermal layer, with an adequate mesh.

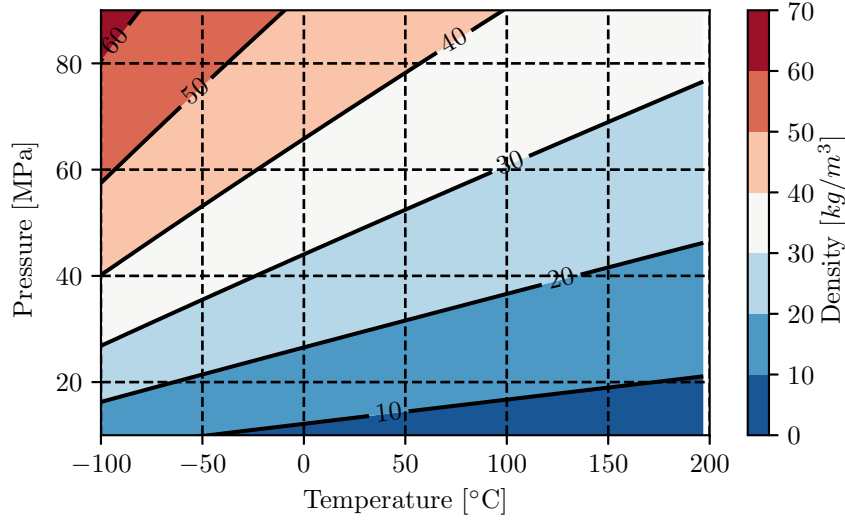


Figure 3: Hydrogen density as a function of pressure and temperature, issued from NIST [37].

Concerning the boundary conditions, for the turbulent kinetic energy k and the turbulent dissipation rate ω , no wall law is used in the heterogeneous case and a wall law (in OpenFOAM, `kLowReWallFunction`) [34] is employed in the homogeneous case. A no slip condition is used on the walls for the velocity. At the inlet, a uniform mass flowrate is imposed. It is deduced from the experimental pressure input as represented in figure 2 (green curve). For the temperature, a continuity of temperature and heat flux is imposed between the different regions. As the perfect gas approximation is not valid in the considered range of pressure and temperature, real gas data are required to determine the thermodynamical properties. In the literature, several gas models have been used and details can be found in the review [35] and [36]. Here, the relevant properties of hydrogen are obtained using the National Institute of Standards and Technology (NIST) tabulated data from [37]: (i) the density [kg/m^3], (ii) the thermal conductivity [$W/m/K$], (iii) the specific thermal capacity [$J/kg/K$], (iv) the kinematic viscosity [$kg/m/s$] and (v) the specific enthalpy [J/kg]. These properties are read from tables. For example, figure 3 represents a plot of the density table as a function of pressure and temperature.

3. Numerical Method

3.1. Solver


The most suitable solver in OpenFOAM is called `chtMultiRegionFoam` [38] as it is required, in the fluid region, to simulate a transient, buoyant and turbulent flow, which exchanges heat with walls. The `ChtMultiRegionFoam` solver

can run a transient simulation with two algorithms. The Pressure Implicit with
190 Splitting of Operators (PISO) algorithm [39, 40], solves the coupled momen-
tum and density equations. The thermodynamic properties (such as density,
viscosity, conductivity) are computed explicitly using the last known pressure
and temperature values. It involves one velocity predictor step and, by default,
two pressure corrector steps at each temporal iteration, to calculate the velocity
195 and pressure fields. To maintain the stability and accuracy of the simulation, it
is recommended to use a Courant–Friedrichs–Lewy number (CFL), lower than
1.

The PIMPLE algorithm [41] is named after a contraction of the PISO and the
Semi-Implicit Method for Pressure Linked Equations (SIMPLE) [42] algorithms.
200 It consists in executing, at each time step, several PISO iterations with updated
thermodynamic properties of the fluid, using the last known solution. With
this iterative process, $CFL > 1$ is allowed, i.e. larger time steps and faster
computations.

No significant difference has been observed in the results by using these
205 two algorithms. The decision of using one instead of the other was motivated
by the possible reduction in computation time. The PIMPLE algorithm was
used for the homogeneous case and the PISO algorithm for the heterogeneous
case. Regarding time and space discretization, first order schemes were used
to maintain the stability of the simulations. Both cases ran using constrained
210 maximum CFL values, with time step ranging from 10^{-4} s to 10^{-6} s .

3.2. Mesh

The meshing process is based on a 3D CAD model from Hexagon provided
during the HyTransfer project [8]. The mesh was generated with two open-
source tools: (i) Salome [43], and (ii) cfMesh [44]. Figure 4A shows a general
215 view of the 3D meshes in the (x,y) plane. Here, focus is placed on the meshing
strategy of the fluid region, which is more challenging than the solid regions.
The objective is to generate a mesh mainly composed of hexahedral cells, with
a refinement adapted to the expected physics. The difference of scales between
the inner pipe area and the main bulk require a variable refinement strategy to
220 reach the relevant cell size in each region. A view at the injection region can be
found in figure 4B. A typical cell size in the bulk is to 5mm. Considering that a
turbulent jet typically expands with an angle of 12° [45], the refinement follows
a conical shape, with a slightly larger angle. Figure 4C visualizes this region. In
the boundary layer regions, the mesh is composed of five layers with a growth
225 rate of 1.4. This design leads to $y^+ < 1$ on all walls for the heterogeneous case,
and a wall law is not required. For the homogeneous case, $y^+ \approx 1$ could not be
reached in the the injection region, a $y^+ < 50$ was enforced and a wall law is
used.

3D simulations have been carried out: (i) on the full tank geometry, or (ii)
230 on half of the domain using as a cutting plane (x,y). The first ones will be named
full 3D and the second ones **3D**. In addition to the 3D meshes, 2D axisymmetric
meshes, named **2D**, were also employed. These meshes represent a slice of the

Case	Type	Fluid region	Solid regions	Total
Homogeneous	2D	15 605	6 373	21 978
	3D	816 156	493 243	1 309 399
	full 3D	1 664 904	986 486	2 651 390
Heterogeneous	2D	11 273	5 873	17 146
	3D	651 482	449 126	1 100 608
	full 3D	1 302 964	898 252	2 201 216

Table 3: Number of cells for each case, in the fluid and solid regions.

domain with one cell depth. They have the same refinement property as the 3D meshes. The number of cells for each mesh is reported in table 3.

235 3.3. Validation

Validation of the solver and mesh was performed on the 2D cases in order to reduce computational costs. The homogeneous configuration was chosen for mesh convergence study, due to its higher velocities. Even though gravity is not taken into account in the 2D approach, the thermal gradients are limited in this configuration and the 2D results can be compared with the experimental data. Three cases were simulated, using a coarse mesh (9 193 cells), a medium mesh (15 605 cells) and a fine mesh (34 378 cells). Less than 1 °C of difference in the averaged temperature was noted over the integration time. The medium mesh was selected to design the 3D mesh. Time step sensitivity was studied on this medium mesh by dividing the time step by a factor of 2. This leads to less than 1 °C of difference in the averaged temperature.

245 Full 3D case and 3D case were compared over 15 seconds in the homogeneous case; the differences in temperature are negligible. In order to limit the computation cost, complete simulations were performed on the 3D cases, i.e. half of the tank. This strategy was also used by the JRC [16] and ALAT [46].

4. Results and discussion

4.1. Velocity and temperature fields

255 Figures 5, 6, 7, 8 show snapshots of the velocity magnitude (upper panel) and the temperature field (lower panel) at three different times over a filling scenario, for the 2D and 3D homogeneous cases, and the 2D and 3D heterogeneous cases. A x-axis symmetry is applied to the 2D cases to ease visualization. For the homogeneous case, the velocity colorbar is scaled between 0 and 10 *m/s* to highlight the jet penetration and the velocity decay over time. For heterogeneous case, the velocity colorbar is scaled between 0 and 1 *m/s*, for the same purpose.

260 Complementary videos of 3D cases are available in the **Supplemental Data**. For each case: the maximum magnitude of velocity is at the top left corner, an averaged value of the thermal field is indicated at the bottom left corner and an isoline of the averaged value of the thermal field is superimposed on the thermal field (bottom panel).

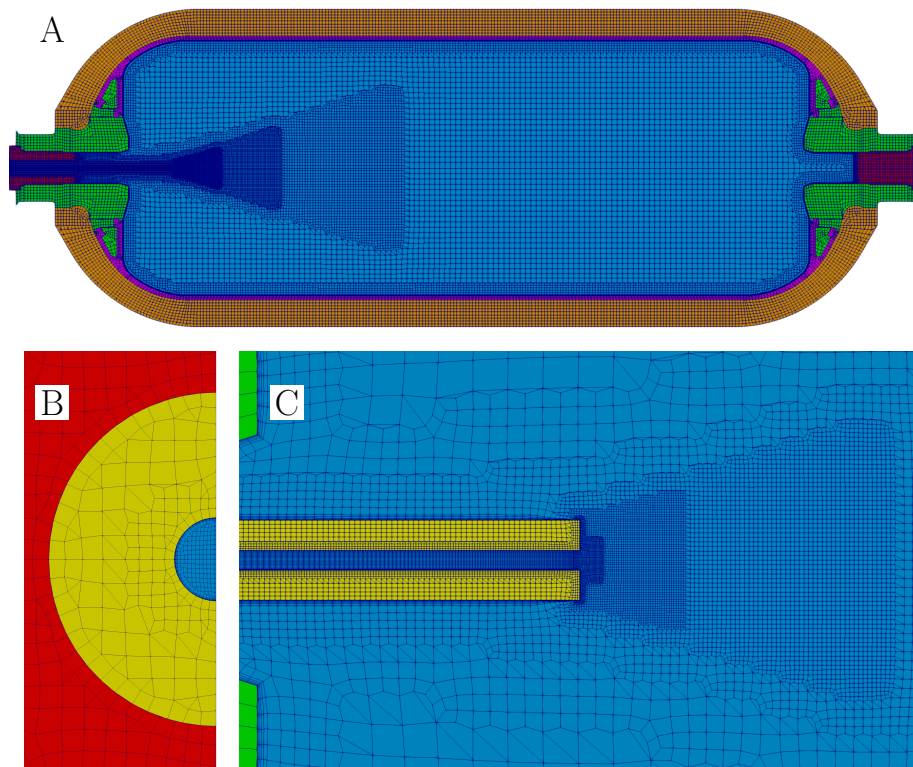


Figure 4: Computational meshes: A) a global overview of all regions in the (x,y) plane for the homogeneous case, B) slice at the inlet plane for the heterogeneous case, C) zoom around the injector for the heterogeneous case.

265 Supplementary video related to this article can be found at <https://doi.org/10.1016/j.ijhydene.2022.03.20>

In the 2D simulations (figures 5 and 7), due to the axisymmetry assumption, gravity is neglected. High temperature spots appear in the regions which are not reached by the cold jet, like the areas above and below the pipe, close to the liner and left boss wall. The jet remains parallel to the x-axis.

270 For the 3D homogeneous case (figure 6), the jet is flapping up and down in the (x,y) plane. In the video, it can be seen that the maximum temperature is not localized in the upper part but is oscillating around the injection area, with the same frequency as the jet flapping frequency. The thermal field is homogeneous, i.e. not vertically stratified.

275 For the 3D heterogeneous case (figure 8), before 50 s the jet is moving upward, as in the initial phase of flapping, but then it starts deflecting toward the lower part. A vertical gradient of temperatures appears, which is depicted by the horizontal isoline of temperature (lower panels at $t = 310$ s and $t = 610$ s in figure 8).

280 4.2. Global quantities

In the experiments, temperatures are sampled by a limited number of probes. An arithmetic average on probes may not be a representative value for an averaged temperature of the entire thermal field. Using the CFD, it is possible to average directly the temperature field

$$T_{av-field} = \frac{\sum_i T_i v_i}{V_{tank}}, \quad (2)$$

285 by weighting each cell temperature T_i by the cell volume v_i over the total volume V_{tank} , or to average the 10 temperature values $T_{probe,i}$ where probes are experimentally located

$$T_{av-probes} = \frac{\sum_i^{10} T_{probe,i}}{10}. \quad (3)$$

290 Due to its higher thermal disparity, the heterogeneous case is more relevant to compare over these two averaging approaches. The difference is lower than 1.5 °C before $t = 100$ s and lower than 0.5 °C after $t = 100$ s. Therefore, the averaged temperature from the experimental probes will be regarded as the reference value for further comparisons. The same question arises for the absolute pressure. CFD results show that the pressure field is close to uniform in the tank. Therefore, a single measurement point in the tank is already relevant to characterize the bulk pressure.

295 Figure 9 presents a comparison of the averaged temperature and pressure between the 2D, 3D and experimental cases, for the homogeneous case A) and for the heterogeneous case B). Figure 10 presents the heat flux q (4) which can be calculated by

$$q = \sum_i \lambda_{eff} \Delta T s_i, \quad (4)$$

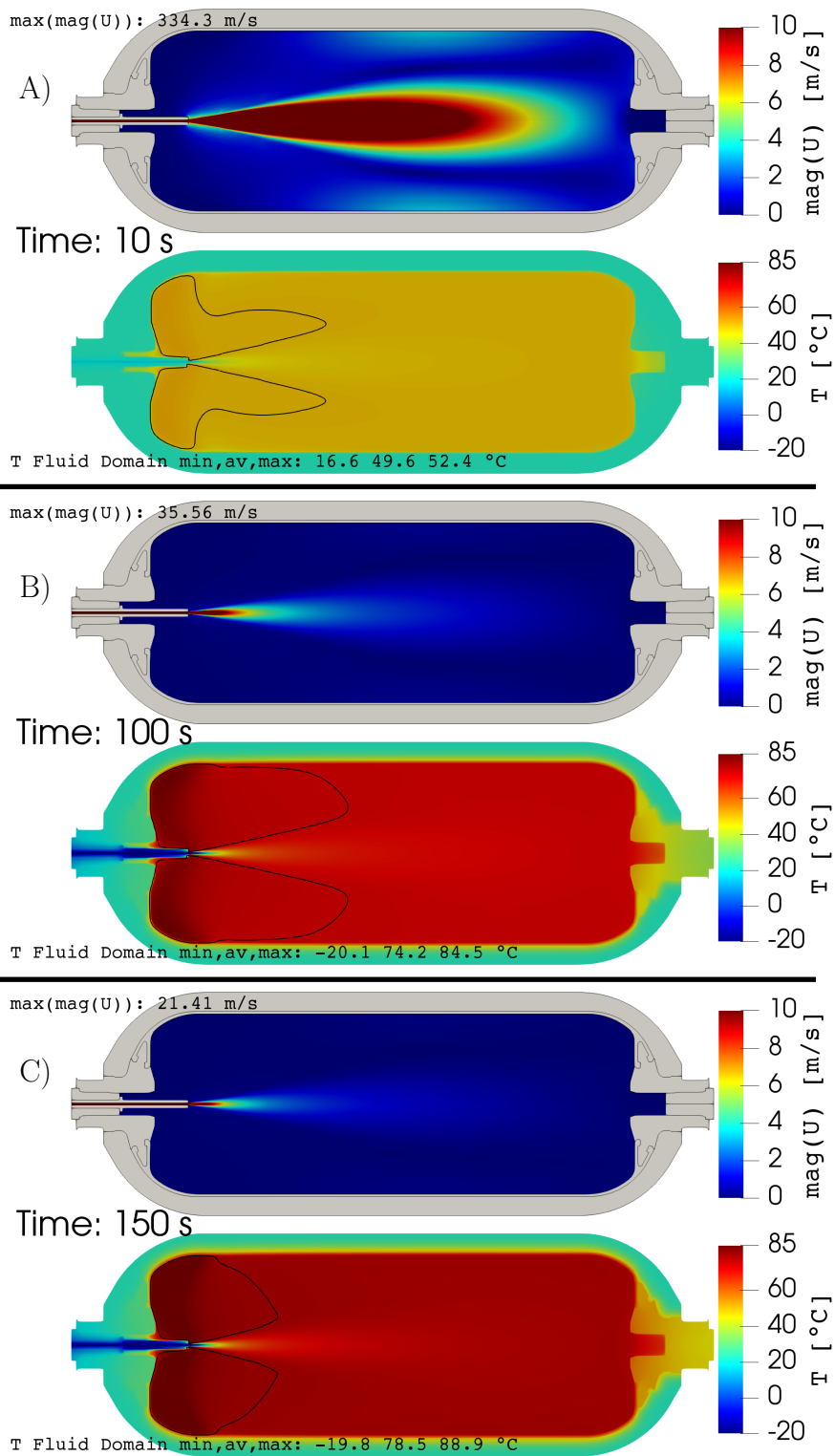


Figure 5: Homogeneous 2D case. For each time instant: A) $t = 10$ s, B) $t = 100$ s and C) $t = 150$ s. The upper panel represents the velocity magnitude field, the lower panel represents the temperature field. The black isoline corresponds to averaged temperature. A x-axis symmetry is applied to ease visualization.

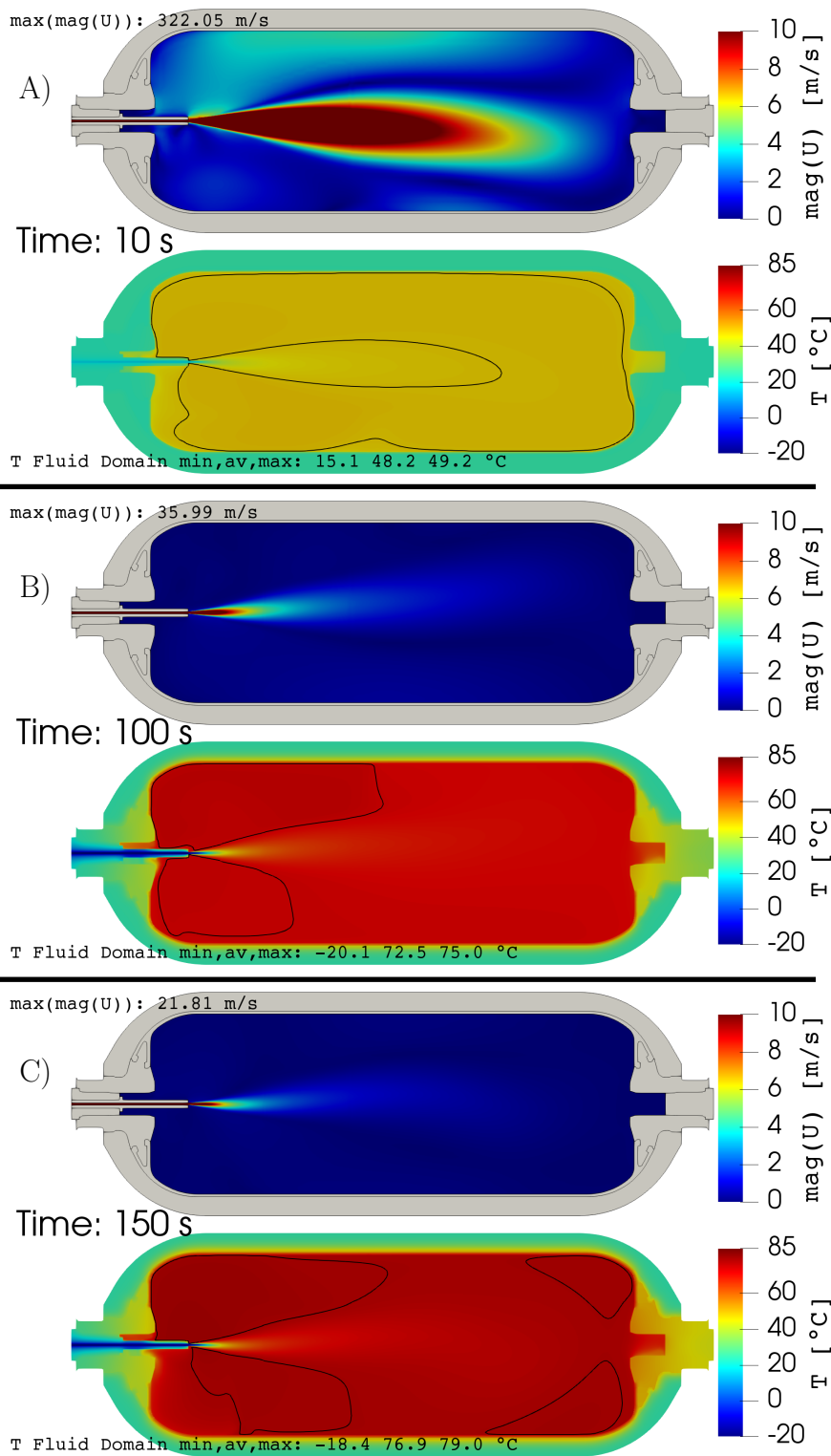


Figure 6: Homogeneous 3D case. For each time instant: A) $t = 10$ s, B) $t = 100$ s and C) $t = 150$ s. The upper panel represents the velocity magnitude field, the lower panel represents the temperature field. The black isoline corresponds to averaged temperature.

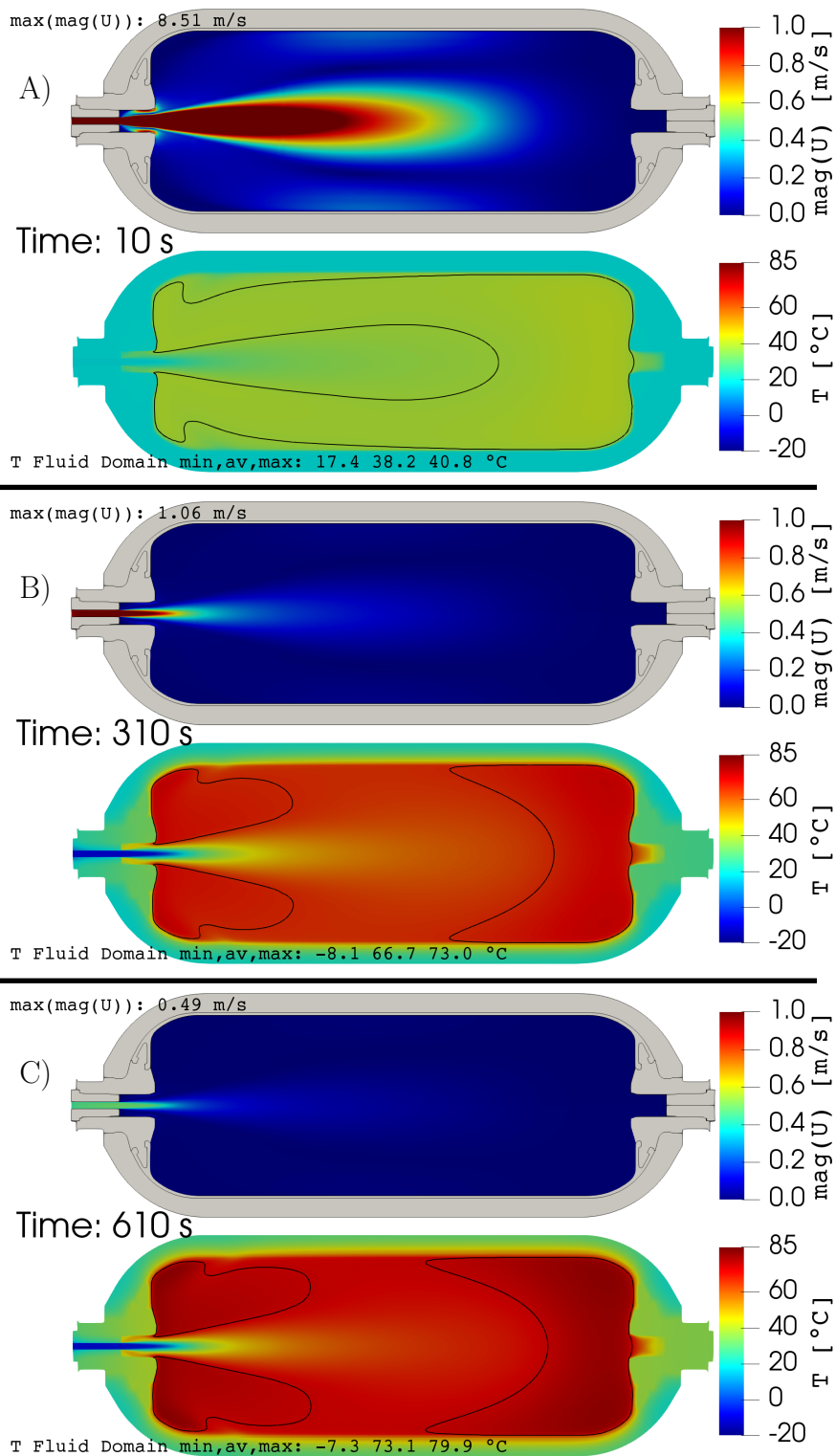


Figure 7: Heterogeneous 2D case. For each time instant: A) $t = 10$ s, B) $t = 310$ s and C) $t = 610$ s. The upper panel represents the velocity magnitude field, the lower panel represents the temperature field. The black isoline corresponds to averaged temperature. A x-axis symmetry is applied to ease visualization.

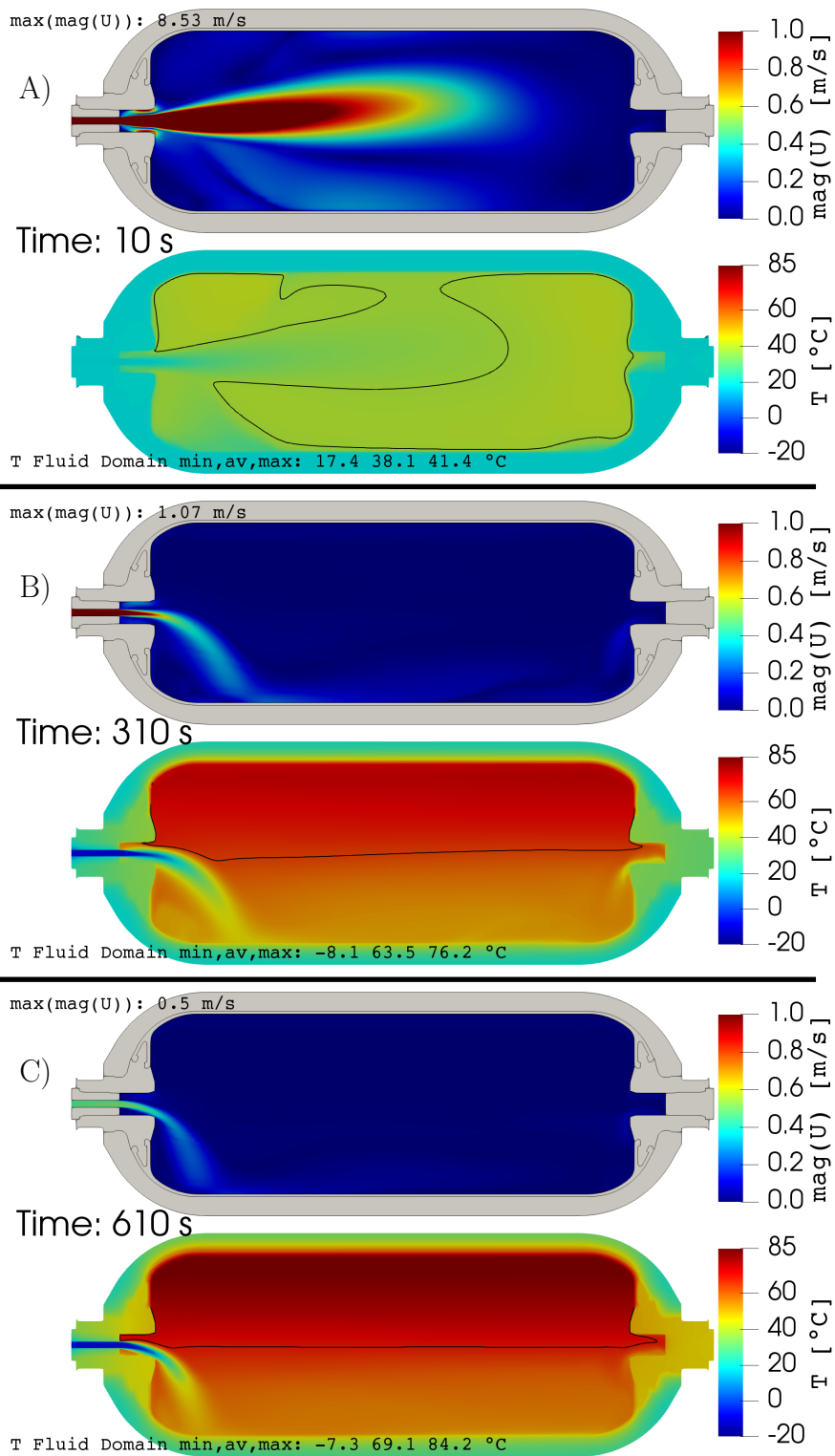


Figure 8: Heterogeneous 3D case. For each time instant: A) $t = 10$ s, B) $t = 310$ s and C) $t = 610$ s. The upper panel represents the velocity magnitude field, the lower panel represents the temperature field. The black isoline corresponds to averaged temperature.

where s_i is the cell surface at wall, ΔT is the difference of temperature between the one at wall and the one at the first cell center and λ_{eff} [$W/m/K$] is the effective thermal conductivity defined as

$$\lambda_{eff} = \lambda + \lambda_t , \quad (5)$$

where λ is the thermal conductivity and λ_t is the turbulent thermal conductivity,

$$\lambda_t = \frac{c_p \mu_t}{Pr_t} , \quad (6)$$

with the turbulent Prandtl number $Pr_t = 0.85$; c_p [$J/kg/K$] is the specific heat capacity and μ_t [$kg/m/K$] the turbulent dynamic viscosity.

Figure 10 displays the averaged surface temperature at fluid-solid interfaces using the following expression to weight the average using a local surface:

$$T_{wall} = \frac{\sum_i T_i s_i}{S} |_{fluid-solid\ wall} . \quad (7)$$

In the above expression, T_i is the cell temperature at wall, s_i is the cell surface at wall and S is the total surface of the wall.

300 Concerning the homogeneous case, figure 9A shows that the averaged temperature issued from the 3D field is within ± 1 °C from the experimental value. In the 2D case, the averaged temperature is higher and farther from the experimental value, compared to the 3D case. This difference of averaged temperature is induced by a difference of heat transfer. Figure 10A shows that the global
 305 heat flux (dotted line) is slightly larger for the 3D case than for the 2D case. This small difference is due to less heat flux through bosses and plugs for the 2D case. The larger flux through the liner does not counterbalance this trend. For the 2D case the gravity is neglected and therefore no natural convection is possible. In areas where heat transfer is led by natural convection, like plug cavity, the heat flux is underestimated. In addition, the 2D assumption constrains
 310 the jet on the x-axis, while it is free to flap in the (x,y) plane in the 3D case. This may result in a better mixing of the bulk and avoid some stagnant hot or cold spots. As shown in figure 10C, the deviations of heat flux is associated with large deviations in wall temperature predictions between the 2D and 3D
 315 simulations.

Concerning the heterogeneous case, the probe averaged temperature issued from the 3D simulations is within ± 3.5 °C from the experimental value before $t = 300$ s , and ± 1 °C after, as showing in figure 9B. The 2D case shows again a higher averaged temperature. In the heterogeneous case, gravity plays
 320 a role even more important than in the homogeneous case. As can be seen in figure 8, due to buoyancy forces, the jet tends to plunge towards the lower part of the tank. In the 2D axisymmetric case, this phenomenon and the vertical thermal stratification cannot be captured. This leads to a non physical thermal disparity and to an underestimation of the velocity close to the bottom wall
 325 (figure 7). A consequence is a significant difference of heat transfer on every walls, between the 2D and 3D cases, as highlighted in figure 10B. As shown in figure 10C, this leads to lower temperatures on solid walls, even though the averaged temperature in the fluid region is higher.

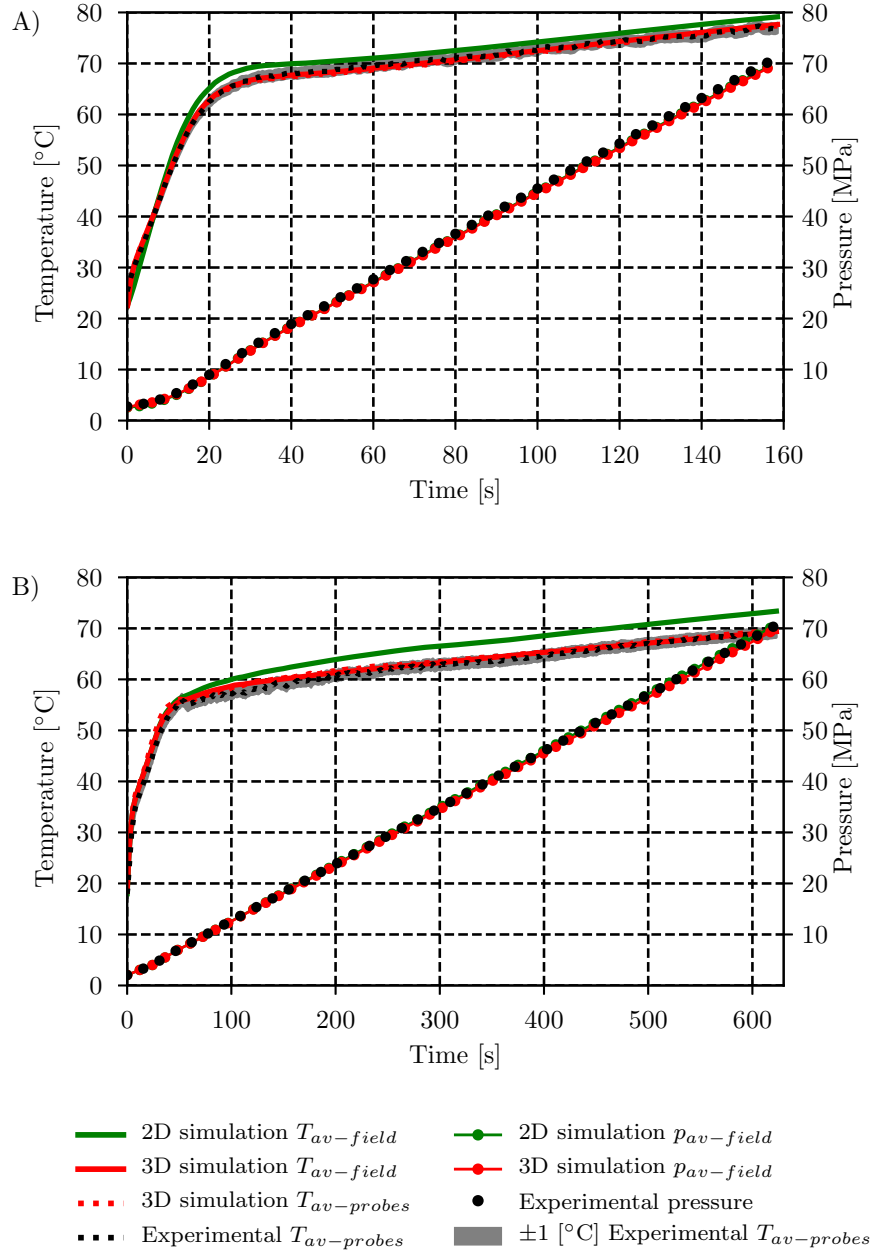


Figure 9: Comparison between the averaged values of the temperature (left axis) and pressure (right axis) issued from the present simulations and the experiment, in the fluid region, for the A) homogeneous and B) heterogeneous cases.

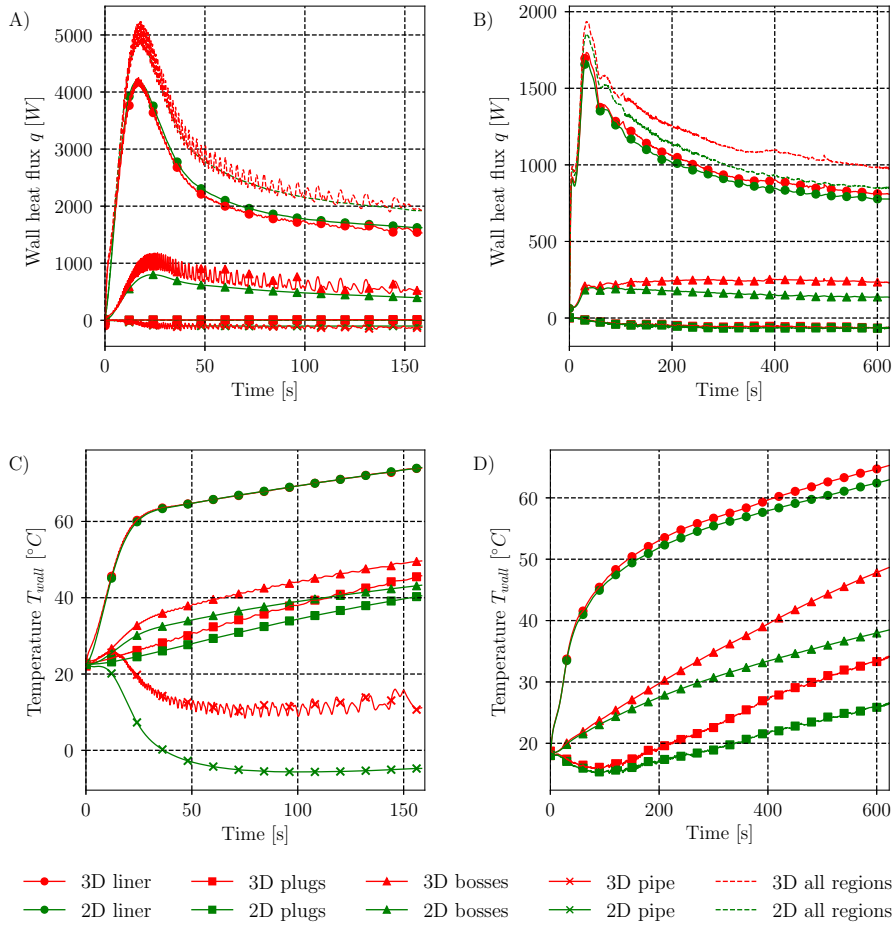


Figure 10: A), B) wall heat flux and C), D) temperature at fluid-solid interfaces as functions of time, for the A), C) homogeneous and B), D) heterogeneous cases.

4.3. Local quantities

330 Figures 11 and 12 present a comparison of probe temperatures issued from the 3D simulations and the experiments, for the homogeneous and the heterogeneous cases, respectively.

In the homogeneous case (figure 11), the simulation globally matches the experimental values. As shown in figure 6 no thermal stratification occurs and the probe values remain close to the averaged temperature value.

335 In the heterogeneous case (12), the simulation results are close to the experimental values until $t = 150$ s, when the thermal gradient starts to develop. Then the simulation tends to underestimate the thermal gradient: in the upper part of the tank (TT760,TT764,TT767), the simulation values are lower than the experimental values and in the lower part of the tank (TT761,TT765,TT768), the simulation values are higher than experimental values. Turbulence is playing a major role in the process of thermal diffusion and its modeling may explain the differences in the heterogeneous case simulation. The $k - \omega$ SST model predicts high levels of turbulent viscosity in regions supposedly laminar. This may result in higher effective thermal diffusion and then in lower gradients of temperature. Homogeneous cases with lower thermal gradients are less impacted by this phenomenon. Turbulence models capturing the laminar-turbulent transition may be a solution. The $k - \omega$ SST Scale-Adaptive Simulation (SAS) [47] has been mentioned by ALAT [46, 35] or the $\Gamma - \Theta$ model [23] has been used by the JRC [21] in the latter study. The emergence of thermal gradients was captured but not their precise magnitudes. The impact of such advanced models remains to be investigated.

5. Conclusion

335 Two filling scenarios of a horizontal gaseous tank, leading to two different thermal behaviors, a homogeneous case and a heterogeneous case, have been simulated and compared to experimental data issued from the HyTransfer project [8]. The simulations have been carried out in 2D using an axisymmetry assumption and in 3D by considering half of the tank.

360 In the homogeneous case, where no thermal stratification occurs, the 2D and 3D simulation averaged temperature are close to the experimental measurements. Due to the restrictions imposed to the fluid under 2D assumption, the inner jet cannot cool areas close to the injector as in the 3D case. This results in a hot spot close to the injector, 10 °C above the averaged temperature at 150 s. A phenomenon of jet flapping is highlighted by the 3D simulations. This phenomenon seems responsible for the periodic motion of the hot spot close to the injector, where the temperature is only 2 °C above the averaged temperature at 150 s. Future work should focus on clarifying jet oscillation mechanism and its link to heat transfer.

370 In the heterogeneous case, where thermal stratification occurs, the 2D simulation does not capture the vertical heterogeneity and the thermal gradient onset cannot be detected. The 3D simulation predicts an averaged temperature

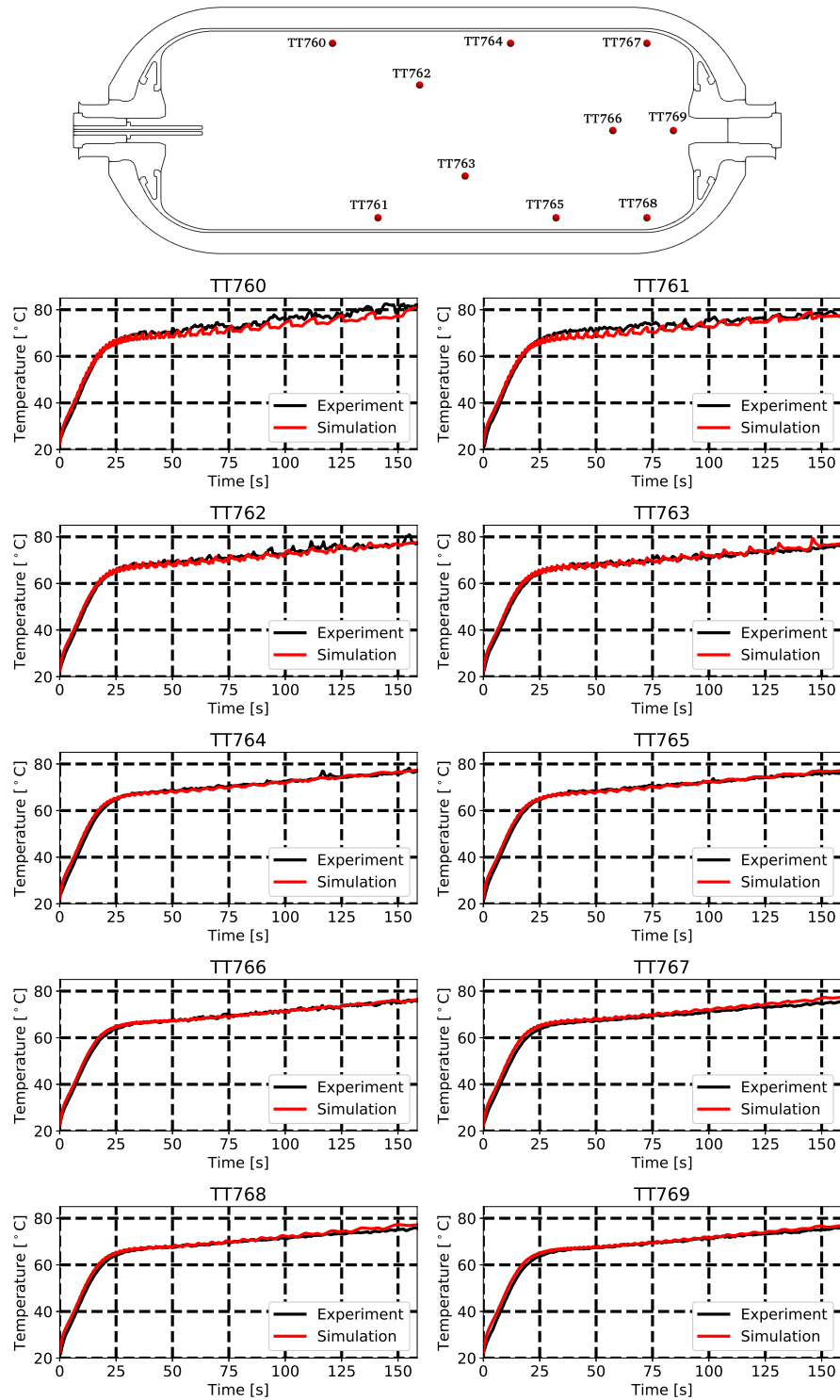


Figure 11: Comparison between the local temperature values issued from the 3D simulation and the experiment, in the homogeneous case. Probe locations are indicated in the upper panel.

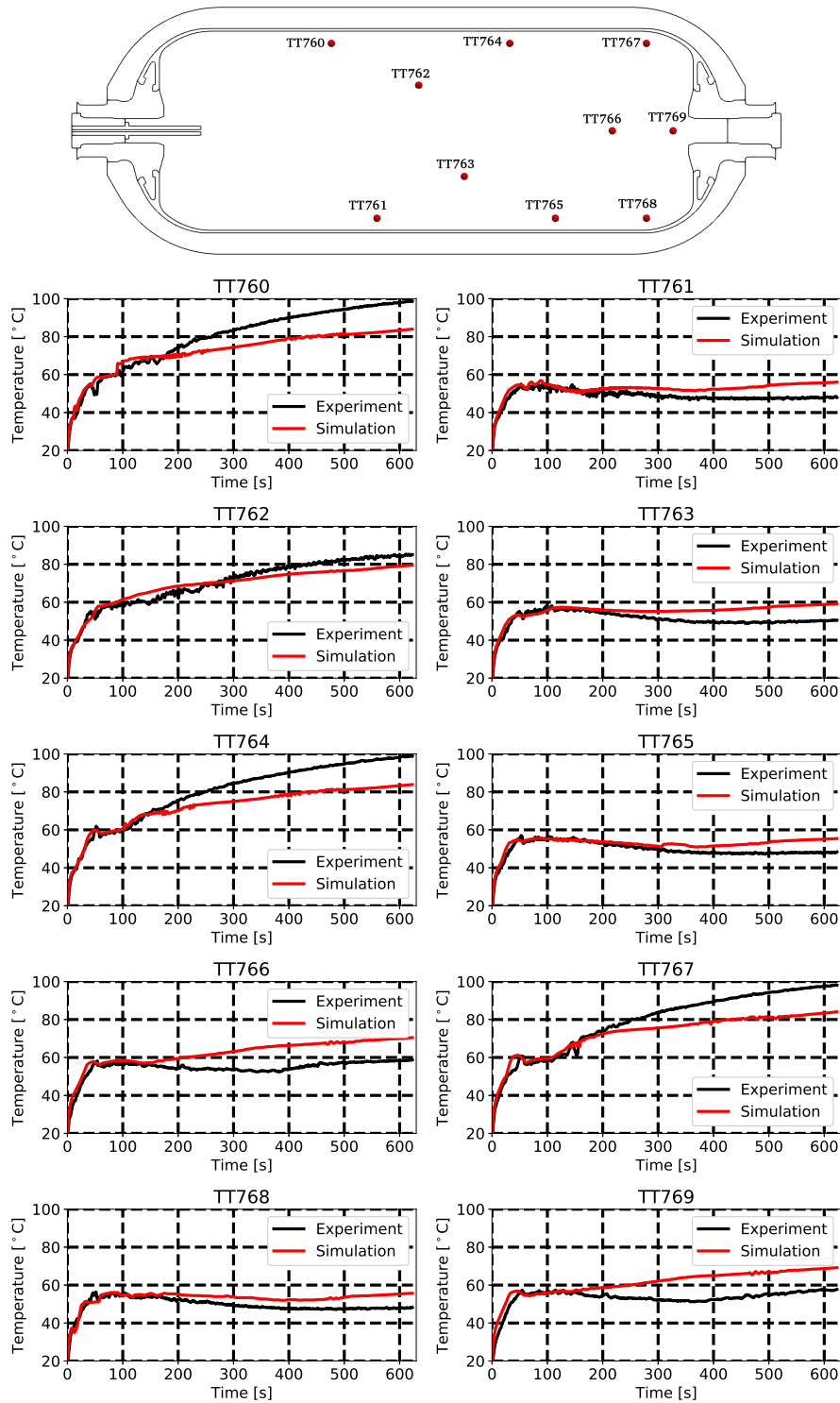


Figure 12: Comparison between the local temperature values issued from the 3D simulation and the experiment, in the heterogeneous case. Probe locations are indicated in the upper panel.

close to the experimental one. It captures the deflection of the jet, which is one of the key processes in the emergence of the thermal gradients. The instant at which the thermal gradients appear is well estimated. The thermal gradients are however underestimated. At the end of the filling process (630 s), the differences of maximum temperature between the simulation results and the experimental measurements at probe TT764 and TT761 are +15 °C and −8 °C, respectively. It is suspected to be a consequence of the $k - \omega$ SST turbulence model which tends to over predict the turbulence level and the associated thermal diffusion. Advanced models like the $k - \omega$ SST SAS model, should be investigated to improve the prediction of thermal gradients.

From a phenomenological perspective, CFD provides insights into the flow physics and thermal behavior inside the tank. Such insights are expected to impact the development of 0D models and help optimizing tank filling strategy.

Acknowledgment

This study was carried on as part of a PhD work funded by Air Liquide Innovation Campus Paris and the National Association of Recherche and Technology (ANRT). It was performed using HPC resources from CALMIP (grants 2019 and 2020, p19025)

References

- [1] Q. Nouvelot, P. Karzel, N. Hart, E. Vyazmina, V. Mattelaer, C. D. Sinding, A. Ruiz, Performance metrics for refuelling protocols for heavy duty hydrogen vehicles, fCH-04-2-2019:Refuelling Protocols for Medium and Heavy-Duty Vehicles (2020).
URL https://prhyde-cdn.s3-accelerate.amazonaws.com/wp-content/uploads/2020/10/14133040/PRHYDE_Deliverable-D2-1_final.pdf
- [2] H. Council, A sustainable pathway for the global energy transition (2017).
URL <http://hydrogencouncil.com/wp-content/uploads/2017/11/Hydrogen-scaling-up-Hydrogen-Council.pdf>
- [3] I. Simonovski, D. Baraldi, D. Melideo, B. Acosta-Iborra, Thermal simulations of a hydrogen storage tank during fast filling, International Journal of Hydrogen Energy 40 (36) (2015) 12560–12571. doi:10.1016/j.ijhydene.2015.06.114.
URL <https://linkinghub.elsevier.com/retrieve/pii/S0360319915015992>
- [4] F. C. S. Committee, Fueling protocols for light duty gaseous hydrogen surface vehicles (dec 2016). doi:https://doi.org/10.4271/J2601_201612.
URL https://doi.org/10.4271/J2601_201612

- 410 [5] D. Melideo, D. Baraldi, CFD analysis of fast filling strategies
for hydrogen tanks and their effects on key-parameters, Inter-
national Journal of Hydrogen Energy 40 (1) (2015) 735–745.
doi:10.1016/j.ijhydene.2014.10.138.
URL [https://linkinghub.elsevier.com/retrieve/pii/
415 S0360319914030146](https://linkinghub.elsevier.com/retrieve/pii/S0360319914030146)
- [6] R. Ortiz Cebolla, B. Acosta, N. de Miguel, P. Moretto, Ef-
fect of precooled inlet gas temperature and mass flow rate on
final state of charge during hydrogen vehicle refueling, Interna-
tional Journal of Hydrogen Energy 40 (13) (2015) 4698–4706.
420 doi:<https://doi.org/10.1016/j.ijhydene.2015.02.035>.
URL [https://www.sciencedirect.com/science/article/pii/
S036031991500364X](https://www.sciencedirect.com/science/article/pii/S036031991500364X)
- [7] Y. Kang, S. M. Cho, D. K. Kim, Charging strategy through
analysis of charging influence factors of ultra-light hydrogen stor-
425 age with polyethylene terephthalate liner, International Jour-
nal of Hydrogen Energy 46 (13) (2021) 9174–9185. doi:<https://doi.org/10.1016/j.ijhydene.2021.01.007>.
URL [https://www.sciencedirect.com/science/article/pii/
S0360319921000148](https://www.sciencedirect.com/science/article/pii/S0360319921000148)
- 430 [8] E. i. European Commission, E. researchers, Hytransfer, FCH JU 2012-1-
325277 (2013).
URL <https://cordis.europa.eu/project/id/325277/reporting>
- [9] W. C. Reynolds, Analytical investigation of the blowdown and charging
processes in a single gas receiver, including the effects of heat transfer,
435 Tech. rep., Stanford University (1955).
- [10] C. Muto, An experimental investigation of the effects of heat transfer during
charging and blowdown of single Gas receivers., 1959.
URL <https://apps.dtic.mil/sti/pdfs/AD0487800.pdf>
- 440 [11] T. Bourgeois, F. Ammouri, M. Weber, C. Knapik, Evaluating the
temperature inside a tank during a filling with highly-pressurized gas,
International Journal of Hydrogen Energy 40 (35) (2015) 11748–11755.
doi:10.1016/j.ijhydene.2015.01.096.
URL [https://linkinghub.elsevier.com/retrieve/pii/
S0360319915001640](https://linkinghub.elsevier.com/retrieve/pii/S0360319915001640)
- 445 [12] V. Molkov, M. Dadashzadeh, D. Makarov, Physical model of on-
board hydrogen storage tank thermal behaviour during fuelling,
International Journal of Hydrogen Energy 44 (8) (2019) 4374–4384.
doi:10.1016/j.ijhydene.2018.12.115.
URL [https://linkinghub.elsevier.com/retrieve/pii/
450 S0360319918340837](https://linkinghub.elsevier.com/retrieve/pii/S0360319918340837)

- [13] T. Terada, H. Yoshimura, Y. Tamura, H. Mitsuishi, S. Watanabe, Thermal behavior in hydrogen storage tank for fev on fast filling (2nd report) (2008). doi:10.4271/2008-01-0463.
URL <https://www.sae.org/content/2008-01-0463/>
- 455 [14] C. Devilliers, D7.5 hytransfer final synthesis of the project findings for the industry public (2017).
- [15] O. Redlich, J. N. S. Kwong, On the thermodynamics of solutions. v. an equation of state. fugacities of gaseous solutions., Chemical Reviews 44 (1) (1949) 233–244. doi:10.1021/cr60137a013.
460 URL <https://pubs.acs.org/doi/abs/10.1021/cr60137a013>
- [16] D. Melideo, D. Baraldi, B. Acosta-Iborra, R. Ortiz Cebolla, P. Moretto, CFD simulations of filling and emptying of hydrogen tanks, International Journal of Hydrogen Energy 42 (11) (2017) 7304–7313. doi:10.1016/j.ijhydene.2016.05.262.
465 URL <https://linkinghub.elsevier.com/retrieve/pii/S0360319916307078>
- [17] P. Ouellette, P. G. Hill, Turbulent transient gas injections, Journal of Fluids Engineering 122 (4) (2000) 743–752. doi:10.1115/1.1319845.
470 URL <https://asmedigitalcollection.asme.org/fluidsengineering/article/122/4/743/461883/Turbulent-Transient-Gas-Injections>
- [18] M. C. Galassi, D. Baraldi, B. Acosta Iborra, P. Moretto, CFD analysis of fast filling scenarios for 70 MPa hydrogen type IV tanks, International Journal of Hydrogen Energy 37 (8) (2012) 6886–6892. doi:10.1016/j.ijhydene.2012.01.041.
475 URL <https://linkinghub.elsevier.com/retrieve/pii/S0360319912000912>
- [19] M. C. Galassi, E. Papanikolaou, M. Heitsch, D. Baraldi, B. A. Iborra, P. Moretto, Assessment of CFD models for hydrogen fast filling simulations, International Journal of Hydrogen Energy 39 (11) (2014) 6252–6260.
480 doi:10.1016/j.ijhydene.2013.03.164.
URL <https://linkinghub.elsevier.com/retrieve/pii/S0360319913008422>
- [20] D. Melideo, D. Baraldi, M. C. Galassi, R. Ortiz Cebolla, B. Acosta Iborra, P. Moretto, CFD model performance benchmark of fast filling simulations of hydrogen tanks with pre-cooling, International Journal of Hydrogen Energy 39 (9) (2014) 4389–4395. doi:10.1016/j.ijhydene.2013.12.196.
485 URL <https://linkinghub.elsevier.com/retrieve/pii/S0360319913031881>
- [21] D. Melideo, D. Baraldi, N. De Migue, B. Acosta, Effects of the injector direction on the temperature distribution during filling of hydrogen tanks, HySafe, 2017.
490

- [22] D. Melideo, D. Baraldi, N. De Miguel Echevarria, B. Acosta Iborra, Effects of some key-parameters on the thermal stratification in hydrogen tanks during the filling process, *International Journal of Hydrogen Energy* 44 (26) (2019) 13569–13582. doi:10.1016/j.ijhydene.2019.03.187.
495 URL <https://linkinghub.elsevier.com/retrieve/pii/S0360319919312169>
- [23] R. B. Langtry, F. R. Menter, Correlation-based transition modeling for unstructured parallelized computational fluid dynamics codes, *AIAA Journal* 47 (12) (2009) 2894–2906. doi:10.2514/1.42362.
500 URL <https://arc.aiaa.org/doi/10.2514/1.42362>
- [24] B. Ravinel, B. Acosta, N. De Migue, P. Moretto, O.-C. Rafael, J. Goran, v. d. L. Ulrich, D4.1 report on the experimental filling test campaign (2017).
505 URL https://s02291b7740b89df1.jimcontent.com/download/version/1493713659/module/11623534399/name/HyTransfer_Report%20on%20the%20experimental%20filling%20test%20campaign_public.pdf
- [25] N. de Miguel, B. Acosta, P. Moretto, R. Ortiz Cebolla, Influence of the gas injector configuration on the temperature evolution during refueling of on-board hydrogen tanks, *International Journal of Hydrogen Energy* 41 (42) (2016) 19447–19454. doi:10.1016/j.ijhydene.2016.07.008.
510 URL <https://linkinghub.elsevier.com/retrieve/pii/S0360319916307340>
- [26] The OpenFOAM foundation (2021).
515 URL <https://openfoam.org/>
- [27] T. Perelman, On conjugated problems of heat transfer, *International Journal of Heat and Mass Transfer* 3 (4) (1961) 293–303. doi:https://doi.org/10.1016/0017-9310(61)90044-8.
520 URL <https://www.sciencedirect.com/science/article/pii/0017931061900448>
- [28] B. Eckhardt, T. M. Schneider, B. Hof, J. Westerweel, Turbulence transition in pipe flow, *Annual Review of Fluid Mechanics* 39 (1) (2007) 447–468. doi:10.1146/annurev.fluid.39.050905.110308.
525 URL <http://www.annualreviews.org/doi/10.1146/annurev.fluid.39.050905.110308>
- [29] F. R. Menter, Two-equation eddy-viscosity turbulence models for engineering applications, *AIAA Journal* 32 (8) (1994) 1598–1605. doi:10.2514/3.12149.
530 URL <https://arc.aiaa.org/doi/10.2514/3.12149>
- [30] M. Kmecova, O. Sikula, M. Krajcik, Circular free jets: CFD simulations with various turbulence models and their comparison with theoretical

- solutions, IOP Conference Series: Materials Science and Engineering 471 (2019) 062045. doi:10.1088/1757-899X/471/6/062045.
 535 URL <http://stacks.iop.org/1757-899X/471/i=6/a=062045?key=crossref.e61902386a0e31c386ae819342bb6b6f>
- [31] A. Meslem, F. Bode, C. Croitoru, I. Nastase, Comparison of turbulence models in simulating jet flow from a cross-shaped orifice, European Journal of Mechanics - B/Fluids 44 (2014) 100–120.
 540 doi:10.1016/j.euromechflu.2013.11.006.
 URL <https://linkinghub.elsevier.com/retrieve/pii/S0997754613001313>
- [32] A. Aliferis, S. Burkeland, M. Jessen, C. Meek, Pipe flow simulation for reynolds number up to 1 000 000 (2017).
- 545 [33] A. Hedlund, Evaluation of rans turbulence models for the simulation of channel flow, Master’s thesis, Uppsala University, Department of Information Technology.
- [34] L. Fangqing, A thorough description of how WallFunctions are implemented InOpenFOAM, In Proceedings of CFD with OpenSource Software (2016).
 550 URL http://www.tfd.chalmers.se/~hani/kurser/OS_CFD_2016
- [35] T. Bourgeois, F. Ammouri, D. Baraldi, P. Moretto, The temperature evolution in compressed gas filling processes: A review, International Journal of Hydrogen Energy 43 (4) (2018) 2268–2292.
 555 doi:10.1016/j.ijhydene.2017.11.068.
 URL <https://linkinghub.elsevier.com/retrieve/pii/S0360319917343860>
- [36] M. Li, Y. Bai, C. Zhang, Y. Song, S. Jiang, D. Grouset, M. Zhang, Review on the research of hydrogen storage system fast refueling in fuel cell vehicle, International Journal of Hydrogen Energy 44 (21) (2019) 10677–10693. doi:10.1016/j.ijhydene.2019.02.208.
 560 URL <https://linkinghub.elsevier.com/retrieve/pii/S0360319919308663>
- [37] E. Lemmon, M. Huber, M. McLinden, Nist standard reference database 23: reference fluid thermodynamic and transport properties-refprop, version 9.1 (2013-05-07 2013).
 565 URL https://tsapps.nist.gov/publication/get_pdf.cfm?pub_id=912382
- [38] ChtMultiRegionFoam (2021).
 URL <https://openfoamwiki.net/index.php/ChtMultiRegionFoam>
- 570 [39] The PISO algorithm in OpenFOAM (2021).
 URL http://openfoamwiki.net/index.php/OpenFOAM_guide/The_PISO_algorithm_in_OpenFOAM

- [40] R. Issa, Solution of the implicitly discretised fluid flow equations by operator-splitting, *Journal of Computational Physics* 62 (1) (1986) 40–65. doi:[https://doi.org/10.1016/0021-9991\(86\)90099-9](https://doi.org/10.1016/0021-9991(86)90099-9).
575 URL <https://www.sciencedirect.com/science/article/pii/0021999186900999>
- [41] The PIMPLE algorithm in OpenFOAM (2021).
580 URL https://openfoamwiki.net/index.php/OpenFOAM_guide/The_PIMPLE_algorithm_in_OpenFOAM
- [42] L. S. Caretto, A. D. Gosman, S. V. Patankar, D. B. Spalding, Two calculation procedures for steady, three-dimensional flows with recirculation (1973).
- [43] Salome (2021).
585 URL <https://www.salome-platform.org/>
- [44] cfMesh (2021).
URL <https://cfmesh.com/cfmesh/>
- [45] G. Horn, M. W. Thring, Angle of spread of free jets, *Nature* 178 (1956) 205–206. doi:<https://doi.org/10.1038/178205a0>.
- 590 [46] D. Zaepffel, F. Mathey, B. Ravinel, T. Bourgeois, F. Ammouri, CFD analysis of the different flow regimes occurring during the filling of a hydrogen vehicle tank (2016).
- [47] F. Menter, M. Kuntz, R. Bender, A scale-adaptive simulation model for turbulent flow predictions (2003). doi:10.2514/6.2003-767.
595 URL <http://arc.aiaa.org/doi/10.2514/6.2003-767>

3.2 Additional results

3.2.1 Gas temperatures

In the experimental set-up from ALAT, 10 probes were available in the gas. The question is whether the arithmetic average of the 10 temperatures from probes is representative of an averaged gas temperature. Also, the temperature is an intensive quantity and there is no natural way to average the temperature. For scenario D10Q2 where the thermal field is the most heterogeneous, four different averages have been considered using the temperature field issued from the CFD: (i) arithmetic (3.1), (ii) geometric (3.2), (iii) harmonic (3.3) and (iv) enthalpic (3.4), and defined as

$$T_{av \text{ arithmetic field}} = \frac{\sum_i v_i T_i}{V} \quad (3.1)$$

$$T_{av \text{ geometric field}} = \exp\left(\frac{\sum_i v_i \ln(T_i)}{V}\right) \quad (3.2)$$

$$T_{av \text{ harmonic field}} = \frac{V}{\sum_i \frac{v_i}{T_i}} \quad (3.3)$$

$$T_{av \text{ enthalpic field}} = \frac{\sum_i v_i \rho_i c_{p,i} T_i}{\sum_i v_i \rho_i c_{p,i}} \quad (3.4)$$

There are compared with the arithmetic average temperature calculated with the 10 temperatures issued from the probe locations in figure 3.1. Figure 3.1 shows the maximum deviation between all averages is approximately 0.5 °C. This is within the precision range of the physical temperature probes, i.e. thermocouples. The arithmetic average of the temperature on the 10 probes is considered as a consistent indicator of the averaged gas temperature.

The averaged gas temperature from OpenFOAM CFD results can be compared with SOFIL, the 0D model from Air Liquide [43, 70]. The averaged gas temperature can also be compared with the CFD results from ALAT [59]. The details of the study were reported in an internal document. They used the same tank and the same filling conditions. ALAT carried out 3D CFD simulations on half of the geometrical domain. They used the CFD software Fluent 16 and the $k - \omega$ SST turbulence model. The database from the NIST was used as EOS for hydrogen. The mesh was composed of 640 000 cells. Figure 3.2 displays the comparison of the averaged gas temperature for scenario D3Q8 issued from OpenFOAM CFD, ALAT CFD, SOFIL (0D model) and the experimental measurements. Figure 3.3 displays the same comparison but applied to scenario D10Q2. The prediction of the averaged gas temperature for all numerical approaches is good, especially at the end of the filling where the averaged temperature is maximum.

The 10 temperatures located in the gas can be compared with the results from OpenFOAM and from ALAT. Figure 3.4 displays this comparison for the scenario D3Q8 and figure 3.5 for scenario D10Q2. It can be seen that for scenario D3Q8, the homogeneous thermal state is well captured. For scenario D10Q2, the heterogeneous thermal state is present but the amplitude of the thermal gradient is underestimated. This trend is observed for both simulation cases. The underestimation of the maximal temperature is approximately 12 °C below the experimental measurement for the results from OpenFOAM and 15 °C for the results from ALAT. The maximal, averaged and minimal temperatures issued from the experiment measurements and the CFD studies are reported in table 3.1.

The CFD is able to detect the onset of stratification but fails to predict a maximum temperature. This is problematic to detect when the temperature in the gas exceeds 85 °C. The results from OpenFOAM are similar to the results from Fluent. The $k - \omega$ SST turbulence model is used for both CFD studies. It is suspected to cause the difference reported with the experimental results. This motivates further investigation of the impact of the turbulence model on the thermal behavior.

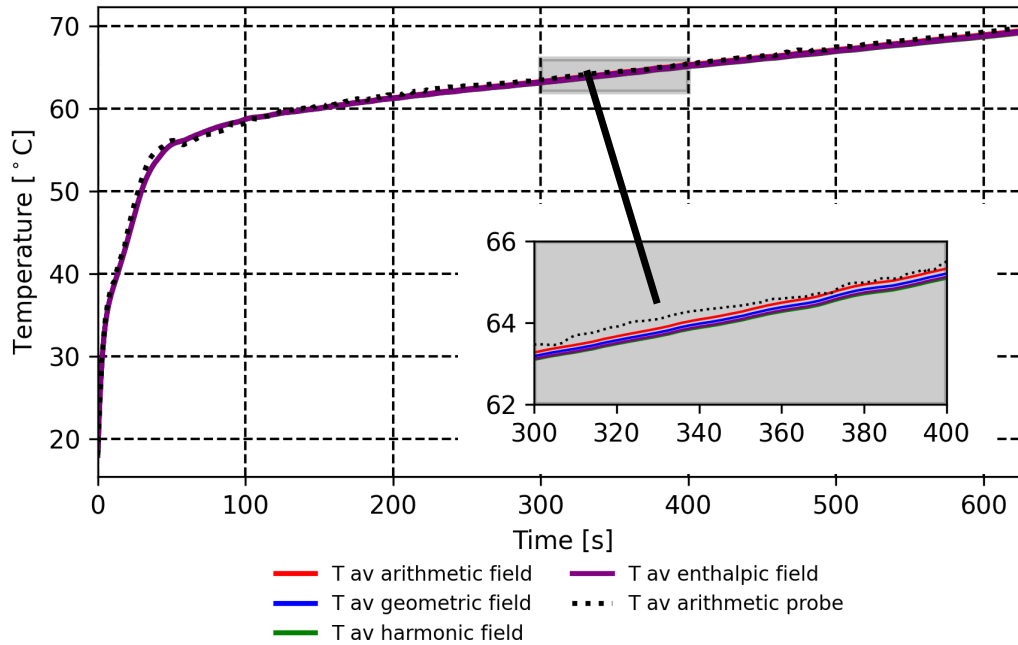


Figure 3.1 – For scenario D10Q2. Comparison of different averaging methods: (i) arithmetic average over the thermal field (red line), (ii) geometric average over the thermal field (blue line), (iii) harmonic average over the thermal field (green line), (iv) enthalpic average over the thermal field (purple line) and (v) arithmetic average over the 10 probes (dashed black line).

	T_{min} [°C]	T_{av} [°C]	T_{max} [°C]	$T_{max} - T_{av}$ [°C]
Experiment [41]	47.9	69.2	98.9	29.7
This study (OpenFOAM)	56.5	71.47	87.4	15.9
ALAT (Fluent)	55.4	67.7	84.0	14.3

Table 3.1 – The maximum, averaged and minimum temperatures from OpenFOAM and ALAT compared with the experimental results [41].

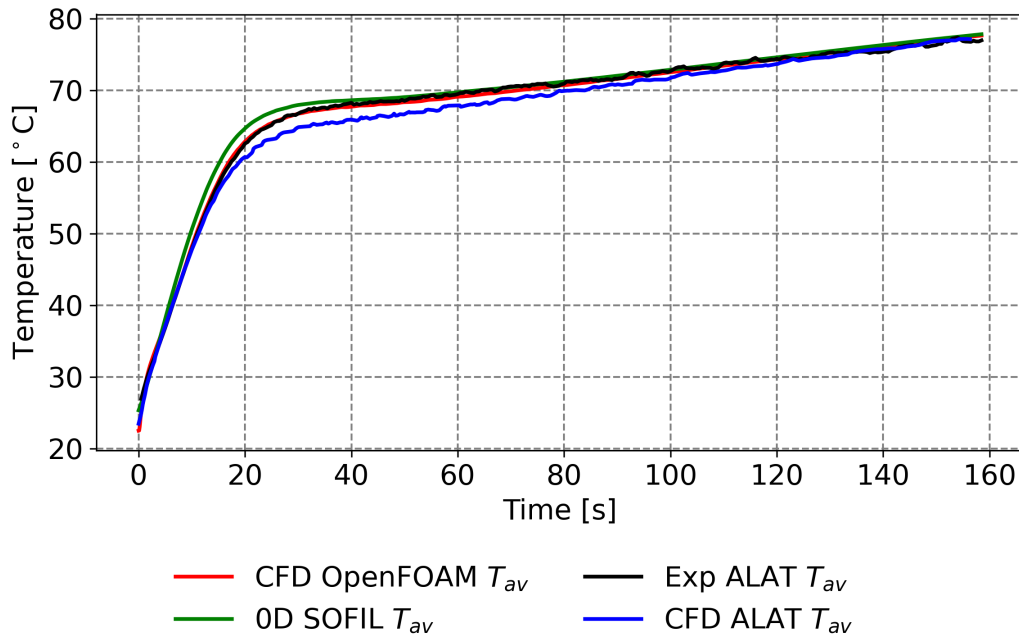


Figure 3.2 – For scenario D3Q8, i.e. the homogeneous case: the averaged temperature is reported as a function of time; results from OpenFOAM (CFD), ALAT (CFD) and SOFIL (0D model) and compared with the experimental measurements [41].

3.2.2 Heat exchanged between the gas and the walls

The heat transfer between the gas and the walls is an element modeled in 0D models using a heat transfer coefficient. The CFD does not require modeling of heat transfer. The results from CFD can be compared with the results from a 0D model to estimate the heat transfer modeling validity. Figure 3.6 displays a comparison between the results from OpenFOAM (2D-axisymmetric and 3D) and the results from SOFIL (0D) for scenario D3Q8 (panels A, B, C) and scenario D10Q2 (panels E, F, G). It can be seen that SOFIL is overestimating the temperature on the liner wall for both scenarios by approximately 5 °C. However, for scenario D10Q2, the heat transfer modeled by SOFIL is closer to that predicted by 3D CFD than that predicted by 2D-axisymmetric CFD. It can be seen that for both scenarios, the main heat exchanged between the gas and the walls is through the liner ($\approx 75\%$ of the total heat exchanged) followed by the heat exchanged through the bosses ($\approx 25\%$ of the total heat exchanged). The remaining heat exchanged is negligible.

The heat power for the 2D-axisymmetric CFD results and 3D CFD results can be detailed by presenting the heat power through (i) the left and right bosses and plugs, (ii) the upper part and the lower part for the liner and (iii) the inner part and outer part for the pipe. Figure 3.7 displays this comparison for scenario D3Q8 (panels A, C, E, G, I) and scenario D10Q2 (panels B, D, F, H). The difference of total heat power reported between the 2D-axisymmetric CFD results and the 3D CFD results for scenario D10Q2 (panel B) appears to be due to a smaller heat power at boss walls for the 2D-axisymmetric CFD (panel F). For 2D-axisymmetric CFD, the gravity is not taken into account so natural convection cannot occur. In areas close to the pipe, the plugs and the bosses, where few forced convection occurs, the absence of natural convection reduces drastically the heat exchanged. For scenario D10Q2, where velocities in the gas are smaller, this trend is enhanced. For the liner, the forced convection is dominant and the absence of natural convection does not affect substantially the heat exchanged. Therefore the heat power at liner wall is well estimated by 2D-axisymmetric

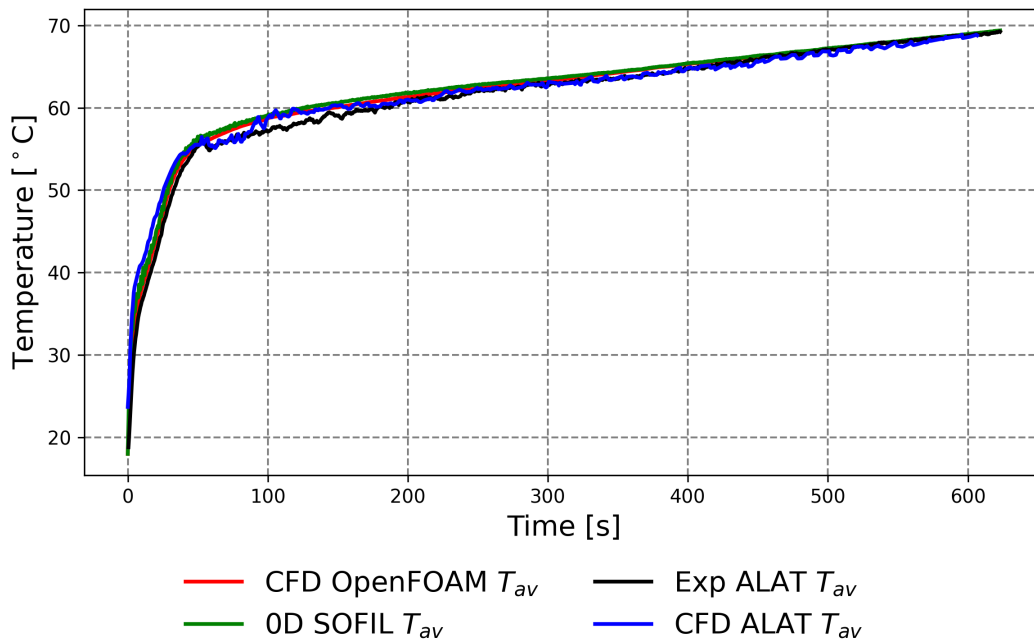


Figure 3.3 – For scenario D10Q2, i.e. the heterogeneous case: the averaged temperature is reported as a function of time; results from OpenFOAM (CFD), ALAT (CFD) and SOFIL (0D model) and compared with the experimental measurements [41].

CFD (panels G, H).

The 3D CFD results show that a thermal stratification occurs for scenario D10Q2 (panel H). The upper part of the liner exchanges more heat with the gas than the lower part of the liner. This cannot be predicted by 2D-axisymmetric CFD. It is interesting to see that the heat powers through plugs and bosses are largely different on the right part and left part of the tank. By noticing that, a different 0D model approach could be considered where the different regions of the tank would be modeled as nodes. Using an electrical analogy, the nodes would be linked with thermal resistance and capacity extracted from 3D CFD results. The upper and lower parts of a same solid region could be modeled as different nodes. Each node would have its own averaged temperature. This would give more possibility of temperature disparity in the tank for a 0D model than by using 1D wall modeling. An initial vertical thermal gradient in the tank, due to sun exposure for example, could be taken into account.

3.2.3 Comparison between OpenFOAM results and experimental measurements for the temperatures located between the liner and the composite

During the experiments, for the type IV 37 L tank, 30 temperature probes (TC1 to TC30) were placed between the liner and the composite wrap. Among those probes, two were defective, the probes TC23 and TC25. They are removed from the study. Figures 3.8 and 3.9 display a comparison of the temperatures between the probes issued from the experiment and the 3D CFD OpenFOAM study for scenarios D3Q8 and D10Q2 respectively. For the CFD, there is no gap between the liner and the composite so, when a virtual probe is placed at the location given in the experimental report, it can be located in the liner, in the composite or in the bosses. A virtual probe gives a temperature interpolated from neighbour

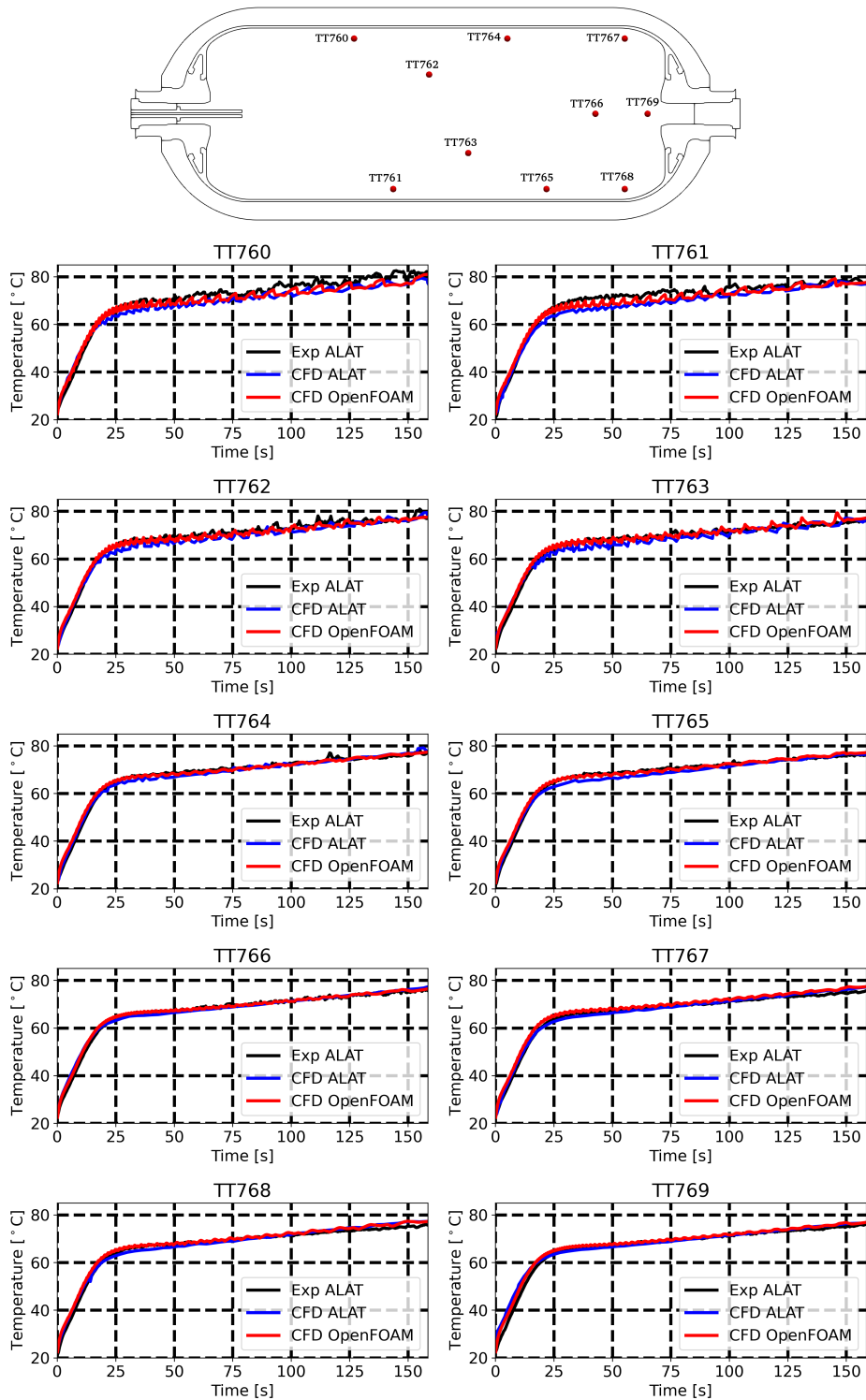


Figure 3.4 – For scenario D3Q8, i.e. the homogeneous case: comparison between the local temperature values issued from the OpenFOAM CFD results, ALAT CFD results and the experimental measurements. Probe locations are indicated in the upper panel.

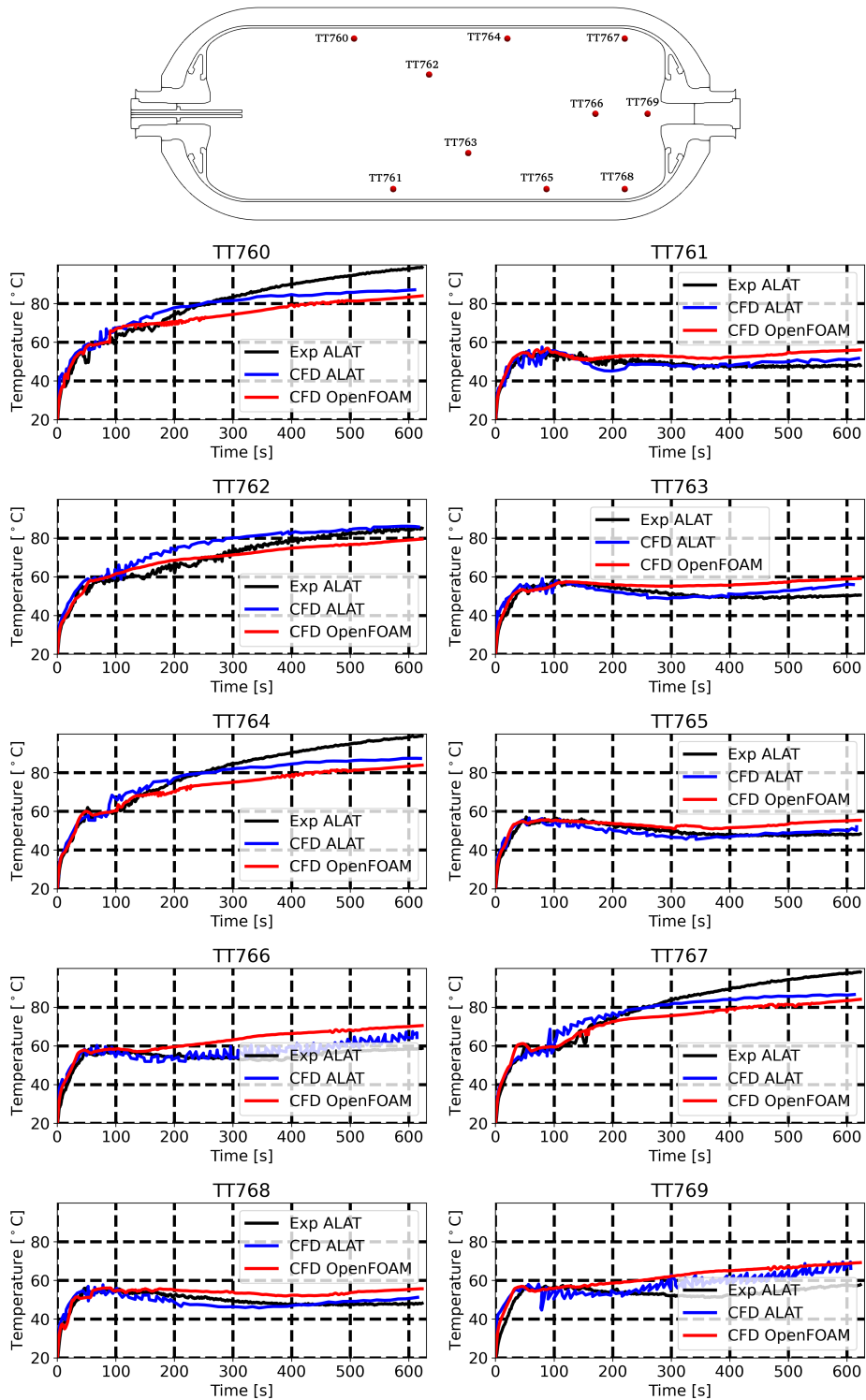


Figure 3.5 – For scenario D10Q2, i.e. the heterogeneous case: comparison between the local temperature values issued from the OpenFOAM CFD results, ALAT CFD results and the experimental measurements. Probe locations are indicated in the upper panel.

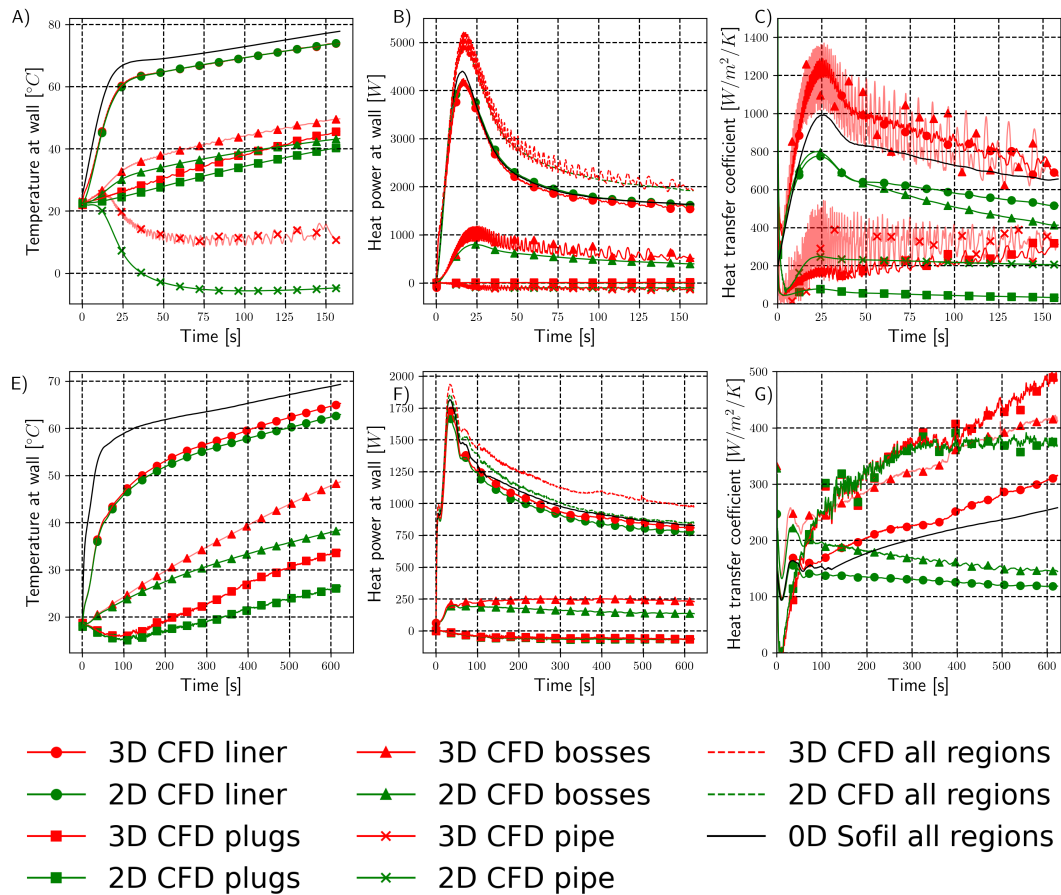


Figure 3.6 – Temperature at wall, heat power at wall, heat transfer coefficient (absolute value) for the 2D-axisymmetric CFD results (in green), the 3D CFD results (in red) and 0D SOFIL results (in black). The panels (A, B, C) concern scenario D3Q8 and the panels (D, E, F) concern scenario D10Q2.

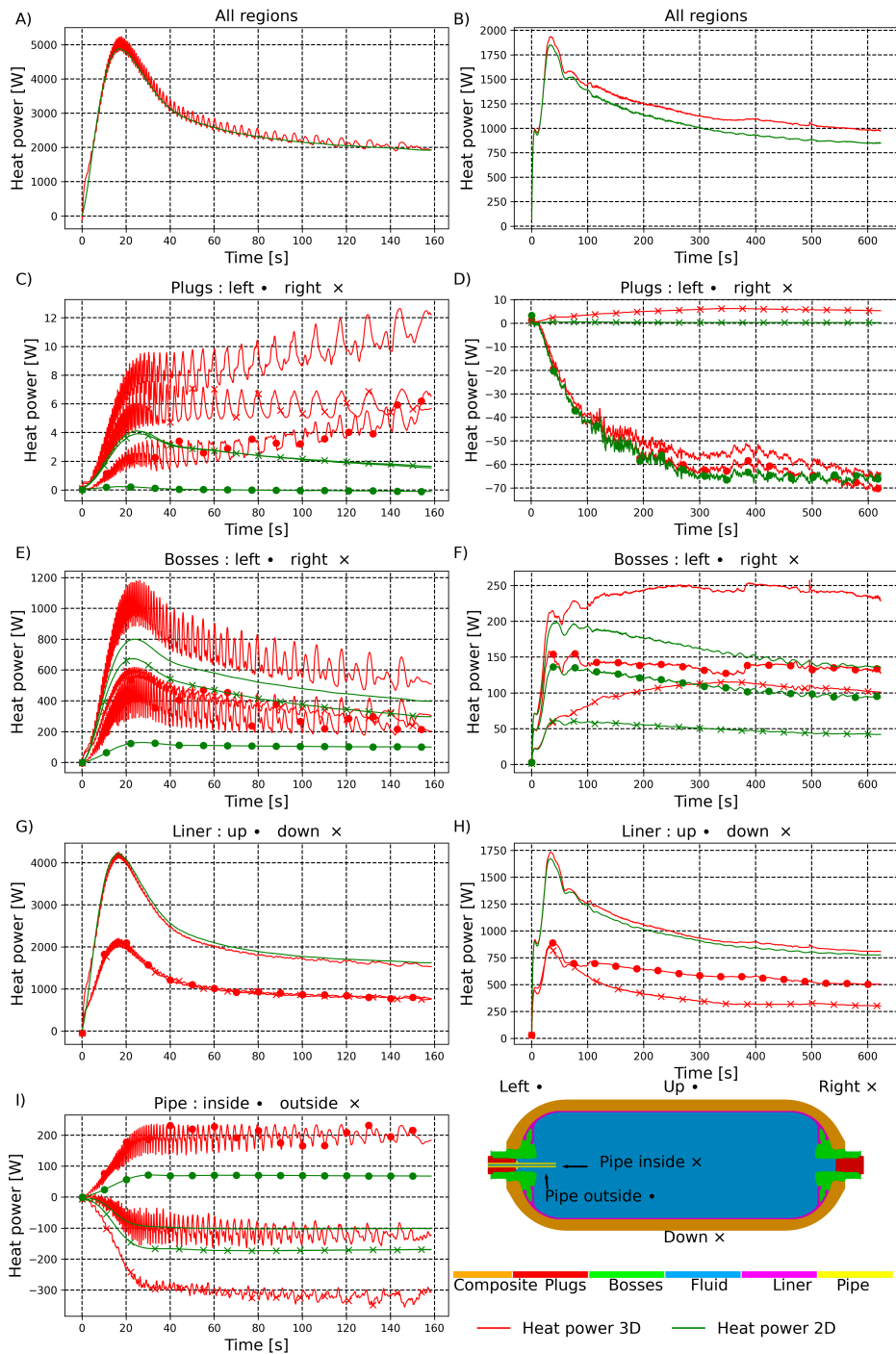


Figure 3.7 – Heat power for the 2D-axisymmetric results (in green) and the 3D results (in red). Panels (A, C, E, G, I) concern scenario D3Q8 and panels (B, D, F, H) concern scenario D10Q2. The heat power for a region is reported separately for (i) the left and right for the bosses and plugs, (ii) the upper part and lower part for the liner and (iii) the inner part and outer part for the pipe.

cell temperatures. Consequently, if the tank geometry modeled by CAD slightly differs from the real tank geometry, important temperature differences can be found. Hence, for the CFD results of the D3Q8 scenario, figure 3.8 shows that the temperatures from probes located where the liner is flat and with a constant thickness (TC5, TC6, TC7, TC8, TC9, TC10, TC24, TC22, TC21, TC20) are better predicted than the other located where the liner is curving. Figure 3.9 shows the remark is also valid for the CFD results of scenario D10Q2. However, figure 3.9 also shows an underestimation of the maximal temperature in the liner (see TC5, TC6, TC7, TC8, TC9, TC10) in accordance with underestimation of the maximum temperature in the gas.

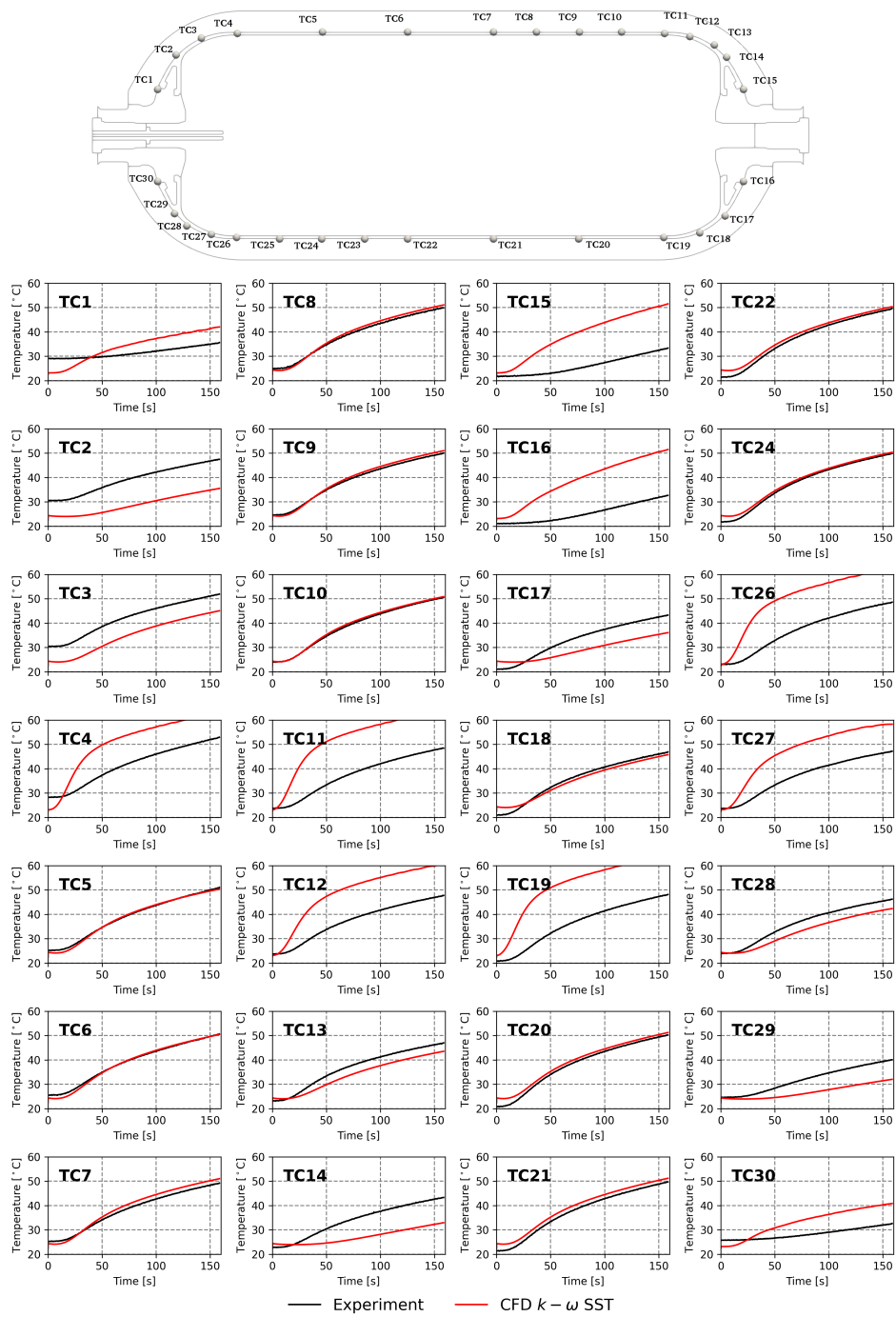


Figure 3.8 – For scenario D3Q8, i.e. the homogeneous case: comparison of the temperatures located between the liner and the composite for the results issued from the 3D OpenFOAM CFD and the experimental measurements.

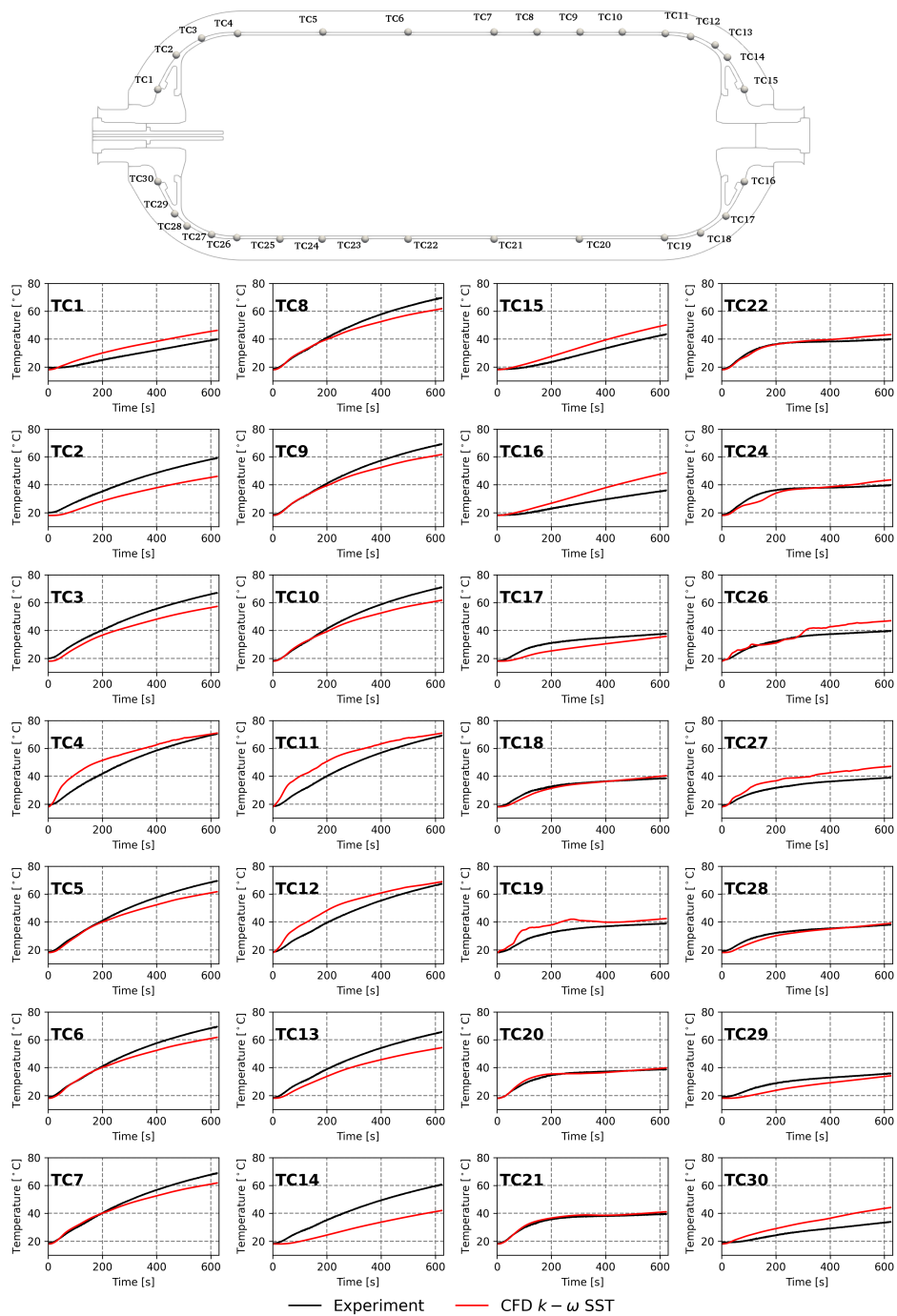


Figure 3.9 – For scenario D10Q2, i.e. the homogeneous case: comparison of the temperatures located between the liner and the composite for the results issued from the 3D OpenFOAM CFD and the experimental measurements.

Chapter 4

Improvement of CFD approach

Introduction

The CFD results obtained for the two contrasted scenarios 3.1 correctly predict the thermal state for the homogeneous case, i.e scenario D3Q8. For the heterogeneous case, i.e. scenario D10Q2, the averaged temperature is well predicted. The onset of thermal stratification, detected at 180 s from experimental measurements, is predicted with CFD at a similar time but the amplitude of the thermal gradient is underestimated (see figure 4.1). An identical conclusion can be formulated after analyzing the CFD results from ALAT reported in an unpublished document. The CFD software Fluent 16 was employed and the mesh was different from that used for the present CFD study with OpenFOAM. The $k - \omega$ SST turbulence model was used for both CFD studies.

The $k - \omega$ SST turbulence model over-predicts the turbulence viscosity in stagnation areas where the flow should be laminar. Advanced turbulence models which capture the transition between the turbulent state and the laminar state appear as good candidates to improve CFD prediction. The $k - \omega$ SST $\gamma - Re_\theta$ turbulence model [57, 58] was used in studies from the JRC [54, 55] but led to an underestimation of the thermal gradient amplitude. No comparisons with previous turbulence models were carried out, such as comparison with the $k - \omega$ SST or $k - \epsilon$ Realizable turbulence model. The potential of improvement associated with the $k - \omega$ SST $\gamma - Re_\theta$ turbulence model was not evaluated. The $k - \omega$ SST SAS turbulence model was mentioned in [31] to improve the thermal gradient capture.

As the $k - \omega$ SST $\gamma - Re_\theta$ and the $k - \omega$ SST SAS turbulence model are available in OpenFOAM, a study has been carried out with these two turbulence models. The simulations start at 180 s with the results issued from $k - \omega$ SST turbulence model. This corresponds to the onset of thermal stratification. The $k - \omega$ SST $\gamma - Re_\theta$ turbulence model did not give satisfying results: the results have been very similar to the results from the $k - \omega$ SST turbulence model. The CFD simulation performed with this model has been stopped after 20 s. The results issued from $k - \omega$ SST SAS turbulence model are presented in the following.

A numerical experiment where the turbulence is not modeled has also been carried out. As the mesh is not fine enough to consider the simulation as a DNS, it has been named cDNS for coarse DNS. The purpose of the cDNS is to under-estimate turbulence diffusion and to investigate the impact on thermal gradient amplitude.

The study aims to be submitted in the IJHE. Entitled *Advanced turbulence modeling improves thermal gradient prediction during compressed hydrogen tank filling*, the study is the object of section 4.1.

4.1 Advanced turbulence modeling improves thermal gradient prediction during compressed hydrogen tank filling

Advanced turbulence modeling improves thermal gradient prediction during compressed hydrogen tank filling

Rémi GONIN^{a,b,*}, Pierre HORGUE^a, Romain GUIBERT^a, David FABRE^a,
Rémi BOURGUET^a, Fouad AMMOURI^b, Elena VYAZMINA^b

^a*Institut de mécanique des fluides de Toulouse (IMFT), Université de Toulouse, CNRS, 2 allée Camille Soula, Toulouse, France*

^b*Air Liquide Innovation Campus Paris, 1 Chemin de la Porte des Loges, Les Loges-en-Josas, France*

Abstract

In order to use gaseous hydrogen for mobility of light and heavy duty vehicles, the temperature in the tank must not exceed 85 °C for safety reasons. Prior experiments reported that a vertical thermal stratification can occur during the filling of horizontal tanks under specific conditions. Thermodynamic modeling of hydrogen tank filling can predict the average gas temperature but not the onset of stratification. In previous studies, computational fluid dynamics (CFD) simulations were able to predict the onset of stratification with however an underestimation of thermal gradient magnitudes. In this work, the $k - \omega$ SST turbulence model, which predicts high levels of eddy-viscosity in stagnation areas and over-diffuses the temperature, is replaced by the $k - \omega$ SST SAS turbulence model, which is found to be more appropriate for CFD simulation of tank filling.

Keywords: compressed hydrogen, tank filling, thermal gradient, CFD, turbulence modeling

Highlights

- The effect of turbulence modeling on thermal gradient prediction is clarified.
- The $k - \omega$ SST turbulence model underestimates the thermal gradients.
- The $k - \omega$ SST SAS turbulence model improves thermal gradient prediction.

*Corresponding author

Email address: remi.gonin@airliquide.com (Rémi GONIN)

- The $k - \omega$ SST SAS turbulence model is applied to different filling scenarios.

10 1. Introduction

The use of hydrogen as an energy carrier is motivated by its ability to produce an electrical power without rejecting CO_2 to the atmosphere. The COP 26 summit urges on a net-zero target of greenhouse gas emissions for mid-century [1]. Hydrogen can replace fossil-fuel to match this requirement [2].

15 In this perspective, the automobile industry develops high pressure storage of hydrogen for light and heavy duty [3] fuel-cell vehicles. During the filling of gaseous tanks, the gas pressure is increasing and induces an elevation of the gas temperature. The J2601 standard of the Society of Automobile Engineers (SAE) organism [4] requires the maximal temperature inside the tank to not exceed
 20 $85\text{ }^\circ C$. Type IV tanks use plastic as liner and a composite material wrap around to limit tank weight and endure the pressure force of the 700 bar compressed hydrogen. These materials are thermal insulators, which limits heat exchanges between the compressed gas in the tank and the exterior environment. Type IV tanks are likely to exceed $85\text{ }^\circ C$ during filling.

25 The final averaged gas temperature in the tank depends on the temperature of the injected hydrogen [5, 6]. A cooling process is applied to the injected hydrogen to maintain the final averaged temperature below $85\text{ }^\circ C$. The final averaged gas temperature also depends on the filling time. A shorter filling time, which requires a higher mass flowrate, limits heat exchanges between the
 30 inner gas and the walls of the tank [7, 8]. However, for longer filling time, i.e. smaller mass flowrate, the injected gas has a lower velocity, limiting the mixing process inside fluid bulk. A criterion of 5 m/s for the velocity of gas at the injection was suggested in [9] to maintain the mixing. This criterion was confirmed in subsequent studies [10, 11]. A limited mass flowrate may lead
 35 to thermal heterogeneities inside the tank: despite the fact that the averaged temperature is within the thermal recommendation, local hot spots exceeding the thermal recommendation can occur.

The HyTransfer project [12] investigated the filling of hydrogen tanks laid horizontally for different tank geometries and different filling scenarios. During
 40 the experiments, a type IV 37 L tank provided by $\text{\textcircled{R}}$ Hexagon (with a length to diameter aspect ratio of 2.4) showed contrasted thermal behaviors, depending on the injection diameter and mass flowrate. Figure 1 shows a schematic of the tank and presents the fluid region and the different solid regions. The experimental measurements from Air Liquide Advanced Technology (ALAT) used 10 probes
 45 of temperature in the fluid region. Their locations are represented in figure 1.

These experimental measurements were performed for 3 injector diameters (3 mm , 6 mm and 10 mm) and 2 mass flowrates (2 g/s and 8 g/s). The 10 mm diameter is obtained by injecting directly through the plug aperture, without injection pipe. The above mentioned mass flowrate values are averaged
 50 over the filling time. To designate them, the injection diameter D and the mass flowrate Q followed by the corresponding values are used. For example, the case

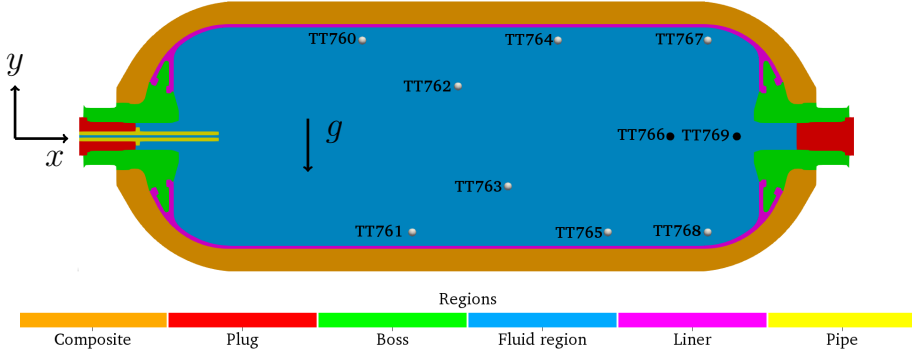


Figure 1: Type IV 37 L tank provided by $\text{\textcircled{R}}$ Hexagon with a 3 mm axial injector. View through the (x,y) plane. Probe locations are indicated by circles: probes located in the (x,y) plane in white and probes located outside the (x,y) plane in black.

	Type IV 37 L tank					
Scenario name	D3Q2	D3Q8	D6Q2	D6Q8	D10Q2	D10Q8
Injection diameter [mm]	3	3	6	6	10	10
Averaged mass flowrate [g/s]	2	8	2	8	2	8
Injection velocity* [m/s]	[190;4.2]	[280;17]	[62;1.1]	[73;2.0]	[22;0.41]	[28;1.1]
$T_{max} - T_{av}$ [°C]	8.36	6.35	26.76	11.28	30.03	24.39

Table 1: Thermal gradients for the type IV 37 L tank from ALAT[13]. *Estimated assuming a uniform velocity profile in the pipe and using the density calculated via the measured inlet temperature and pressure in the tank, the measured mass flowrate and pipe cross section.

D10Q2 corresponds to the scenario with the injector diameter of 10 mm and the averaged mass flowrate of 2 g/s. Table 1 presents different filling scenarios with the thermal gradient occurring at the end of the filling and an estimate of the injection velocity. To complete table 1, figure 2 gives the temperatures measured during the experimental campaigns [13] for the above mentioned cases.

Panels (A) and (F) are the extreme scenarios in terms of thermal gradients: (A) is the most homogeneous case and (F) the most heterogeneous case. These two cases were studied previously [14] using three dimensional (3D) computational fluid dynamics (CFD) simulations performed with the software OpenFOAM[15]. The geometrical domain selected for the simulations was a half of the tank geometry, using a symmetry assumption about the (x,y) plane to save computational resources. The D3Q8 CFD results matched the experimental data regarding both the averaged temperature and the local probe temperatures in the fluid. The D10Q2 CFD results matched the experimental data regarding the averaged temperature of the fluid and detected the onset of stratification. However, the thermal stratification magnitude was underestimated. This is consistent with the results of ALAT [16] where the same turbulence model, the $k-\omega$ Shear Stress Transport (SST) model [17] was used, with a different CFD code and a different mesh.

Figure 3, issued from a previous study [14], summarizes the thermal behav-

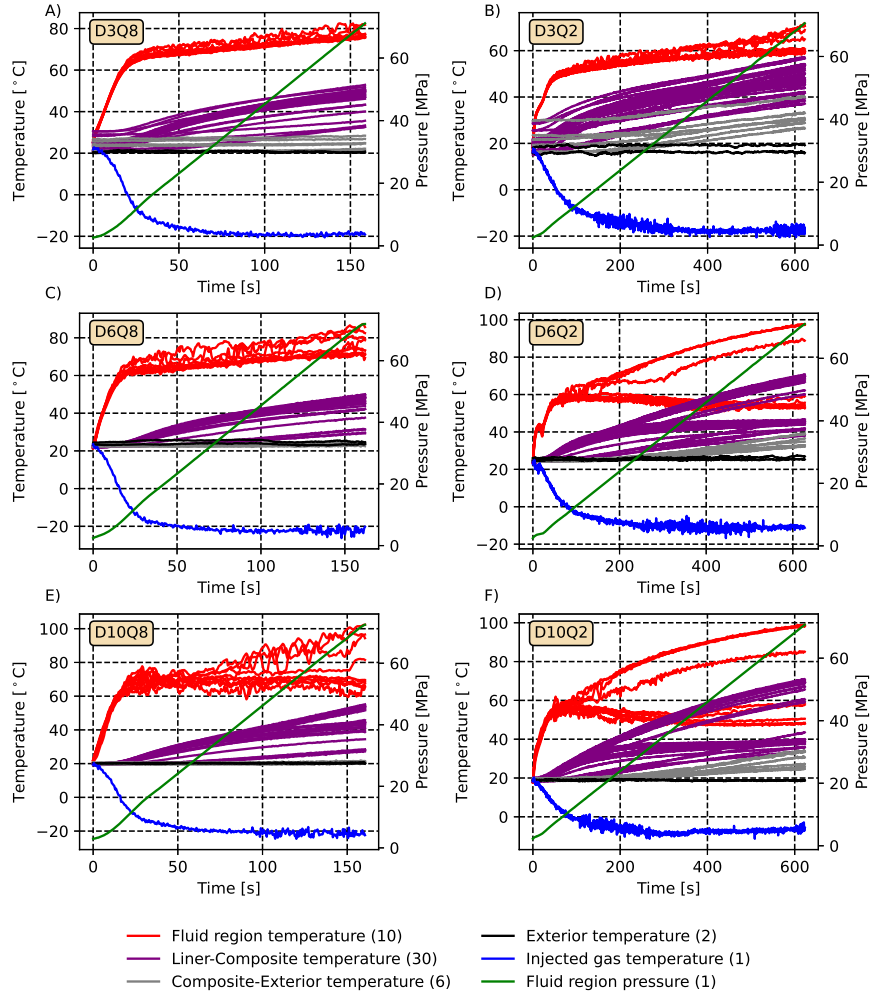


Figure 2: Experimental measurements from HyTransfer [13], for six cases: (A) D3Q8, (B) D3Q2, (C) D6Q8, (D) D6Q2, (E) D10Q8, (F) D10Q2. The number of temperature probes used in the different tank regions is added in brackets in the legend. The temperatures are indicated on the left axis and the pressure is indicated on the right axis

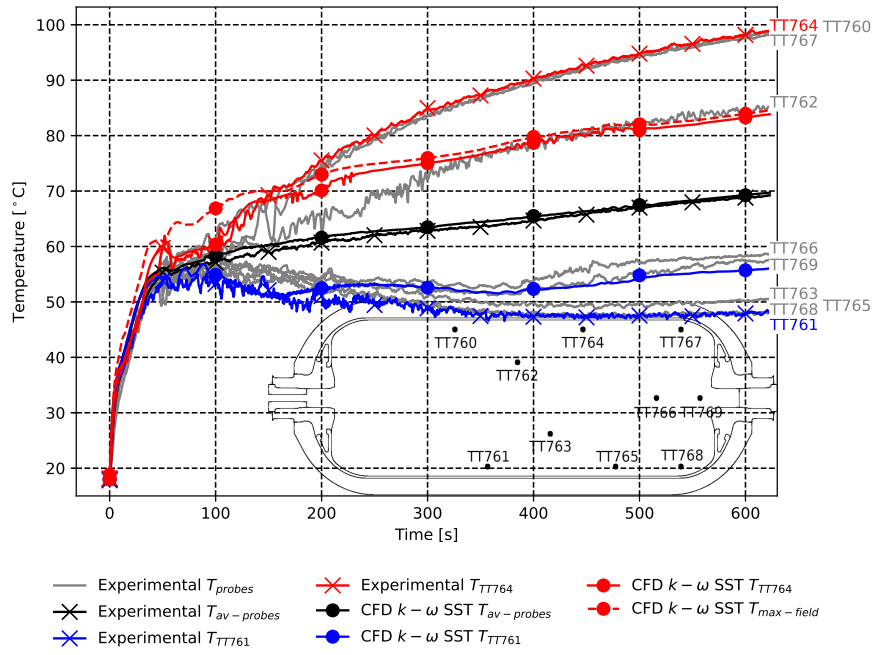


Figure 3: Scenario D10Q2. Comparison between the experimental measurements and CFD results using the $k - \omega$ SST model, concerning the averaged and local temperature values. The averaged temperature $T_{av-probes}$ is the arithmetic average of the 10 probe temperatures located in the fluid region. The maximum temperature value issued from the CFD thermal field is represented by a red dashed line.

ior in the tank, for the D10Q2 case, i.e. the most heterogeneous case. The averaged temperature in the tank (black) is plotted together with values from temperature probes (grey). The temperatures of the probes TT764 and TT761 exhibit the maximum and minimum values among probe data (red and blue respectively). The average CFD temperature matches well the experimental data ($T_{exp} - T_{CFD} = -0.12 \text{ }^\circ\text{C}$). At probe TT764, CFD temperature is lower than the experimental one ($T_{exp} - T_{CFD} = 15.05 \text{ }^\circ\text{C}$). At probe TT761, CFD temperature is higher than the experimental one ($T_{exp} - T_{CFD} = -8.01 \text{ }^\circ\text{C}$). The maximum temperature in the CFD thermal field (red dashed line) is close to the CFD value at probe TT764.

The turbulence modeling approach could explain the deviation from the experimental data. The $k - \omega$ SST turbulence model tends to over-predict turbulent kinetic energy, leading to high values of the turbulent viscosity [18]. As the viscosity plays an important role in the thermal diffusion process, the $k - \omega$ SST turbulence model is suspected to over-predict thermal diffusion and thus to underestimate the thermal gradient magnitude.

The objective of this paper is to clarify the role of turbulence modeling in the thermal stratification process and to suggest a more accurate turbulence model for tank filling simulations.

Models based on Unsteady Reynolds-Averaged Navier–Stokes (URANS) approach are considered due to their reduced computational costs. To limit the turbulence level in areas where the flow may still be laminar, advanced turbulence models are considered.

A CFD case with no turbulence model is considered with the same mesh as in the previous D10Q2 simulation [14]. This case would work as a Direct Numerical Simulation (DNS) if the mesh and time step were fine enough. That is why this numerical experiment is called the coarse-DNS (cDNS) case. It aims at investigating the effect of turbulence modeling in the URANS equations, on the thermal field.

2. Physical system and modeling approach

2.1. Physical system

During gas injection in a closed volume, the pressure and temperature gradually rise. Figure 1 represents the geometrical configuration. The tank is laying in horizontal position along the x-axis, such as the gas injection. The gravity (\mathbf{g}) is acting vertically along the y-axis. The tank is axisymmetric about the x-axis. It is composed of 4 or 5 solid regions, depending on the presence of an injection pipe: (i) a composite wrap which undergoes the mechanical constraint due to gas pressure, (ii) a plastic liner which limits the molecular diffusion of hydrogen through the wall, (iii) metallic bosses, (iv) plugs at each tank extremities and (v) a metallic injection pipe. The fluid region is the volume enclosed by the solid regions. The tank is surrounded by air at atmospheric pressure and ambient temperature.

The simulations are initialized using the pressure and temperature values issued from the experiments [13]. The temperature data come from 10 probes

located in the fluid region as shown in figure 1. Probe locations are given in the HyTransfer project document [13]. The inlet temperature and tank pressure were also measured and reported in [13]. Figure 2, adapted from [13], shows plots of all probe measurements for the different filling scenarios examined with the type IV 37 L tank.

2.2. Modeling approach

The simulations are based on a coupled fluid dynamics and heat transfer model, called Conjugate Heat Transfer (CHT) method [19].

The energy balance equation is solved in solid regions to simulate the thermal diffusion across tank walls. The set-up is the same as in the previous study [14].

The governing equations in the fluid region are the Navier-Stokes equations, i.e. the mass, momentum and energy balance equations.

The Reynolds number based on plug aperture diameter (10 mm) evolves from 45 000 to 15 000 during the filling. For these Reynolds numbers, the flow is turbulent in the injection area [20]. The turbulence is modeled using the URANS approach with the Boussinesq eddy-viscosity assumption [21].

For the velocity, a no-slip condition is used on the walls while a uniform mass flowrate is imposed at the inlet. It is deduced from the experimental pressure input represented in figure 2 (green line). A continuity of temperature and heat flux is imposed between the different regions.

The ideal gas equation of state is not valid for hydrogen considering the present ranges of pressure and temperature [5]. Real gas data from the National Institute of Standards and Technology (NIST) [22] are used to determine the thermodynamics.

2.3. Turbulence modeling

In the URANS equation system [23], turbulence effects are taken into account via the Reynolds stress tensor τ_{ij} [$kg/m/s^2$], which contributes to the total viscosity tensor. Using the Boussinesq eddy-viscosity assumption

$$\tau_{ij} = 2\mu_t S_{ij} - \frac{2}{3}\rho k \delta_{ij} , \quad (1)$$

the Reynolds stress tensor is linked to the turbulent viscosity μ_t [$kg/m/s$], the turbulent kinetic energy k [m^2/s^2], the Kronecker delta δ_{ij} [1] and the density ρ [kg/m^3]. The mean rate of strain tensor S_{ij} [$1/s$] is

$$S_{ij} = \frac{1}{2} \left(\frac{\partial U_i}{\partial x_j} + \frac{\partial U_j}{\partial x_i} \right) , \quad (2)$$

where U [m/s] is the Reynolds-Averaged velocity field. Turbulence models are designed to model τ_{ij} via μ_t [$kg/m/s$]. However, μ_t [$kg/m/s$] also plays an important role in thermal diffusion. In the energy equation, the effective thermal conductivity λ_{eff} [$W/m/K$] is defined as

$$\lambda_{eff} = \lambda + \lambda_t , \quad (3)$$

where λ is the thermal conductivity and λ_t is the turbulent thermal conductivity,

$$\lambda_t = \frac{c_p \mu_t}{Pr_t}, \quad (4)$$

where $Pr_t = 0.85$ is the turbulent Prandtl number and c_p [$J/kg/K$] is the specific heat capacity. The effective thermal diffusivity is directly linked to the effective thermal conductivity:

$$\alpha_{eff} = \frac{\lambda_{eff}}{\rho c_p}. \quad (5)$$

The choice of the turbulence model is a key element for temperature prediction since it impacts the prediction of the turbulent viscosity and therefore the prediction of the effective thermal diffusivity.

A previous study [24] pointed out that the $k - \epsilon$ Realizable turbulence model is the most suitable for CFD simulation of hydrogen tank filling. The comparison test was performed for an axisymmetric case where gravity was not taken into account. The benchmark was based on the averaged temperature only. The influence of the different models on temperature distribution is unknown. This model was recently used to investigate the temperature distribution during the filling stage of a hydrogen tank [25, 26, 27]. The model captures correctly the round jet physics [28] which is an important part of the fluid dynamics in the tank. However, the thermal boundary layer at wall must be modeled by a wall function, which is problematic for precise heat transfer predictions [29].

Therefore, to avoid the use of wall functions and correctly capture the thermal layer, the $k - \omega$ SST model [17] was selected. In previous studies [14, 16], this turbulence model was able to capture the averaged value of the temperature and the onset of stratification while underestimating thermal gradient amplitudes. The model involves two equations to predict the eddy-viscosity: one is based on the conservation of the turbulent kinetic energy k [m^2/s^2] and the other one is based on the conservation of the specific rate of dissipation of the turbulent kinetic energy ω [$1/s$].

The idea behind the $k - \omega$ SST turbulence model is to merge two other two-equations eddy-viscosity models, the $k - \omega$ and $k - \epsilon$ models. An advantage of the $k - \omega$ model is to be applicable until the viscous layer. Its major downside is its sensitivity to the freestream condition [30], which can lead to less accurate predictions than the $k - \epsilon$ model. Therefore, the $k - \omega$ SST turbulence model is designed to switch between the $k - \omega$ model close to walls and the $k - \epsilon$ model in other regions. This model is intensively used in the industry [31].

A limitation of the $k - \omega$ SST model is the over-predicted turbulence kinetic energy in stagnation regions [18]. This becomes problematic when the cooled jet coming from the injected gas is deviated towards the lower part of the tank and the upper part of the tank becomes a stagnation area. Increasing the turbulent kinetic energy in this area would, from a thermal perspective, increase temperature diffusion and limit gradient amplitude, which is consistent with the observations reported in the previous study [14]. Therefore, advanced

turbulence models which limit the production of turbulent kinetic energy, and consequently turbulent viscosity, are expected to improve gradient prediction.

The $\gamma - Re_\theta$ model [32, 33] is a 4-equation model designed to capture the laminar-turbulent transition phenomenon. It is derived from the $k - \omega$ SST model and includes two additional equations for the intermittency γ and the momentum thickness Reynolds number Re_θ . It was used by the Joint Research Centre (JRC) of the European Commission [34, 35] to study the thermal distribution during hydrogen tank filling. It was able to detect the onset of stratification but underestimated the thermal amplitude, compared to the experimental measurements [34].

In a preliminary phase of the present study, several tests have been carried out using the $\gamma - Re_\theta$ model with OpenFOAM [36]. No substantial difference with the $k - \omega$ SST model has been noted and the investigation of the $\gamma - Re_\theta$ model was stopped.

The Scale Adaptive Simulation (SAS) concept was applied to the $k - \omega$ SST model [37] to avoid the over-prediction of eddy-viscosity. The SAS concept consists in comparing the turbulent length-scale L issued from the $k - \omega$ SST model to the von Kármán length scale $L_{\nu K}$, a three-dimensional generalization of the boundary layer thickness. Depending on the ratio $\frac{L}{L_{\nu K}}$, a source term Q_{SAS} is added in the balance equation of ω , correcting the production of ω , and therefore impacting the turbulent viscosity μ_t .

The model is available in OpenFOAM [38] and supplementary details can be found in [17, 37, 39]. The corrected value of turbulent viscosity μ_t in stagnation areas is expected to improve the prediction of temperature gradients.

In addition, to investigate the influence of the turbulent viscosity on the temperature field, a numerical experiment with no turbulence model is performed: the cDNS case. In this case, the flow is considered to be fully resolved, filtering the small scale structures of turbulence. This approach will therefore tends to minimize thermal diffusion and thus maximize temperature gradients. The equation system is the same as for the DNS studies, although the mesh is not fine enough to capture the smallest scale as theorized in the Kolmogorov theory [40]. For example, in the injection area, the smallest scale η [m], can be linked to the Reynolds number $Re = \frac{u_{inj} D}{\nu}$ by the relationship $\eta \sim D Re^{-3/4}$, with the injection velocity u_{inj} [m/s], the injection diameter D [m] and the kinematic viscosity ν [m^2/s]. For the D10Q2 case, $Re \approx 1.5 \cdot 10^4$ at minimum, consequently this scale is at maximum $\eta = 7.3 \cdot 10^{-6}$ m. The smallest cell size is $4.9 \cdot 10^{-5}$ m. The DNS simulation conditions are not satisfied but the simulation may still give insights into the impact of turbulence modeling.

To save computational resources, the different simulations have been initialized at 180 s based on the $k - \omega$ SST results; this corresponds to the beginning of thermal stratification.

3. Numerical Method

The OpenFOAM solver chtMultiRegionFoam [41] is used to perform the CHT simulation. In the fluid region, the solver uses the Pressure Implicit with

$T_{exp} - T_{CFD}$ [$^{\circ}C$]\CFD approaches	$k - \omega$ SST	$k - \omega$ SST SAS	cDNS
av(T) t_f [$^{\circ}C$]	-0.12	0.11	-0.73
TT764 t_f [$^{\circ}C$]	15.05	2.17	-4.82
TT761 t_f [$^{\circ}C$]	-8.01	-1.79	5.66

Table 2: Temperature deviations between the experimental data and CFD simulation results at the end of the filling, for each CFD approach.

Splitting of Operators (PISO) algorithm [42, 43]. A variable time step is used to maintain the Courant–Friedrichs–Lewy number (CFL) lower than 1 during the simulations.

A symmetry assumption is used to reduce CFD cost. Only half of the tank, cut through the (x,y) plane, is considered. The mesh is issued from the heterogeneous case described in the previous study [14]. It is composed of 651 482 cells in the fluid region and 449 126 cells in the solid regions. A $y^+ < 1$ numerical criterion on walls is maintained to avoid wall functions. Mesh validation results were reported in the previous study [14].

4. Results

4.1. Comparison of gradient prediction

Figure 4 shows a comparison of the CFD results with the experimental measurements. For the averaged gas temperature, all simulation approaches match the experimental data. Considering the maximum temperature, probe TT764, the $k - \omega$ SST case underestimates the temperature while the cDNS case overestimates the temperature. The $k - \omega$ SST SAS case results are in-between, in better agreement with the experimental data than the other CFD approaches, even though slightly lower.

On the TT761 probe, the $k - \omega$ SST model overestimates the temperature while the cDNS case underestimates the temperature. The $k - \omega$ SST SAS case is slightly higher than the experimental value.

The values of the averaged and probe temperature deviations ($T_{exp} - T_{CFD}$) at the final time (630 s) for the different CFD approaches are presented in table 2.

A detailed monitoring of each probe is presented in figure 5. It can be noted that the $k - \omega$ SST SAS case is closer to the experimental data on the higher and lower probes than on the central probes (TT762, TT766, TT769).

The $k - \omega$ SST SAS case shows better prediction of the thermal gradients (i.e. closer to the experimental data), than the $k - \omega$ SST and the cDNS cases.

4.2. Field comparison

Figure 6 presents, for scenario D10Q2 at three times (200 s, 400 s, 600 s), the temperature fields simulated by the $k - \omega$ SST (upper panel) and $k - \omega$ SST SAS (lower panel) turbulence models. Likewise, figure 7 depicts the effective

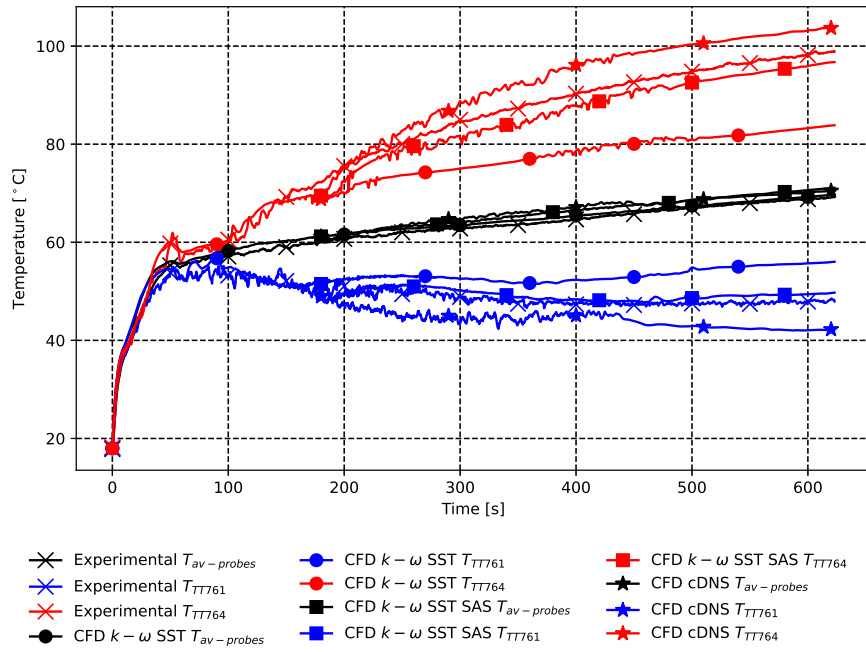


Figure 4: Scenario D10Q2. Comparison between the experimental measurements and CFD results concerning the averaged and local temperature values, for each CFD approach. The results of the $k-\omega$ SST model simulation are issued from [14].

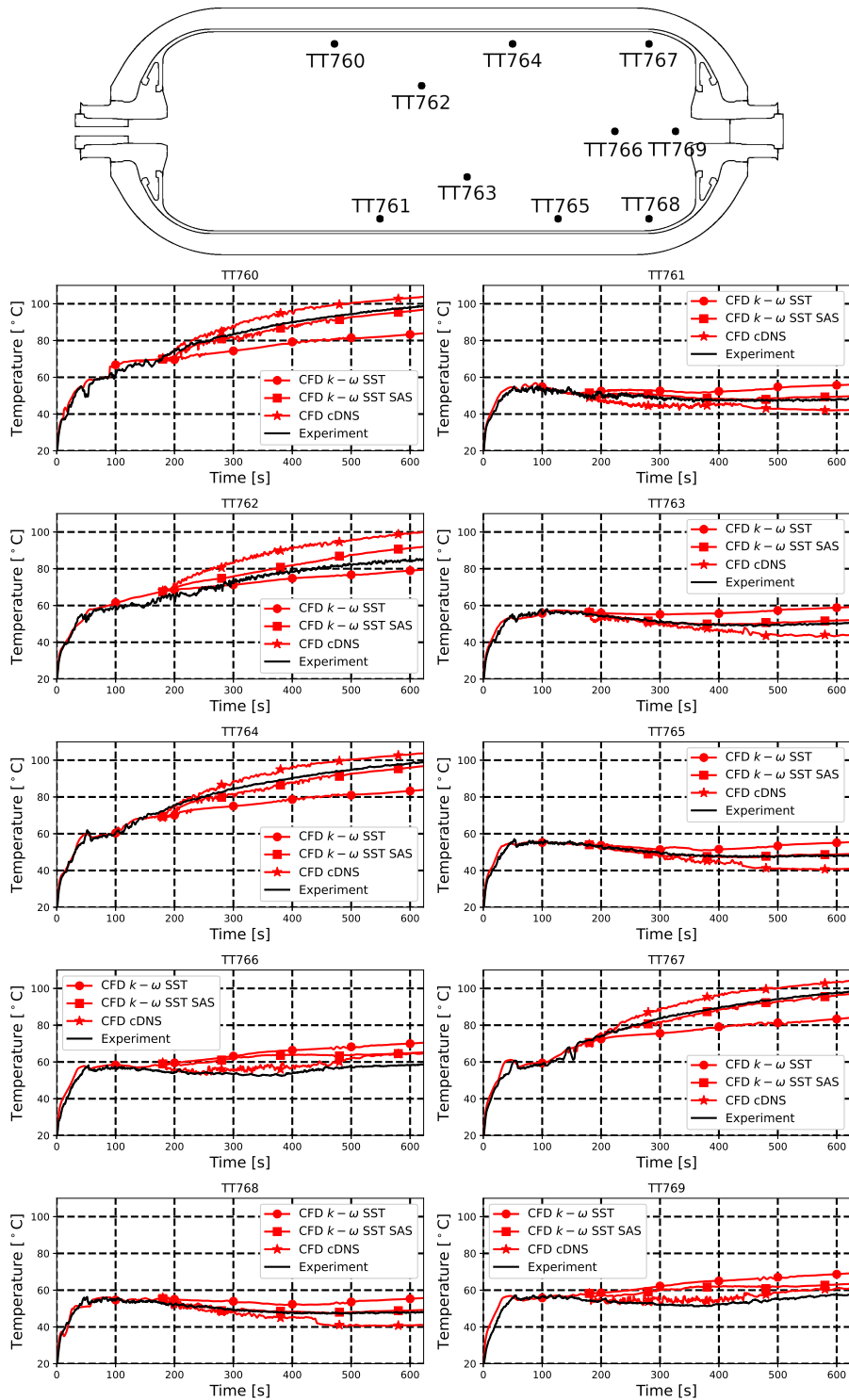


Figure 5: Scenario D10Q2. Comparison between the local temperatures issued from the simulations and the experiment. Probe locations are indicated at the top of the figure.

thermal diffusivity. In figures 6 and 7, the fields are located in the symmetry plane.

The source term Q_{SAS} , added to the ω balance equation in the $k-\omega$ SST SAS model, limits the level of turbulent viscosity. The effective thermal diffusivity behaves like the turbulent viscosity (expression (5)). Figure 7 shows that the level of effective thermal diffusivity is reduced when the $k-\omega$ SST SAS model is used. In the stagnation area where there is no mixing, the lower effective thermal diffusivity strongly influences the temperature field. Figure 6 shows that, for each time, the averaged temperature (given above the thermal field) is similar for the two turbulence models, while the maximum temperature (also reported above the thermal field) is significantly different. For example at 600 s, the difference of maximum temperature between the $k-\omega$ SST SAS and $k-\omega$ SST turbulence models reaches approximately 13 °C.

A complementary video of scenario D10Q2 using the $k-\omega$ SST SAS model is available in the **Supplemental Data**. It presents the thermal field at the upper panel and the velocity field at the lower panel.

5. Application to other filling scenarios

The comparison reported in section 4 shows that the $k-\omega$ SST SAS turbulence model substantially improves the thermal gradient prediction for scenario D10Q2. Two other filling scenarios are selected to confirm the accuracy of this approach, scenarios D6Q2 and D6Q8.

For both scenarios, a mesh composed of 704 209 cells in the fluid region is employed. The processing time depends on the solver algorithm and the inlet velocity. It has been found that the PISO solver is computationally more efficient for velocities below 10 – 20 m/s while the PIMPLE algorithm [44] is faster for higher velocities, using a $CFL > 1$. Consequently, a PIMPLE-PISO switch has been performed at 100 s for scenario D6Q2 and at 80 s for scenario D6Q8.

5.1. Scenario D6Q2

Like scenario D10Q2, scenario D6Q2 leads to a large difference between the averaged and maximum gas temperatures issued from the probes (figure 2,D), $T_{max} - T_{av} = 30.03$ °C and $T_{max} - T_{av} = 26.76$ °C, respectively. Unlike scenario D10Q2, scenario D6Q2 involves an injection pipe, which is usually present during tank filling in real conditions.

Figure 8 compares the average and local probe temperatures issued from the experimental measurements with the CFD results. For scenario D10Q2, measurements from the probes TT760, TT764 and TT767 tend to converge during the filling. The probe TT760 temperature rises at 90 s, then the probe TT764 temperature at 130 s and finally the probe TT767 temperature at 180 s. At the final time, the temperatures measured by probes TT760, TT764 and TT767 are very close. The CFD results predict a similar phenomenon, i.e. a local increase of temperature (a hot spot) occurs near the injection region where

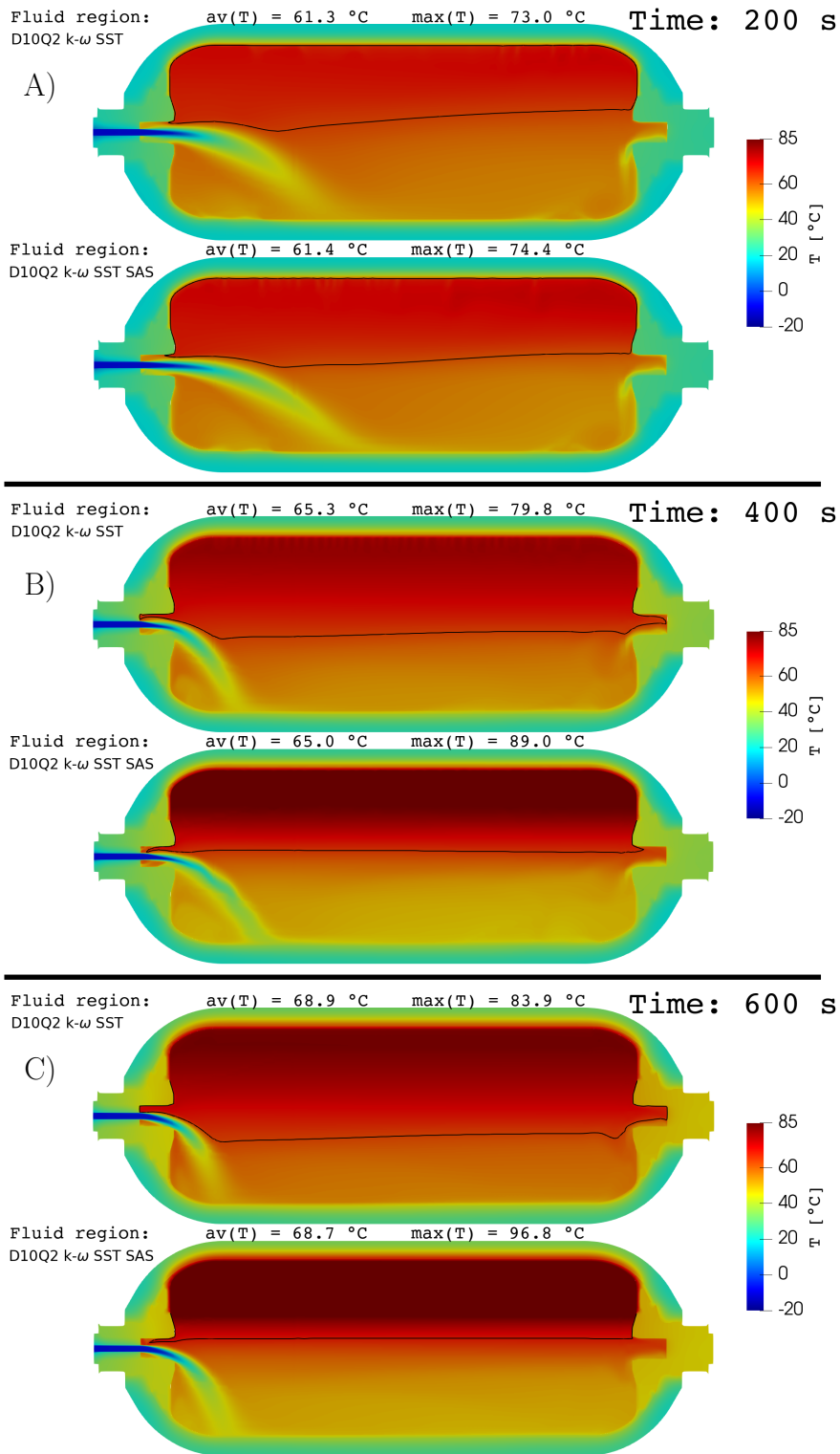
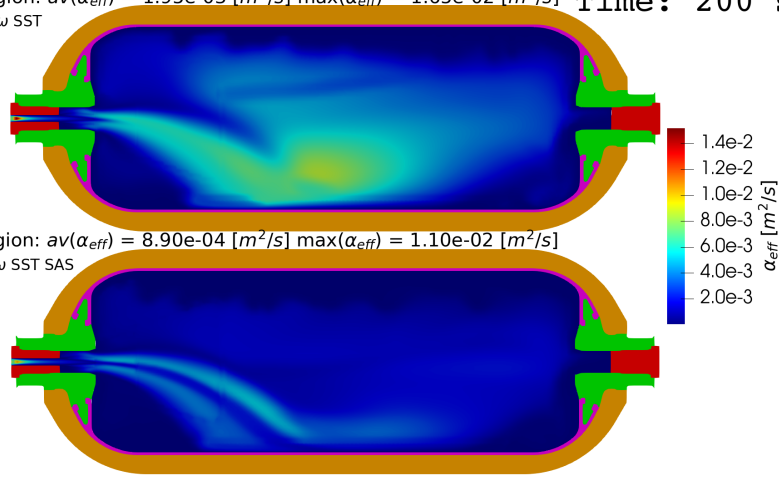


Figure 6: Scenario D10Q2. Comparison of the temperature fields predicted by the $k-\omega$ SST (upper panels) and $k-\omega$ SST SAS (lower panels) turbulence models, at time instant: (A) 200 s, (B) 400 s and (C) 600 s. The black line corresponds to the isline of averaged temperature.

Fluid region: $av(\alpha_{eff}) = 1.95e-03 [m^2/s]$ $max(\alpha_{eff}) = 1.65e-02 [m^2/s]$ **Time: 200 s**
D10Q2 k- ω SST

A)

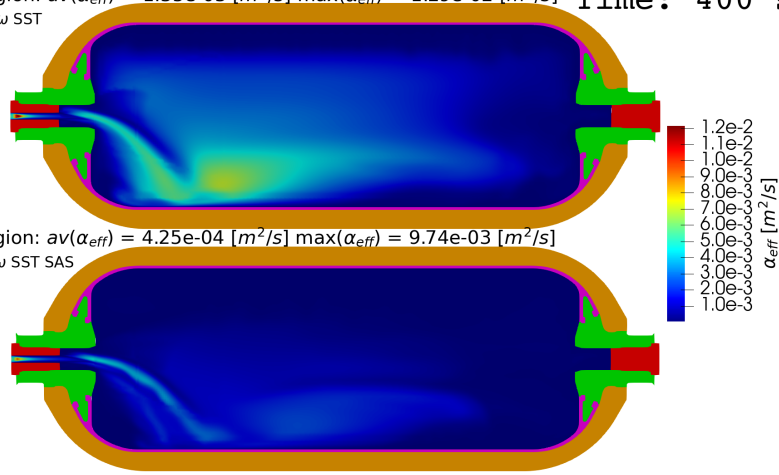


Fluid region: $av(\alpha_{eff}) = 8.90e-04 [m^2/s]$ $max(\alpha_{eff}) = 1.10e-02 [m^2/s]$
D10Q2 k- ω SST SAS



Fluid region: $av(\alpha_{eff}) = 1.35e-03 [m^2/s]$ $max(\alpha_{eff}) = 1.29e-02 [m^2/s]$ **Time: 400 s**
D10Q2 k- ω SST

B)

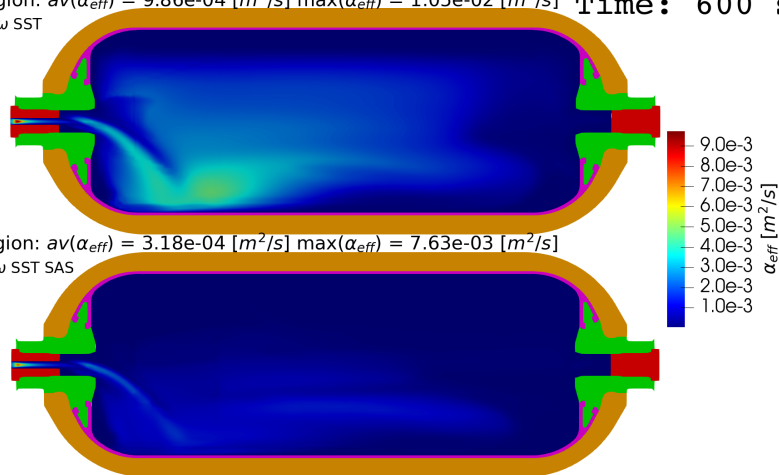


Fluid region: $av(\alpha_{eff}) = 4.25e-04 [m^2/s]$ $max(\alpha_{eff}) = 9.74e-03 [m^2/s]$
D10Q2 k- ω SST SAS



Fluid region: $av(\alpha_{eff}) = 9.86e-04 [m^2/s]$ $max(\alpha_{eff}) = 1.05e-02 [m^2/s]$ **Time: 600 s**
D10Q2 k- ω SST

C)



Fluid region: $av(\alpha_{eff}) = 3.18e-04 [m^2/s]$ $max(\alpha_{eff}) = 7.63e-03 [m^2/s]$
D10Q2 k- ω SST SAS



Figure 7: Scenario D10Q2. Comparison of the effective thermal diffusivity fields predicted by the $k - \omega$ SST (upper panels) and $k - \omega$ SST SAS (lower panels) turbulence models, at time instant: (A) 200 s, (B) 400 s and (C) 600 s.

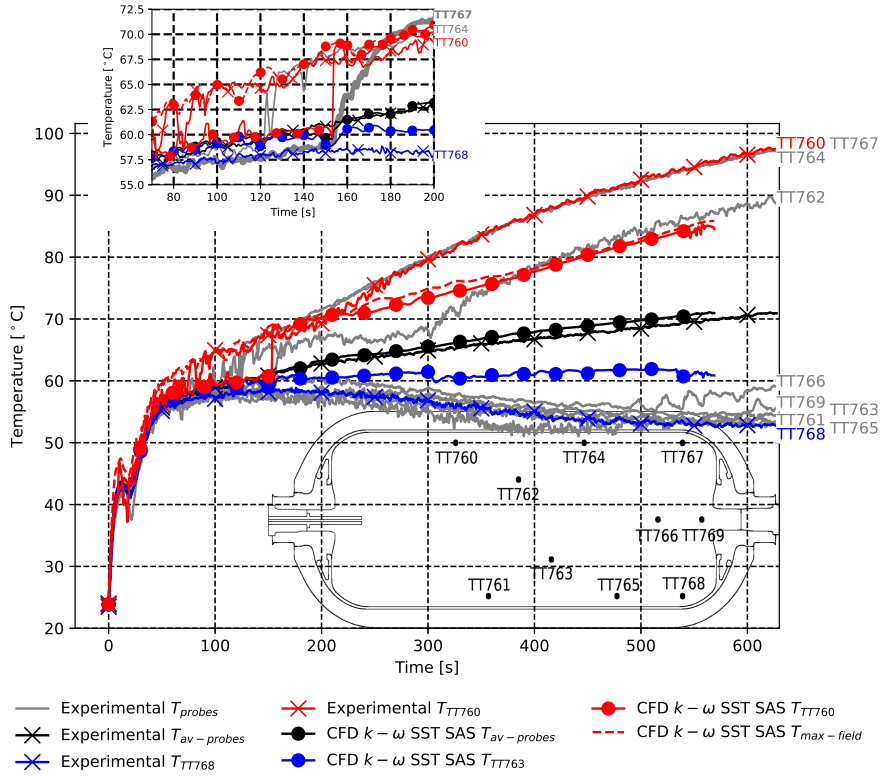
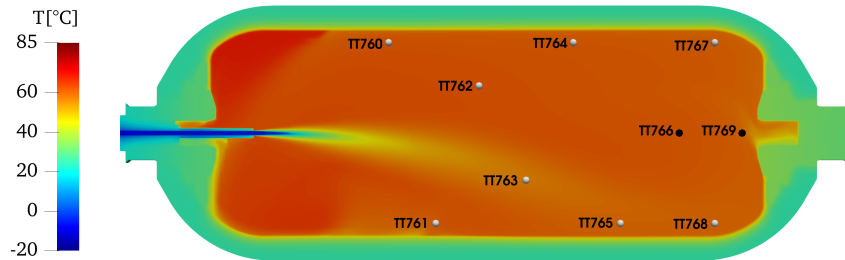


Figure 8: Scenario D6Q2. Comparison between the averaged and local temperature values issued from the experimental measurements and the CFD results using the $k - \omega$ SST SAS turbulence model. The maximum temperature value issued from the CFD thermal field is represented by a red dashed line. The upper panel is a zoomed view in the time interval [70 s 200 s], to see the delay of probe TT760 temperature between CFD and experimental results.

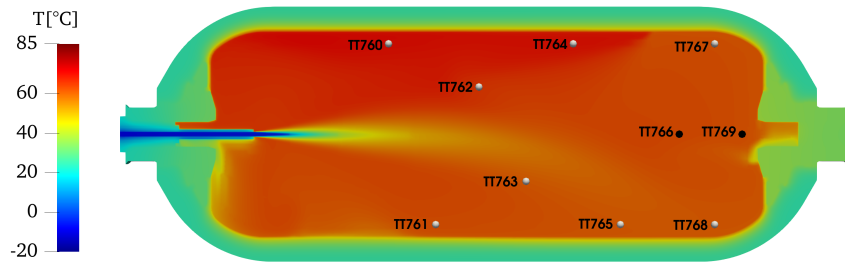
the gas is not cooled by the injected gas. Once the buoyancy forces dominate the jet momentum forces, the jet is deflected and the hot spot is convected along the upper part, crossing successively probes T760, TT764 and TT767. Figure 9 shows that the hot spot is close to the injector region at $t = 150$ s. At $t = 200$ s, the hot spot crossed probes TT760 and TT764 but not probe TT767. At $t = 450$ s, the hot spot has reached the rear region of the tank. The CFD predicts this phenomenon with a delay compared to the experimental measurements. In figure 8, the temperature raise for probe TT760 occurs at 150 s in the CFD results versus 90 s in the experiment.

After 150 s, the maximum gas temperature issued from CFD results (red dashed line) is similar to the temperature from probe TT760. This suggests that probe TT760 is correctly located to measure the maximum temperature in the tank at the end of the filling.

Time: 150 s



Time: 200 s



Time: 450 s

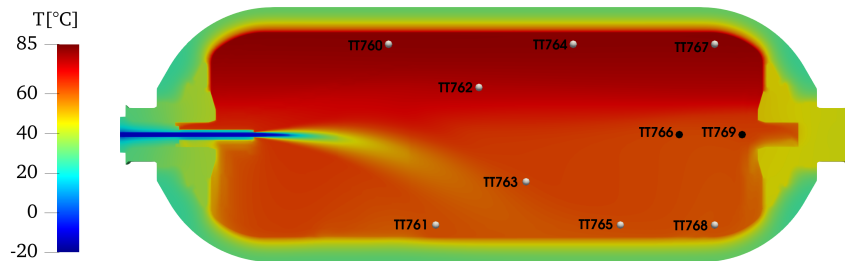


Figure 9: Scenario D6Q2: the temperature field in the (x,y) plane is reported at time $t = 150$ s, $t = 200$ s and $t = 450$ s. The convection of the hot spot is visible between $t = 150$ s and $t = 200$ s.

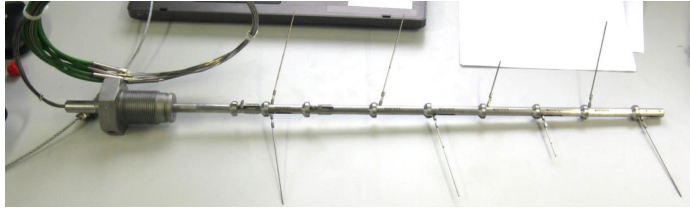


Figure 10: Thermocouple tree photograph reproduced from the report concerning the experimental tests of the HyTransfer project [13].

The CFD simulation predicts a lower vertical thermal gradient than that measured experimentally. At time $t = 568.9$ s, the difference of temperature for probe TT760 between the experimental measurements and the CFD results is $T_{exp} - T_{CFD} = 10.1$ °C. The difference for probe TT768 is $T_{exp} - T_{CFD} =$
 315 -8.02 °C.

The difference between the experimental measurements and the CFD results are larger than for the D10Q2 scenario. No results issued from the $k - \omega$ SST model are available and the impact of the SAS approach cannot be estimated for the D6Q2 scenario.

320 The discrepancies could be explained by the presence of the experimental measurement device in the gas region. A thermocouple tree (figure 10) has been inserted at the rear region of the tank. Considering the D6Q2 configuration, with an injection pipe, the injection outlet is closer to the thermocouple extremity. This results in a potential interaction between the jet and the measurement
 325 device, leading possibly to less thermal mixing and larger thermal gradients. Moreover, the jet is deflected earlier in the D10Q2 scenario. Figures 6 and 9 show that in this scenario, at $t = 200$ s, the jet is more deflected than in the D6Q2 scenario at $t = 450$ s, reducing the potential influence of the measurement device in the D10Q2 scenario. The influence of the experimental measurement
 330 device on the actual thermal field remains to be clarified.

5.2. Scenario D6Q8

Scenario D6Q8 leads to a limited gradient, with a maximum of 11.28 °C between the averaged and maximum gas temperatures issued from the probes (figure 2,C)). It represents an interesting case to test the $k - \omega$ SST SAS turbulence model in a scenario involving an important thermal mixing by the inner
 335 jet.

Figure 11 compares the average and local probe temperatures issued from the experimental measurements and the CFD simulation. The minimum temperature is not observed at the lowest probes (TT761,TT765,TT768), but at
 340 the TT763 probe. This can be explained as follows: due to the gravity, the cold jet is deflected and hits the TT763 probe, which is closer to the injector outlet than the TT765 probe. The averaged and local temperatures predicted by the CFD simulation are close to the experimental measurements.

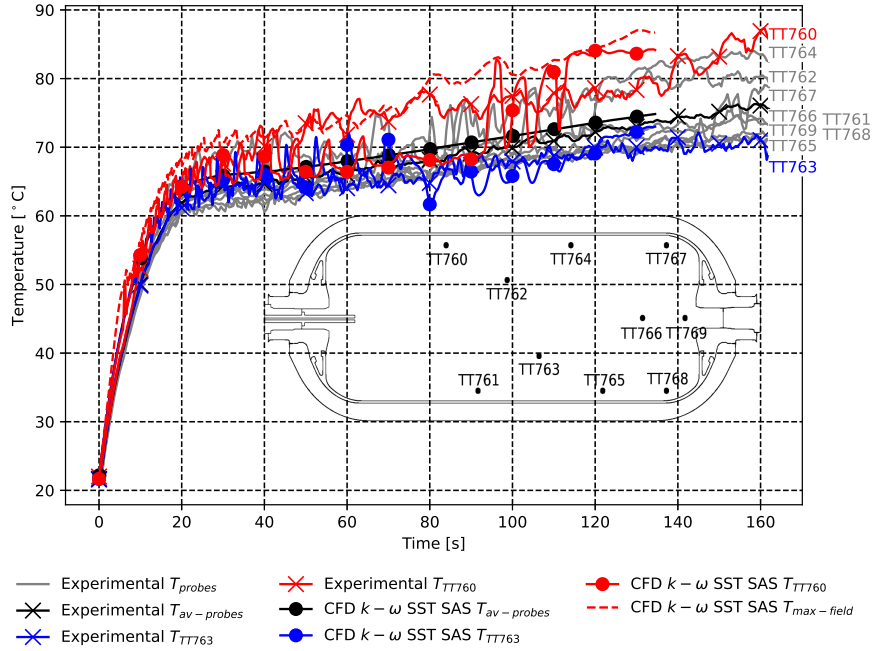


Figure 11: Scenario D6Q8. Comparison between the averaged and local temperature values issued from the experimental measurements and the CFD results using the $k - \omega$ SST SAS turbulence model. The maximum temperature value issued from the CFD thermal field is represented by a red dashed line.

345 The jet oscillates in the tank. By oscillating up and down, it successively
cools down the upper part and the lower part of the tank. The temperatures
from probes TT763 and TT760 oscillate in phase opposition (figure 11). When
the jet stops oscillating (close to 70 s), the same phenomenon as for scenario
D6Q2 occurs: with the deflection of the jet, a hot spot is convected from the
injector region to the tank rear region, and a vertical thermal gradient develops.

350 6. Conclusion

The objective of this work was to improve the CFD prediction of thermal
gradients during the filling stage of a hydrogen tank. Previous studies
[14, 16, 34] had shown that URANS approach associated with the $k - \omega$ SST
turbulence model, tends to underestimate thermal gradients. Here, the impact
of turbulence modeling on thermal gradient prediction was investigated on an
experimental case, issued from the HyTransfer project [12] and leading to large
thermal gradients. The underprediction of the thermal gradient magnitude by
the $k - \omega$ SST model was attributed to an overestimation of the eddy-viscosity,
which plays a key role in thermal diffusion. An advanced turbulence model, the

360 $k - \omega$ SST SAS model, was used to balance the eddy-viscosity production, and it was shown to substantially improve the prediction for this filling scenario.

The accuracy of the $k - \omega$ SST SAS model was assessed on a second filling scenario leading to large thermal gradients. The CFD results underestimate the maximum gas temperature by 10.1 °C compared to the experimental measurements. This difference could be attributed to the measurement device present in the tank during the experiments, which may potentially interact with the jet. The impact of the measurement device on thermal mixing needs to be clarified.

365 The $k - \omega$ SST SAS turbulence model leads to accurate thermal predictions for a third scenario with limited thermal gradients. It requires similar computational resources compared to the $k - \omega$ SST turbulence model. Consequently, the present study suggests to use the $k - \omega$ SST SAS turbulence model for CFD simulation of tank filling.

370 Complementary videos of scenarios D6Q2 and D6Q8 using the $k - \omega$ SST SAS model are available in the **Supplemental Data**.

375 **Acknowledgment**

This study was carried of as a part of a PhD work funded by Air Liquide Innovation Campus Paris and the National Association of Recherche and Technology (ANRT). It was performed using HPC resources from CALMIP (grants 2019, 2020, 2021 and 2022 p19025).

380 **References**

- [1] UNFCCC, Conference of the parties serving as the meeting of the parties to the paris agreement (2021).
URL https://unfccc.int/sites/default/files/resource/cma2021_L16_adv.pdf
- 385 [2] Hydrogen for net-zero : A critical cost-competitive energy vector (2021).
URL <https://hydrogencouncil.com/wp-content/uploads/2021/11/Hydrogen-for-Net-Zero.pdf>
- [3] Q. Nouvelot, P. Karzel, N. Hart, E. Vyazmina, V. Mattelaer, C. D. Sinding, A. Ruiz, Performance metrics for refuelling protocols for heavy duty hydrogen vehicules, fCH-04-2-2019:Refuelling Protocols for Medium and Heavy-Duty Vehicules (2020).
390 URL https://prhyde-cdn.s3-accelerate.amazonaws.com/wp-content/uploads/2020/10/14133040/PRHYDE_Deliverable-D2-1_final.pdf
- 395 [4] F. C. S. Committee, Fueling protocols for light duty gaseous hydrogen surface vehicles (dec 2016). doi:https://doi.org/10.4271/J2601_201612.
URL https://doi.org/10.4271/J2601_201612

- 400 [5] D. Melideo, D. Baraldi, M. C. Galassi, R. Ortiz Cebolla, B. Acosta Iborra, P. Moretto, CFD model performance benchmark of fast filling simulations of hydrogen tanks with pre-cooling, *International Journal of Hydrogen Energy* 39 (9) (2014) 4389–4395. doi:<https://doi.org/10.1016/j.ijhydene.2013.12.196>. URL <https://www.sciencedirect.com/science/article/pii/S0360319913031881>
- 405 [6] D. Melideo, D. Baraldi, CFD analysis of fast filling strategies for hydrogen tanks and their effects on key-parameters, *International Journal of Hydrogen Energy* 40 (1) (2015) 735–745. doi:<https://doi.org/10.1016/j.ijhydene.2014.10.138>. URL <https://www.sciencedirect.com/science/article/pii/S0360319914030146>
- 410 [7] C. Dicken, W. Mérida, Measured effects of filling time and initial mass on the temperature distribution within a hydrogen cylinder during refuelling, *Journal of Power Sources* 165 (1) (2007) 324–336. doi:<https://doi.org/10.1016/j.jpowsour.2006.11.077>. URL <https://www.sciencedirect.com/science/article/pii/S0378775306024244>
- 415 [8] G. Wang, J. Zhou, S. Hu, S. Dong, P. Wei, Investigations of filling mass with the dependence of heat transfer during fast filling of hydrogen cylinders, *International Journal of Hydrogen Energy* 39 (9) (2014) 4380–4388. doi:<https://doi.org/10.1016/j.ijhydene.2013.12.189>. URL <https://www.sciencedirect.com/science/article/pii/S0360319913031819>
- 420 [9] T. Terada, H. Yoshimura, Y. Tamura, H. Mitsuishi, S. Watanabe, Thermal behavior in hydrogen storage tank for fcv on fast filling (2nd report) (2008). doi:10.4271/2008-01-0463. URL <https://www.sae.org/content/2008-01-0463/>
- 425 [10] T. Bourgeois, T. Brachmann, F. Barth, F. Ammouri, D. Baraldi, D. Melideo, B. Acosta-Iborra, D. Zaepffel, D. Saury, D. Lemonnier, Optimization of hydrogen vehicle refuelling requirements, *International Journal of Hydrogen Energy* 42 (19) (2017) 13789–13809, special Issue on The 21st World Hydrogen Energy Conference (WHEC 2016), 13-16 June 2016, Zaragoza, Spain. doi:<https://doi.org/10.1016/j.ijhydene.2017.01.165>. URL <https://www.sciencedirect.com/science/article/pii/S0360319917303312>
- 430 [11] N. de Miguel, B. Acosta, P. Moretto, R. Ortiz Cebolla, Influence of the gas injector configuration on the temperature evolution during refueling of on-board hydrogen tanks, *International Journal of Hydrogen Energy* 41 (42) (2016) 19447–19454.
- 435

- 440 doi:<https://doi.org/10.1016/j.ijhydene.2016.07.008>.
URL <https://www.sciencedirect.com/science/article/pii/S0360319916307340>
- [12] E. i. European Commission, E. researchers, Hytransfer, FCH JU 2012-1-325277 (2013).
445 URL <https://cordis.europa.eu/project/id/325277/reporting>
- [13] B. Ravinel, B. Acosta, N. De Migue, P. Moretto, O.-C. Rafael, J. Goran, v. d. L. Ulrich, D4.1 report on the experimental filling test campaign (2017).
URL https://s02291b7740b89df1.jimcontent.com/download/version/1493713659/module/11623534399/name/HyTransfer_Report%20on%20the%20experimental%20filling%20test%20campaign_public.pdf
450
- [14] A computational fluid dynamic study of the filling of a gaseous hydrogen tank under two contrasted scenarios, International Journal of Hydrogen Energy 47 (55) (2022) 23278–23292. doi:<https://doi.org/10.1016/j.ijhydene.2022.03.260>.
455 URL <https://www.sciencedirect.com/science/article/pii/S0360319922014100>
- [15] The OpenFOAM foundation (2022).
460 URL <https://openfoam.org/>
- [16] D. Zaepffel, F. Mathey, B. Ravinel, T. Bourgeois, F. Ammouri, CFD analysis of the different flow regimes occurring during the filling of a hydrogen vehicle tank (2016).
- [17] F. R. Menter, Two-equation eddy-viscosity turbulence models for engineering applications, AIAA Journal 32 (8) (1994) 1598–1605. doi:10.2514/3.12149.
465 URL <https://arc.aiaa.org/doi/10.2514/3.12149>
- [18] F. R. Menter, A. R. Center., Improved two-equation k - [omega] turbulence models for aerodynamic flows [microform] / Florian R. Menter, National Aeronautics and Space Administration, Ames Research Center ; National Technical Information Service, distributor Moffett Field, Calif. : [Springfield, Va, 1992].
470
- [19] T. Perelman, On conjugated problems of heat transfer, International Journal of Heat and Mass Transfer 3 (4) (1961) 293–303. doi:[https://doi.org/10.1016/0017-9310\(61\)90044-8](https://doi.org/10.1016/0017-9310(61)90044-8).
475 URL <https://www.sciencedirect.com/science/article/pii/0017931061900448>
- [20] B. Eckhardt, T. M. Schneider, B. Hof, J. Westerweel, Turbulence transition in pipe flow, Annual Review of Fluid Mechanics 39 (1) (2007) 447–468.

- 480 doi:10.1146/annurev.fluid.39.050905.110308.
URL <http://www.annualreviews.org/doi/10.1146/annurev.fluid.39.050905.110308>
- [21] F. G. Schmitt, About boussinesq's turbulent viscosity hypothesis: historical
485 remarks and a direct evaluation of its validity, *Comptes Rendus Mécanique*
335 (9) (2007) 617–627, joseph Boussinesq, a Scientist of bygone days and
present times. doi:<https://doi.org/10.1016/j.crme.2007.08.004>.
URL <https://www.sciencedirect.com/science/article/pii/S1631072107001386>
- [22] E. Lemmon, M. Huber, M. McLinden, Nist standard reference database 23:
490 reference fluid thermodynamic and transport properties-refprop, version
9.1 (2013-05-07 2013).
URL https://tsapps.nist.gov/publication/get_pdf.cfm?pub_id=912382
- [23] R. Manceau, Industrial codes for CFD, lecture (Feb. 2021).
495 URL <https://hal.inria.fr/hal-03207431>
- [24] A. Suryan, H. D. Kim, T. Setoguchi, Comparative study of turbu-
lence models performance for refueling of compressed hydrogen tanks,
International Journal of Hydrogen Energy 38 (22) (2013) 9562–9569.
doi:10.1016/j.ijhydene.2012.07.055.
500 URL <https://app.dimensions.ai/details/publication/pub.1025692856>
- [25] V. Ramasamy, E. Richardson, Thermal response of high-aspect-
ratio hydrogen cylinders undergoing fast-filling, *International Jour-
nal of Heat and Mass Transfer* 160 (2020) 120179. doi:<https://doi.org/10.1016/j.ijheatmasstransfer.2020.120179>.
505 URL <https://www.sciencedirect.com/science/article/pii/S001793102033115X>
- [26] H. Li, Z. Lyu, Y. Liu, M. Han, H. Li, The effects of infill on
hydrogen tank temperature distribution during fast fill, *Internation-
al Journal of Hydrogen Energy* 46 (17) (2021) 10396–10410.
510 doi:<https://doi.org/10.1016/j.ijhydene.2020.12.133>.
URL <https://www.sciencedirect.com/science/article/pii/S0360319920347479>
- [27] X. Wu, J. Liu, J. Shao, G. Deng, Fast filling strategy of type iii
515 on-board hydrogen tank based on time-delayed method, *Internation-
al Journal of Hydrogen Energy* 46 (57) (2021) 29288–29296.
doi:<https://doi.org/10.1016/j.ijhydene.2021.01.094>.
URL <https://www.sciencedirect.com/science/article/pii/S0360319921001865>

- 520 [28] T.-H. Shih, W. W. Liou, A. Shabbir, Z. Yang, J. Zhu, A new k-
epsilon eddy viscosity model for high reynolds number turbulent
flows, *Computers & Fluids* 24 (3) (1995) 227–238. doi:[https://doi.org/10.1016/0045-7930\(94\)00032-T](https://doi.org/10.1016/0045-7930(94)00032-T).
URL <https://www.sciencedirect.com/science/article/pii/004579309400032T>
- 525 [29] F. Menter, T. Esch, Element of industrial heat transfer predictions (2001).
- [30] F. R. Menter, Influence of freestream values on k-omega turbulence model
predictions, *AIAA Journal* 30 (6) (1992) 1657–1659. arXiv:<https://doi.org/10.2514/3.11115>, doi:10.2514/3.11115.
530 URL <https://doi.org/10.2514/3.11115>
- [31] F. Menter, M. Kuntz, R. Langtry, Ten years of industrial experience with
the sst turbulence model, *Heat and Mass Transfer* 4 (01 2003).
- [32] F. R. Menter, R. Langtry, S. Völker, Transition modelling for general pur-
pose CFD codes 77 (1) 277–303. doi:10.1007/s10494-006-9047-1.
535 URL <http://link.springer.com/10.1007/s10494-006-9047-1>
- [33] R. B. Langtry, F. R. Menter, Correlation-based transition modeling for un-
structured parallelized computational fluid dynamics codes, *AIAA Journal*
47 (12) (2009) 2894–2906. doi:10.2514/1.42362.
URL <https://arc.aiaa.org/doi/10.2514/1.42362>
- 540 [34] D. Melideo, D. Baraldi, N. De Migue, B. Acosta, Effects of the injector
direction on the temperature distribution during filling of hydrogen tanks
(2017).
- [35] D. Melideo, D. Baraldi, N. De Miguel Echevarria, B. Acosta Iborra,
Effects of some key-parameters on the thermal stratification in hydrogen
545 tanks during the filling process, *International Journal of Hydrogen Energy*
44 (26) (2019) 13569–13582. doi:10.1016/j.ijhydene.2019.03.187.
URL <https://linkinghub.elsevier.com/retrieve/pii/S0360319919312169>
- [36] Langtry-menter k-omega shear stress transport (sst) (2021).
550 URL <https://www.openfoam.com/documentation/guides/latest/doc/guide-turbulence-ras-k-omega-sst-lm.html>
- [37] F. Menter, Y. Egorov, A Scale Adaptive Simulation Model using Two-
Equation Models. arXiv:<https://arc.aiaa.org/doi/pdf/10.2514/6.2005-1095>, doi:10.2514/6.2005-1095.
555 URL <https://arc.aiaa.org/doi/abs/10.2514/6.2005-1095>
- [38] Scale-adaptive simulation based on the k-omega-sst (2021).
URL https://www.openfoam.com/documentation/guides/latest/api/classFoam_1_1RASModels_1_1kOmegaSSTSAS.html

- 560 [39] Y. Egorov, F. Menter, Development and application of sst-sas turbulence
model in the desider project (2008).
- [40] D. S.-K. Ting, Chapter 4 - turbulence scales, in: D. S.-K. Ting (Ed.),
Basics of Engineering Turbulence, Academic Press, 2016, pp. 69–98.
doi:<https://doi.org/10.1016/B978-0-12-803970-0.00004-0>.
URL [https://www.sciencedirect.com/science/article/pii/
565 B9780128039700000040](https://www.sciencedirect.com/science/article/pii/B9780128039700000040)
- [41] ChtMultiRegionFoam (2021).
URL <https://openfoamwiki.net/index.php/ChtMultiRegionFoam>
- [42] The PISO algorithm in OpenFOAM (2021).
URL [http://openfoamwiki.net/index.php/OpenFOAM_guide/The_
570 PISO_algorithm_in_OpenFOAM](http://openfoamwiki.net/index.php/OpenFOAM_guide/The_PISO_algorithm_in_OpenFOAM)
- [43] R. Issa, Solution of the implicitly discretised fluid flow equations by
operator-splitting, Journal of Computational Physics 62 (1) (1986) 40–65.
doi:[https://doi.org/10.1016/0021-9991\(86\)90099-9](https://doi.org/10.1016/0021-9991(86)90099-9).
URL [https://www.sciencedirect.com/science/article/pii/
575 0021999186900999](https://www.sciencedirect.com/science/article/pii/0021999186900999)
- [44] The PIMPLE algorithm in OpenFOAM (2021).
URL [https://openfoamwiki.net/index.php/OpenFOAM_guide/The_
PIMPLE_algorithm_in_OpenFOAM](https://openfoamwiki.net/index.php/OpenFOAM_guide/The_PIMPLE_algorithm_in_OpenFOAM)

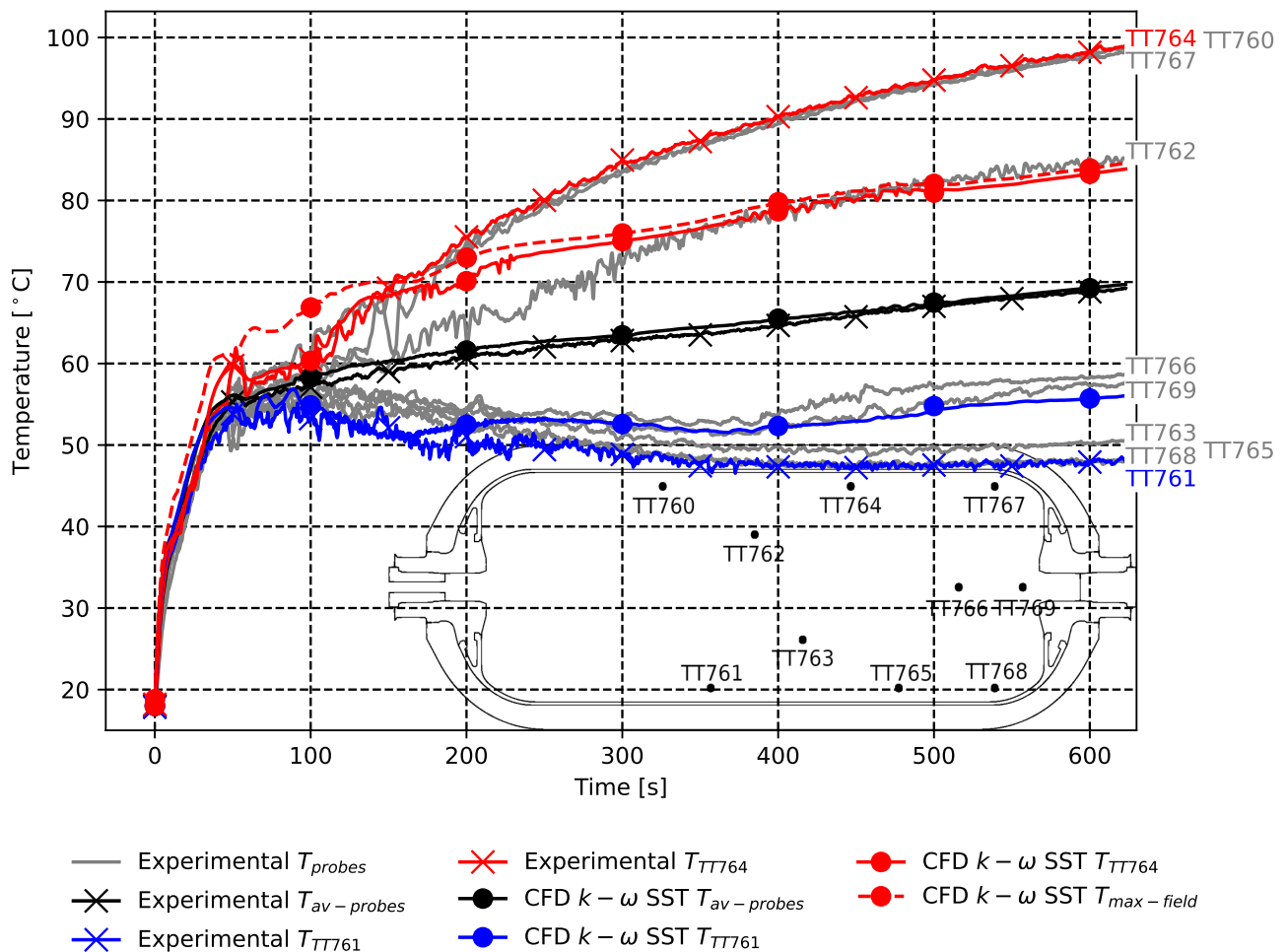


Figure 4.1 – Scenario D10Q2. Comparison between the experimental measurements and CFD results using the $k - \omega$ SST model, concerning the averaged and local temperature values. The averaged temperature $T_{av-probes}$ is the arithmetic average of the 10 probe temperatures located in the fluid region. The maximum temperature value issued from the CFD thermal field is represented by a red dashed line..

4.2 Additional results

4.2.1 Gas temperatures

Figures 4.2 and 4.3 compare the temperatures between the CFD results and the experimental measurements for the 10 probes in the gas. In figure 4.2, temperature oscillations are visible before $t = 80$ s. It corresponds to the oscillation of the jet. For the experimental measurements, perturbations of temperature appear for the probe TT760 at $t = 40$ s, for the probe TT764 at $t = 80$ s and for the probe TT767 at $t = 140$ s. This suggests, the convection of the hot spot of temperature at the top of the fluid region identified for the scenario D6Q2 is also occurring for the scenario D6Q8. Likewise, the CFD results seem delayed with the perturbation of temperature for the probe TT760 at $t = 90$ s. In figure 4.3, the delay between the CFD results and the experimental measured appears plainly for the probe TT760, probe TT764 and probe TT767 (approximately 50 s).

4.2.2 Heat exchanged between the gas and the walls

Figures 4.4 and 4.5 show that the presence of a turbulence model has a limited impact on the total heat power at wall for all regions. In figure 4.4, (panel D), it can be seen that the upper part of the liner exchanges more heat for the cDNS case, followed by the $k - \omega$ SST SAS case compared with the $k - \omega$ SST case. The trend is the opposite for the lower part of the liner. This is a consequence of the higher thermal gradient amplitude present in the gas for cDNS case, followed by the $k - \omega$ SST SAS case when compared with the $k - \omega$ SST case. The total heat power, i.e. the sum of the heat power from the upper part and lower part, is however similar for all CFD studies.

In figure 4.5, (panels B and C) it can be seen that the absence of turbulent thermal diffusion for the cDNS case (in green) induces a reduction of the heat power on walls on the left side for the plugs and the bosses.

At $t = 430$ s, for the cDNS case, a numerical scheme had to be changed for stability reason. The new numerical scheme chosen, more stable but more diffusive, reduces the oscillation of the heat power. In figure 4.5, panel C, the above mentioned effects are clearly visible.

4.2.3 Comparison between OpenFOAM results and experimental measurements for the temperatures between the liner and the composite

Figure 4.6 displays a comparison of the temperatures recorded by the 28 probes located between the liner and the composite for the $k - \omega$ SST CFD results (in red), the $k - \omega$ SST SAS CFD results (in blue), the cDNS CFD results (in green) and the experimental measurements (in black). It shows that the temperatures from probes located where the liner is flat and with a constant thickness (TC5, TC6, TC7, TC8, TC9, TC10, TC24, TC22, TC21, TC20) are better predicted by the CFD with $k - \omega$ SST SAS turbulence model.

It changed the thermal mixing in the gas the tank. The temperatures in walls are impacted by the thermal stratification in the gas. The improvement of temperature prediction with the $k - \omega$ SST SAS turbulence model is thus also visible in figure 4.6. The cDNS overestimates the thermal gradient amplitude.

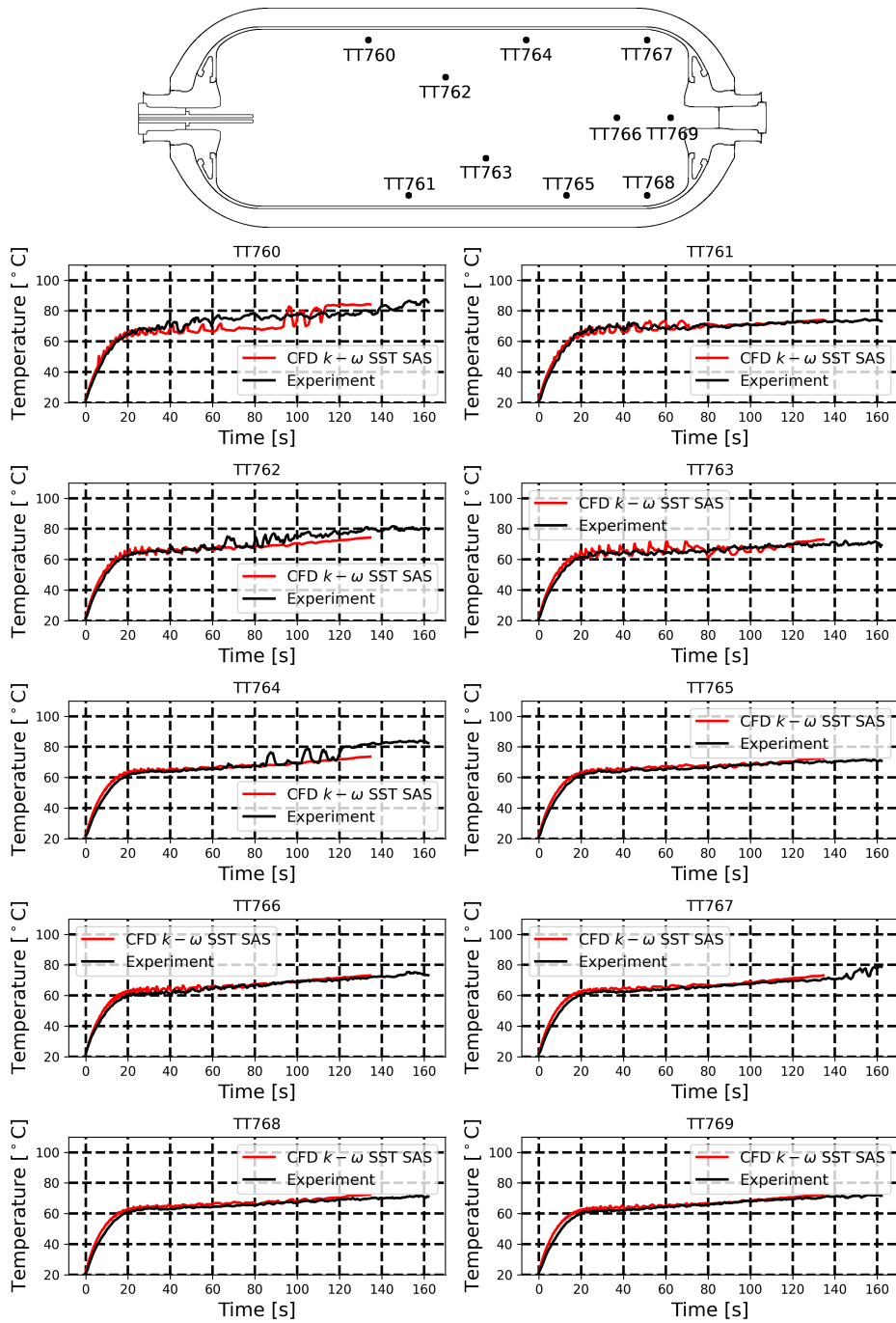


Figure 4.2 – For the scenario D6Q8. Comparison between the local temperature values issued from the OpenFOAM CFD results and the experimental measurements. Probe locations are indicated in the upper panel.

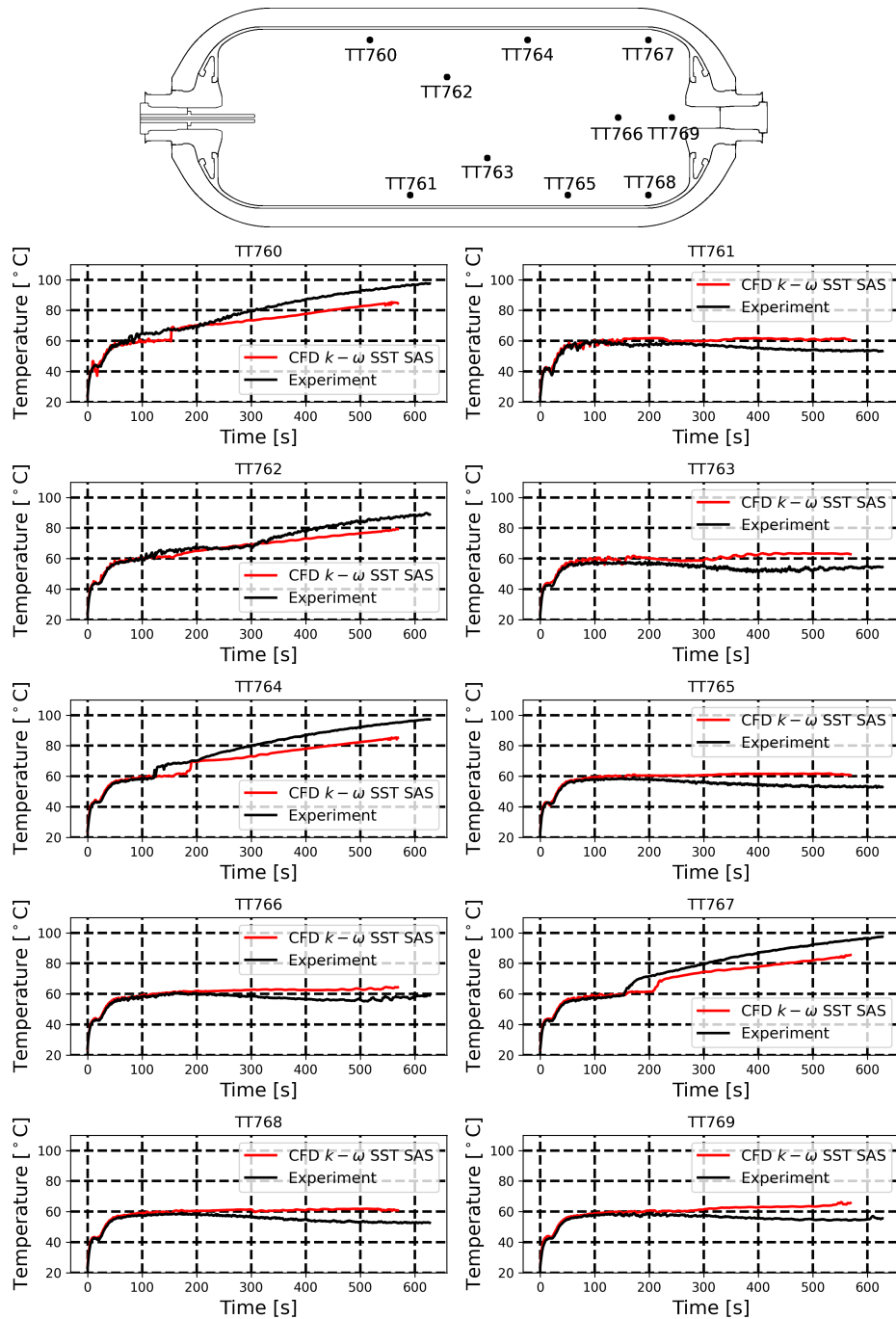


Figure 4.3 – For the scenario D6Q2. Comparison between the local temperature values issued from the OpenFOAM CFD results and the experimental measurements. Probe locations are indicated in the upper panel.

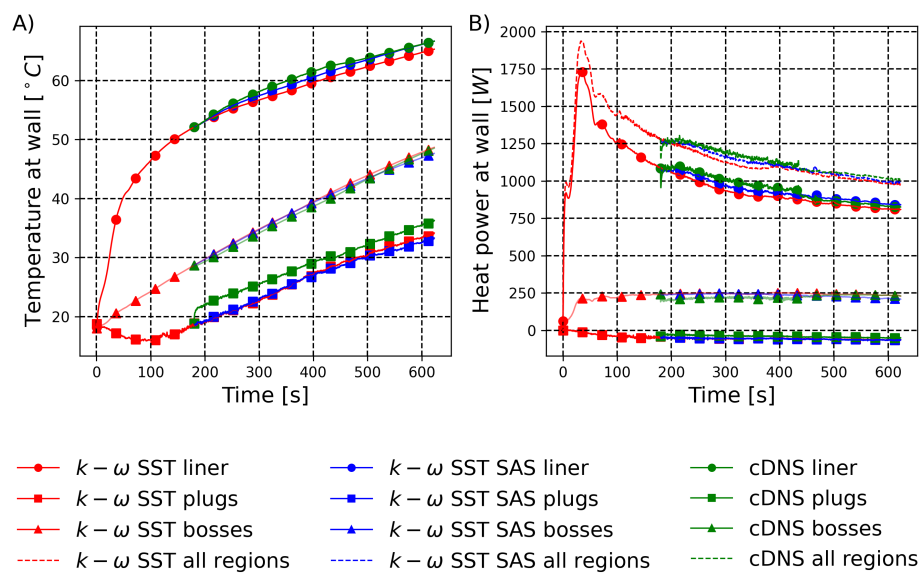


Figure 4.4 – Scenario D10Q2. Temperature at wall (panel A) and heat power at wall (panel B) for the $k-\omega$ SST CFD results (in red), the $k-\omega$ SST SAS CFD results (in blue) and the cDNS CFD results (in green).

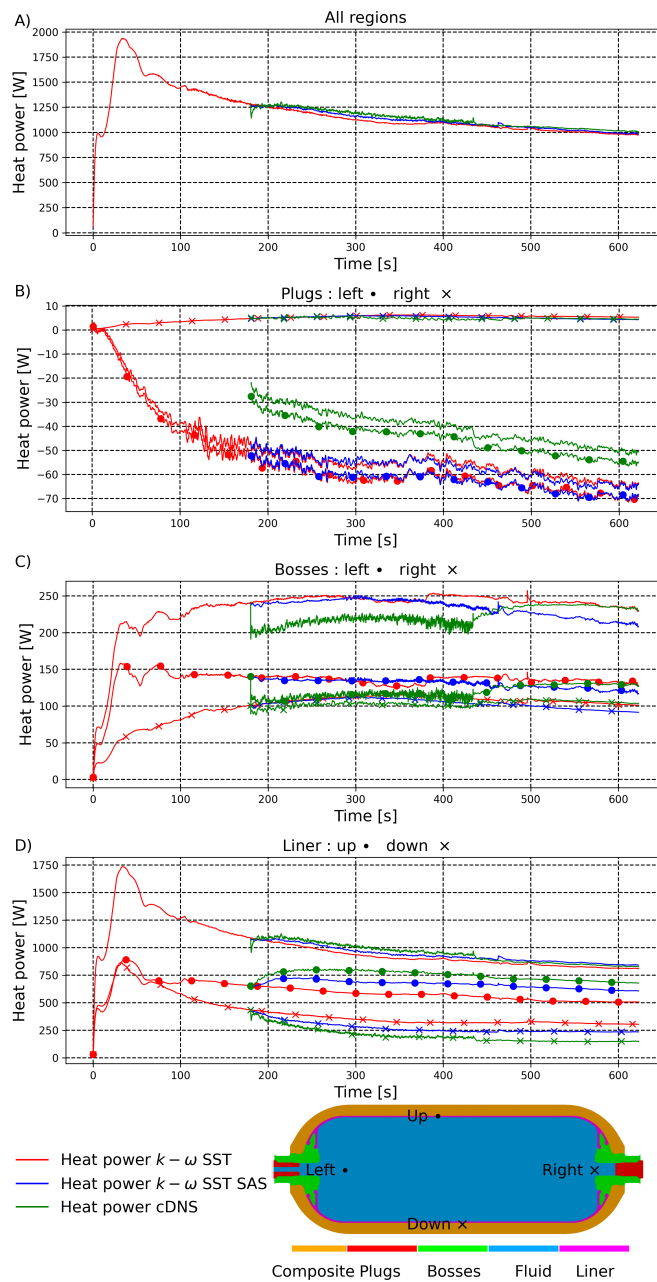


Figure 4.5 – Scenario D10Q2. Heat power for the $k - \omega$ SST CFD results (in red), the $k - \omega$ SST SAS CFD results (in blue) and the cDNS CFD results (in green). The heat power for a region is reported separately for (i) the left and right for the bosses and plugs, (ii) the upper part and the lower part for the liner and (iii) the inner part and outer part for the pipe.

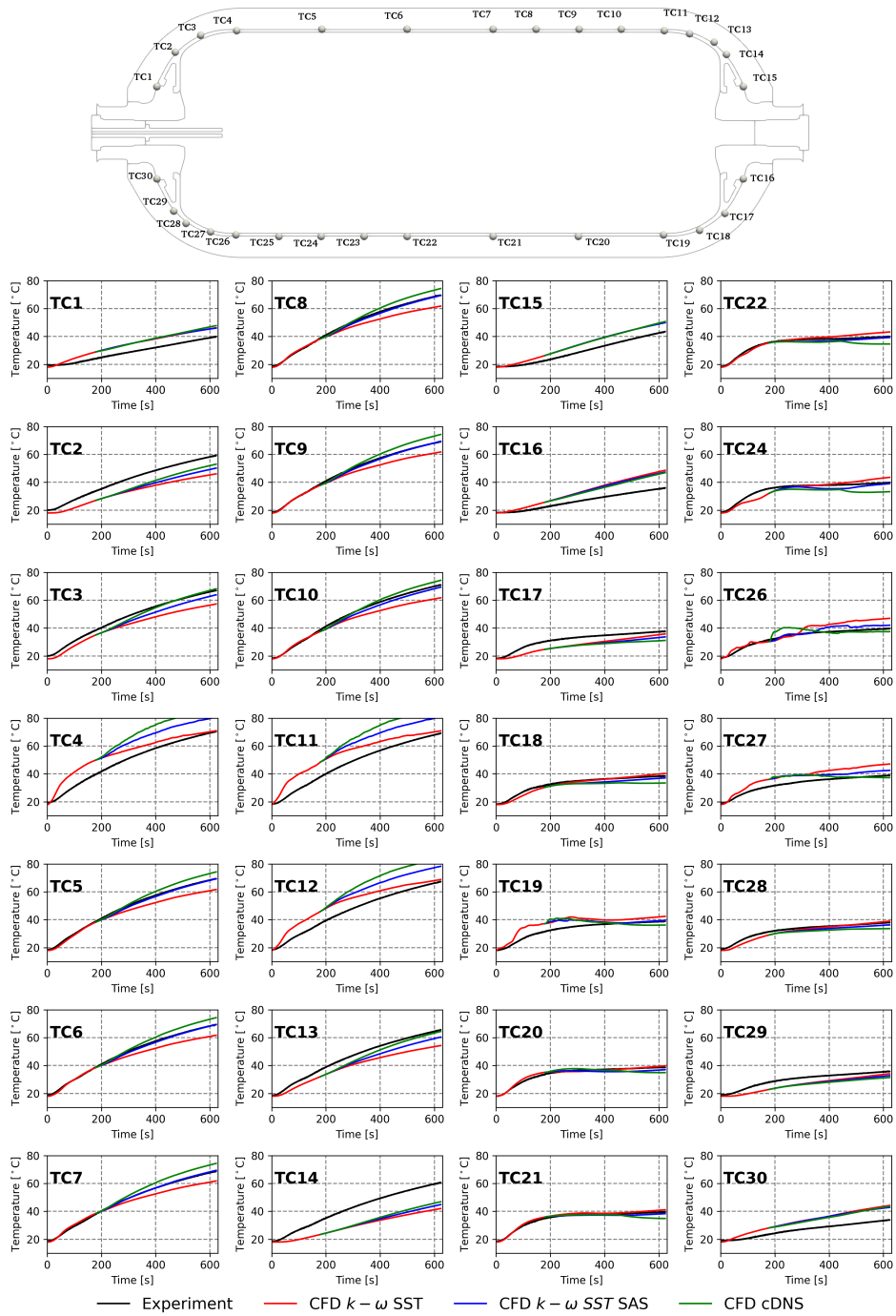


Figure 4.6 – Scenario D10Q2. Comparison of the temperature located between the liner and the composite for the results issued from the $k-\omega$ SST CFD simulation (in red), the $k-\omega$ SST SAS CFD simulation (in blue) and the cDNS CFD simulation (in green) and the experimental measurements (in black).

Chapter 5

Simplified model to predict the thermal stratification

Introduction

Thermodynamic modeling of hydrogen tank filling, i.e. 0D models, consider the gas in the tank as a unique isothermal volume. Based on thermodynamical considerations, i.e. mass and energy balance equations, the temperature predicted each time step is a spatial average, as well as other quantities like the density or the pressure.

These models cannot detect neither the onset of thermal stratification, nor the maximum temperature of the gas inside the tank. For now, only CFD approaches can predict the onset of stratification and estimate the amplitude of the thermal gradient. However, CFD approaches require important computational resources and time. This disqualifies CFD approaches to perform parametric studies or a live-stream temperature prediction for embedded application.

Previous CFD studies highlighted the phenomenon of jet deflection for horizontal filling [25, 55]. The phenomenon has been likewise highlighted in chapters 3 and 4. Indeed, as the injected gas is cooled down and released at the pipe outlet in the warm gas bulk, it is forming a round jet sinking down towards the lower part of the tank due to buoyancy forces. The jet breaks the horizontal symmetry and dumps the cold gas towards the lower part of the tank. This flow dynamic is a key factor of the onset of thermal stratification.

In the literature, free round jets released in a homogeneous environment with a different density than the jet density were deeply investigated. Early mention of buoyant round jet theory can be found in the work of Morton et al. [120]. Morton detailed the equation system leading to the buoyant round jet model. A complete description of the equation system can be found in the publication of Jirka [121] or in the book of Lee and Chu [122]. The buoyant round jet model includes the case of a fluid release in linear-stratified environment.

The model can be applied for the release of hot or cold gas into the atmosphere or the release of lighter or heavier fluid (like water with a different salinity), into ocean [123].

One of the major assumption of the model is the unbounded condition of the environment, i.e. free jet, which seems contradictory with the confined configuration of a tank filling. However, the CFD results, validated by experimental data (see chapter 4), give the velocity field in the tank. The buoyant round jet model results can be compared with the CFD results and the relevance of the method can be evaluated.

The buoyant round jet model requires initial values which can be provided by a 0D model. Therefore, it does not need a CFD calculation to describe the jet trajectory. A relationship between jet deflection in the tank and the thermal gradient

is suggested in section 5.2.2. This relationship aims to use the jet trajectory in the tank to evaluate the maximum temperature.

5.1 Reference data

5.1.1 Experimental data

Experiments were carried out during the HyTransfer project [41] from 2013 to 2016. During the experiments, a type IV 37 L tank filled horizontally with an axial injector showed contrasted thermal gas behaviors depending on the injector diameter and mass flowrate. Six filling scenarios were performed. There are designated by the injection diameter D and the averaged mass flowrate Q followed by the corresponding values used. For example the scenario D6Q2 corresponds to the scenario with an injector diameter of 6 mm and an averaged mass flowrate of 2 g/s.

During the experimental measurements, 10 probes of temperature were placed in the gas, noted $T_{probe,i}$, see section 2.1.1. The maximum gas temperature T_{max} and minimum gas temperature T_{min} at the tend of the filling are defined as

$$T_{max} = \max(T_{probe,i}) \quad (5.1)$$

and

$$T_{min} = \min(T_{probe,i}), \quad (5.2)$$

and an averaged gas temperature T_{av} is calculated as followed :

$$T_{av} = \frac{\sum_i^{10} T_{probe,i}}{10}. \quad (5.3)$$

Table 5.1 presents, at the final filling time, the difference between $T_{max} - T_{av}$ which can be considered as a good indicator to evaluate the presence of thermal gradient.

	Type IV 37 L tank					
Scenario	D3Q2	D3Q8	D6Q2	D6Q8	D10Q2	D10Q8
$T_{max} - T_{av}$ [°C]	8.36	6.35	26.76	11.28	30.03	24.39

Table 5.1 – Thermal gradients for 6 filling scenarios of the type IV 37 L tank [41]. Selected case in bold.

The pipe diameter and the injected mass flowrate determine the inlet velocity. As previous studies highlighted [25, 29], the higher the inlet velocity is, the better the thermal mixing is. The scenario D10Q2 is the scenario with the largest diameter and the lowest mass flowrate. It is producing the maximum thermal gradient amplitude. To obtain 10 mm for the injector diameter, the tank was directly filled through the plug aperture, with no pipe inside the tank. This configuration does not exist in a real filling condition. This situation is problematic to use the buoyant round jet model because the gas is released first not in the main bulk but in the boss cavity, which corresponds to a sudden pipe expansion situation and not a free jet release situation, see picture 5.1. Also, the jet is hitting the boss wall which disturbs its trajectory.

This is why, for the following study, the scenario D6Q2 is selected. It also led to a large thermal gradient (see table 5.1) but has an injector pipe of 100 mm long inside the tank.

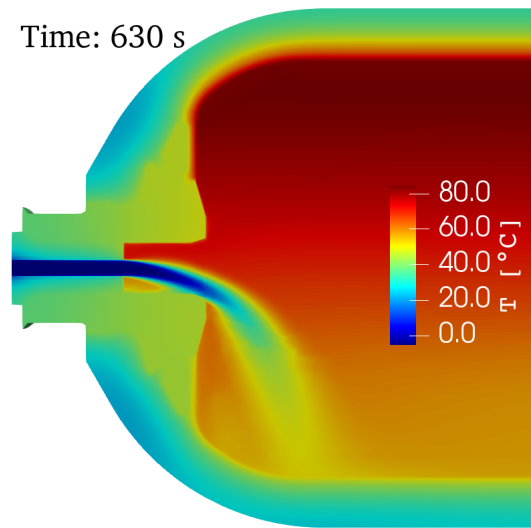


Figure 5.1 – For the scenario D10Q2. For the time 630 s. View of the thermal field at the injection region from the plane (x,y) . In the boss cavity at left, the jet is bounded. It impacts the boss wall and get deflected. Outside the boss cavity, the jet impacts the liner lower wall.

5.1.2 CFD Results

During the experimental measurements, the occurrence of thermal gradients can be detected but for a limited locations on temperatures and no knowledge on velocities. To clarify the mechanism leading to the thermal gradient, the CFD approach has been used, see chapter 3 and 4.

In section 4.1, the 3D CFD simulation of the scenario D6Q2 has been obtained using the software OpenFOAM. Thanks to the CFD approach, the complete map of the thermal field and velocity magnitude field in the tank are obtained. Figure 5.2 shows, when the thermal gradient occurs, the jet is deflected towards the lower part of the tank. The deflected jet brings cold gas at the lower part of the tank. This is responsible for the vertical thermal stratification. The jet deflection is due to a competition between the inertia force of the jet and the negative buoyancy force on the jet. It changes its trajectory from axial to deflected when the buoyancy force becomes dominant. The buoyant round jet model is designed to model this phenomenon.

5.2 The buoyant round jet model

5.2.1 Model development

This section is dedicated to the development of the buoyant round jet model. It contains the different hypotheses and simplifications leading to the final equation system.

The pipe is cylindrical, then the gas released from the pipe outlet is assumed to be a round jet, i.e. circular-symmetric along its centerline. The jet centerline is described by a curvilinear abscissa s [m]. The pipe outlet corresponds to the initial point ($s = 0$ m). Initially, the jet radius b [m] is equal to the pipe radius r_0 [m]. At the pipe outlet, the velocity and density profiles are taken as a top-hat profile with a uniform value u_0 [m/s] and ρ_0 [kg/m³] respectively. In the exterior environment, the gas is considered at rest, i.e. no velocity. The density ρ_{ref} [kg/m³] is the reference density for the exterior environment. The exterior environment can be stratified, i.e. a gradient of density can be present, then the

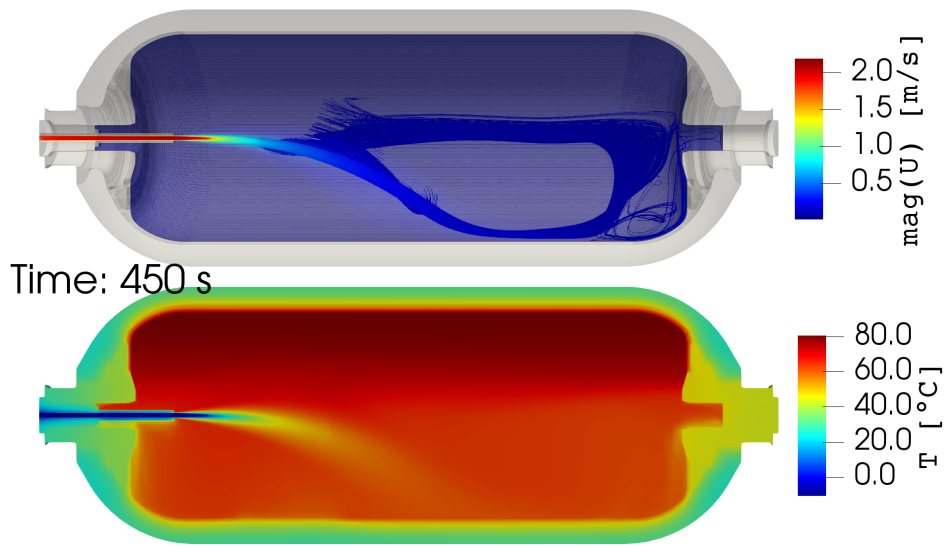


Figure 5.2 – For the scenario D6Q2, CFD results at time 450 s. The upper panel represents the velocity magnitude field with transparency, to see stream-lines coming from the pipe inlet. The lower panel represents the temperature field.

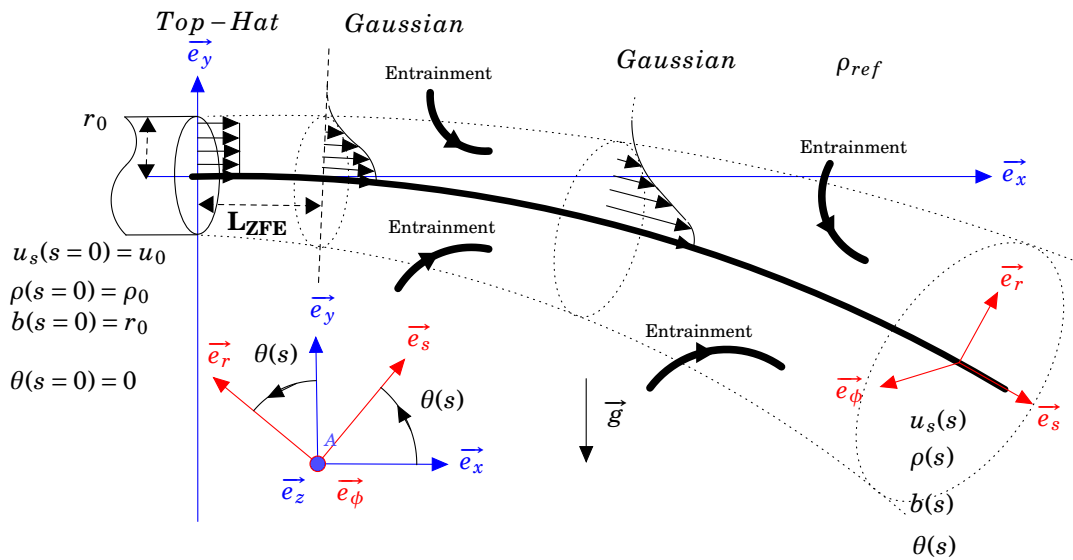


Figure 5.3 – Horizontal release of a buoyant round jet.

surrounding density of the jet ρ_{grad} [kg/m^3] is different than ρ_{ref} .

A fixed Cartesian coordinate system $(\vec{e}_x, \vec{e}_y, \vec{e}_z)$ sets the reference frame. The gravity acceleration is oriented in the \vec{e}_y direction. A local cylindrical coordinate system $(\vec{e}_s, \vec{e}_r, \vec{e}_\phi)$ is set to follow the curvilinear abscissa s , see figure 5.3.

A transition area called Zone of Flow Establishment (ZFE) is identified [124] where a turbulent jet is released. In this zone, the jet velocity and density profile will shift from a top-hat profile to a Gaussian profile. Once the flow is established, the jet profile remains Gaussian and self-similar along its trajectory. Consequently the ZFE needs to be treated separately. Four assumptions are needed for the model:

- (i) The flow is steady-state, i.e. there is no temporal evolution of the jet. Mathematically speaking, time derivative components in Navier-Stokes equations are neglected.
- (ii) The pressure is considered uniform, i.e. the pressure gradient is neglected.
- (iii) The viscosity effects are neglected. As the flow is fully turbulent at the pipe outlet (high Reynolds number), the viscous forces are neglected in front of inertial forces.
- (iv) The difference between the initial density ρ_0 and the exterior environment density ρ_{ref} is considered small enough to use the Boussinesq simplification, i.e. the variation of the fluid density is only considered in the buoyancy term in the Navier-Stokes equations.

The buoyant round jet model is based on balance equations for the mass flux, momentum flux and buoyancy flux for a perpendicular plane of the jet centerline at the abscissa s . The balance equations are divided by the reference density ρ_{ref} . The variables of the equation system are: (i) the mass flux Q [m^3/s], (ii) the momentum flux M [m^4/s^2] and (iii) the buoyancy flux J [m^4/s^2]. They are defined as:

$$Q = \int_0^{2\pi} \int_0^{\infty} u_s r dr d\phi, \quad (5.4)$$

$$M = \int_0^{2\pi} \int_0^{\infty} u_s^2 r dr d\phi, \quad (5.5)$$

$$J = \int_0^{2\pi} \int_0^{\infty} g' u_s r dr d\phi, \quad (5.6)$$

where u_s is the velocity magnitude along the \vec{e}_s axis and g' the reduced gravity defined as

$$g' = \frac{\rho_{grad} - \rho}{\rho_{ref}} g. \quad (5.7)$$

In the ZFE, the effect of the buoyancy forces are neglected, i.e. the jet remains on the x-axis. Initially at $s = 0$ m, the top-hat approximation allows to access Q and M values:

$$Q(0) = \pi u_0 r_0^2, \quad (5.8)$$

$$M(0) = \pi u_0^2 r_0^2. \quad (5.9)$$

Using a correlation [125], the length of the ZFE can be linked to the pipe radius:

$$L_{ZFE} \approx 9,79 r_0. \quad (5.10)$$

In [125], the mass flux at the end of the ZFE is linked to the one at the beginning

$$\frac{Q(L_{ZFE})}{Q(0)} = 1 + 0.083 \frac{L_{ZFE}}{2r_0} + 0.013 \left(\frac{L_{ZFE}}{2r_0} \right)^2 . \quad (5.11)$$

Then using (5.10), (5.11) becomes

$$Q(L_{ZFE}) = 1.72 Q(0) . \quad (5.12)$$

The momentum flux is conserved:

$$M(L_{ZFE}) = M(0) . \quad (5.13)$$

Outside the ZFE, the round jet is self-similar and its shape can be considered as Gaussian [122]. The velocity profile is

$$u_s(s, r) = u_c(s) e^{-\frac{r^2}{b^2}} , \quad (5.14)$$

where $u_c(s)$ is the velocity at the jet centerline. Likewise, the density profile is

$$\rho(s, r) = \rho_{grad}(y) + (\rho_c(s) - \rho_{grad}(y)) e^{-\frac{r^2}{(\lambda b)^2}} , \quad (5.15)$$

where $\rho_c(s)$ is the density at the jet centerline. λ , is a parameter to correct the Gaussian variance for the density profile if different than the velocity profile. In the literature, it can be found $\lambda = 1$ in [120], $\lambda = 1.2$ in [121] or $\lambda = 1.19$ in [122]. The density profile (5.15) is substituted in the reduced gravity term (5.7) which becomes

$$g'(s, r) = g_c(s) e^{-\frac{r^2}{(\lambda b)^2}} , \quad (5.16)$$

where $g_c(s)$ is the reduced gravity term at the jet centerline. Using (5.14) and (5.16), the variables Q , M and J can be linked to u_c , b and g_c :

$$Q = \pi b^2 u_c , \quad (5.17)$$

$$M = \frac{1}{2} \pi b^2 u_c^2 , \quad (5.18)$$

$$J = \frac{\lambda^2}{\lambda^2 + 1} \pi b^2 u_c g_c . \quad (5.19)$$

Hence (5.19) can be expressed via Q :

$$J = \frac{\lambda^2}{\lambda^2 + 1} Q g_c . \quad (5.20)$$

The mass balance applied on a plane perpendicular of the jet centerline links the axial velocity u_s , parallel with the abscissa s and the radial velocity u_r , perpendicular with the abscissa s .

$$\frac{\partial}{\partial s} \left[\int_0^{+\infty} 2\pi r u_s dr \right] + \lim_{r \rightarrow \infty} 2\pi r u_r = 0 \quad (5.21)$$

and using the integral variable Q , equation (5.21) becomes

$$\frac{\partial Q}{\partial s} = - \lim_{r \rightarrow \infty} 2\pi r u_r . \quad (5.22)$$

The quantity $-\lim_{r \rightarrow \infty} 2\pi r u_r$ is finite and represents the mass entrainment E . It refers to the mass absorbed and entrained by the spread of the jet. Morton et al. [120] introduced the entrainment rate α which models the entrainment via a relationship between to the axis velocity u_c and the jet radius b :

$$E = 2\pi b u_c \alpha . \quad (5.23)$$

α is taking from experimental measurements. Considering the initial condition (jet-like, i.e. flow driven by its momentum or plume-like i.e. flow driven by its buoyancy) and the position along the jet trajectory, the value α can vary. According to [126], the range of values for the entrainment rate of a pure jet and a pure plume, α_{jet} and α_{plume} respectively, are

$$0.046 < \alpha_{jet} < 0.057 \text{ and } 0.07 < \alpha_{plume} < 0.011 . \quad (5.24)$$

It must be noted, in [126], a *top-hat* velocity approximation outside the ZFE is used instead of a Gaussian one. Then a factor $1/\sqrt{2}$ needs to be applied to the values in [126] to obtain values in (5.24). The values are consistent with the values given in the work of Jirka [121], $\alpha_{jet} = 0.055$ and $\alpha_{plume} = 0.083$, and in the book from Lee and Chu [122] $\alpha_{jet} = 0.057$ and $\alpha_{plume} = 0.088$. The entrainment can be written using the momentum flux M and equation (5.22) can be rewritten as:

$$\frac{\partial Q}{\partial s} = (8\pi M)^{1/2} \alpha . \quad (5.25)$$

The momentum balance applied on a plane perpendicular to the jet centerline shows that the momentum flux along the \vec{e}_x direction is constant and the momentum flux along the \vec{e}_y direction is affected by the buoyancy:

$$\vec{e}_x / \frac{\partial M \cos(\theta)}{\partial s} = 0 \quad (5.26)$$

$$\vec{e}_y / \frac{\partial M \sin(\theta)}{\partial s} = (\lambda^2 + 1) \frac{JQ}{2M} \quad (5.27)$$

Here, θ [rad] is the angle between the directions \vec{e}_s and \vec{e}_x , see figure 5.3. It measures the deflection of the jet from the horizontal x-axis. For axial injectors, θ is initially null at the outlet, i.e. $\theta(0) = 0$ rad. Equations (5.26) and (5.27) can be rewritten as:

$$\frac{\partial M}{\partial s} = (\lambda^2 + 1) \frac{JQ}{2M} \sin(\theta) , \quad (5.28)$$

$$\frac{\partial \theta}{\partial s} = (\lambda^2 + 1) \frac{JQ}{2M^2} \cos(\theta) . \quad (5.29)$$

For homogeneous exterior environment, i.e. $\rho_{grad} = \rho_{ref}$, the buoyancy flux is constant along the jet. However, if the exterior environment is linear-stratified, Jirka [121] gives the evolution of the buoyancy flux along the jet as

$$\frac{\partial J}{\partial s} = Q \frac{g}{\rho_{ref}} \frac{\partial \rho_{grad}(y)}{\partial y} \sin(\theta) . \quad (5.30)$$

where ρ_{grad} is the gradient density as a function of y . ρ_{ref} remains a constant, consistent with the Boussinesq

approximation. For each point at the jet centerline $(x(s), y(s), 0)$, its local displacement along the jet trajectory is given by the vector $ds \vec{e}_s$. Therefore, the trajectory can be expressed as:

$$\frac{\partial x}{\partial s} = \cos(\theta), \quad (5.31)$$

$$\frac{\partial y}{\partial s} = \sin(\theta). \quad (5.32)$$

Finally, using the equations (5.25), (5.28), (5.29), (5.30), (5.31) and (5.32) the equation system of the buoyant round jet model is obtained:

$$\begin{aligned} \frac{\partial Q}{\partial s} &= (8\pi M)^{1/2} \alpha \\ \frac{\partial M}{\partial s} &= (\lambda^2 + 1) \frac{JQ}{2M} \sin(\theta) \\ \frac{\partial J}{\partial s} &= Q \frac{g}{\rho_{ref}} \frac{\partial \rho_{grad}(y)}{\partial y} \sin(\theta) \\ \frac{\partial \theta}{\partial s} &= (\lambda^2 + 1) \frac{JQ}{2M^2} \cos(\theta) \\ \frac{\partial x}{\partial s} &= \cos(\theta) \\ \frac{\partial y}{\partial s} &= \sin(\theta) \end{aligned} \quad (5.33)$$

The initial conditions are:

$$\begin{aligned} Q(L_{ZFE}) &= 1.72\pi r_0^2 u_0 \\ M(L_{ZFE}) &= \pi u_0^2 r_0^2 \\ J(L_{ZFE}) &= \frac{\lambda^2}{\lambda^2 + 1} Q(L_{ZFE}) \frac{\rho_{grad}(0) - \rho_0}{\rho_{ref}} g \\ \theta(L_{ZFE}) &= 0 \\ x(L_{ZFE}) &= L_{ZFE} = 9,79 r_0 \\ y(L_{ZFE}) &= 0 \end{aligned} \quad (5.34)$$

For the filling of a tank, the fluid region is bounded. In the plane (x,y), the length x of the jet is limited by the length $L_{tank} - L_{pipe}$ representing the length of the tank minus the length of the pipe inside the tank. The length y is limited by the inner radius of the tank R_{int} . The model is not designed to predict the flow behavior after impacting a wall. Therefore, only the jet trajectory before impacting a wall is predicted.

The averaged gas density ρ_{av} in the tank is taken as the reference density ρ_{ref} for the buoyant round jet model.

The buoyant round jet model needs for initial conditions the inlet velocity u_0 , the inlet density ρ_0 and the averaged density ρ_{av} . These values can be obtained via a 0D model for the filling of a tank. In this study, the 0D model used is SOFIL, see section 2.2.2. These models consider the gas in the tank as a unique isothermal volume. At a given time, they are designed to predict an averaged gas pressure and temperature, p_{tank} and T_{tank} , and via the equation of state (EOS) of the hydrogen, the averaged gas density in the tank ρ_{av} can be deduced. The filling mass flowrate \dot{m} [kg/s] and the injected temperature T_{inj} [°C] are inputs for SOFIL, i.e. there are known in SOFIL. Consequently, the density ρ_0 can be calculated via the EOS, see (5.35). The injection velocity u_0 is then deduced, see (5.36):

$$\rho_0 = \rho(T_{in,j}, p_{tank}), \quad (5.35)$$

$$u_0 = \frac{\dot{m}}{\pi r_0^2 \rho_0}. \quad (5.36)$$

The two closure parameters α and λ are chosen to give the closest agreement with the CFD calculations. Then, for the following results, presented in section 5.4, $\alpha = 0.055$ and $\lambda = 1$. The value of α is similar to the value given for a free round jet given by Jirka [121]. The value of λ is similar to the value given by Muto [61]. This implies, the velocity and density profile are taken similar in the following. The sensitivity of the model for these parameters is studied in section 5.4.2.

5.2.2 Thermal gradient correction

For a homogeneous environment, $\forall s \rho_{grad}(y) = \rho_{av}$. The buoyancy flux is constant along the jet trajectory, i.e. $\forall s, J(s) = J_0$. When the environment density is linear-stratified, the buoyancy flux along the jet trajectory is decreasing, see (5.30). The presence of a density gradient tends to limit the jet trajectory deflection (see 5.4.2). For the filling of a hydrogen tank, the pressure in the tank can be considered uniform. The density gradient ρ_{grad} is a consequence of the thermal gradient. Using a CFD post-process for the scenario D6Q2, the density gradient ρ_{grad} as a function of y can be extracted:

$$\rho_{grad}(y) = \frac{1}{S_{x,z}(y)} \iint_{S_{x,z}(y)} \rho_{CFD}(x,y,z) dx dz, \quad (5.37)$$

where ρ_{CFD} is the density in the gas from the CFD results and $S_{x,z}(y)$ is the surface (x,z) crossing the fluid domain at the height y . Figure 5.4 presents $\frac{\rho_{grad}(y)}{\rho_{av}}$ as a function of y for different times, from 50 s to 550 s, reported with different colors. The densities near walls are higher than densities in the main gas bulk because walls are colder. It can be seen that for times before 200 s, a density gradient is not established yet. As presented in section 4.1, between 150 s and 200 s, a hot spot of temperature is convected for the region near the pipe to the opposite region in the tank. This phenomenon can be observed on the density gradient: between 150 s and 200 s the density in the upper part of the tank decreases suddenly. The density (thermal) stratification happens when the jet is enough deflected to hit the lower part of the tank, i.e. at $s = s_{impact}$, $y = -R_{int}$ and $x = L_{tank} - L_{injection}$. At $y = -R_{int}$, the density is maximum and is designated as ρ_{max} . The minimum density is designated as ρ_{min} . At $y = 0$ m, the density is the median density, designated as ρ_m . After 200 s, ρ_m is getting larger than ρ_{av} due to the faster elevation of temperature in the upper part compared to the diminution of the temperature in the upper part. From these observations, the upper part and the lower part of the tank must be considered separately.

The density profile is then modeled with a piecewise function of two linear functions defined in the upper part and in the lower part of the tank:

$$\rho_{grad}(y) = \begin{cases} (\rho_m - \rho_{max}) \frac{y}{R_{int}} + \rho_m & \text{if } y \in [-R_{int}, 0] \\ (\rho_{min} - \rho_m) \frac{y}{R_{int}} + \rho_m & \text{if } y \in [0, R_{int}] \end{cases}, \quad (5.38)$$

Equation (5.30) can be rewritten

$$\frac{\partial J}{\partial s} = \frac{Qg}{R_{int}} \frac{\rho_m - \rho_{max}}{\rho_{ref}} \sin(\theta). \quad (5.39)$$

The maximum density ρ_{max} is evaluated using the density of the jet centerline at the impact, i.e. $\rho_c(s_{impact}) = \rho_{max}$. Attempts of linking ρ_m to input parameters (e.g. u_0 , ρ_0 , ρ_{ref} , ρ_{max} , $L_{tank} - L_{pipe}$) did not produce satisfying results.

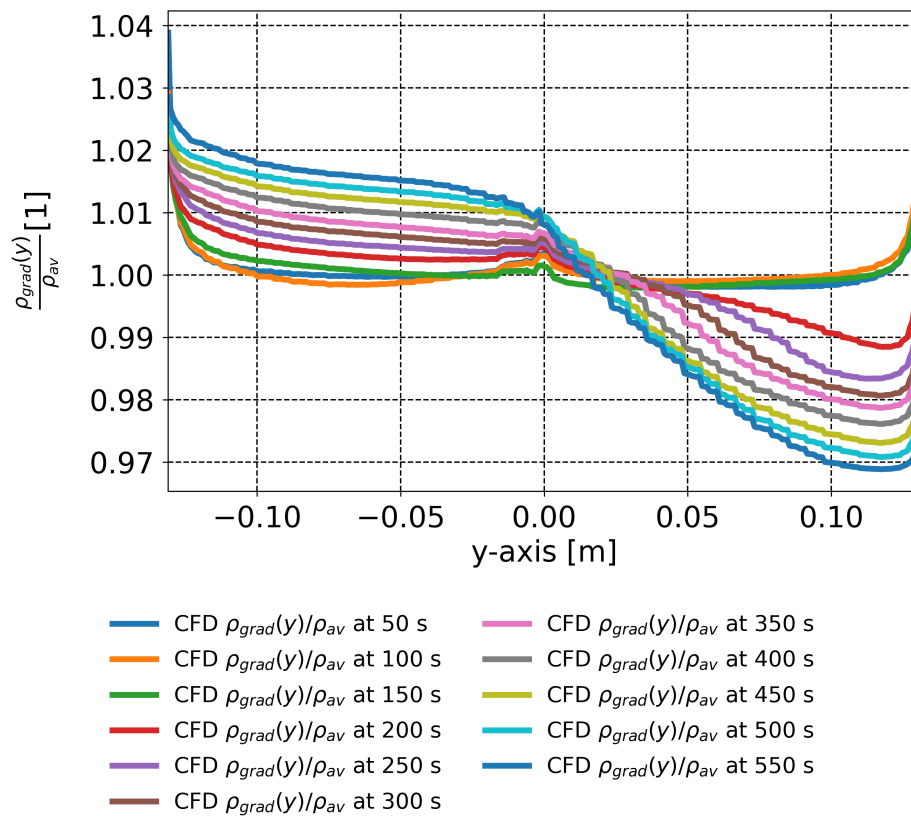


Figure 5.4 – For the scenario D6Q2. From CFD results, the rate $\frac{\rho_{grad}(y)}{\rho_{av}}$, as a function of y , is reported for times from 50 s to 550 s.

From CFD results, an empirical relationship is extracted:

$$\rho_m = 0.4(\rho_{max} - \rho_{av}) + \rho_{av} . \quad (5.40)$$

The value ρ_{min} is estimated using the link between the density gradient and the averaged density:

$$\rho_{av} = \frac{1}{V} \iiint_V \rho_{grad}(y) dx dy dz . \quad (5.41)$$

Considering the tank as a cylinder, i.e. $\iint_{S_{x,z}(y)} dx dz = 2(\sqrt{R_{int}^2 - y^2})L_{tank}$, (5.41) can be rewritten as

$$\rho_{av} = \frac{1}{\pi R_{int}^2 L_{tank}} \int_{-R_{int}}^{R_{int}} \rho_{grad}(y) 2(\sqrt{R_{int}^2 - y^2}) L_{tank} dy , \quad (5.42)$$

and then using (5.38),

$$\rho_{min} = \frac{3\pi}{2}(\rho_{av} - \rho_m) + 2\rho_m - \rho_{max} . \quad (5.43)$$

5.2.3 Numerical method

To describe the jet centerline trajectory, a forward Euler method is used:

$$\begin{pmatrix} Q(s+ds) \\ \vdots \\ y(s+ds) \end{pmatrix} = \begin{pmatrix} Q(s) \\ \vdots \\ y(s) \end{pmatrix} + \begin{pmatrix} \frac{\partial Q}{\partial s}(s) \\ \vdots \\ \frac{\partial y}{\partial s}(s) \end{pmatrix} ds . \quad (5.44)$$

The second term in the right-hand side of the equation (5.44) is the equation system (5.33). In (5.33), the density gradient ρ_{grad} is required but ρ_{grad} is a consequence of the jet deflection. To solve this problem, the jet centerline trajectory equation is inserted in a loop where the density gradient is taken null initially. Once the first trajectory is calculated, the density at the impact ρ_{max} is deduced and the density gradient is estimated. A new trajectory is calculated etc. This loop lasts until the density at the impact is converged, i.e. $|\rho_{max} - \rho_{max}^{OLD}| < Res$ where ρ_{max}^{OLD} is the previous density at the impact and Res a residual value (in this study 10^{-3} kg/m^3). To optimize the calculation, the spatial step ds used in (5.44) is defined as s_{impact}/N_{point} with a number of points N_{point} (in this study 200). This refines the spatial step ds when the jet is deflected, i.e. when s_{impact} becomes smaller.

5.3 CFD post-process

With the CFD software OpenFOAM, it is possible to implement the post-treatment extracting from the 3D CFD result of the scenario D6Q2 (see section 4.1) data comparable with the buoyant round jet model prediction. The 3D CFD simulations consider only the half the tank (symmetry assumption). In the following content, to ease comprehension, the expressions are made using the full domain geometry. Consequently, multiplication factors will be required on extensive variables, such as volumes and surfaces, when a half domain geometry is used instead.

During the CFD simulations, at a given time, the values ρ_0 and u_0 are averaged value of densities and velocities at the pipe inlet surface. The value ρ_{av} is taken as the average of the density field, weighted by the volume of cells,

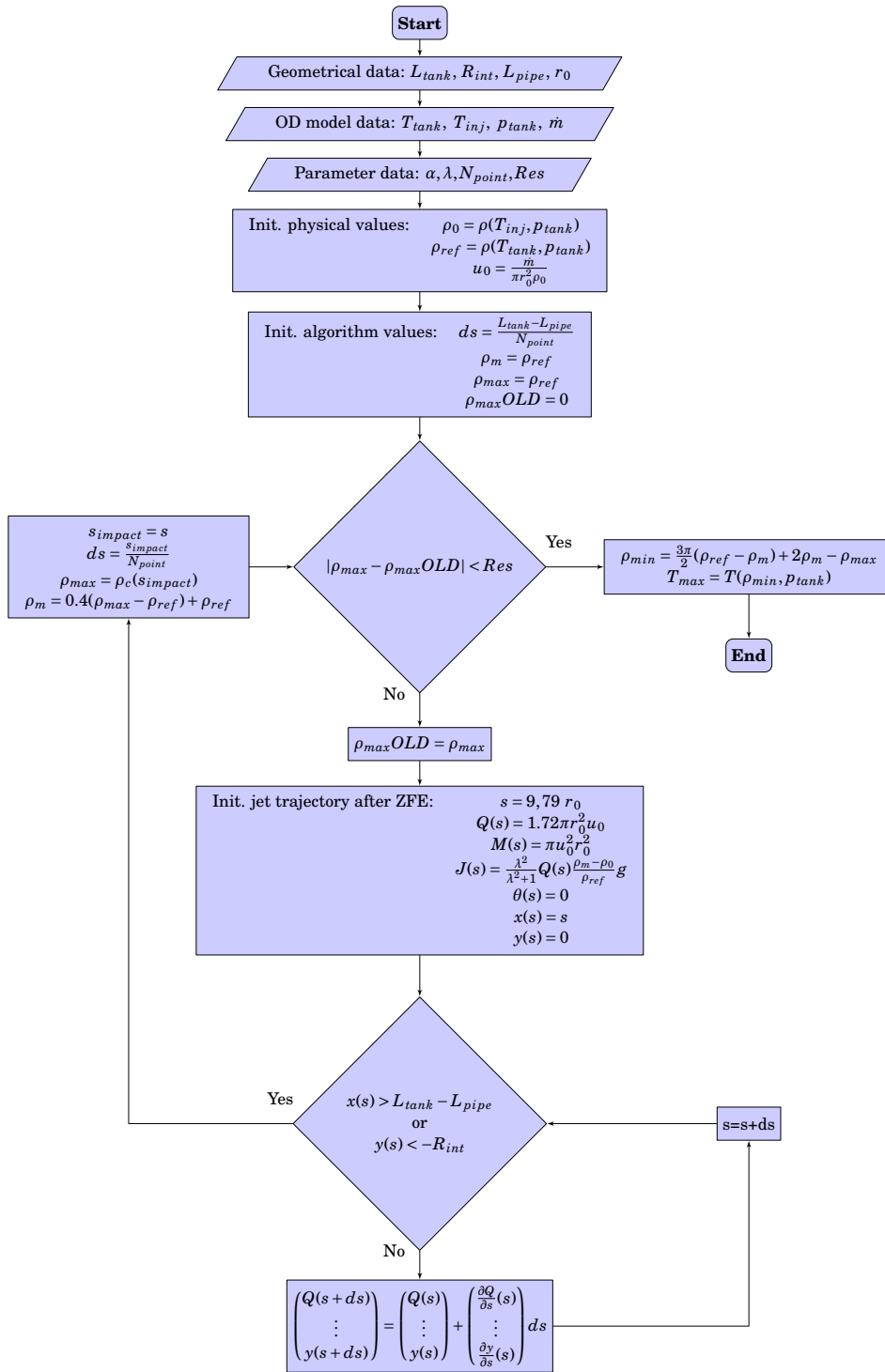


Figure 5.5 – Flowchart of the buoyant round jet model algorithm using as input a OD model and as output the maximum temperature in the tank.

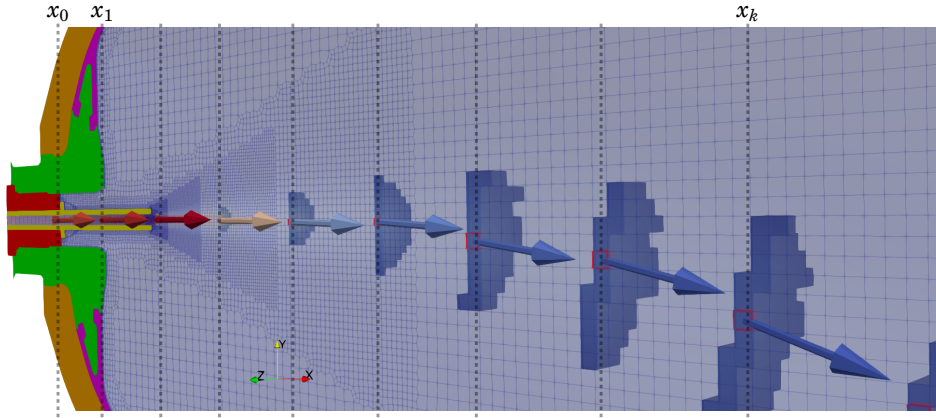


Figure 5.6 – OpenFOAM post-process for the scenario D6Q2. Framed in red the cells in the planes (y,z) where the velocity magnitude is maximum, i.e. $u_c(s)$. For this cell, the velocity direction is represented with a vector. The vector is not proportional to the velocity magnitude to ease visualization. In each normal plane, cells with a velocity $u_i \vec{e}_s$ verifying the criterion $u_i < u_c e^{-1}$ are visible. A limited number of planes (y,z) are represented to ease visualization.

$$\rho_{av} = \frac{\sum_i v_i \rho_i}{V} . \quad (5.45)$$

The jet is round, i.e. circular-symmetric in the orthogonal plane to its centerline trajectory. In this plane, the center of the jet is, by definition, where the velocity magnitude is maximum. The maximum velocity magnitude is assumed to be higher than the velocities in the recirculation region and the jet trajectory is expected to not be too deflected to become a counter flow, i.e.

$$\forall s, |\theta(s)| < \frac{\pi}{2} . \quad (5.46)$$

Figure 5.6 presents vertical lines x_0, x_1, \dots, x_k along the \vec{e}_x axis, corresponding to the normal planes (x,z) . For each normal plane (\vec{e}_y, \vec{e}_z) the cell with the maximum velocity magnitude is selected (reported with a red frame in figure 5.6). The velocity vector $\vec{u}_c(s)$ from these cell centers gives a direction vector \vec{e}_s of the jet centerline:

$$\vec{e}_s = \frac{\vec{u}_c(s)}{u_c(s)} . \quad (5.47)$$

Using the cell positions and the cell velocity vectors, it is possible to obtain the normal planes $(\vec{e}_r, \vec{e}_\phi)$ to the jet centerline. For each normal plane, a surface S issued from the intersection of the plane and the mesh is extracted. This surface is composed of i numbers of local surfaces s_i corresponding to i cells intersected by the plane. For the velocity at the center of the local surface s_i , the component of the velocity carried by \vec{e}_s , called u_i , is selected. Outside the ZFE, the velocity profile is Gaussian and follows the law given in equation (5.14). At $r = b$, the velocity is equal to $u_c(s)e^{-1}$. Using this criterion, surfaces where the velocity u_i is lower than $u_c(s)e^{-1}$ are removed.

For the following, S now designates the surface where the threshold criterion is applied and i designates the number of the local surfaces s_i composing S . To obtain the jet radius b , an equivalent radius is calculated using

$$b = \sqrt{\frac{\sum_i s_i}{\pi}} . \quad (5.48)$$

The mass flux Q is deduced using the mass flux issued from the surface S , called $Q|_S$. Hence, Q and $Q|_S$ are linked:

$$\begin{aligned} Q|_S &= \int_0^{2\pi} \int_0^b u_s r dr d\phi \\ &= \pi u_c b^2 (1 - e^{-1}) \\ &= Q(1 - e^{-1}). \end{aligned} \quad (5.49)$$

In the CFD results, $Q|_S$ is obtained using

$$Q|_S = \sum_i u_i s_i. \quad (5.50)$$

Using equations (5.49) and (5.50), finally

$$Q = \frac{1}{1 - e^{-1}} \sum_i u_i s_i. \quad (5.51)$$

The same process is used for the momentum flux M :

$$M = \frac{1}{1 - e^{-2}} \sum_i u_i^2 s_i. \quad (5.52)$$

J is deduced using the Q and λ ,

$$J = \frac{\lambda^2}{1 + \lambda^2} g_c Q. \quad (5.53)$$

For λ , using the Gaussian profile of the reduced gravity g' , at $r = \lambda b$, the reduced gravity must be equal to $g_c(s)e^{-1}$. Because tank walls are colder than the main fluid bulk, cells at walls can be as cold as cells inside the jet. Consequently, when the criterion $g_c(s)e^{-1}$ is used, cells at walls are selected. If $\lambda = 1.5$, which is a larger value than found in the literature, the round surface with a radius $1.5b$ is where the velocities are below $u_c(s)e^{-(1.5)^2}$. With this second criterion and the first criterion $g_c(s)e^{-1}$, the surface S can be selected without having the cells at walls. The jet radius b is known from (5.48), λ can be deduced:

$$\lambda = \frac{1}{b} \sqrt{\frac{S}{\pi}}. \quad (5.54)$$

Using (5.25), α is calculated:

$$\alpha = \frac{\frac{\partial Q}{\partial s}}{(8\pi M)^{1/2}}, \quad (5.55)$$

with Q , M and s issued from the CFD post-process and the term $\frac{\partial Q}{\partial s}$ numerically calculated.

5.4 Results and discussion

5.4.1 Comparison between the CFD results and the buoyant round jet model results

In this section, for the scenario D6Q2, the CFD results issued from the post-process (5.3) and the buoyant round jet model results (5.2) are compared.

Figures 5.7 and 5.8 compare the CFD results and the buoyant round jet model results at 150 s and at 200 s. This time interval corresponds to the onset of stratification. Figure (5.7,J) shows that no density gradient is present in the gas. Figure (5.8,J) shows that a density gradient is occurring in the gas.

Figure (5.7,A) shows that for the model, the jet is deflected and impacts the right wall of the tank, i.e. $x(s_{impact}) =$

$L_{tank} - L_{injection}$. This impact point is close to the lower wall, i.e. $y(s_{impact}) \approx -R_{int}$. Figure (5.8,A) shows that, for the model, the impact point is at the lower part of the tank, i.e. $y(s_{impact}) = -R_{int}$ and $x(s_{impact}) \approx L_{tank} - L_{injection}$. This is consistent with criterion that the thermal stratification occurs when the jet impacts the lower part of the tank. For the CFD simulation, at 150 s and 200 s, the jet is still oscillating in the tank. This affects its deflection. Hence, at 200 s, the jet is less deflected than at 150 s due to the oscillation. At 150 s and 200 s, it can be noted that the velocity at the inlet is close to 5 m/s (panel A) which is consistent with the observation of Terada [29].

For both 150 s and 200 s, the centerline velocity (panel B) and density (panel C), the jet radius (panel D), the mass flux (panel E), the momentum flux (panel F) and the buoyancy flux (panel G) are correctly predicted by the model. For the momentum flux (panel F), it is possible to recalculate the momentum flux using the centerline velocity $u_c(s)$ and the jet radius $b(s)$ given by the CFD results. If the velocity has a top-hat profile (i.e. uniform), the momentum flux can be calculated as

$$M(s) = \pi u_c(s)^2 b(s)^2 \quad (5.56)$$

and is reported with a marker + in panel F. If the velocity has a Gaussian profile, the momentum flux can be calculated as

$$M(s) = \frac{1}{2} \pi u_c(s)^2 b(s)^2 \quad (5.57)$$

and is reported with a marker x in panel F. It can be seen that the momentum flux value at the pipe inlet ($s = -L_{pipe}$) calculated with 5.56 is close to the momentum flux value after the ZFE ($s = L_{ZFE}$) calculated with 5.57. This confirms that the velocity profile is changing from top-hat in the pipe to Gaussian after the ZFE while the momentum flux stays constant. In panel H, it can be seen that a constant value $\alpha = 0.055$ of the entrainment rate is consistent with the CFD results. In panel J, it can be seen that a constant value $\lambda = 1$ of the Gaussian variance is more consistent with the CFD results at the pipe outlet than closer to the impact point.

Figures 5.9, 5.10 and 5.11 compare the CFD results and the buoyant round jet model results for the times 350 s, 450 s and 550 s, after the onset of stratification. For figures 5.9, 5.10 and 5.11, it can be seen that the jet deflection predicted by the model is more important than the one from the CFD results (panel A). In panel I, it can be seen that the Gaussian variance is close to 1 at $s = L_{ZFE}$ but is rising after. The presence of a density gradient might jeopardize the method to extract λ described in section 5.3. Consequently, values given by the CFD post-process are probably a coarse estimation. When similar values of λ are used in the model (e.g. $\lambda = 2$), the jet trajectory is more distant from the CFD results. Also, $\lambda = 2$ superior than all values given in the literature.

For the panels B, C, D, E, F, and H, the results given by the CFD and the model are close exempt near the impact point. The presence of the wall disturbs the jet trajectory.

5.4.2 Influence of the physical parameters α , λ and ρ_{grad} on the modeling

The numerical parameters N_{point} and Res are set to get a converged solution ($N_{point} = 200$ and $Res = 10^{-3} \text{ kg/m}^3$). As previously stated, the two closure parameters α and λ are chosen to give the closest agreement with the CFD calculations ($\alpha = 0.055$ and $\lambda = 1$). They are chosen to stay consistent with values found in the literature (e.g. [126]). The buoyant round jet is transitioning between a pure-jet behavior (at the pipe outlet) towards a pure-plume behavior (hypothetically, far from the outlet). The entrainment rate would vary likewise from a pure-jet entrainment rate ($\alpha = 0.055$ [121]) towards a pure-plume entrainment rate ($\alpha = 0.083$ [121]). Figure 5.12 shows that the consequence of a larger entrainment rate on the jet trajectory is a larger deflection. This discards the model trajectory prediction from the CFD results. With a larger entrainment rate, the jet centerline velocity and density get distant from the CFD results.

Using the larger value $\lambda = 1.2$ (suggested in [121]) instead of $\lambda = 1$, figure 5.13 shows that the consequence on the jet

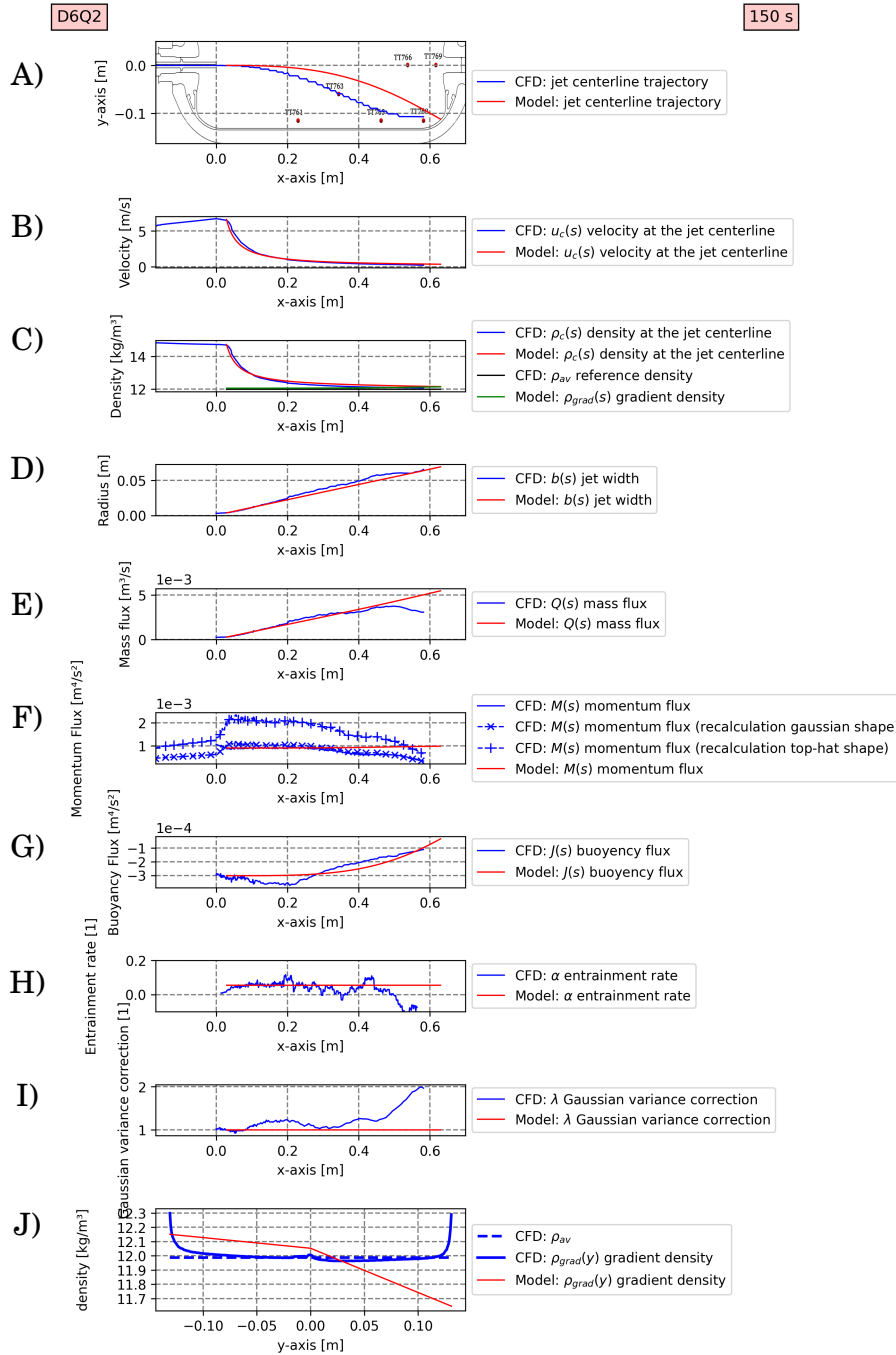


Figure 5.7 – For the scenario D6Q2. For the time 150 s. Results from the buoyant round jet model are reported in red, results from the CFD simulation are reported in blue. As a function of x : A) trajectory of the jet centerline, B) centerline velocity, C) centerline density, D) jet radius, E) mass flux, F) momentum flux, G) buoyancy flux, H) entrainment rate, I) Gaussian variance correction. Panel J) concerns the density gradient as a function of y .

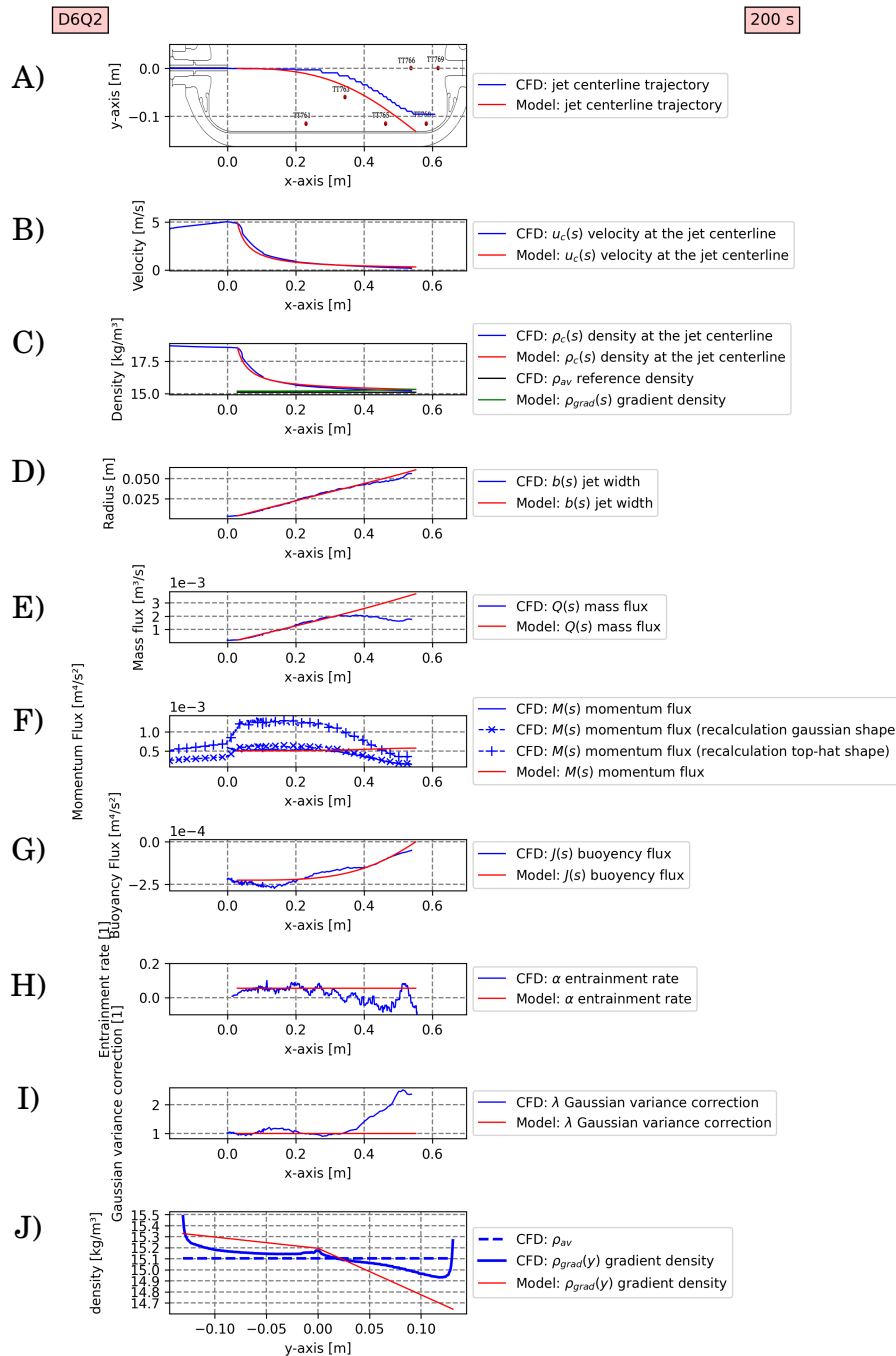


Figure 5.8 – For the scenario D6Q2. For the time 200 s. Results from the buoyant round jet model are reported in red, results from the CFD simulation are reported in blue. As a function of x : A) centerline position, B) centerline velocity, C) centerline density, D) jet radius, E) mass flux, F) momentum flux, G) buoyancy flux, H) entrainment rate, I) Gaussian variance correction. Panel J) concerns the density gradient as a function of y .

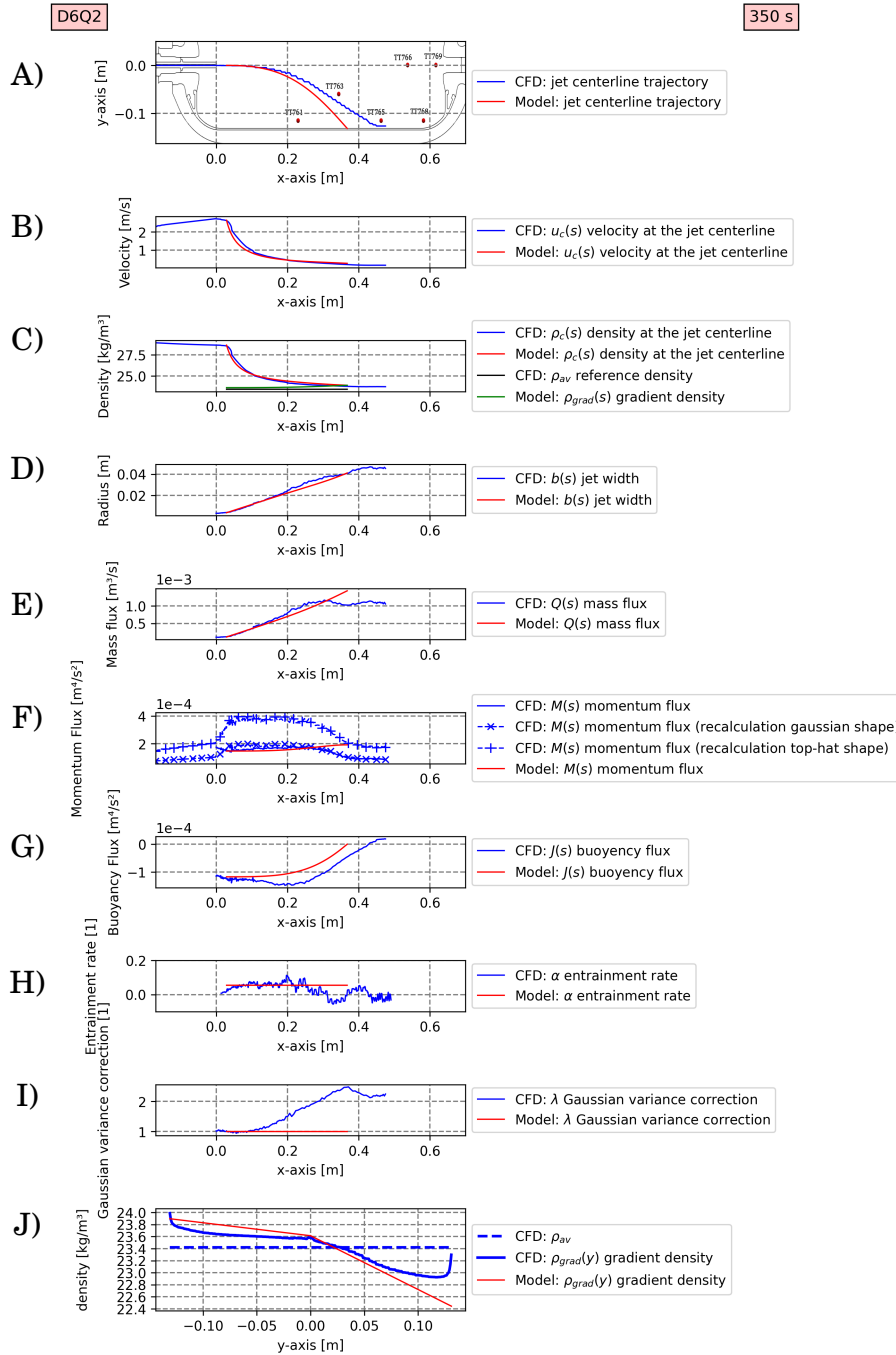


Figure 5.9 – For the scenario D6Q2. For the time 350 s. Results from the buoyant round jet model are reported in red, results from the CFD simulation are reported in blue. As a function of x : A) centerline position, B) centerline velocity, C) centerline density, D) jet radius, E) mass flux, F) momentum flux, G) buoyancy flux, H) entrainment rate, I) Gaussian variance correction. Panel J) concerns the density gradient as a function of y .

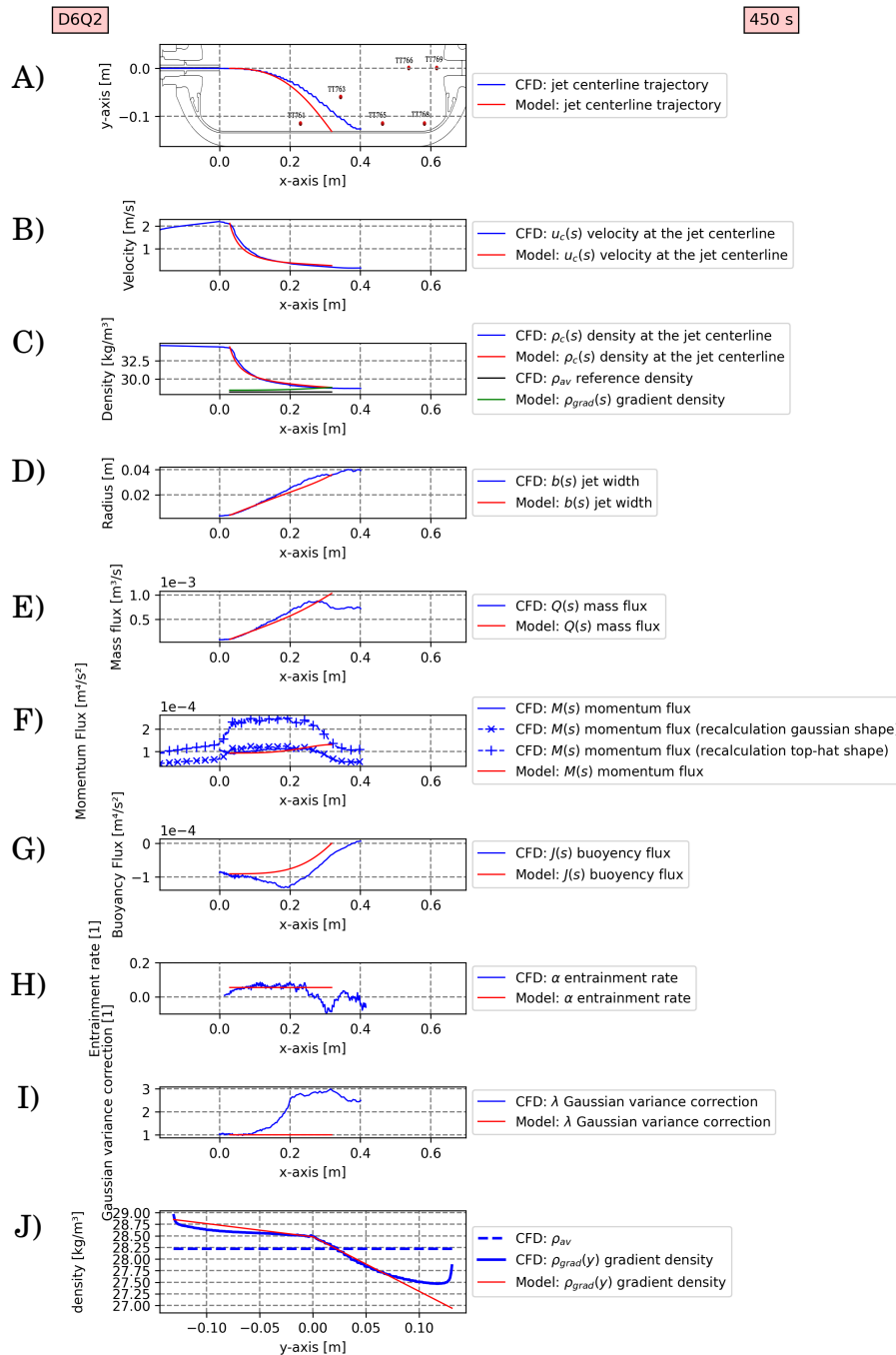


Figure 5.10 – For the scenario D6Q2. For the time 450 s. Results from the buoyant round jet model are reported in red, results from the CFD simulation are reported in blue. As a function of x : A) centerline position, B) centerline velocity, C) centerline density, D) jet radius, E) mass flux, F) momentum flux, G) buoyancy flux, H) entrainment rate, I) Gaussian variance correction. Panel J) concerns the density gradient as a function of y .

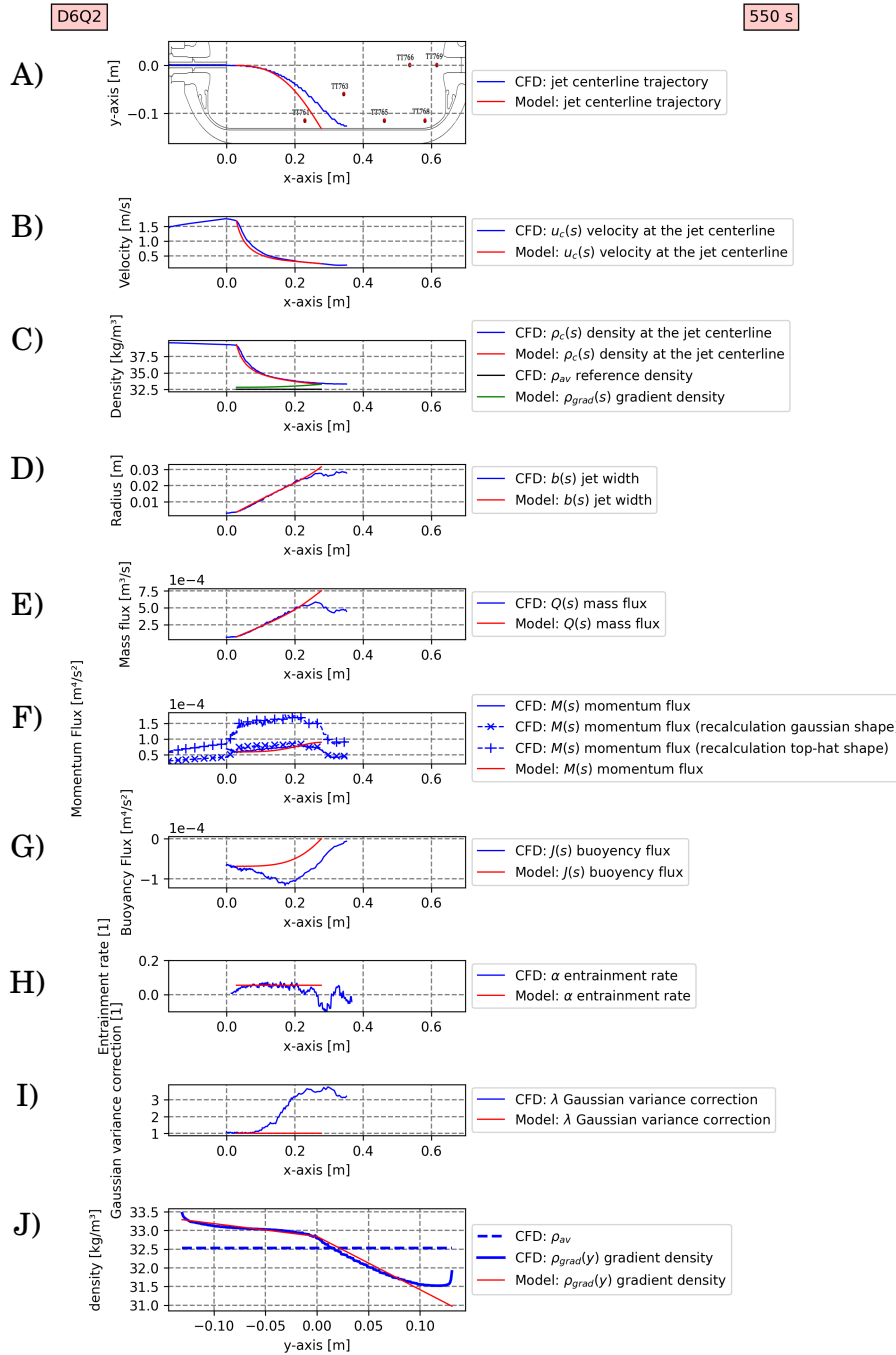


Figure 5.11 – For the scenario D6Q2. For the time 550 s. Results from the buoyant round jet model are reported in red, results from the CFD simulation are reported in blue. As a function of x : A) centerline position, B) centerline velocity, C) centerline density, D) jet radius, E) mass flux, F) momentum flux, G) buoyancy flux, H) entrainment rate, I) Gaussian variance correction. Panel J) concerns the density gradient as a function of y .

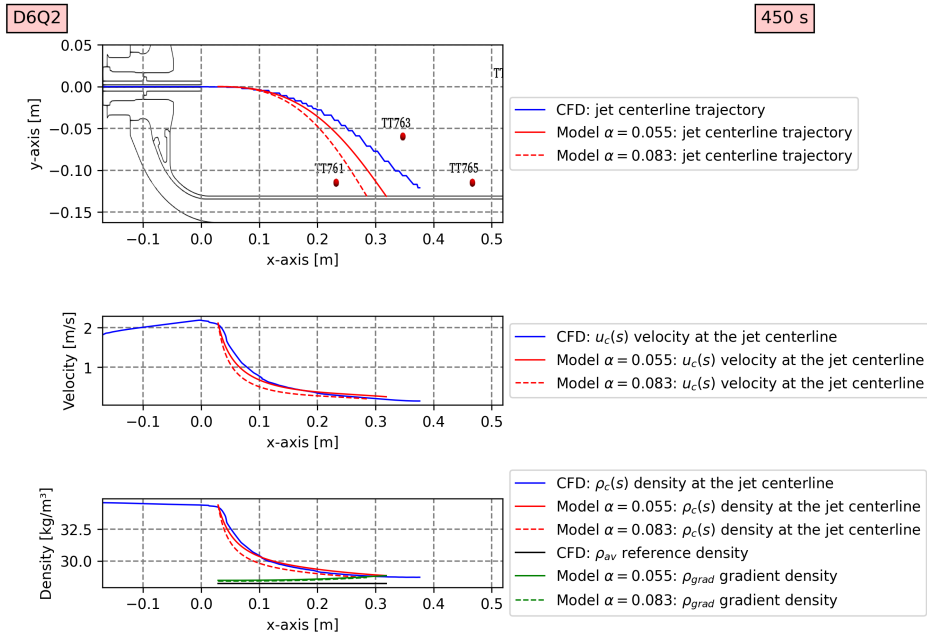


Figure 5.12 – For the scenario D6Q2. For the time 450 s. Influence of the entrainment rate on the jet centerline trajectory and on the centerline velocity and density. In blue results from CFD, in red (solid line) results from the round buoyant jet with the reference entrainment rate and (dashed line) with a larger entrainment rate.

trajectory is also a larger deflection compared to the CFD results. The effect of λ for the range [1,1.2] appears negligible on the jet centerline velocity and density.

Figure 5.14 compares the jet trajectory for a case with a linear-stratified environment and a case with a uniform environment (i.e. $\rho_{grad} = \rho_{av}$). It can be seen that the case with no stratification is more deflected. This result was predictable. With a linear-stratified environment, $\rho_{grad}(-R) = \rho_c(s_{impact})$, when the jet is close to the lower liner wall, $g_c(s) \approx 0 \text{ m/s}^2$, (see (5.15) and (5.16)), i.e. $J(s) \approx 0 \text{ m}^4/\text{s}^2$ (see (5.19)). Then, the jet is less deflected when it gets closer to the lower liner wall. The effect of the linear-stratified environment on the jet centerline velocity and density appears negligible.

5.4.3 Comparison between the experimental data and the buoyant round jet model results

Figure 5.15 presents the results of the buoyant round jet model for the 6 filling scenarios of the type IV 37 L tank from the experimental campaign HyTransfer [41]. Measured temperatures are reported in black. Temperatures from the buoyant round jet model are reported in red. The ratio $\frac{-y(s_{impact})}{R_{int}}$ is reported in blue. When the ratio equals 1, it means the jet impacts the lower part of the tank. Figure 5.15 shows that $\frac{-y(s_{impact})}{R_{int}} = 1$ corresponds to the onset of stratification. With the buoyant jet model, it can be predicted that no thermal stratification occurs for the scenarios D3Q8, D3Q2 and D6Q8 and stratification occurs for the scenarios D6Q2, D10Q8 and D10Q2.

When $\frac{-y(s_{impact})}{R_{int}} < 1$, the statement $\rho_{max} = \rho_c(s_{impact})$ is not valid for this situation. Then the minimum temperature, i.e. the maximum gradient density, estimated by the model is colder than the measured one.

Then, when $\frac{-y(s_{impact})}{R_{int}} = 1$, the maximum temperature, i.e. the minimum gradient density, estimated by the model depends largely to the gradient density profile (5.38) and the evaluation of the median density (5.40). However, (5.38) and

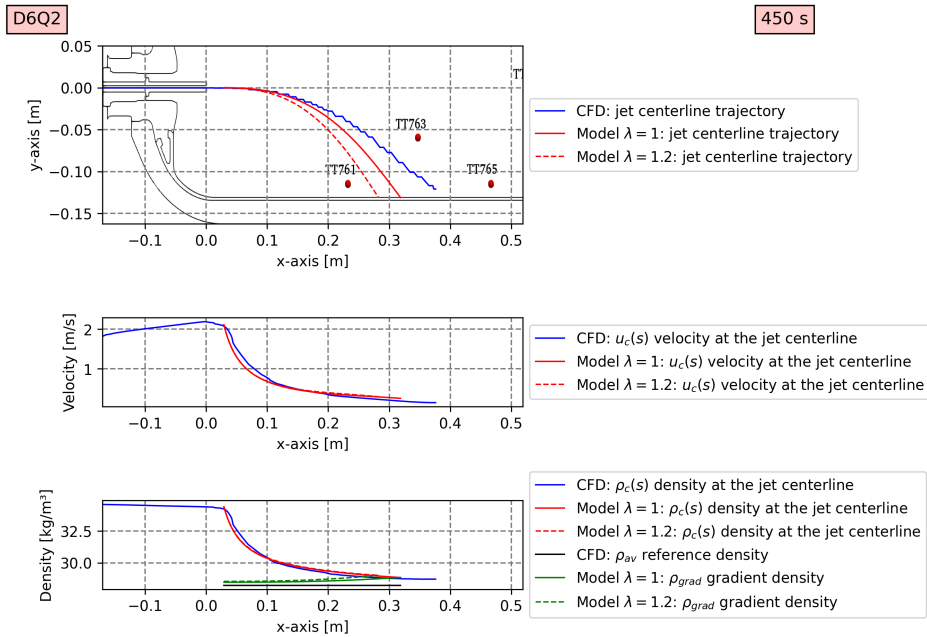


Figure 5.13 – For the scenario D6Q2. For the time 450 s. Influence of the Gaussian variance of the density profile on the jet centerline trajectory and on the centerline velocity and density. In blue results from CFD, in red (solid line) results from the round buoyant jet with the reference Gaussian variance of the density profile and (dashed line) with a larger Gaussian variance of the density profile.

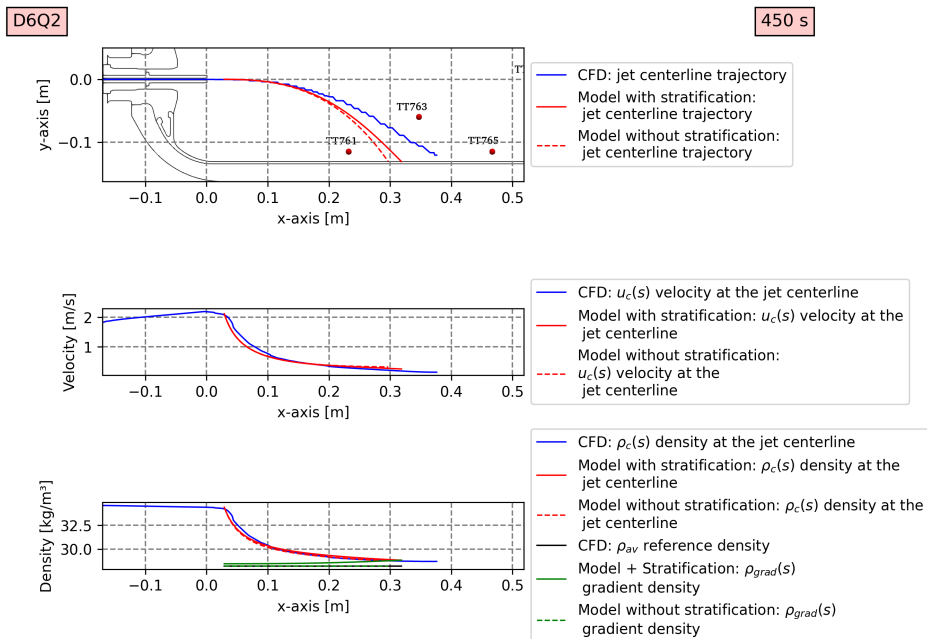


Figure 5.14 – For the scenario D6Q2. For the time 450 s. Influence of the exterior environment on the jet centerline trajectory and on the centerline velocity and density. In blue results from CFD, in red (solid line) results from the round buoyant jet with a linear-stratified environment and (dashed line) with a uniform environment.

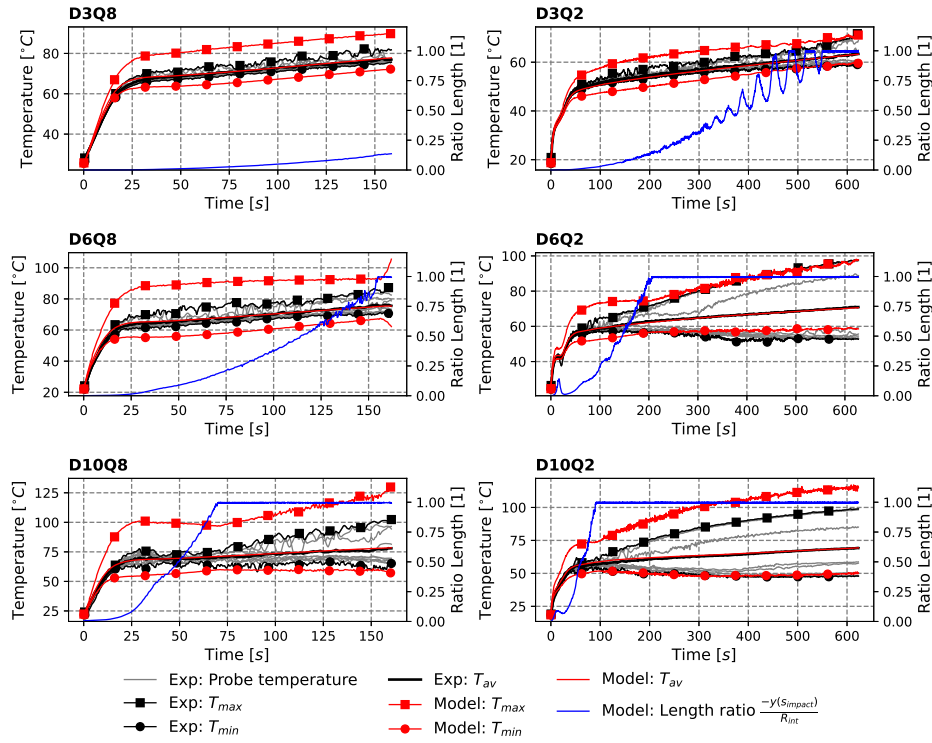


Figure 5.15 – The 6 different panels correspond to 6 filling scenarios of the type IV 37 L tank from the experimental campaign HyTransfer [41]. The minimum (circle marker) and maximum (square marker) temperatures given in red are issued from the buoyant round jet model. The averaged temperature given in red is issued from SOFIL. The minimum (circle marker) and maximum (square marker) temperatures given in black are issued from the minimum and maximum temperatures from the probes. The averaged temperature from probes is (5.3) given in black. The other probe temperatures are reported in grey to show that the vertical thermal gradient is present in the tank.

(5.40) are designed using CFD results from the scenario D6Q2. Hence, the maximum temperature issued from the model for the scenario D6Q2 is in good agreement with the maximum temperature measured while for the scenarios D10Q2 and D10Q8, the maximum temperature is largely overestimated. With a different median density law, it is possible to largely improve the prediction of the scenarios D10Q2 and D10Q8 but to the detriment of the scenario D6Q2.

For the scenarios D10Q2 and D10Q8, the median density is closer to the averaged density than for the scenario D6Q2. To suggest a direction for further research on the evaluation of the median density, the competition between the thermal diffusion and the jet deflection and natural convection could be investigated. Hence, the thermal diffusion tends to stabilize the symmetry of the thermal field ($\rho_m \rightarrow \rho_{av}$). The cold gas injected tends to break the symmetry of the thermal field. The natural convection due to the colder walls would also disturb the thermal field.

5.4.4 Discussion on the 5 m/s

In the literature [29], for a type IV 65 L tank, a criterion on the velocity of the injected gas has been suggested, 5 m/s, to maintain the thermal mixing, i.e. to avoid the vertical thermal stratification. This criterion has been confirmed on the type IV 37 L tank during the experimental campaign HyTransfer [31, 41]. Figure 5.16 shows that using the buoyant round jet model, the jet is impacting the lower liner wall when the inlet velocity is close to 5 m/s, in agreement with [29].

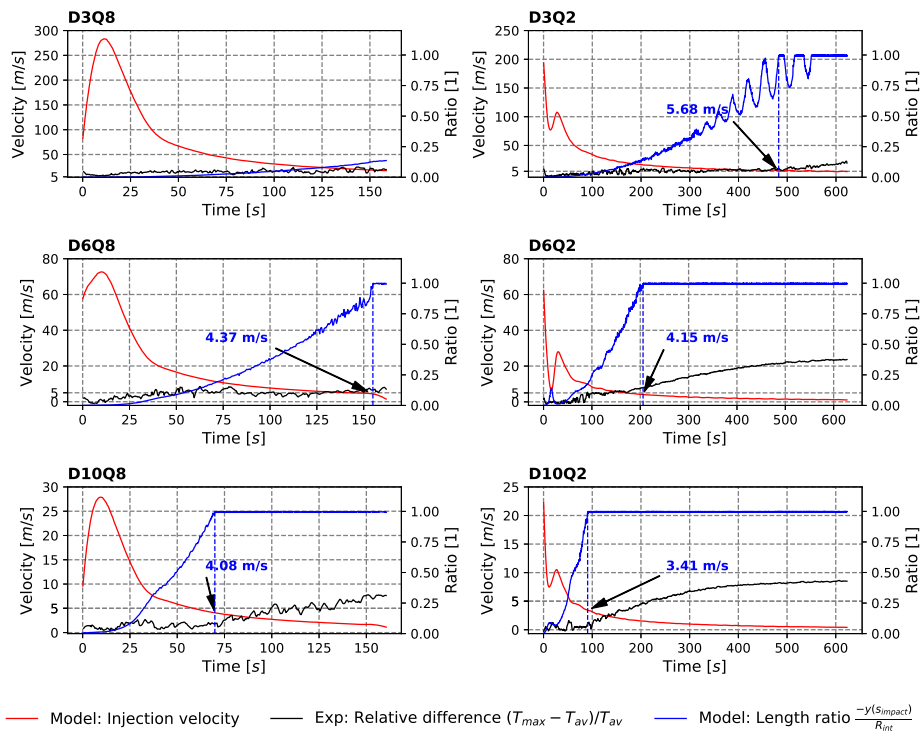


Figure 5.16 – The 6 different panels correspond to 6 filling scenarios of the type IV 37 L tank from the experimental campaign HyTransfer [41]. The inlet velocity is given in red and is indicated on the left y-axis. Length ratio of the jet deflection from the x-axis y_{max} over the tank inner radius R_{int} is given in blue and is indicated on the right y-axis. The velocity corresponding to the first velocity when $y_{max} = R_{int}$ is reported in blue on the graph. The temperature ratio $\frac{T_{max} - T_{av}}{T_{av}}$ is given in black and is indicated on the right y-axis.

The buoyant round jet model does not have an analytical solution to its equation system (5.33) allowing to link the inlet velocity with the impact coordinate. To suggest a simpler criterion able to detect the onset of stratification without computing the full jet trajectory, simplifications of the equation system (5.33) are suggested. At the onset of stratification, the density gradient is assumed negligible, i.e. $\forall s, J(s) = J(L_{ZFE})$. The angle θ is assumed small enough to linearize the cosine and sine functions:

$$\cos(\theta) \approx 1, \quad (5.58)$$

$$\sin(\theta) \approx \theta. \quad (5.59)$$

The momentum flux is assumed constant, i.e. $\forall s, M(s) = M(L_{ZFE})$. The value of λ and α are taken as 1 and 0.055. The equation system (5.33) becomes:

$$\frac{\partial Q}{\partial s} = 0.055(8\pi M(L_{ZFE}))^{1/2} \quad (5.60)$$

$$\frac{\partial \theta}{\partial s} = \frac{J(L_{ZFE})Q}{M(L_{ZFE})^2} \quad (5.61)$$

$$\frac{\partial x}{\partial s} = 1 \quad (5.62)$$

$$\frac{\partial y}{\partial s} = \theta. \quad (5.63)$$

Then, (5.60) can be integrated using (5.62),

$$Q = 0.055 \left(8\pi M(L_{ZFE})^{1/2} \right) (x - 9.79r_0) + Q(L_{ZFE}), \quad (5.64)$$

followed by (5.61),

$$\theta = 0.055 \frac{J(L_{ZFE})}{M(L_{ZFE})^{1.5}} (2\pi)^{1/2} (x - 9.79r_0)^2 + \frac{J(L_{ZFE})Q(L_{ZFE})}{M(L_{ZFE})^2} (x - 9.79r_0), \quad (5.65)$$

and finally (5.63),

$$y = 0.055 \frac{J(L_{ZFE})}{M(L_{ZFE})^{1.5}} \frac{(2\pi)^{1/2}}{3} (x - 9.79r_0)^3 + \frac{J(L_{ZFE})Q(L_{ZFE})}{2M(L_{ZFE})^2} (x - 9.79r_0)^2. \quad (5.66)$$

At the first impact point, $y = -R_{int}$ and $x = L_{tank} - L_{pipe}$. To ease reading, \tilde{L} is defined as:

$$\tilde{L} = L_{tank} - L_{pipe} - 9.79r_0. \quad (5.67)$$

The equation (5.66) can be rewritten:

$$-R_{int} = 0.055 \frac{J(L_{ZFE})}{M(L_{ZFE})^{1.5}} \frac{(2\pi)^{1/2}}{3} \tilde{L}^3 + \frac{J(L_{ZFE})Q(L_{ZFE})}{2M(L_{ZFE})^2} \tilde{L}^2. \quad (5.68)$$

Finally, using the local variables u_0 , r_0 and gc_0 , (5.68) can be rewritten:

$$\frac{R_{int}}{\tilde{L}^2} = \frac{-gc_0}{u_0^2} \left(\frac{0.0946\sqrt{2}}{6} \frac{\tilde{L}}{r_0} + \frac{1.72^2}{4} \right). \quad (5.69)$$

This allows to define a Richardson number Ri , where, when $Ri = 1$, the jet impacts the lower part of the tank and the

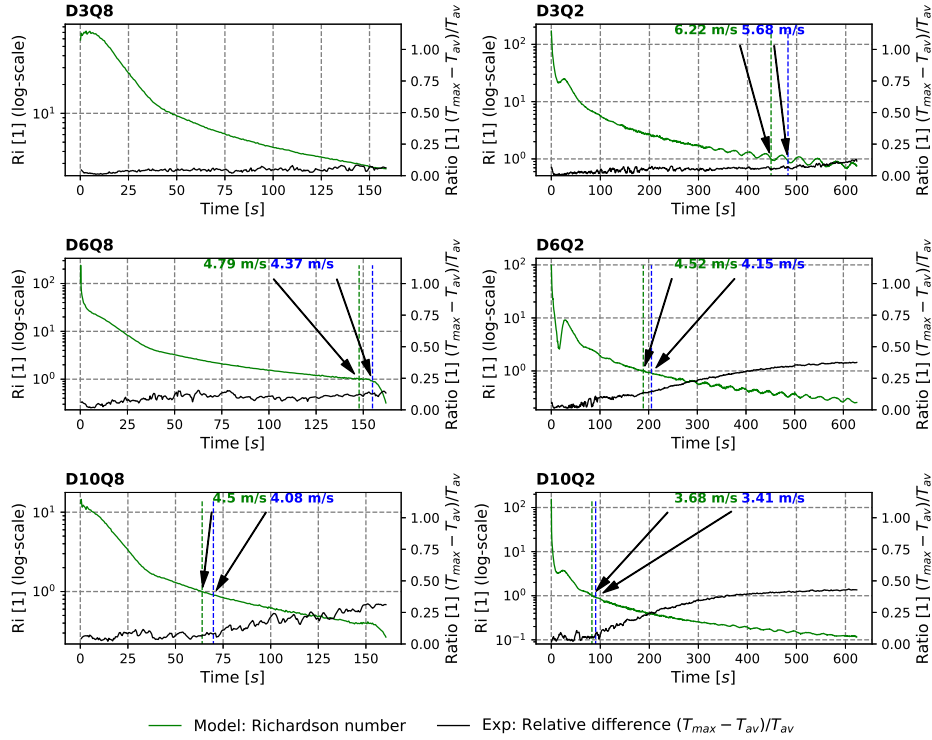


Figure 5.17 – The 6 different panels correspond to 6 filling scenarios from the experimental campaign HyTransfer [41] on the type IV 37 L tank. The Richardson number, defined in (5.71), is given in green and is indicated on the left y-axis. It is reported in a log-scale to ease reading. The temperature ratio $\frac{T_{max} - T_{av}}{T_{av}}$ is given in black and is indicated on the right y-axis. The inlet velocity corresponding to the first $Ri = 1$ is reported in green on the graph. The velocity corresponding to the first velocity when $-y_{s_{impact}} = R_{int}$ obtained with the buoyant round jet model is reported in blue on the graph.

thermal stratification occurs:

$$Ri = \frac{\frac{\rho_0 - \rho_{ref}}{\rho_{ref}} g \tilde{L}^2}{u_0^2} \frac{\tilde{L}^2}{R_{int}} (0.022 \frac{\tilde{L}}{r_0} + 0.74). \quad (5.70)$$

Figure 5.17 presents, for each scenario, the inlet velocity corresponding to $Ri = 1$ displayed in green, jointly with the inlet velocity corresponding to $-y_{s_{impact}} = R_{int}$ obtained with the buoyant round jet model. The two values are close and correspond to the onset of the thermal stratification.

When $Ri = 1$, a critic inlet velocity u_{critic} [m/s] can be defined:

$$u_{critic} = \sqrt{\frac{\rho_0 - \rho_{ref}}{\rho_{ref}} g \frac{\tilde{L}^2}{R_{int}} (0.022 \frac{\tilde{L}}{r_0} + 0.74)}. \quad (5.71)$$

If the inlet velocity goes below this critic inlet velocity, thermal gradients occur.

For the type IV 65 L tank in the Terada study [29], the critic velocity can be estimated. It is mentioned that $R_{int} = 0.2$ m and $L_{tank} = 0.832$ m. The term $\frac{\rho_0 - \rho_{ref}}{\rho_{ref}}$ is evaluated at the end of the filling: the final pressure is 350 bar, the injected is temperature 10 °C and the averaged temperature is approximately 70 °C; then $\rho_0 = 24.35$ kg/m³ and $\rho_{ref} = 20.69$ kg/m³. The pipe diameter chosen is the 10 mm diameter. There is no mention of an injector pipe, then

$$\tilde{L} = L_{tank} - 9.79r_0 = 0.783 \text{ m.}$$

For this pipe diameter, Terada observed that the thermal gradients occur when the inlet velocity is approximately 5 m/s. After calculation, $u_{critic} = 4.72 \text{ m/s}$ which is consistent with this observation.

Conclusion

To summarize, despite the bounded nature of the flow dynamics, the buoyant round jet theory is able to produce results in agreement with the flow dynamics from the CFD approach. For the 6 filling scenarios considered, it allows to predict the onset of stratification using only data provided by a 0D model (in this study SOFIL). The calculation time of this model is a couple of seconds compared with a complete 3D CFD simulation requiring months on a HPC station. The prediction of the maximum temperature in the gas remains a point to improve. For now, the method estimating the maximum temperature in the gas is too dependent on the density gradient law which may vary with the tank geometry and injector length within the tank. A Richardson number equal to 1 at the onset of the thermal stratification is defined for horizontal axially filled tanks. Maintaining this Richardson number below 1 could be a criterion for future filling protocol to avoid a thermal stratification. It can be noted that the buoyant round jet model and the Richardson number are not specific for hydrogen and could be used for tank filled with other gases.

Chapter 6

Complementary studies

Introduction

Complementary studies have been carried out during this thesis. After noticing the flapping of the jet in the tank for 3D CFD simulations (3.1), additional studies have been done to better understand the impact of the symmetry assumption on the jet freedom (6.1) and analysis the oscillation frequency of the jet (6.2).

In chapter 3, the importance of performing 3D CFD simulations instead of 2D-axisymmetric CFD simulations to capture the physic has been highlighted. The motivation to reduce the numerical resources and time required to carry out the 3D CFD simulations leads to design a new method to predict only the thermal state at the end of the filling(6.3). In connection with long-duration 3D simulations, a first part of 3D CFD simulation of the emptying of a hydrogen tank has been carried out (6.4).

In the purpose of improving the knowledge of the thermal state for experimental cases, a method has been developed to estimate the temperatures at the interface between the gas and the liner from temperatures measured at the interface between the liner and the composite (6.5).

6.1 Full 3D CFD simulation of scenario D3Q8

During the filling of a tank with gaseous hydrogen, the injected gas creates a jet inside the main fluid bulk. In chapter 3, it has been highlighted that the inner jet flaps in the symmetry plane (x,y). This is supposed to be a consequence of the symmetry assumption used during the CFD simulation of the scenario D3Q8, i.e. the homogeneous case. This assumption is examined in this section. A 3D CFD case without symmetry assumption is performed, i.e. a simulation on the complete geometrical domain. Due to the important numerical resources required to carry out a full 3D CFD simulation, the simulation has been terminated after 20 s, for a 160 s filling time. The numerical parameters are the same as those chosen for the 3D CFD simulation performed on half of the domain for the scenario D3Q8. In this section, the 3D CFD case without symmetry assumption is referred to as the **full 3D** CFD case and the 3D CFD case on half of the domain is referred to as the **3D** CFD case.

The full 3D CFD case gives more freedom to the inner jet. The jet can flap in any direction. Figures 6.1 and 6.2 show snapshots of the velocity field in the planes (x,y) and (x,z). As a reminder, the gravity is aligned with the y-axis. The jet centerline, defined in chapter 5, is reported in red. Three planes (y,z) at $x = -0.2\text{ m}$, $x = 0\text{ m}$ and $x = 0.2\text{ m}$ show the jet in cross-section planes of the tank. At $t = 1\text{ s}$, the jet is not destabilized yet and stays on the x-axis. At $t = 5\text{ s}$, the jet

starts being destabilized. This phenomenon appears at a similar time for the 3D CFD case. The destabilization occurs simultaneously in the planes (x,y) and (x,z). At $t = 7$ s, the jet is fully destabilized and flaps. During the 20 s simulated, the jet does not flap in a particular plane, i.e. its trajectories are not contained in one plane. For example at $t = 10$ s the jet is in the plane (x,y) and at $t = 15$ s the jet is in the plane (x,z). At $t = 20$ s the jet is both in between.

With the increase of temperatures in the main gas bulk and the pre-cooling of the injected gas, the buoyancy force is expected to impose the gravity direction as a privileged direction. It was expected that the plane (x,y) would become the plane containing the jet. The full 3D CFD case fluid dynamics is thus expected to tend towards the 3D CFD case dynamics. This phenomenon was not observed after 20 s and a longer period would be necessary to confirm this prediction.

The full 3D CFD case has a different dynamics compared to the 3D CFD case, due to the additional freedom given to the jet. The impact on the thermal field is be estimated hereafter. The 2D-axisymmetric CFD case is also included. For the 2D-axisymmetric CFD case, the jet does not flap and the gravity is not considered. For the averaged gas temperature, see figure 6.3, the difference is marginal. After 20 s, only 0.34 °C of difference on the averaged gas temperature is noted between the full 3D and the 3D CFD cases. Between the full 3D and the 2D-axisymmetric CFD cases, the difference is -2.38 °C .

The effect of the symmetry assumption on temperature distribution in the gas can be investigated using the standard deviation around the averaged gas temperature:

$$\sigma_{T_{av}} = \sqrt{\frac{\sum_i (T_i - T_{av})^2 v_i}{\sum_i v_i}} \quad \text{with} \quad T_{av} = \frac{\sum_i T_i v_i}{\sum_i v_i} . \quad (6.1)$$

It can be considered as an indicator of the thermal mixing in the tank. A large value of $\sigma_{T_{av}}$ indicates a heterogeneous thermal field. Reciprocally, if the thermal field is uniform, $\sigma_{T_{av}} = 0$ °C. The standard deviation for the full 3D, 3D and 2D-axisymmetric CFD cases (scenario D3Q8) are displayed in figure 6.4. It can be seen that the 3D CFD case and the full 3D CFD case exhibit close standard deviations. The 2D-axisymmetric CFD case has a larger standard deviation than the 3D CFD cases. This suggests that the thermal state of the full 3D CFD case and the 3D CFD case are similar.

Conclusion

To summarize, the full 3D CFD case has showed that the fluid dynamics predicted is less constrained than for 3D CFD case. However, this does not seem to play an important role in the temperature field. The averaged gas temperature and the temperature distribution predicted by the CFD simulation are not significantly altered by the symmetry assumption. As it reduces the numerical cost, the symmetry assumption is overall beneficial for this CFD application.

6.2 Jet oscillation frequency

As mentioned in chapter 3, for the scenario D3Q8, the inner jet flow oscillates inside the tank during the filling. A preliminary study is performed in this section to investigate the frequency of jet oscillation. For this purpose, the selected marker of the flapping is the centerline of the jet, defined in chapter 5. A point located on the jet centerline is described by its coordinates (x, y). For this study, 8 points on the jet centerline uniformly distributed along the x-axis are considered. Figure 6.5 shows the location of the points at $t = 100$ s.

Figure 6.6 presents, for the 8 points considered, their ordinate y as a function of time. The value $y(t)$ is considered to measure the magnitude of the oscillation. It can be seen that the jet is flapping with different magnitudes along the x-axis. The coarse resolution of the mesh is responsible for the staircase aspect of the curves (if the magnitude $y(t)$ is lower than a cell size, the CFD cannot detect the variation).

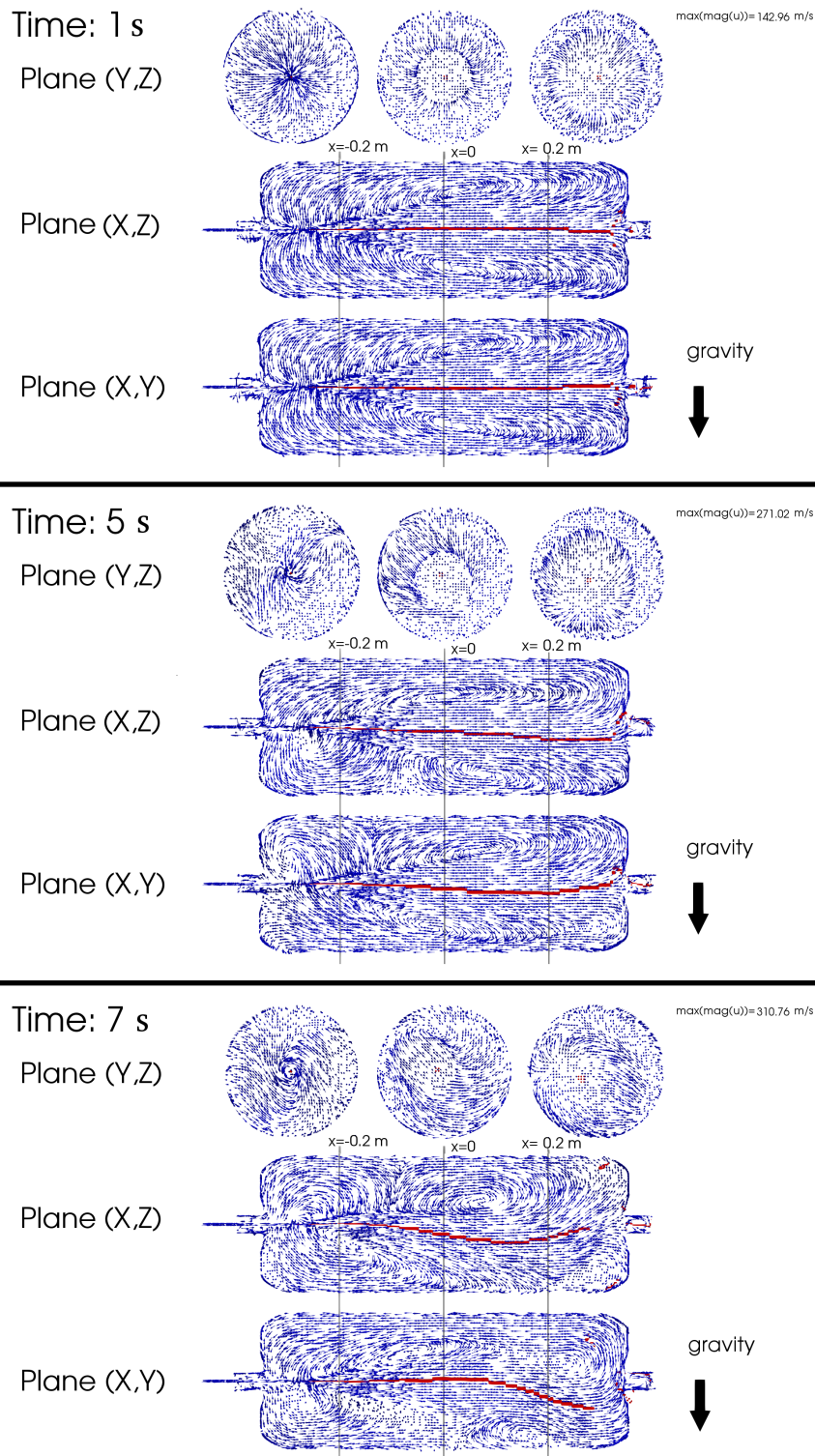


Figure 6.1 – Scenario D3Q8. The vector field displayed presents the direction of the velocities of the gas. The vector field is not scaled with the velocity magnitude to ease visualization. The centerline of the jet is reported in red. The three panels concern times $t = 1 \text{ s}$, $t = 5 \text{ s}$ and $t = 7 \text{ s}$.

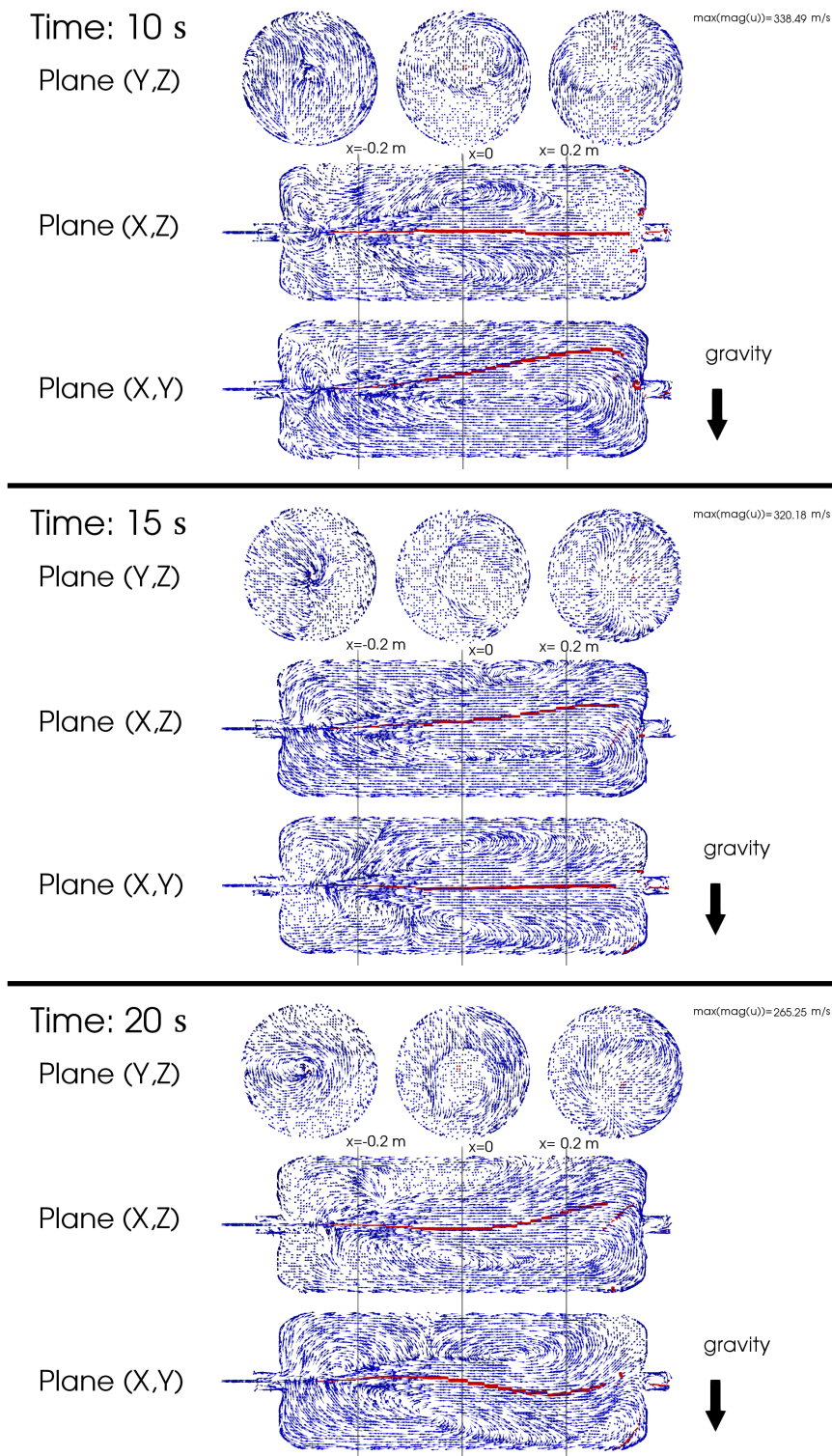


Figure 6.2 – Scenario D3Q8, full 3D case. The vector field displayed presents the direction of the velocities of the gas. The vector field is not scaled with the velocity magnitude to ease visualization. The centerline of the jet is reported in red. The three panels concern times $t = 10 \text{ s}$, $t = 15 \text{ s}$ and $t = 20 \text{ s}$.

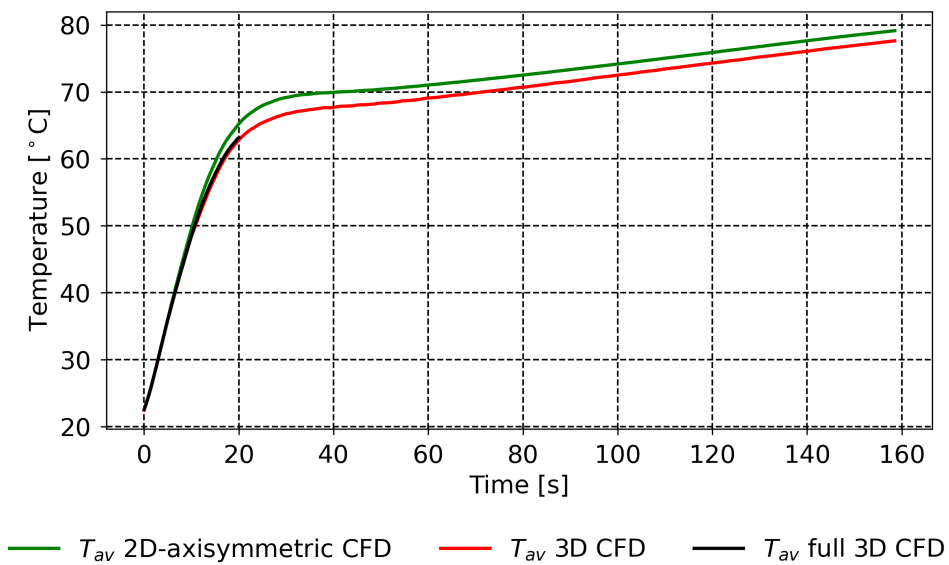


Figure 6.3 – Scenario D3Q8, full 3D case. Averaged gas temperature as a function of time for the full 3D (black), 3D (red) and 2D-axisymmetric CFD cases (green).

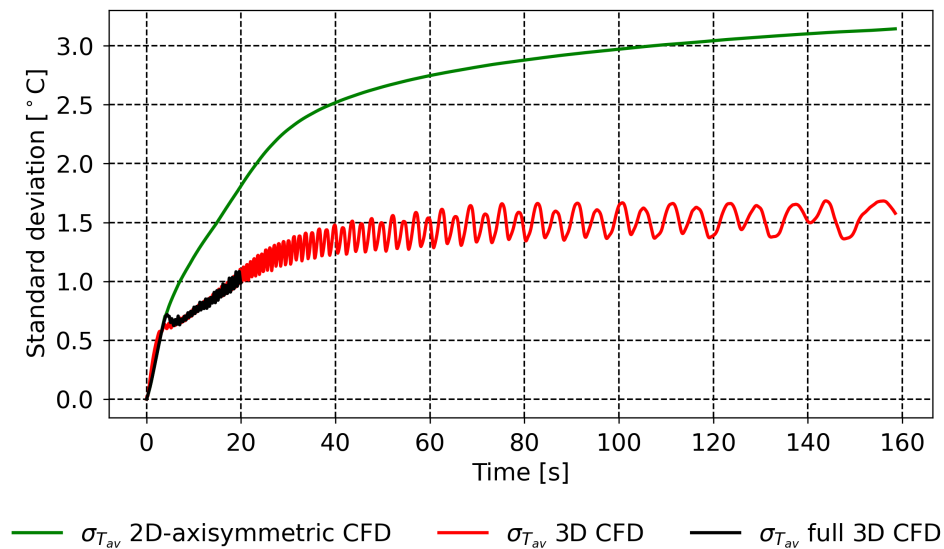


Figure 6.4 – Scenario D3Q8. The standard deviation around the averaged gas temperature as a function of time for the full 3D CFD case (in black), the 3D CFD case (in red) and the 2D-axisymmetric CFD case (in green).

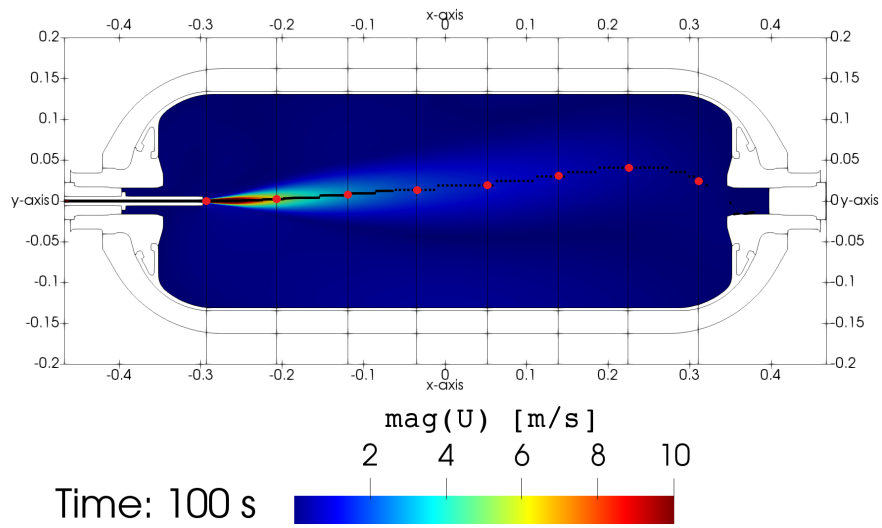


Figure 6.5 – Scenario D3Q8. Eight points on the jet centerline are uniformly distributed along the x-axis (red dots). The jet centerline trajectory is indicated in black.

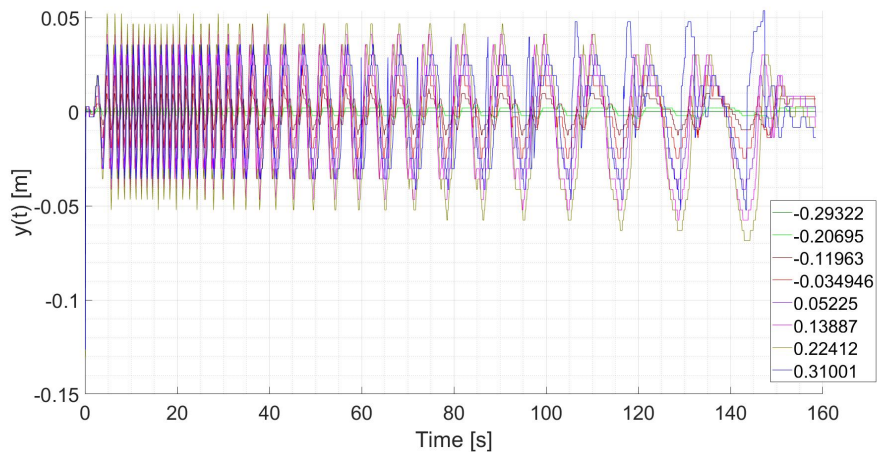


Figure 6.6 – Scenario D3Q8. For 8 points along the x-axis (given in the frame on the graph), the corresponding, y positions are reported as a function of time.

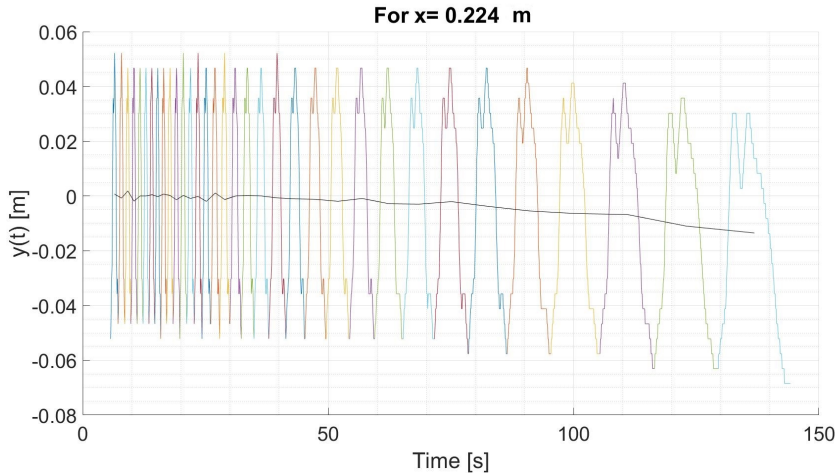


Figure 6.7 – Scenario D3Q8. For the position $x = 0.224 \text{ m}$, y is reported as a function of time. A sliding time-average is applied and shows that, in average, the y position deflects toward the lower part of the tank along the time.

It appears oscillation magnitude increases with the distance from the pipe outlet. The oscillations at the different positions appear synchronized, except for the point at $x = 0.31 \text{ m}$. The convection time $\tau_{conv} = \frac{L_{tank}}{u_{inj}}$ [s] is small, maximum 0.031 s before 140 s , this explains why no phase difference is visible between the successive points. For the point located at $x = 0.31 \text{ m}$, its proximity with the wall might perturb its dynamics. The point located at $x = 0.224 \text{ m}$ is selected in the following. Figure 6.7 presents for the point at $x = 0.224 \text{ m}$ the ordinate y as a function of time. The oscillation is pseudo-periodic. The pseudo-period of the oscillation $T(t)$ [s] is varying with time. In figure 6.7, different colors are used to ease the visualization of each pseudo-period. Based on the pseudo-period, a time-averaged of $y(t)$ is computed reported in black. This highlights, even if the jet is flapping, its centerline at $x = 0.224 \text{ m}$ is, on average, deflected towards the lower part of the tank, due to gravity effects.

A Sliding Discrete Fourier Transform (SDFT) is applied on $y(t)$. A SDFT performs a fast Fourier transform on a succession of time-windows. The time-windows can overlap. On every time-window, the fast Fourier transform reveals the main frequencies. The frequencies f are constant on a time-windows but thanks to the succession of time-windows, the frequencies can be expressed as a function of time.

Figure 6.8 displays the SDFT with a colormap graph of the magnitudes as a function of the frequencies and time. On the right axis, y position is reported. A main frequency $f_1(t)$ and two others frequencies, $f_2(t)$ and $f_3(t)$, can be identified. It appears that $f_2(t) = 3f_1(t)$ and $f_3(t) = 5f_1(t)$. The secondary frequencies are odd harmonics of the main frequency. This result could be predicted. The oscillation of the jet appears to be symmetric, so $y(t) \approx -y(t + \frac{T(t)}{2})$ and only odd products of the main frequency can verify this property.

Figure 6.9 presents another visualization of the same SDFT. Each color represents a time-window of the SDFT. For each time-window, the magnitudes are reported as functions of the frequencies. It can be seen that the magnitude associated with the main frequency f_1 is almost constant ($\approx 0.48 \text{ m}$). The magnitudes for the two secondary frequencies are also almost constant and similar ($\approx 0.008 \text{ m}$).

The frequencies are decreasing with time. It appears that the frequencies vary linearly with the inlet velocity. The Strouhal number based on the inlet velocity u_{inj} and the internal tank diameter D_{int} ($D_{int} = 0.2695 \text{ m}$ for the present

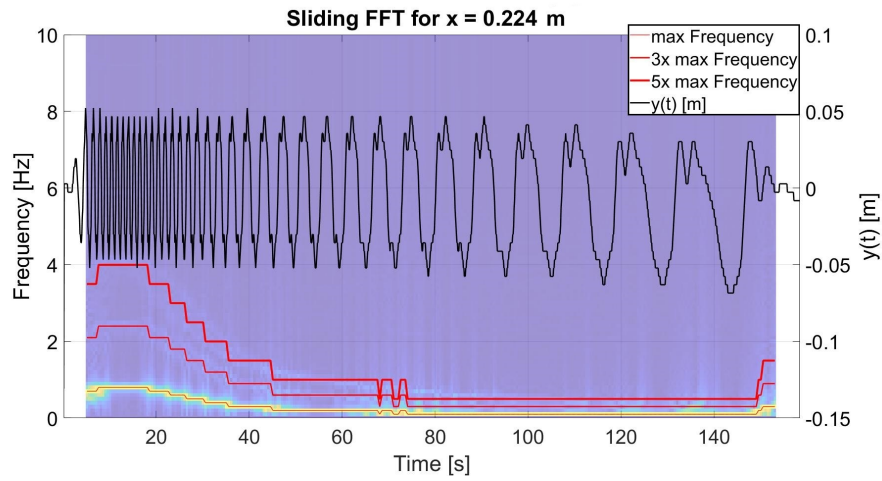


Figure 6.8 – Scenario D3Q8. For the position $x = 0.224$ m on the x -axis, colormap graph of the magnitudes associated to the frequencies as a function of time. On the right axis, y is reported.

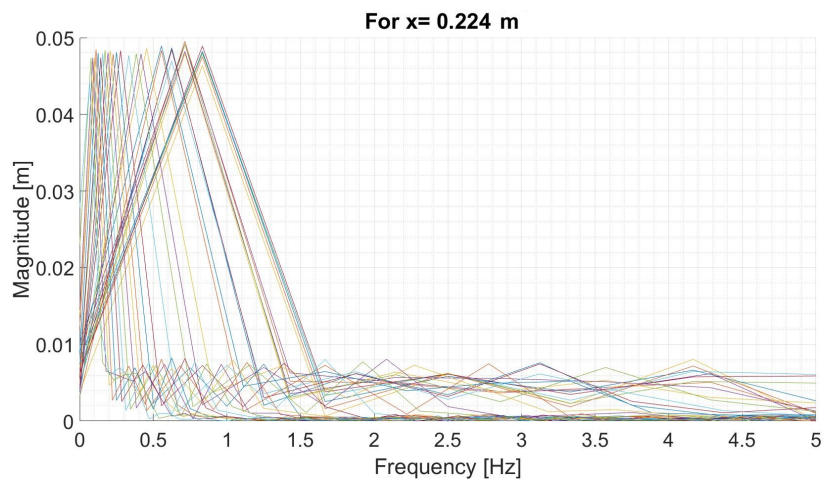


Figure 6.9 – Scenario D3Q8. For the position $x = 0.224$ m on the x -axis, for every time-window, (different colors), the magnitudes are reported as a function of frequencies.

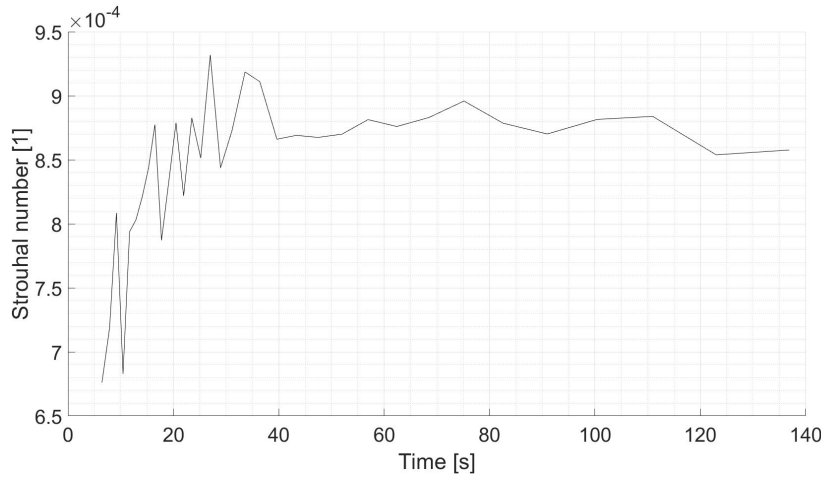


Figure 6.10 – Scenario D3Q8. For the position $x = 0.224$ m, the Strouhal number is reported as a function of the time.

tank [41]) is defined as

$$St = \frac{f D_{int}}{u_{inj}} . \quad (6.2)$$

Figure 6.10 presents this Strouhal number as a function of time. After $t = 30$ s, the Strouhal number remains within the interval $[8.5 \cdot 10^{-4}, 9.10 \cdot 10^{-4}]$. The displacement $y(t)$ can be approximated as

$$y(t) = A_1 \cos(2\pi f(t)t + B_1) + A_2 \cos(6\pi f(t)t + B_2) + A_3 \cos(10\pi f(t)t + B_3) \text{ with } f(t) = \frac{St u_{inj}}{D_{int}} . \quad (6.3)$$

Figure 6.11 presents a comparison between $y(t)$ issued from the CFD simulation (red) and $y(t)$ reconstructed (blue) as defined in (6.3). The amplitudes A_1 , A_2 and A_3 are set with the values found in figure 6.9. The values B_1 , B_2 and B_3 are the initial phases of each components of the signal. The values have been set empirically. The Strouhal number, (6.2), is taken slightly larger than values displayed in figure 6.10. Figure 6.11 presents the results for $x = 0.224$ m. The reconstructed signal provides an accurate estimate of the original one between $t = 30$ s, when the Strouhal becomes almost constant, and $t = 100$ s, when gravity effects break the x-axis symmetry of the oscillation, i.e. others harmonics arise. The same process has been carried out for $x = 0.139$ m, see figure 6.12.

Conclusion

To summarize, it appears that the velocities at the pipe outlet drives the frequency of jet oscillation inside the tank. Additional studies could be carried out the influence of the tank geometry on the Strouhal number and on the magnitudes of the flapping. In chapter 6.1, the difference of thermal distribution between the 2D-axisymmetric and the 3D CFD case for the scenario D3Q8 has been established and reported in figure 6.4. The difference must be due to the absence of jet oscillation for the 2D-axisymmetric CFD case. The effects of the oscillation on the thermal mixing remains an aspect to clarify. A better knowledge of jet oscillation and its impact on the thermal field could bring innovative solutions to enhance thermal mixing in the tank and limit thermal stratification.

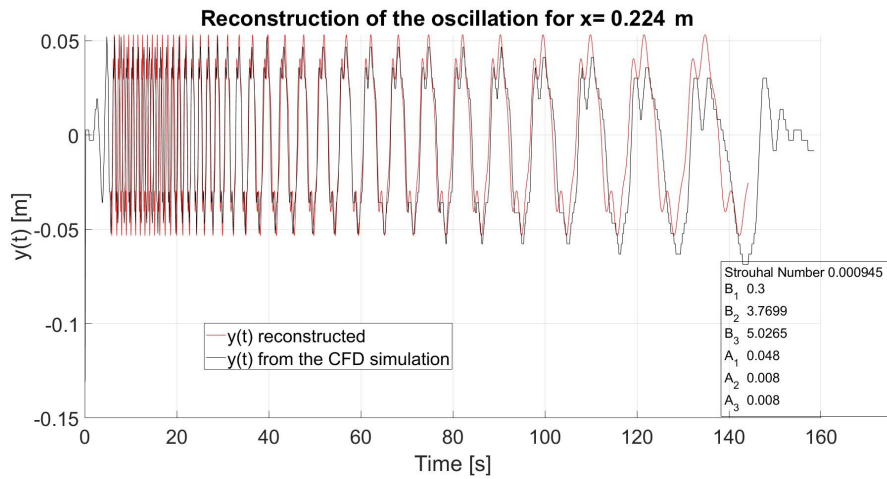


Figure 6.11 – Scenario D3Q8. For the position $x = 0.224$ m, the position $y(t)$ from the CFD simulation (black) is compared with the reconstructed signal (red).

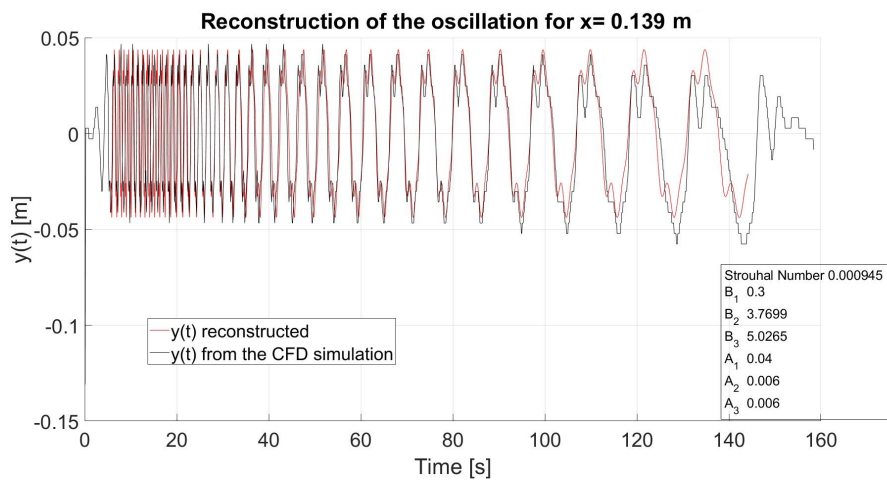


Figure 6.12 – Scenario D3Q8. For the position $x = 0.139$ m, the position $y(t)$ from the CFD simulation (black) is compared with the reconstructed signal (red).

6.3 Steady-state like method

When a vertical thermal stratification occurs, it can be seen that the cold jet in the tank does not flap. In fact, the velocity and the temperature fields change relatively slowly over time. Based on this observation, the steady-state buoyant jet theory has been used to capture the deflection of the inner jet. However, filling a closed volume with gas cannot be considered as a steady-state situation. The mass will increase over the time, i.e. the pressure and the density will increase. Beside, the gas inside the tank is cooled down by heat flux exchange with the wall and due to the cooler injected gas. The rise of the gas temperature is only possible because of fluid compressibility effects.

The idea developed in this section is to bring the unsteady simulation towards a Steady-State Like (SSL) simulation by removing the unsteady phenomena. With a steady-state simulation, a given time, in this example $t = t_{target}$, could be directly targeted without simulating the previous times, which could save substantial computational resources. During the filling of the tank, the inlet velocity decreases even if the mass flowrate is almost constant, because the pressure and density are gradually rising. When a constant $CFL_{max} = 1$ is imposed for the CFD simulation, the time step increases. Consequently, the latest time steps are less numerically expensive than the previous ones. Also, the thermal state at the end of the filling is usually the purpose of the simulation, in order to estimate the vertical thermal gradient. Thus, focusing on the prediction of the thermal state at the end of the filling scenario would reduce drastically the computational cost.

6.3.1 Numerical method

To transform the unsteady simulation into a SSL simulation, the mass of hydrogen in the tank must remain constant. This can be achieved by adding to the mass balance equation, see (6.4), a sink term:

$$\text{mass: } \frac{\partial \rho}{\partial t} + \frac{\partial \rho U_i}{\partial x_i} = \frac{\dot{m}_{inj}}{V} . \quad (6.4)$$

The sink term removes exactly the mass injected at the pipe inlet. A hypothesis used is that the mass is uniformly removed in the tank. The total enthalpy must be conserved as well over time. It is achieved by adding a source term q_{source} in the energy balance equation, see (6.5):

$$\begin{aligned} \text{energy: } & \frac{\partial}{\partial t} \left[\rho \left(h + \frac{1}{2} U_i U_i \right) \right] + \frac{\partial}{\partial x_j} \left[\rho U_j \left(h + \frac{1}{2} U_i U_i \right) \right] \\ & = \frac{\partial p}{\partial t} + \frac{\partial U_i \tau_{ij}^{eff}}{\partial x_j} + \rho U_i g_i - \frac{\partial q_i^{eff}}{\partial x_i} + q_{source} . \end{aligned} \quad (6.5)$$

The source term is warming the gas, to balance the heat exchanged with by the cooler walls and the cooler injected gas at the inlet. As the source term value cannot be predicted, the idea is to extract the difference of total enthalpy between the initial time $t = t_{target}$ and the time of the current iteration $t = t_i$, and to add this difference to the next time iteration as a source term:

$$q_{source}(t = t_{i+1}) = \frac{\sum_i \rho_i h_i v_i | (t = t_{target}) - \sum_i \rho_i h_i v_i | (t = t_i)}{\Delta t} . \quad (6.6)$$

Consequently, for a selected time, i.e. $t = t_{target}$, the mass and the total enthalpy of the gas are conserved. However, the mass and the total enthalpy must be initialized with a value corresponding to the target time $t = t_{target}$. This can be achieved with the 0D model SOFIL [43, 70]. Via a rapid SOFIL calculation, i.e. from 1 to 2 minutes, an averaged temperature and pressure of the gas can be extracted for the time $t = t_{target}$.

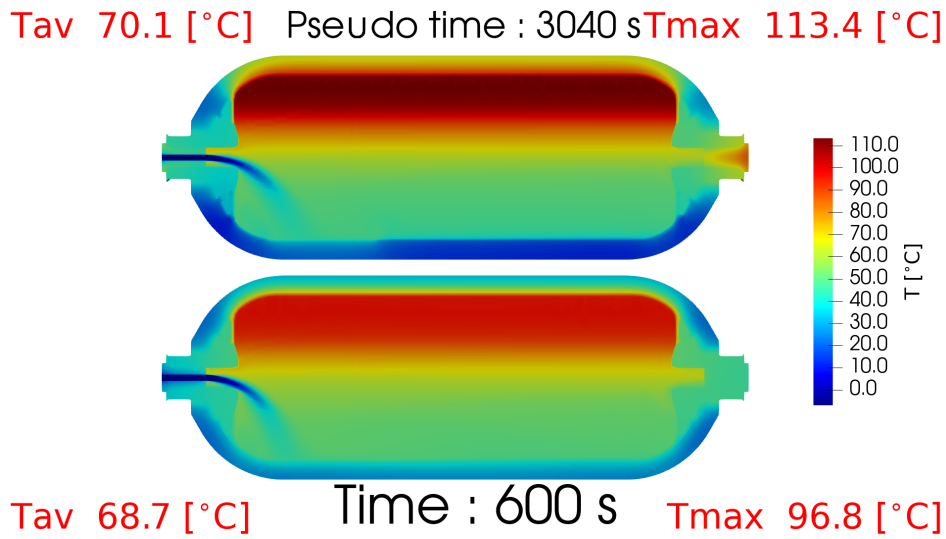


Figure 6.13 – Scenario D10Q2 at $t_{target} = 600$ s. Illustration of a steady-state like 3D simulation where the thermal equilibrium is reached for the walls between the heat exchanged with the fluid and the heat exchanged with the exterior environment (after 3040 s pseudo time iterations). The upper panel shows the thermal state for the SSL 3D simulation while the lower panel shows the unsteady 3D simulation results. For the SSL simulation, the maximum temperature reached by the fluid is higher because the wall temperatures are high.

For the solid regions, another approach is selected. It has been found that fluid thermal state converges only after the temperatures of solid regions have converged. If the same method as for the fluid region is adopted for the solid regions, the thermal state of the solids will converged when an equilibrium is found between the heat given by the fluid and the heat exchanged with the exterior environment. This situation happens only when the filling is very long, far above 10 minutes. For instance, the characteristic time $\tau_{diffusion}$ [s] for heat diffusion across the composite can be estimated. Knowing the thickness of the composite $L_{composite}$, the diffusion time can be estimated using the relationship:

$$\tau_{diffusion} = \frac{L_{composite}^2}{\alpha_{composite}} \tag{6.7}$$

The calculated value is $\tau_{diffusion} = 978.6$ s while for the scenario D10Q2, the filling time is 630 s. The end of the filling does not correspond to a situation where the heat from the fluid and the heat exchanged with the exterior environment are balanced. Therefore, using the same method as for the fluid region for the solid regions leads to an erroneous estimation of the temperatures in the solid regions, which impacts the estimation of the temperatures in the fluid region. Figure 6.13 shows a simulation result where 3040 s of pseudo time iterations have been performed, see upper view. The heat flux between the fluid region and the exterior environment is balanced and the thermal state in the tank does not evolve anymore. The maximum temperature reached is 113.4 °C, which is higher than the maximum temperature given by the unsteady simulation using the $k - \omega$ SST SAS turbulent model simulation 96.8 °C.

An alternative approach is adopted. The solid region temperatures are not initialized at $t = t_{target}$ but at $t = 0$ s. The fluid region will warm the solid regions and the solid region temperatures will rise. When the total enthalpy of a solid region exceeds the total enthalpy at the time $t = t_{target}$, the thermal field is frozen. When frozen, the thermal field of the solid regions acts as a fixed temperature boundary for the other regions. The total enthalpy at $t = t_{target}$ is evaluated using SOFIL. SOFIL can give the temperature along the radial direction for walls (1D). The averaged temperature of the

Regions	Fluid	Plugs	Bosses	Liner	Composite
T_{av} [°C] 0D SOFIL	68.9	58.22	43.71	58.22	41.66
H_{total} [J] 3D OpenFOAM	3.23369e+06	21973.5	599324	769967	3.54749e+06

Table 6.1 – Averaged temperatures estimated with SOFIL and corresponding total enthalpy using (6.8) at $t = 600$ s.

\dot{m}_{inj} [kg/s]	T_{inlet} [°C]	p [bar]	T_{ext} [°C]	k_a [W/m ² /K]
8.44e-04	-7.095	680.19	18.71	6

Table 6.2 – Initial conditions based on results from SOFIL at $t = 600$ s.

liner is estimated using an average of the temperature at the interface between the gas and the liner and the temperature at the interface between the liner and the composite. The temperature of the composite is estimated using an average of the temperature at the interface between the liner and the composite and the composite exterior wall temperature. The temperatures of the bosses and the plugs are set equal to the liner temperature. The total enthalpy for the solid regions is calculated using the averaged temperature via the relationship:

$$H_{total} = V \rho c_p T_{av} . \quad (6.8)$$

The method is summarized in the flowchart 6.14. To conclude, the SSL method must be seen as an unsteady simulation of a steady-state situation. The simulation is terminated once the thermal field is converged, i.e. the maximum of temperature for the fluid remains constant. Note than an attempt to remove the temporal term in the calculation and use a SIMPLE algorithm has been tried without success.

6.3.2 Application

The method has been applied to the scenario D10Q2 at $t = 600$ s. SOFIL results of the complete filling, see figure 6.15, give the temperatures in the gas and in walls at different positions. Using these temperatures, the temperatures and the corresponding total enthalpies at $t = 600$ s for each region are calculated and reported in table 6.1. The other initial conditions needed for the CFD simulation are reported in table 6.2. The method used the same numerical schemes, mesh, EOS for hydrogen and turbulence model, i.e. $k - \omega$ SST SAS, than the unsteady CFD for the scenario D10Q2. The unsteady results used for comparison are taken from the previous study detailed in chapter 4.

Figure 6.16 shows the results of the CFD SSL. The time of the SSL simulation is called pseudo time. The reason is to emphasize that the time is concrete for the simulation process but does not correspond to the simulated time which is $t = 600$ s. It can be seen that the maximum temperature in the fluid region rapidly converges when the thermal state of the liner is frozen. The thermal state from the plugs never reaches the total enthalpy estimated by the method. This means the evaluated averaged temperature in the plugs at $t = 600$ s was too important. This is not a problem, the fluid region and the plugs converge in temperature. Figure 6.17 compares the thermal field from the SSL simulation (upper panel) with the unsteady simulation (lower panel). The two fields are very close while the initial values for the SSL simulation come from SOFIL and have no links with the previous CFD results. It can be noted that the simulation could be stopped at 520 s to get the maximum temperature in the fluid region. In order to reach complete convergence of all regions, the simulation has been prolonged.

The SSL method gives a maximum as temperature of 98.5 °C. The maximum temperature predicted by the unsteady simulation is 96.8 °C. The maximum temperature measured is 98.2 °C. The difference on the temperature for both

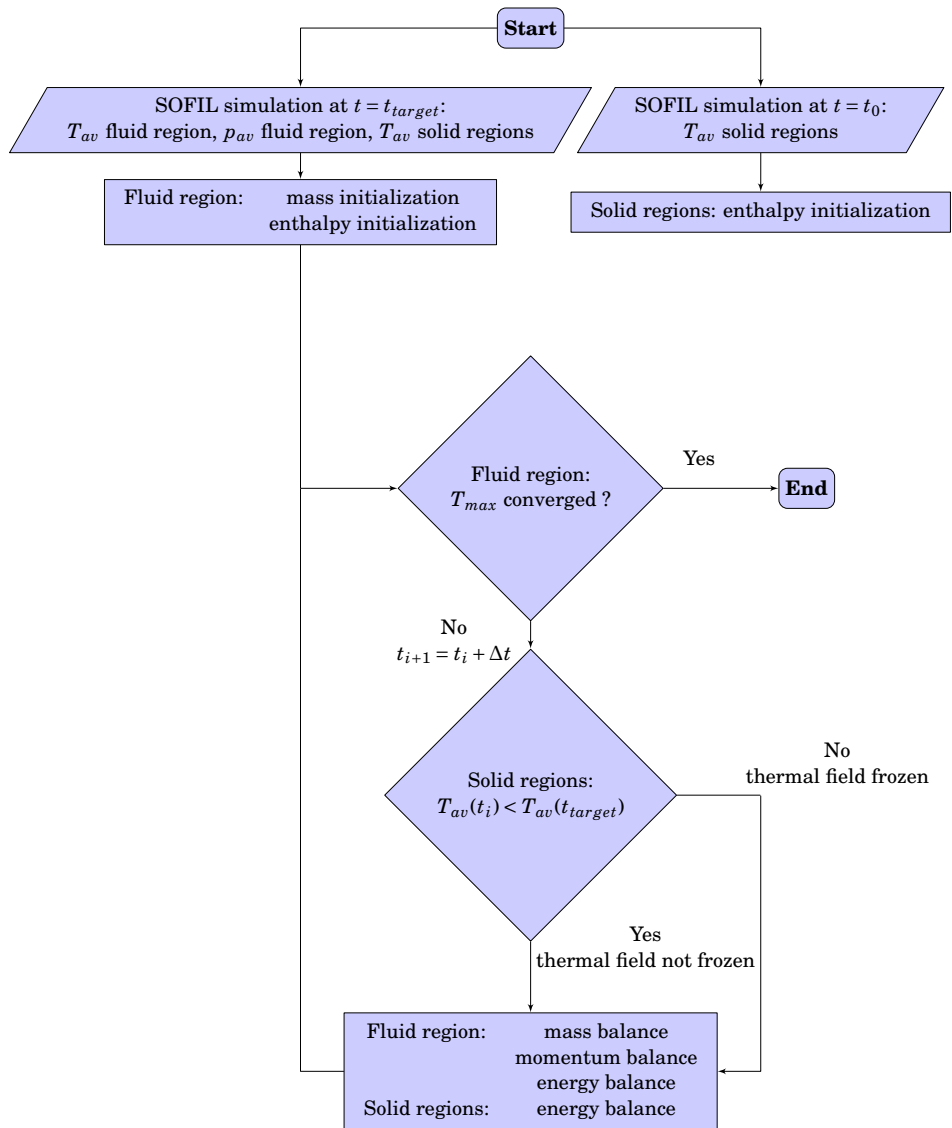


Figure 6.14 – Flowchart of the steady-state like method.

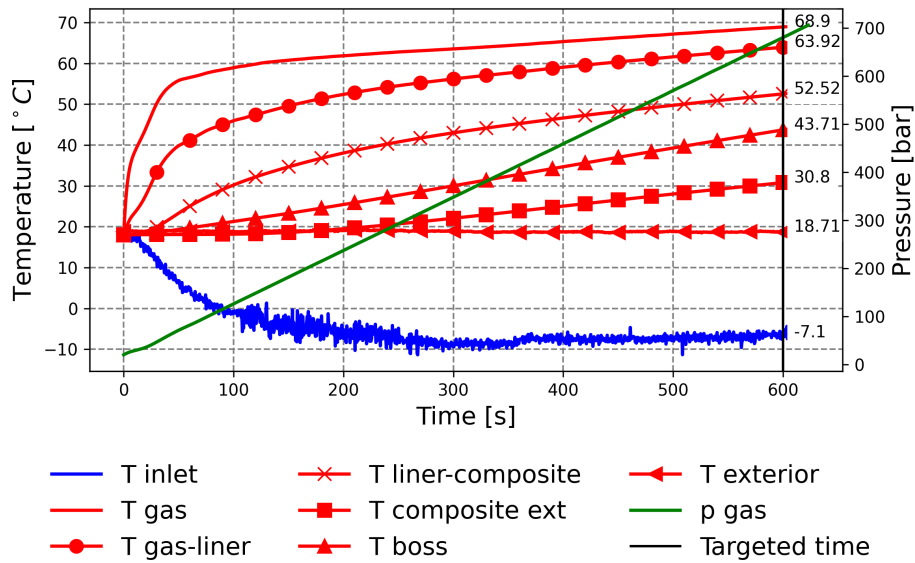


Figure 6.15 – SOFIL simulation results. The temperatures are indicated on the left axis and the pressure on the right axis.

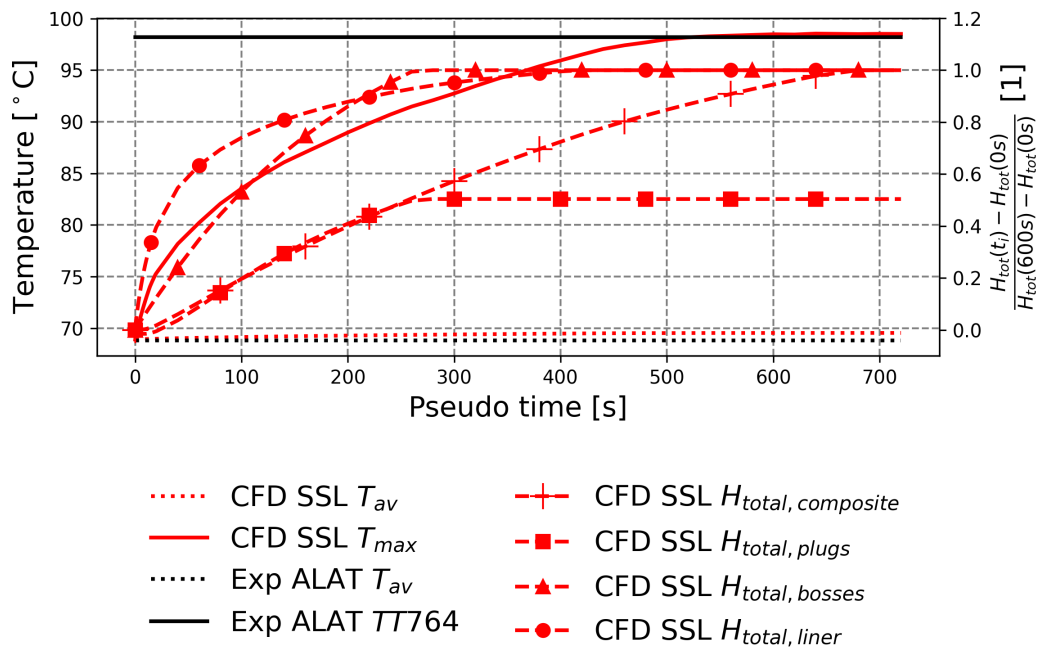


Figure 6.16 – Scenario D10Q2 at $t_{target} = 600$ s. The SSL results are compared to experimental measurements from ALAT [41]. The thermal probe TT764 gave the highest temperature for the gas during the filling. The temperatures are indicated on the left axis. The total enthalpy for the different regions is written under the form $\frac{H_{tot}(t_i) - H_{tot}(0s)}{H_{tot}(600s) - H_{tot}(0s)}$ in order to get a value between 0 and 1 and is indicated on the right axis.

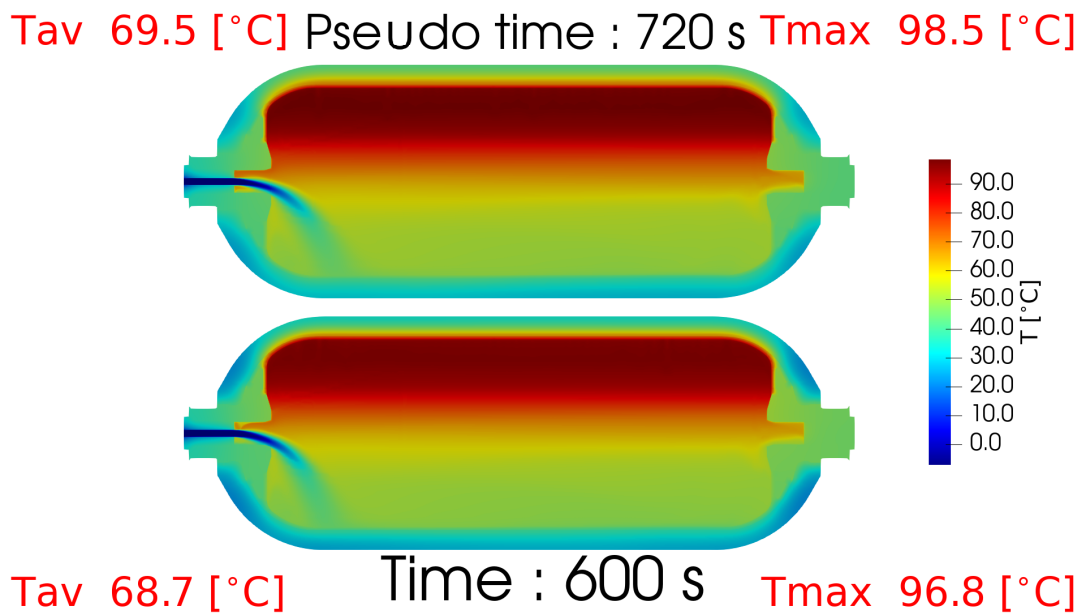


Figure 6.17 – Scenario D10Q2 at $t_{target} = 600$ s. Illustration of a SSL 3D simulation where the thermal equilibrium is reached. Each solid region enthalpy has reached the one at $t_{target} = 600$ s. Thus, each thermal state of solid regions is frozen. The upper panel shows the thermal state for the SSL 3D simulation while the lower panel shows for the unsteady 3D simulation results.

simulation cases is 1.7 °C degree while the unsteady simulation took months (around 6 months) to perform on 108 cores of a HPC station while the SSL method took 2 weeks on a 20 cores personal computer (with the same mesh).

Conclusion

For this application case, the SSL method shows its ability to predict the results of the unsteady simulation at $t = 600$ s. It is faster and uses less computational resources than the unsteady simulation. Additional tests need to be carried out in future studies with other tanks and other filling or emptying scenarios where experimental data are available to validate the SSL method. The SSL method might also be applicable to investigate jet flapping and jet deflection. By fixing the velocity with the SSL method, the effect of the injector shape or orientation on the jet oscillation and deflection and more generally on the thermal mixing could also be investigated.

6.4 Emptying case

A case of tank emptying scenario has also been investigated. During the experimental campaign [42], several emptying scenarios have been tested. For the 37 L tank, the reference emptying scenario was the 3 mm injector and the 0.376 g/s averaged emptying mass flowrate. The emptying scenario started at a gas pressure of 619.3 bar. It was stopped when the pressure reached 20 bar. The initial temperature is taken uniform at 26.77 °C for all regions. The emptying lasted 3443.5 s. Only 768 s have been simulated in the present work. The simulation has been carried out using the PISO algorithm. The time step is limited by the pipe flow where the mesh cell sizes are the smallest and the velocity the highest. In order to accelerate the calculation, a CFL has been imposed as $CFL < 5$. The cells with a $CFL > 1$ are all

	CFD OpenFOAM T_{av}	CFD OpenFOAM $T_{min, gas-liner}$	0D SOFIL T_{av}	Exp ALAT T_{av}	CFD OpenFOAM T_{inlet}	CFD OpenFOAM T_{outlet}
T [°C]	9.96	10.29	9.92	10.35	10.43	9.41

Table 6.3 – Reference emptying case with the 3 mm injector diameter issued from [41]. Temperatures at the end of the calculation at $t = 768$ s for the CFD results from OpenFOAM, results from SOFIL and the experimental measurements.

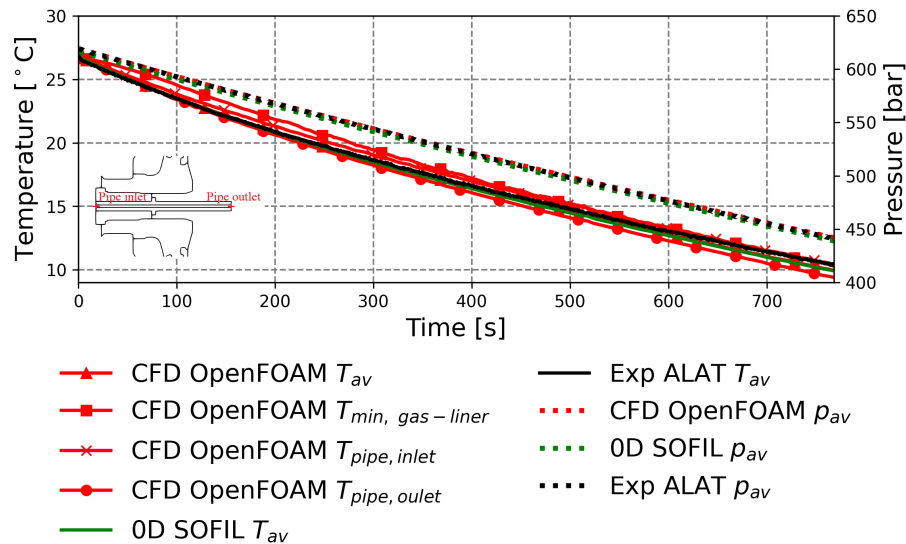


Figure 6.18 – Reference emptying case with the 3 mm injector diameter issued from [41]. Comparison of temperatures and pressure as function of time from the CFD results in red, SOFIL results in green and the experimental measurements in black.

located in the pipe. It has been assumed that they have no effect on the main bulk flow. The simulation is 3D and carried on half of the geometrical domain using a symmetry assumption. The turbulence model used is the $k - \omega$ SST SAS. The mesh for the fluid region is different from that used for the filling scenario D3Q8. As no jet flow is present in the gas, a coarser mesh is used, with 404 836 cells.

Figure 6.18 shows a comparison of the averaged temperature and pressure between the CFD (red), SOFIL (green) and the experimental measurement (black) results. It can be seen that the numerical results match the experimental measurements for the averaged gas temperature and pressure. Two virtual temperature probes have been added for the CFD study at the pipe inlet and outlet (figure 6.18). This allows to estimate if the temperature of the released gas is different from the averaged gas temperature. Figure 6.18 shows that the temperature at the pipe outlet is always lower than the averaged gas temperature. The temperature at the pipe inlet is always higher the gas averaged temperature. This is due to the heat exchanged between the gas and the pipe. The pipe warms the gas from the outlet to the inlet. A probe located at the pipe outlet would measure an underestimated value of the averaged gas temperature. Although a vertical thermal gradient is occurring in the gas during the emptying, the CFD results shows that minimum temperature at the liner wall in contact with the gas remains warmer than the averaged gas temperature. Table 6.3 gives the temperatures from CFD, SOFIL and the experimental measurement results at $t = 768$ s.

Some visualizations are presented in figures 6.19 and 6.20. Two streamline are plotted, one in the middle of the first half of the tank (in black) and one in the middle of the second half of the tank (in grey). It can be seen that before 50 s (panels A and B), the inlet flow dynamic has a important effect on the main bulk. The streamlines converge towards the

	T_{av} [°C]	TT764 [°C]	TT768 [°C]
CFD OpenFOAM	9.96	14.75	7.68
Exp ALAT	10.35	13.5	6.97

Table 6.4 – Emptying scenario for the 37 L tank with a 3 mm injector diameter. Temperatures of the probes TT764 and TT768 at $t = 768$ s for the CFD results and the experimental measurements.

pipe outlet. The averaged gas temperature decreases due to the decompression. The temperatures at the walls become higher than the temperatures in the gas. Consequently, convection forces appear. At 10 s (panel B), convection forces start to overcome on the inlet flow dynamics and change the global flow dynamics. After 50 s, the flow is driven by the convection. The two streamlines do not mix anymore and a recirculation loop is present in each half of the tank. The symmetry assumption may play a role in this flow configuration and a full 3D simulation might change the recirculation dynamics. After 50 s, the action of the inlet flow dynamics becomes negligible on the main bulk. Around the pipe outlet, the velocities are ten times lower than inside the pipe. However, the velocities in the pipe increases because the mass flowrate is constant and the pressure decreases as the averaged gas density. A longer simulation may reveal a critical time when the inlet flow dynamics become significant again.

Figure 6.21 shows a comparison of the 10 temperature probes located in the gas issued from the experimental measurements (continuous line in black) and CFD results (continuous line in red). The averaged gas temperatures (dashed line) issued from the experimental measurements and the CFD results are added on each panel to visualize perceiving the vertical thermal stratification. It can be noted that the trend is the same in the experimental measurements and the CFD results: temperatures from probes located in the upper part (TT760,TT762,TT764,TT767) are higher than the averaged temperature; temperatures from probes located in the lower part (TT761,TT763,TT765,TT768) are lower than the averaged temperature. The CFD results are slightly overestimating the thermal gradient amplitude, (table 6.4).

The difference could be explained by different factors:

- (i) The initial thermal state of the experiment is not uniform. The experiment had at emptying start with a horizontal thermal gradient: probes TT767, TT768 and TT769 had a smaller initial temperature than probes TT760, TT761 and TT762. This could be explained by the uncontrolled exterior environment during the experiment.
- (ii) For the CFD simulations, the temperature in solid regions are set uniform and equal to the fluid region initial temperature. This could act on the fluid region thermal field, by changing the heat exchanged between the gas and the walls.
- (iii) The turbulent viscosity impacts the thermal diffusion by increasing the thermal mixing. The turbulent viscosity also limits the natural convection by weakening flow structures. The recirculation loops appear as important flow structures to capture numerically the thermal mixing. An emptying CFD simulation, without turbulence modeling could be interesting to perform to see the impact of the turbulence modeling on the recirculation loops and on the thermal gradient amplitude.

Conclusion

To summarize, the flow dynamics during the emptying of a gaseous hydrogen tank appears to be driven by the natural convection. A vertical thermal stratification occurs in the tank. The influence of the pipe inlet flow on the thermal field appears negligible at the final time reached in this study. A more advanced time should be reached to confirm if this

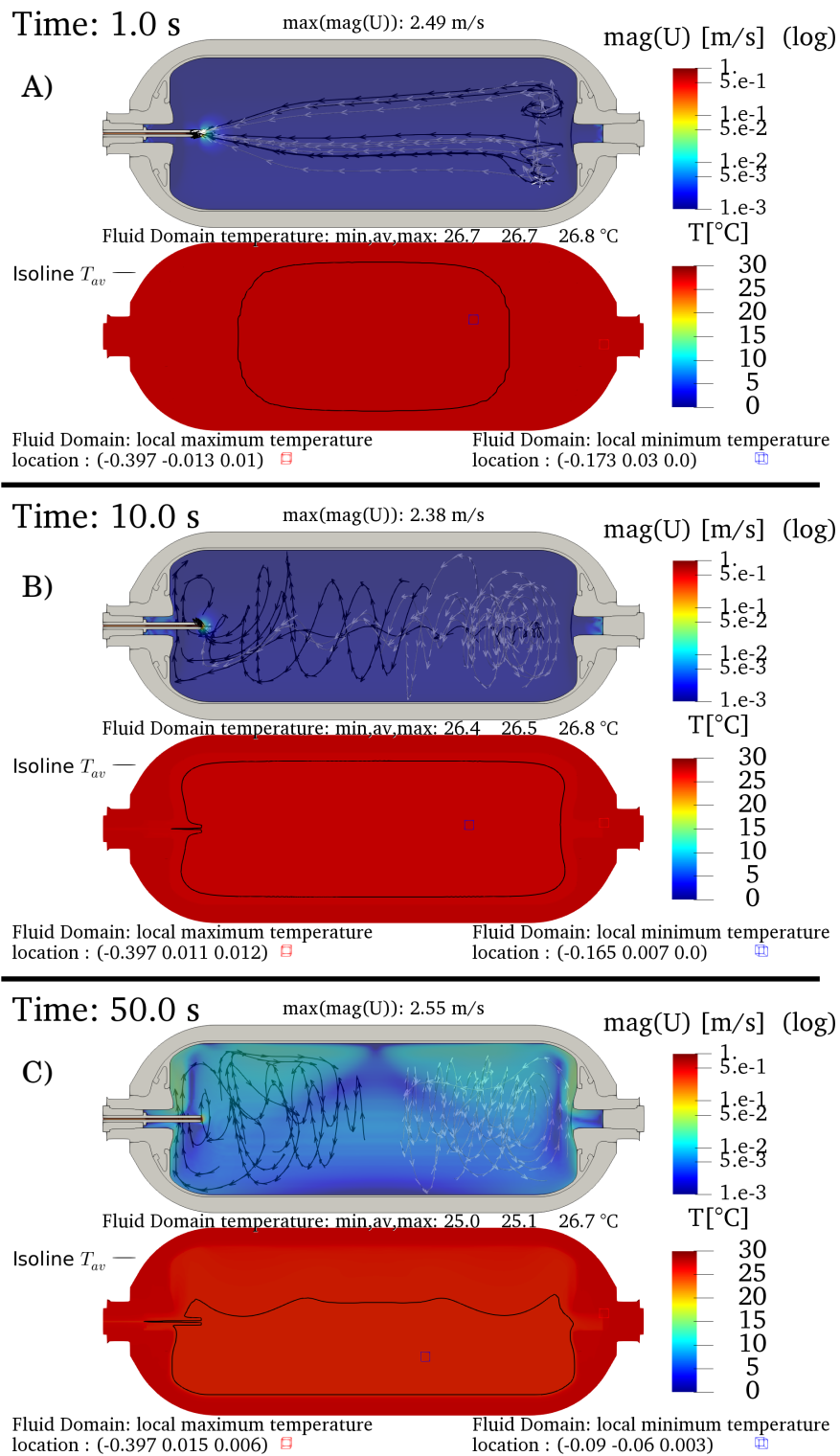


Figure 6.19 – Emptying scenario for the 37 L tank with a 3 mm injector diameter. Panels A, B and C display views of the thermal field (lower view) and the velocity field in logarithmic scale (upper view) corresponding to times 1 s, 10 s and 50 s respectively.

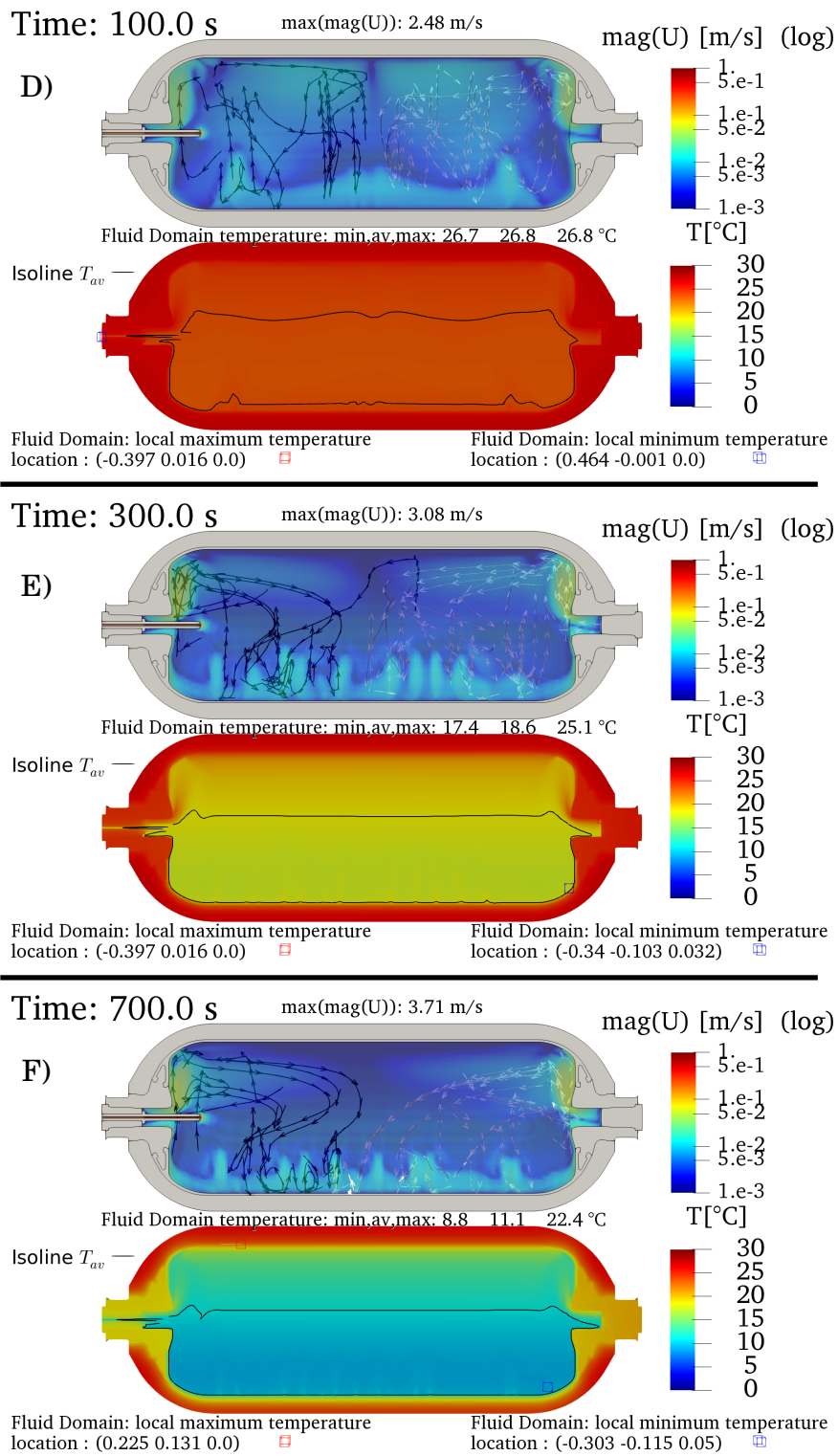


Figure 6.20 – Emptying scenario for the 37 L tank with a 3 mm injector diameter. Panels D, E and F display views of the thermal field (lower view) and the velocity field in logarithmic scale (upper view) corresponding to times 100 s, 300 s and 700 s respectively.

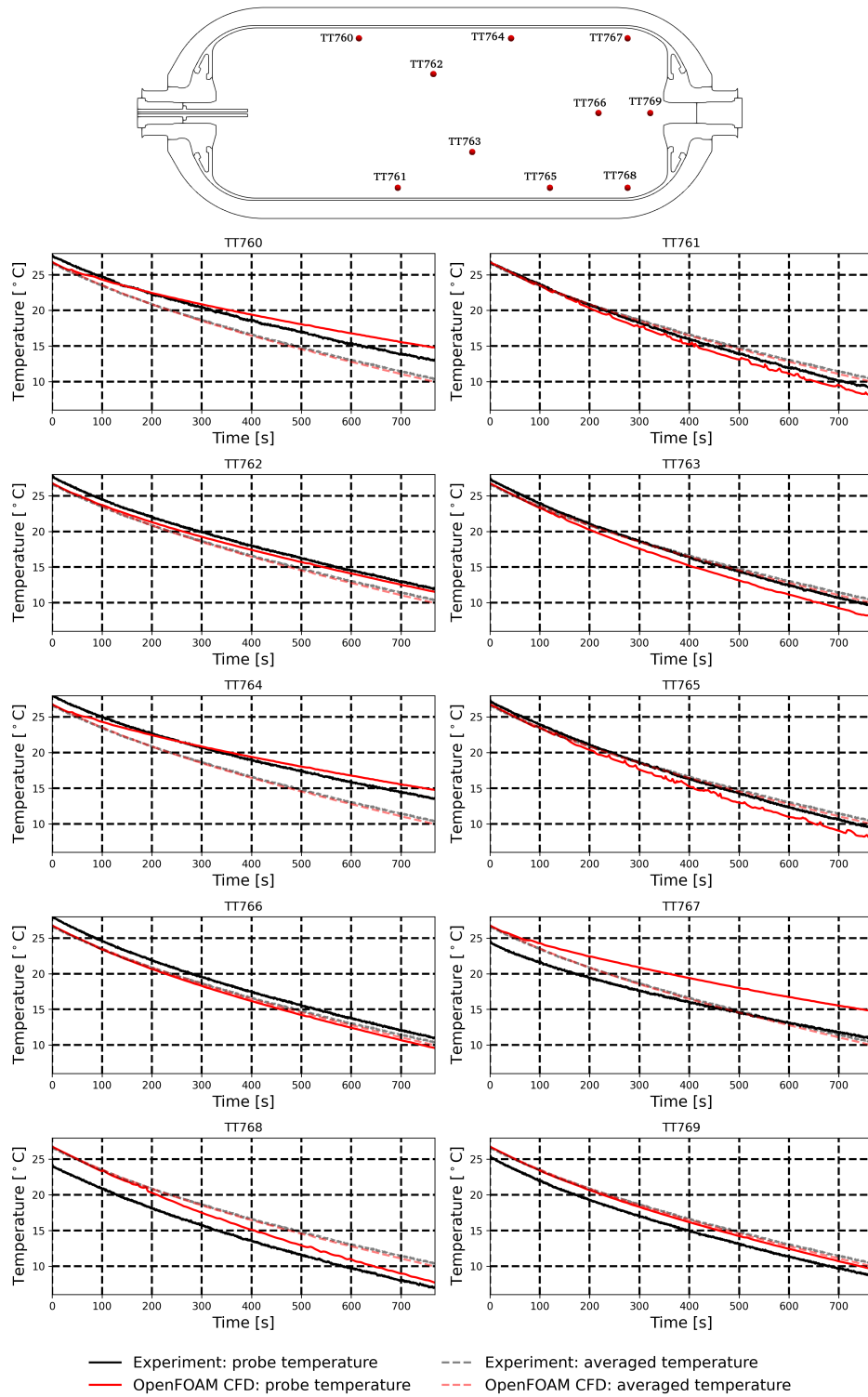


Figure 6.21 – Emptying scenario for the 37 L tank with a 3 mm injector diameter. Temperatures for the probes in the gas at $t = 768$ s for the CFD results and the experimental measurements.



Figure 6.22 – Experimental set-up of the probes placed on the liner external surface, in contact with the composite warp for the type IV 37 L tank.

remains true. The stratified thermal state in the gas is a consequence of the difference of temperature between the gas and the solid walls. The buoyant jet model described in chapter 5 cannot be applied for the emptying of a tank. The link between the thermal gradient and the difference of temperature between the averaged gas and the liner temperatures needs to be investigated, in particular to include the above phenomena in 0D models.

6.5 Inverse model to estimate the temperature at the gas-liner interface

The SAE J2601 standard [18] recommends to keep the temperature for composite tank below $85\text{ }^{\circ}\text{C}$. The temperature in the gas can be difficult to measure. The thermocouple tree inserted in the gas for the experimental measurements is an intrusive device. By disturbing the inner flow with the experimental set-up, the temperatures measured may differ from those in real filling conditions. The thermocouple tree is also overhanging inside the tank, which limits its use for long tank. To avoid these issues, placing the temperature probes at the liner wall, in contact with the gas could appear as a solution. However, it is difficult to place the probes at this position for gas impermeability issues with the connection cables. Also, at the interface between the gas and the liner, the temperature measured is a mix between the temperature of the gas and the temperature of the liner. It is complex to estimate whether the temperature from the probe is closer to the gas or to the liner temperature. It is more convenient to install the temperature probes at the interface between the liner and the composite. Figure 6.22 presents a picture of the experimental set-up for the 37 L tank. The heat exchanged between the probe and each solid region is driven by thermal conduction.

For the type IV 531 L tank considered in HyTransfer [41], the probes in the gas were located in the rear region of the tank. Due to the small number of probes in the gas and the specific location of the probes, only a coarse estimation of the averaged gas temperature and thermal gradient is possible. The objective of this study is to estimate the temperatures at the interface between the gas and the liner from the temperatures between the liner and the composite, issued from the experimental measurement (see figure 6.23). For the type IV 531 L tank, 30 temperature probes were installed between the liner and the composite. The aim is to improve the detection of the thermal gradient occurrence during the filling.

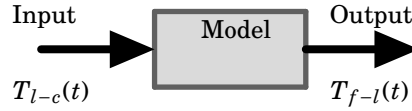


Figure 6.23 – Purpose of the model: predicting the temperatures at the interface between the gas and the liner T_{f-l} from the temperature at the interface between the liner and the composite T_{l-c} .

Frame of the model

The tank wall is composed of two layers: a thin liner layer and a thick composite layer. The thickness of the liner and of the composite is considered to be uniform. The averaged measured thicknesses of the liner and composite are considered. Each layer has its own thermal conductivity λ , density ρ and specific heat capacity c_p , set constant values. It is assumed that there is no thermal resistance between the two layers, i.e. continuity of thermal fluxes and temperatures. An adiabatic thermal boundary condition is applied on the exterior wall. This is illustrated in figure 6.24. Using an electrical analogy, the situation can be seen as two thermal quadripoles in series (figure 6.25).

For one generic thermal quadripoles, the governing equation is the energy balance equation (6.9) and a heat flux ϕ is applied on boundaries (6.10):

$$\rho c_p \frac{\partial T(x, t)}{\partial t} = \lambda \frac{\partial^2 T(x, t)}{\partial x^2}, \quad (6.9)$$

$$\phi(x, t) = -\lambda \frac{\partial T(x, t)}{\partial x}. \quad (6.10)$$

The thermal diffusivity $\alpha = \frac{\lambda}{\rho c_p}$ is introduced. The temperature θ , defined as $\theta(x, t) = T(x, t) - T(x, 0)$, is used for the mathematical development. Equations (6.9) and (6.10) can be written as:

$$\frac{\partial \theta(x, t)}{\partial t} = \alpha \frac{\partial^2 \theta(x, t)}{\partial x^2}, \quad (6.11)$$

$$\phi(x, t) = -\lambda \frac{\partial \theta(x, t)}{\partial x}. \quad (6.12)$$

To solve this system, the Laplace transform method is used. As a reminder, for a function f locally integrable in $[0, +\infty[$, the Laplace transform is defined as:

$$\mathcal{L}(f)(p) = \int_0^{+\infty} f e^{-pt} dt, \quad p \in \mathbb{C}. \quad (6.13)$$

The temporal differentiation of a Laplace transform leads to the relationship:

$$\frac{df(t)}{dt} = p \mathcal{L}(f)(p) - f(0). \quad (6.14)$$

To ease the reading, a Laplace transform of a function f is noted in capital letters, i.e. $\mathcal{L}(f)(p) = F(p)$. The Laplace

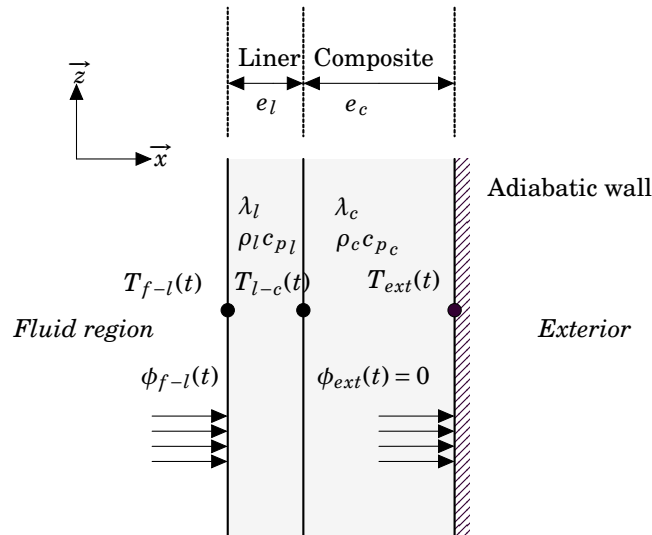


Figure 6.24 – Schematic of a 1D tank wall with two layers: the liner and the composite.

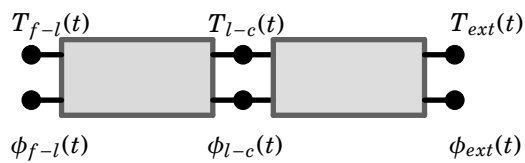


Figure 6.25 – Electrical analogy with two quadripoles.

transform is a function of the variables p and x . Equations (6.11) and (6.12) lead to

$$p\Theta = \alpha \frac{\partial^2 \Theta}{\partial x^2}, \quad (6.15)$$

$$\Phi = -\lambda \frac{\partial \Theta}{\partial x}. \quad (6.16)$$

Equation (6.15) has a known solution,

$$\Theta(x, p) = A_1 \lambda ch\left(\sqrt{\frac{p}{\alpha}} x\right) + A_2 \lambda sh\left(\sqrt{\frac{p}{\alpha}} x\right), \quad (A_1, A_2) \in \mathbb{R}^2, \quad (6.17)$$

with ch and sh the hyperbolic cosine and sine respectively. For a wall of thickness e , using the notation *in* at $x = 0$ and *out* at $x = e$, equations (6.16) and (6.17) lead to the system:

$$\left\{ \begin{array}{l} \Theta_{in} = \Theta(0, p) = A_1 \\ \Theta_{out} = \Theta(e, p) = A_1 ch\left(\sqrt{\frac{p}{\alpha}} e\right) + A_2 sh\left(\sqrt{\frac{p}{\alpha}} e\right) \\ \Phi_{in} = \Phi(0, p) = -A_2 \lambda \sqrt{\frac{p}{\alpha}} \\ \Phi_{out} = \Phi(e, p) = -A_1 \lambda \sqrt{\frac{p}{\alpha}} sh\left(\sqrt{\frac{p}{\alpha}} e\right) - A_2 \lambda \sqrt{\frac{p}{\alpha}} ch\left(\sqrt{\frac{p}{\alpha}} e\right) \end{array} \right. \quad (6.18)$$

The constants A_1 and A_2 , can be substituted by Θ_{in} and Φ_{in} . Then, the system (6.18) can be written under a matrix form which links the input to the output:

$$\begin{bmatrix} \Theta_{out} \\ \Phi_{out} \end{bmatrix} = \begin{bmatrix} ch\left(\sqrt{\frac{p}{\alpha}} e\right) & -\frac{1}{\lambda} \sqrt{\frac{\alpha}{p}} sh\left(\sqrt{\frac{p}{\alpha}} e\right) \\ -\lambda \sqrt{\frac{p}{\alpha}} sh\left(\sqrt{\frac{p}{\alpha}} e\right) & ch\left(\sqrt{\frac{p}{\alpha}} e\right) \end{bmatrix} \begin{bmatrix} \Theta_{in} \\ \Phi_{in} \end{bmatrix}. \quad (6.19)$$

The inverse system of (6.19) is:

$$\begin{bmatrix} \Theta_{in} \\ \Phi_{in} \end{bmatrix} = \begin{bmatrix} ch\left(\sqrt{\frac{p}{\alpha}} e\right) & \frac{1}{\lambda} \sqrt{\frac{\alpha}{p}} sh\left(\sqrt{\frac{p}{\alpha}} e\right) \\ \lambda \sqrt{\frac{p}{\alpha}} sh\left(\sqrt{\frac{p}{\alpha}} e\right) & ch\left(\sqrt{\frac{p}{\alpha}} e\right) \end{bmatrix} \begin{bmatrix} \Theta_{out} \\ \Phi_{out} \end{bmatrix}. \quad (6.20)$$

The system (6.20) links the nodes at the interface between the gas and the liner with the nodes at the exterior wall of the composite

$$\begin{bmatrix} \Theta_{f-l} \\ \Phi_{f-l} \end{bmatrix} = \begin{bmatrix} ch\left(\sqrt{\frac{p}{\alpha_l}} e_l\right) & \frac{1}{\lambda_l} \sqrt{\frac{\alpha_l}{p}} sh\left(\sqrt{\frac{p}{\alpha_l}} e_l\right) \\ \lambda_l \sqrt{\frac{p}{\alpha_l}} sh\left(\sqrt{\frac{p}{\alpha_l}} e_l\right) & ch\left(\sqrt{\frac{p}{\alpha_l}} e_l\right) \end{bmatrix} \begin{bmatrix} ch\left(\sqrt{\frac{p}{\alpha_c}} e_c\right) & \frac{1}{\lambda_c} \sqrt{\frac{\alpha_c}{p}} sh\left(\sqrt{\frac{p}{\alpha_c}} e_c\right) \\ \lambda_c \sqrt{\frac{p}{\alpha_c}} sh\left(\sqrt{\frac{p}{\alpha_c}} e_c\right) & ch\left(\sqrt{\frac{p}{\alpha_c}} e_c\right) \end{bmatrix} \begin{bmatrix} \Theta_{ext} \\ 0 \end{bmatrix}, \quad (6.21)$$

and the nodes at the interface between the liner and the composite with the nodes at the exterior wall of the composite

$$\begin{bmatrix} \Theta_{l-c} \\ \Phi_{l-c} \end{bmatrix} = \begin{bmatrix} ch\left(\sqrt{\frac{p}{\alpha_c}} e_c\right) & \frac{1}{\lambda_c} \sqrt{\frac{\alpha_c}{p}} sh\left(\sqrt{\frac{p}{\alpha_c}} e_c\right) \\ \lambda_c \sqrt{\frac{p}{\alpha_c}} sh\left(\sqrt{\frac{p}{\alpha_c}} e_c\right) & ch\left(\sqrt{\frac{p}{\alpha_c}} e_c\right) \end{bmatrix} \begin{bmatrix} \Theta_{ext} \\ 0 \end{bmatrix}. \quad (6.22)$$

From the systems (6.21) and (6.22), the system (6.23) can be deduced

$$\begin{cases} \Theta_{f-l} = \left(ch\left(\sqrt{\frac{p}{\alpha_l}}e_l\right)ch\left(\sqrt{\frac{p}{\alpha_c}}e_c\right) + \frac{\lambda_c}{\lambda_l}\sqrt{\frac{\alpha_l}{\alpha_c}}sh\left(\sqrt{\frac{p}{\alpha_l}}e_l\right)sh\left(\sqrt{\frac{p}{\alpha_c}}e_c\right) \right) \Theta_{ext} \\ \Theta_{l-c} = ch\left(\sqrt{\frac{p}{\alpha_c}}e_c\right) \Theta_{ext} \end{cases}, \quad (6.23)$$

and the Laplace transform Θ_{l-c} can be linked the Laplace transform Θ_{f-l} :

$$\Theta_{l-c} = \frac{ch\left(\sqrt{\frac{p}{\alpha_c}}e_c\right)}{ch\left(\sqrt{\frac{p}{\alpha_l}}e_l\right)ch\left(\sqrt{\frac{p}{\alpha_c}}e_c\right) + \frac{\lambda_c}{\lambda_l}\sqrt{\frac{\alpha_l}{\alpha_c}}sh\left(\sqrt{\frac{p}{\alpha_l}}e_l\right)sh\left(\sqrt{\frac{p}{\alpha_c}}e_c\right)} \Theta_{f-l}. \quad (6.24)$$

A transfer function $H(p)$ is defined such as

$$H(p) = \frac{ch\left(\sqrt{\frac{p}{\alpha_c}}e_c\right)}{ch\left(\sqrt{\frac{p}{\alpha_l}}e_l\right)ch\left(\sqrt{\frac{p}{\alpha_c}}e_c\right) + \frac{\lambda_c}{\lambda_l}\sqrt{\frac{\alpha_l}{\alpha_c}}sh\left(\sqrt{\frac{p}{\alpha_l}}e_l\right)sh\left(\sqrt{\frac{p}{\alpha_c}}e_c\right)}, \quad (6.25)$$

and so

$$\Theta_{l-c} = H(p)\Theta_{f-l}. \quad (6.26)$$

At this point of the model development, the relationship (6.26) is suitable for a direct problem: knowing Θ_{f-l} , Θ_{l-c} can be deduced. The objective here is to solve the inverse problem: Θ_{f-l} is deduced from Θ_{l-c} . The inverse problem is not a well-posed problem as defined by Hadamard [127]. The problem is ill-conditioned, i.e. small variations of Θ_{l-c} results in large variations of Θ_{f-l} . Solving the inverse problem requires a regularization process. It is detailed in the following. The numerical method used to solve the direct problem is examined first.

6.5.1 Direct problem

The energy equation has been expressed in the frequency domain, (6.26). The solution Θ_{l-c} , needs to be inverted to return to the temporal domain, i.e. $H(p)\Theta_{f-l}$ needs to be inverted. The inverse Laplace transform operation $\mathcal{L}^{-1}(H(p)\Theta_{f-l})$ cannot be performed because Θ_{f-l} is the Laplace transform of a continuous function $\theta_{f-l}(t)$. Only discrete values of θ_{f-l} exist, the measured values, consequently $\theta_{f-l}(t)$ is not continuously defined. Two methods have been considered to solve this difficulty: method 1 where the convolution property of the Laplace transform is used to avoid the Laplace transform of the input; method 2 where the input is a continuous function of triangle spikes affected with the discrete measured values and which allows to obtain Θ_{f-l} .

Method 1: using the convolution property

The first method takes advantage of the convolution property of the Laplace transform: for two functions f and g ,

$$\mathcal{L}\left(\int_0^t f(t-t')g(t')dt'\right) = \mathcal{L}(f) \times \mathcal{L}(g). \quad (6.27)$$

Using (6.27) and equation (6.26), it can be deduced that

$$\theta_{l-c}(t) = \int_0^t h(t-t')\theta_{f-l}(t')dt' \text{ with } h(t) = \mathcal{L}^{-1}H(p). \quad (6.28)$$

The time integration in (6.28) is discretized using a trapezoidal method: for an integrable function f in the interval $[0, t]$,

$$\int_0^t f(t') dt' = \lim_{n \rightarrow \infty} \frac{t}{n} \left(\frac{f(0) + f(t)}{2} + \sum_{k=1}^{n-1} f\left(k \frac{t}{n}\right) \right) \text{ with } n \text{ an integer.} \quad (6.29)$$

The time values t are discretized as: $t = i\Delta t$. Assuming the value i large enough to get precise approximation of the integral, the discretization method (6.29) is applied to $h(t-t')\theta_{f-l}(t')$. Since,

$$\theta_{f-l}(0) = 0 \Rightarrow f(0) = h(t)\theta_{f-l}(0) = 0 \text{ and} \quad (6.30)$$

$$h(0) = \lim_{p \rightarrow +\infty} p H(p) = 0 \Rightarrow f(t) = h(0)\theta_{f-l}(t) = 0, \quad (6.31)$$

equation (6.28) becomes

$$\theta_{l-c}(i\Delta t) = \Delta t \left(\sum_{k=1}^{i-1} h(i\Delta t - k\Delta t) \theta_{f-l}(k\Delta t) \right). \quad (6.32)$$

Using the discrete values $\theta_{f-l}^k = \theta_{f-l}(k\Delta t)$ and $\theta_{l-c}^n = \theta_{l-c}(i\Delta t)$, equation (6.32) is rewritten as

$$\theta_{l-c}^i = \Delta t \left(\sum_{k=1}^{i-1} h((i-k)\Delta t) \theta_{f-l}^k \right). \quad (6.33)$$

Equation (6.33) can be written under a diagonal matrix form

$$\begin{pmatrix} \theta_{l-c}^1 \\ \theta_{l-c}^2 \\ \vdots \\ \theta_{l-c}^{n-1} \\ \theta_{l-c}^n \end{pmatrix} = A \begin{pmatrix} \theta_{f-l}^1 \\ \theta_{f-l}^2 \\ \vdots \\ \theta_{f-l}^{n-1} \\ \theta_{f-l}^n \end{pmatrix}, \quad (6.34)$$

with n the number of time measured and

$$A = \begin{pmatrix} 0 & \dots & \dots & \dots & 0 \\ \Delta t h(\Delta t) & 0 & \cdot & \cdot & \vdots \\ \vdots & \cdot & \ddots & \cdot & \vdots \\ \Delta t h((n-2)\Delta t) & \cdot & \cdot & 0 & \vdots \\ \Delta t h((n-1)\Delta t) & \Delta t h((n-2)\Delta t) & \dots & \Delta t h(\Delta t) & 0 \end{pmatrix}. \quad (6.35)$$

Method 2: using a triangular function as input

The temperatures are measured at the interface between the gas and the liner with the time period of the experimental sampling Δt . For k , a given measure, only $\theta_{f-l}^k = \theta_{f-l}(k\Delta t)$ is known. The continuous function $\theta_{f-l}(t)$ must be constructed from the discrete values $\theta_{f-l}(k\Delta t)$ to obtain Θ_{f-l} and apply $\mathcal{L}^{-1}(H(p)\Theta_{f-l})$. The method, adapted from [128], aims to use triangle spikes as base functions to generate the input in continuous form.

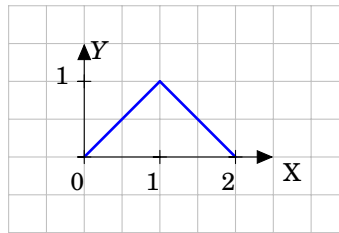


Figure 6.26 – Simple triangle spike function.

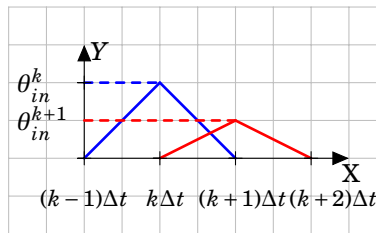


Figure 6.27 – Two spikes associated with the values θ_{f-l}^k and θ_{f-l}^{k+1} .

A single triangular function. This can be defined as piecewise function f constructed with two linear functions:

$$f : t \rightarrow \begin{cases} t, \forall t \in [0, 1] \\ 2 - t, \forall t \in [1, 2] \\ 0, \forall t \in [2, +\infty[\end{cases} \tag{6.36}$$

Figure (6.26) displays this spike function. The Laplace transform of this function is

$$\mathcal{L}(f)(p) = \frac{1}{p^2} - \frac{2e^{-p}}{p^2} + \frac{e^{-2p}}{p^2} . \tag{6.37}$$

Using the time scaling property of a Laplace transform,

$$\forall k \in \mathbb{R}, \mathcal{L}(f(kt)) = \frac{1}{k} F\left(\frac{p}{k}\right) , \tag{6.38}$$

the spike can be located at $t = \Delta t$, at the associated Laplace transform is:

$$\mathcal{L}(f)(p) = \frac{1}{\Delta t p^2} (1 - 2e^{-p\Delta t} + e^{-2p\Delta t}) . \tag{6.39}$$

Using the delay property of the Laplace transform,

$$\forall \tau \in \mathbb{R}, \mathcal{L}(f(t - \tau)) = e^{-\tau p} F , \tag{6.40}$$

the spike can be located at $t = k\Delta t$ and the associated Laplace Transform is:

$$\mathcal{L}(f)(p) = \frac{1}{\Delta t p^2} (1 - 2e^{-p\Delta t} + e^{-2p\Delta t}) e^{-(k-1)\Delta t p} . \tag{6.41}$$

Each value θ_{f-l}^k can be associated with a spike at $t = k\Delta t$. Figure 6.27 shows two spikes associated with the values θ_{f-l}^k and θ_{f-l}^{k+1} respectively. All the spikes can be added using the propriety of linearity of the Laplace transform. The resulting Laplace transform Θ_{f-l} is

$$\Theta_{f-l} = \sum_{k=1}^n \left(\theta_{f-l}^k \frac{1}{\Delta t p^2} (1 - 2e^{-p\Delta t} + e^{-2p\Delta t}) e^{-(k-1)\Delta t p} \right), \quad (6.42)$$

with n the number of time measured. Using the direct problem equation (6.26), $H(p)\Theta_{f-l}$ becomes

$$\Theta_{l-c} = \sum_{k=1}^n \left(\theta_{f-l}^k \frac{H(p)}{\Delta t p^2} (1 - 2e^{-p\Delta t} + e^{-2p\Delta t}) e^{-(k-1)\Delta t p} \right). \quad (6.43)$$

For the quantity $H'(p)^k = \frac{H(p)}{\Delta t p^2} (1 - 2e^{-p\Delta t} + e^{-2p\Delta t}) e^{-(k-1)\Delta t p}$ the inverse Laplace transform can be applied $h'(t)^k = \mathcal{L}^{-1}(H'(p)^k)$. The inverse Laplace transform $\mathcal{L}^{-1}(\Theta_{l-c})$, can be linked with $h'(t)$ and θ_{f-l} as

$$\begin{pmatrix} \theta_{l-c}^1 \\ \theta_{l-c}^2 \\ \vdots \\ \theta_{l-c}^{n-1} \\ \theta_{l-c}^n \end{pmatrix} = A \begin{pmatrix} \theta_{f-l}^1 \\ \theta_{f-l}^2 \\ \vdots \\ \theta_{in}^{n-1} \\ \theta_{f-l}^n \end{pmatrix}, \quad (6.44)$$

with

$$A = \begin{pmatrix} h'(\Delta t)^1 & \cdots & h'(\Delta t)^k & \cdots & h'(\Delta t)^n \\ \vdots & \ddots & \cdot & \cdot & \vdots \\ h'(k\Delta t)^1 & \cdot & h'(k\Delta t)^k & \cdot & h'(k\Delta t)^n \\ \vdots & \cdot & \cdot & \ddots & \vdots \\ h'(n\Delta t)^1 & \cdots & h'(n\Delta t)^k & \cdots & h'(n\Delta t)^n \end{pmatrix}. \quad (6.45)$$

Inversing the Laplace transform

Both methods require to apply an inversion of a Laplace transform (for a Laplace transform $F = \mathcal{L}(f)$, the inverse of Laplace transform is the operation $\mathcal{L}^{-1}(F) = f$). This inversion can be done analytically for simple cases but for more complex cases, a numerical approach is needed. In [128], several inverse numerical methods are mentioned. In this study, the Gaver-Stehfest inversion algorithm [129, 130] and the Hoog et al. inversion algorithm [131, 132] have been considered.

Selecting a method

To compare these two methods, a canonical problem where an analytical solution exists is examined. It consists of a single 1D wall with a thickness $2e = 8.2 \text{ mm}$ and a uniform thermal diffusivity $\alpha = 2.5178e - 07 \text{ m}^2/\text{s}$. An equal and uniform temperature $T_{ext} = 10 \text{ }^\circ\text{C}$ is imposed on at each side, i.e. $T(e, t) = T(-e, t) = T_{ext}$. The initial temperature is set such as $T_i = 0 \text{ }^\circ\text{C}$. The objective is to predict the temperature at the center of the wall T_m . Figure 6.28 presents a schematic view of the problem. The derivation of the analytical solution is omitted in this section but can be found in [133]. For this example, the input and output are: $\theta_{in} = T_{ext} - T_i$ and $\theta_{out} = T_m - T_i$. The Laplace transform of the input is

$$\Theta_{in} = \frac{T_{ext} - T_i}{p}. \quad (6.46)$$

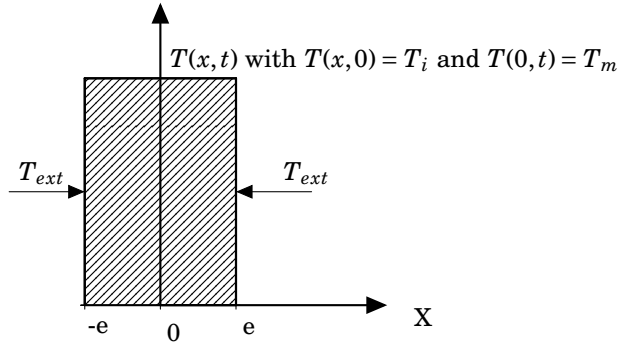


Figure 6.28 – 1D wall with equal and uniform temperature imposed at each side .

The output is linked to the input by the transfer function $H(p)$ such as

$$\begin{aligned} \Theta_{out} &= H(p)\Theta_{in} \\ &= \frac{1}{ch(\sqrt{\frac{p}{\alpha}}e)} \Theta_{in} . \end{aligned} \tag{6.47}$$

The analytical solution is

$$\theta_{out} = 2 \sum_{n=0}^{\infty} (-1)^n \operatorname{erfc}\left[\frac{(2n+1)e}{2\sqrt{\alpha t}}\right] \theta_{in} , \tag{6.48}$$

where erfc is the complementary error function defined as

$$\begin{aligned} \forall x \in \mathbb{R}, \operatorname{erfc}(x) &= 1 - \operatorname{erf}(x) \\ &= 1 - \frac{2}{\sqrt{\pi}} \int_0^x e^{-t^2} dt . \end{aligned} \tag{6.49}$$

The results issued from the two inverse Laplace transform algorithms are reported in figure 6.29. Method 2, with the Gaver-Stehfest algorithm fails to predict a correct θ_{out} temperature difference. The Hoog et al. algorithm is selected. The execution of method 2 is faster than method 1. Method 2 is selected.

6.5.2 Inverse problem

Method 2 and the Hoog et al. inverse Laplace transform algorithm are selected. The direct problem, detailed in (6.44) and (6.45), is

$$\theta_{l-c} = A\theta_{f-l} . \tag{6.50}$$

The temperatures measured at the interface between the liner and the composite are θ_{l-c}^* . Typical approach is typically a least square linear regression. However as the inverse problem is ill-conditioned, a regularization method is applied. The Tikhonov regularization [134] aims to solve inverse problems by minimizing $f(\theta_{f-l})$ defined as

$$\begin{aligned} f(\theta_{f-l}) &= (\theta_{l-c} - \theta_{l-c}^*)^T (\theta_{l-c} - \theta_{l-c}^*) + \alpha \theta_{f-l}^T R^T R \theta_{f-l} \\ &= (A\theta_{f-l} - \theta_{l-c}^*)^T (A\theta_{f-l} - \theta_{l-c}^*) + \alpha \theta_{f-l}^T R^T R \theta_{f-l} , \end{aligned} \tag{6.51}$$

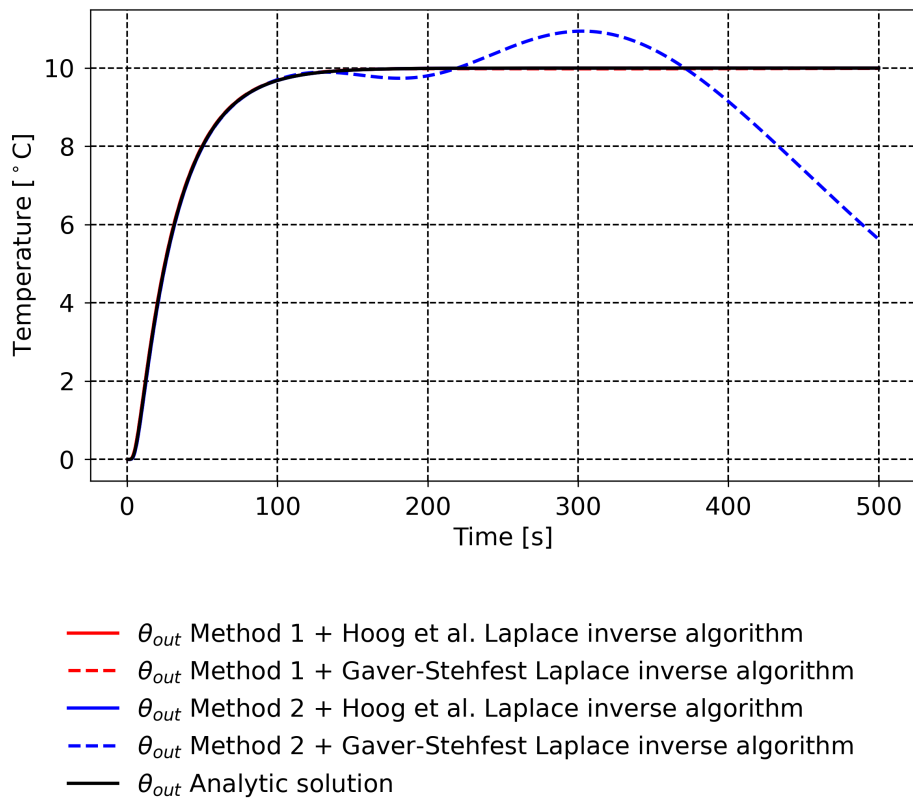


Figure 6.29 – Results for the 1D wall problem: two methods with two inverse Laplace transform algorithms, compared with the analytical solution.

Materials	c_p [J/kg/K]	ρ [kg/m ³]	λ [W/K/m]
Plastic liner	2495.46	924.8	0.35
Carbon wrap composite	1074.19	1433.8	0.55

Table 6.5 – Specific thermal capacity, density and thermal conductivity for the plastic liner and the carbon wrap composite measured in [43] on type IV tanks provided by Hexagon.

and finds the optimal θ_{f-l} . The parameter α is a scalar that needs to be set to help the inversion process. The matrix R is a regularization matrix. The optimal θ_{f-l} is

$$\theta_{f-l} = (A^T A + \alpha R^T R)^{-1} \theta_{l-c}^*{}^T A, \quad (6.52)$$

Based on tests, the second order regularization matrix R is chosen, here represented with a 5x5 matrix for example:

$$R = \begin{pmatrix} 0 & 0 & 0 & 0 & 0 \\ -1 & 2 & -1 & 0 & 0 \\ 0 & -1 & 2 & -1 & 0 \\ 0 & 0 & -1 & 2 & -1 \\ 0 & 0 & 0 & 0 & 0 \end{pmatrix}, \quad (6.53)$$

and $\alpha = 2000$ is selected.

In order to test the inversion process, the temperatures measured at the interface between the liner and the composite θ_{l-c}^* have been used as input of the direct problem. A temperature θ_{test} is calculated,

$$\theta_{test} = A \theta_{l-c}^*. \quad (6.54)$$

The inversion process is applied to θ_{test} ,

$$\theta_{l-c}^{test} = (A^T A + \alpha R^T R)^{-1} \theta_{test}{}^T A, \quad (6.55)$$

and θ_{l-c}^{test} is compared to θ_{l-c}^* to validate the inversion process.

Application to type IV 37 L tank and to type IV 531 L tank from HyTransfer

To perform the calculations, the thermophysical properties of the liner and the composite are assumed to be constant. The thermophysical properties of the liner and the composite for type IV 37 L tank and for type IV 531 L tank from HyTransfer [41] are reported in [43]. They are functions of the temperature within the interval [23 – 100] °C. The constant values considered in this section are the arithmetic average of the values issued from [43]. They are reported in table 6.5. The thickness of the liner layer and the composite layer for the type IV 37 L and 531 L tanks is reported in table 6.6. The model has been tested on both tanks. For type IV 37 L tank, the scenario with an injector diameter of 10 mm and with an averaged mass flowrate of 2 g/s is selected (scenario D10Q2). The maximum, averaged and minimum gas temperatures are correctly captured by the probes in the gas. From the maximum, averaged and minimum temperatures measured between the liner and the composite, maximum, averaged and minimum temperatures between the gas and the liner are estimated by the model. Figure 6.30 presents the results. The testing of the inversion process is applied to the maximum temperature between the liner and the composite and is reported in blue. The inversion test returns the

Tank size [L]	Liner layer thickness e_p [m]	Composite layer thickness e_c [m]
37	0.0041	0.02375
531	0.0064	0.0317

Table 6.6 – Liner layer and composite layer thicknesses for the type IV 37 L and 531 L tanks issued from HyTransfer [42].

correct maximum temperature between the liner and the composite. The averaged temperature at the interface between the gas and the liner estimated via the inverse model is less than $1.5\text{ }^{\circ}\text{C}$ different that the SOFIL value at the end of the filling. It can be noted that the maximum temperature predicted at the interface between the gas and the liner is above $85\text{ }^{\circ}\text{C}$ and above the averaged gas temperature.

For type IV 531 L tank, the scenario with an injector diameter of 25 mm and with an averaged mass flowrate of 2 g/s is selected. Figure 6.31 shows that the temperatures measured in the gas are homogeneous and no thermal gradient is occurring. This is in contradiction with the temperatures measured between the liner and the composite where a difference of $7.7\text{ }^{\circ}\text{C}$ is reported at the end of the filling. It can be noted that the temperature on the exterior surface of the composite is rising. A correction of the model with an external heat transfer may be necessary to improve the prediction.

Conclusion

Additional developments of this model could be carried out to add to the model an external heat transfer and verify if the thermal predictions are improved. This would be archived by adding a new node (T_a, ϕ_a) at the right of the schematic 6.25, imposing the temperature at the ambient temperature. The temperature in the gas could be estimated as well by adding a new node (T_g, ϕ_g) at the left of the schematic 6.25, using the same heat transfer used in SOFIL (2.2.2) between the gas and the liner.

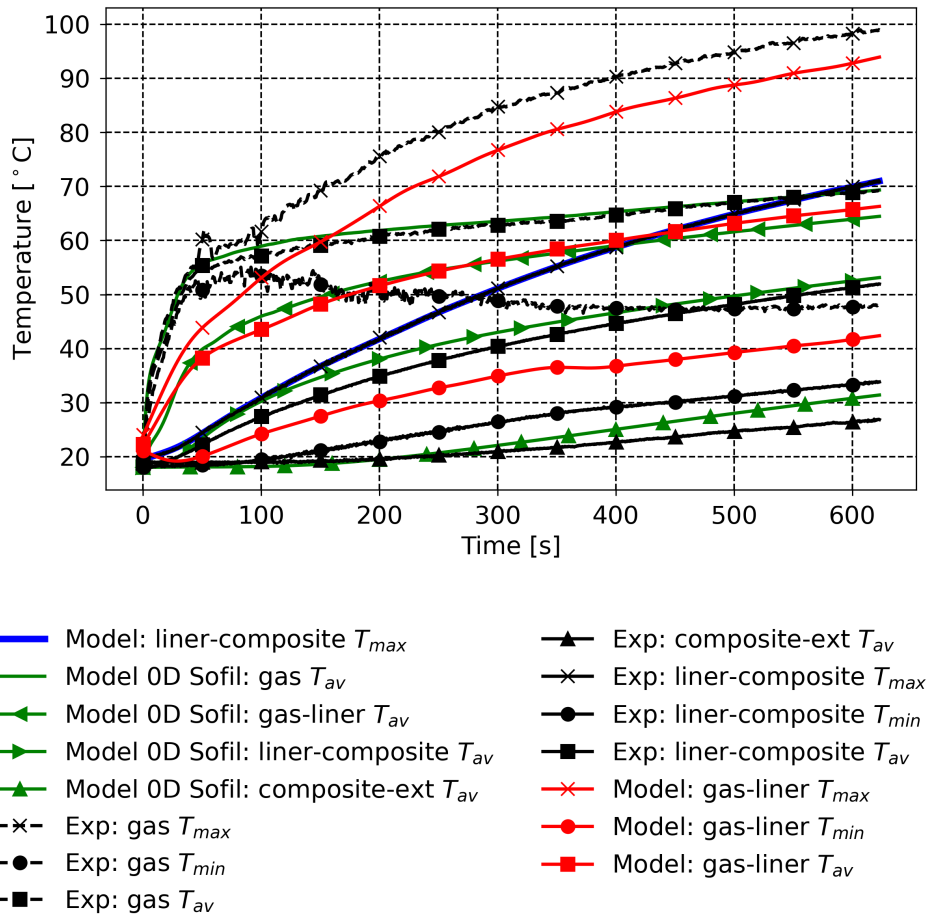


Figure 6.30 – Application of the inverse model to type IV 37 L tank, scenario with an injector diameter of 10 mm and with an averaged mass flowrate of 2 g/s. The temperatures issued from the experimental measurements are reported in black. The temperatures issued from the inverse model are reported in red. The test of the inversion method is performed on the maximum temperature measured between the liner and the composite and is reported in blue. The temperatures from SOFIL are reported in green.

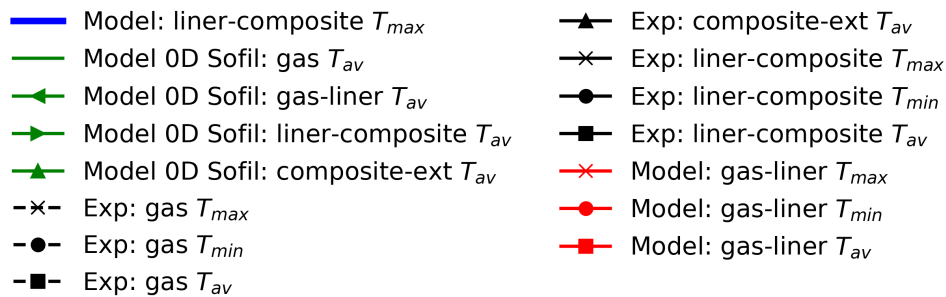
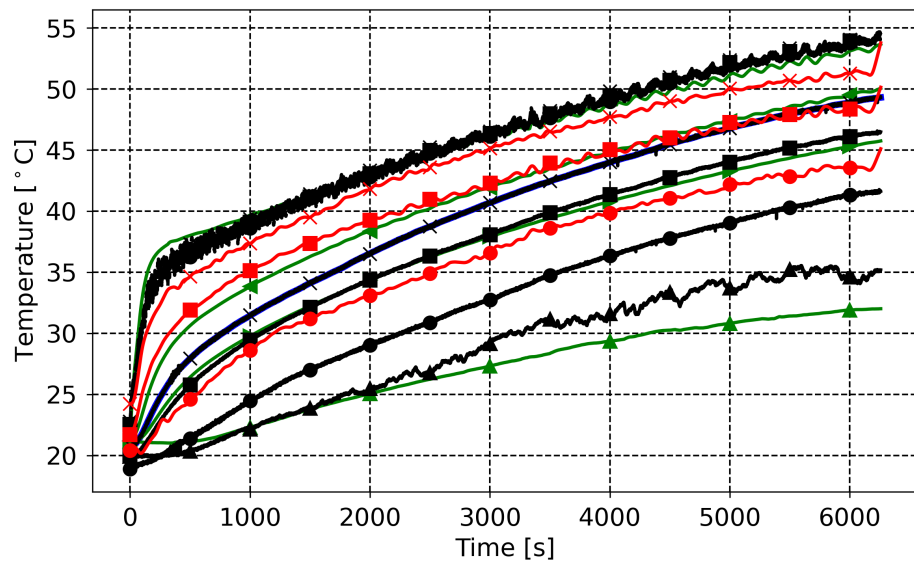


Figure 6.31 – Application of the inverse model to type IV 531 L tank, scenario with an injector diameter of 25 mm and with an averaged mass flowrate of 2 g/s. The temperatures issued from the experimental measurements are reported in black. The temperatures issued from the inverse model are reported in red. The test of the inversion method is performed on the maximum temperature measured between the liner and the composite and is reported in blue. The temperatures from SOFIL are reported in green.

Conclusion and perspectives

During the filling of a gaseous hydrogen tank, the gas temperature inside the tank must not exceed $85\text{ }^{\circ}\text{C}$ for safety reasons for composite material tank. The injected gas is precooled to maintain the averaged gas temperature below this limit. For some filling configurations, a vertical thermal gradient occurs and local temperatures can exceed $85\text{ }^{\circ}\text{C}$, even if the averaged temperature remains below this limit.

The literature review concerning tanks filled horizontally, chapter 1, has indicated that the computational fluid dynamics (CFD) approach can predict the onset of stratification. It has also shown that the maximum temperature predicted by the CFD approach compared to measurement in the gas is generally underestimated. The underlying mechanisms of thermal stratification remain an active area of research. The only criterion, found in the literature, in order to avoid thermal stratification, is to maintain the injection velocity above 5 m/s during the filling.

The present study has used experimental results issued from the HyTransfer project concerning a type IV 37 L tank provided by @Hexagon; these experimental results are described in chapter 2. During experimental measurements, the limited number of thermal probes placed in the gas allowed to detect the presence of stratification. However, the physical mechanisms leading to thermal stratification remained to be clarified.

In chapter 3, a CFD approach in the gas, coupled with thermal conduction simulation in the walls, has been applied to access the thermal and velocity fields. The simulations have been carried out with the software OpenFOAM. For the two filling scenarios leading to the most extreme thermal behaviors, i.e. homogeneous and heterogeneous, 2D-axisymmetric and 3D CFD simulations have been performed. This has been the object of an article published in the International Journal of Hydrogen Energy. The study has highlighted the 3D nature of the thermal stratification and the role of gravity in its development. It has been observed that for the homogeneous case, the jet oscillates while for the heterogeneous case, the jet is deflected towards the lower part of the tank. These phenomena are not captured by the 2D-axisymmetric CFD results. For the homogeneous case, the 3D CFD results accurately predicted the measured temperatures. For the heterogeneous case, the 3D CFD results accurately predicted the averaged gas temperatures and the onset of stratification, but the maximum gas temperature was underestimated. The same conclusions were reported in previous studies with other simulation tools. The improvement of the 3D CFD approach has been identified as an important objective for the present work.

Chapter 4 focused on improving the thermal prediction issued from the CFD approach. The role of turbulence modeling in thermal gradient predictions has been clarified. The $k - \omega$ Shear Stress Transport (SST) turbulence model, used in chapter 3, predicted large levels of turbulence in stagnation areas, leading to an over-diffusion of the temperatures; hence in that case the maximum gas temperature was underestimated. To corroborate this observation, a 3D CFD case without turbulence model was found to overestimate the maximum gas temperature. The $k - \omega$ SST turbulence model with the scale-adaptive simulation (SAS) concept has been identified as a more appropriate model for the simulation of hydrogen tank filling. By adjusting the level of turbulence in stagnation areas, it predicted thermal fields closer to the experimentally measured temperatures. The model has been tested on two other scenarios: a relatively homogeneous

case and a heterogeneous case. For the first scenario, the CFD prediction was satisfactory. For the second scenario, the averaged gas temperature and onset of stratification were predicted but the maximum gas temperature was still underestimated. As no results obtained via the $k - \omega$ SST turbulence model are available for this scenario, the potential improvement due to the $k - \omega$ SST SAS could not be estimated at this step. This filling scenario used a 100 mm long pipe inside the tank, bringing the pipe outlet close to the measurement device. This differs from the previous heterogeneous scenario correctly predicted by the CFD approach. The influence on the thermal distribution of the measurement device inside the gas, should be investigated; it could maybe explain part of the differences noted between the CFD results and the experimental measurements.

The CFD results have highlighted that the cold gas injected forms a jet in the tank and that this jet is deflected towards the lower part of the tank due to buoyancy forces. This phenomenon was found to play a key role in the thermal stratification occurrence. When the jet is deflected, the horizontal symmetry of the flow is broken, which induces a vertical thermal gradient. In chapter 5, the jet was modeled based on the buoyant round jet theory, to obtain its trajectory in the tank without CFD simulations. The buoyant round jet model required only data predicted by a 0D modeling of tank filling (2.2.2). The model developed in this chapter predicted the onset of stratification for six filling scenarios. At the onset of stratification, the injection velocity was found to be consistent with the 5 m/s criterion reported in the literature. A method has been proposed to estimate the maximum gas temperature but additional validation studies seem necessary to assess its accuracy.

Complementary investigations carried out during the present work, concerning both methodology and phenomenology, have been reported in chapter 6:

- * The influence of the symmetry assumption used for the 3D CFD approach, i.e. considering only half of the domain, has been examined in section 6.1. The symmetry assumption constrains the jet to oscillate in the symmetry plane but does not impact the thermal distribution in the tank.
- * The oscillation of the jet was studied in section 6.2. It was shown that the oscillation frequency is proportional to the inlet velocity.
- * In section 6.3, a new 3D CFD method has been developed to carry out Steady State Like (SSL) simulations of tank filling. The method has been designed to save computational resources by targeting a precise time, without simulating prior times. The method allows to estimate the thermal field at the end of a filling scenario in a few weeks on a personal computer, instead of months on a high performance computing station, when the classic unsteady CFD simulation is employed.
- * The 3D simulation results concerning a scenario of tank emptying have been presented in section 6.4. For the time interval simulated, it was shown that the flow is principally driven by the natural convection and that the influence of the pipe flow on the main bulk is negligible.
- * In section 6.5, a method has been developed to estimate the temperature at the interface between the gas and the liner from values measured at the interface between the liner and the composite. Laplace transform method and inversion of ill-posed problem techniques have been used. The method can be applied when few thermal data are available during experimental measurements, to improve the detection of thermal gradients.

Some possible paths for future work:

- The influence of the measurement device on fluid dynamics during the experiments needs to be clarified. The measurement device has never been considered in CFD studies, due to the complexity of the required mesh. However, this device is intrusive: it might disturb the flow and could impact the thermal stratification level. This could partly explain the differences noted between the CFD results and experimental measurements. The SSL method could be used to carry out simulations with and without measurement device in order to estimate its impact on the thermal field, with a limited computational cost.

Two experimental cases using the same filling scenario but with and without measurement device could be considered. By using the method described in section 6.5, the temperature between the liner and the composite could be used to predict the temperature between the gas and the liner. The influence of the measurement device on the gas temperature distribution could thus be estimated.

- Concerning the buoyant round jet model, the prediction of the occurrence of thermal gradients as a function of jet deflection remains an aspect to investigate for larger tanks. For now, it has only been applied to a small tank, i.e. $\frac{L}{D} = 2.4$. The buoyant round jet model may not be applicable for a vertical filling, especially for with an upward injection: the jet would interact with itself, which is not taken into account in the model. The profile of the thermal gradient would also probably be different.

For some tanks, the pipe is oriented upwards to improve thermal mixing but then, it can hit the upper wall. When the jet hits a wall, it loses its momentum, which results in less efficient thermal mixing. The buoyant round jet model could be used to choose an optimal injector angle in order to avoid the impact with the upper wall.

- The SSL method developed in section 6.3 has been proposed to perform rapid CFD calculations. This method should be tested on other filling scenarios and other tank geometries. This new method rapidly predicts the thermal field for a target time of interest without simulating prior times. It could be relevant for an emptying case where the velocities involved are small but the process is long. The method could be coupled with the buoyant round jet model to determine optimal angles of injector orientation: the buoyant round jet model would predict the optimal angle and the SSL method would predict the associated thermal field.
- The oscillation of the jet in the tank and its role in thermal mixing would need to be further examined. New injectors or geometries triggering such flapping may delay stratification.
- Improving thermal mixing independently of the tank or the filling scenario could be the object of future studies. Focus could be placed on the design of the injector, for example to generate swirling or pulsating flows and thus improve thermal mixing.

Bibliography

- [1] U.S. Department of Energy, [Fuel cells](#).
URL https://www.energy.gov/sites/prod/files/2015/11/f27/fcto_fuel_cells_fact_sheet.pdf — Cited on page 1.
- [2] UNFCCC, [Conference of the parties serving as the meeting of the parties to the paris agreement \(2021\)](#).
URL https://unfccc.int/sites/default/files/resource/cma2021_L16_adv.pdf — Cited on page 1.
- [3] [NorthH2 project](#) (2020).
URL <https://www.north2.eu/en/> — Cited on page 1.
- [4] [Air Liquide inaugurates the world's largest low-carbon hydrogen membrane-based production unit in Canada \(2021\)](#).
URL <https://www.airliquide.com/group/press-releases-news/2021-01-26/air-liquide-inaugurates-worlds-largest-low-carbon-hydrogen-membrane-based-production-unit-canada> — Cited on page 1.
- [5] D. G. Caglayan, N. Weber, H. U. Heinrichs, J. Linßen, M. Robinius, P. A. Kukla, D. Stolten, [Technical potential of salt caverns for hydrogen storage in europe](#), *International Journal of Hydrogen Energy* 45 (11) (2020) 6793–6805. doi:<https://doi.org/10.1016/j.ijhydene.2019.12.161>.
URL <https://www.sciencedirect.com/science/article/pii/S0360319919347299> — Cited on page 1.
- [6] [Energy Observer 2](#).
URL <https://www.energy-observer.org/resources/energy-observer-2-liquid-hydrogen> — Cited on page 2.
- [7] [Hydrogen-powered Airbus A380](#).
URL <https://www.h2-view.com/story/hydrogen-powered-airbus-a380-to-take-flight-this-decade/> — Cited on page 2.
- [8] [Alstom Coradia iLint™](#).
URL <https://www.alstom.com/solutions/rolling-stock/coradia-ilinttm-worlds-1st-hydrogen-powered-train> — Cited on page 2.
- [9] [Hyundai XCIENT](#).
URL <https://www.hyundai.news/eu/articles/press-releases/hyundai-xcient-fuel-cell-heads-to-europe-for.html> — Cited on page 2.
- [10] [Toyota Mirai](#).
URL <https://www.toyota.fr/new-cars/mirai/> — Cited on pages 1 and 2.
- [11] [Pragma Industries alpha](#).
URL <https://www.pragma-industries.com/light-mobility/> — Cited on page 2.
- [12] [H2TOOLS, Hydrogen tools, hydrogen properties](#).
URL <https://h2tools.org/hyarc/hydrogen-properties> — Cited on page 1.

- [13] E. Rivard, M. Trudeau, K. Zaghbi, [Hydrogen storage for mobility: A review](#), *Materials* 12 (12) (2019). doi:
[10.3390/ma12121973](https://doi.org/10.3390/ma12121973).
URL <https://www.mdpi.com/1996-1944/12/12/1973> — Cited on page 1.
- [14] D. Hao, X. Wang, Y. Zhang, R. Wang, G. Chen, J. Li, *Automotive Innovation* 3 (2020) 111–122. doi:
<https://doi.org/10.1007/s42154-020-00096-z>. — Cited on page 1.
- [15] A. Sartbaeva, V. L. Kuznetsov, S. A. Wells, P. P. Edwards, [Hydrogen nexus in a sustainable energy future](#), *Energy Environ. Sci.* 1 (2008) 79–85. doi:
[10.1039/B810104N](https://doi.org/10.1039/B810104N).
URL <http://dx.doi.org/10.1039/B810104N> — Cited on pages 1 and 3.
- [16] [Hydrogen and fuel cell technologies office](#).
URL <https://www.energy.gov/eere/fuelcells/hydrogen-storage> — Cited on page 3.
- [17] C. P. Fowler, A. C. Orifici, C. H. Wang, [A review of toroidal composite pressure vessel optimisation and damage tolerant design for high pressure gaseous fuel storage](#), *International Journal of Hydrogen Energy* 41 (47) (2016) 22067–22089. doi:
<https://doi.org/10.1016/j.ijhydene.2016.10.039>.
URL <https://www.sciencedirect.com/science/article/pii/S0360319916330336> — Cited on page 4.
- [18] Fuel Cell Standards Committee, [Fueling protocols for light duty gaseous hydrogen surface vehicles](#) (dec 2016). doi:
https://doi.org/10.4271/J2601_201612.
URL https://doi.org/10.4271/J2601_201612 — Cited on pages 2, 22, and 176.
- [19] D. Melideo, D. Baraldi, M. C. Galassi, R. Ortiz Cebolla, B. Acosta Iborra, P. Moretto, [CFD model performance benchmark of fast filling simulations of hydrogen tanks with pre-cooling](#), *International Journal of Hydrogen Energy* 39 (9) (2014) 4389–4395. doi:
<https://doi.org/10.1016/j.ijhydene.2013.12.196>.
URL <https://www.sciencedirect.com/science/article/pii/S0360319913031881> — Cited on pages 2, 4, 19, 21, 23, 33, and 50.
- [20] D. Melideo, D. Baraldi, [CFD analysis of fast filling strategies for hydrogen tanks and their effects on key-parameters](#), *International Journal of Hydrogen Energy* 40 (1) (2015) 735–745. doi:
<https://doi.org/10.1016/j.ijhydene.2014.10.138>.
URL <https://www.sciencedirect.com/science/article/pii/S0360319914030146> — Cited on page 19.
- [21] Y. Kang, S. Cho, D. Kim, [Charging strategy through analysis of charging influence factors of ultra-light hydrogen storage with polyethylene terephthalate liner](#), *International Journal of Hydrogen Energy* 46 (01 2021). doi:
[10.1016/j.ijhydene.2021.01.007](https://doi.org/10.1016/j.ijhydene.2021.01.007).
- [22] Y. Bai, C. Zhang, H. Duan, S. Jiang, Z. Zhou, D. Grouset, M. Zhang, X. Ye, [Modeling and optimal control of fast filling process of hydrogen to fuel cell vehicle](#), *Journal of Energy Storage* 35 (2021) 102306. doi:
<https://doi.org/10.1016/j.est.2021.102306>.
URL <https://www.sciencedirect.com/science/article/pii/S2352152X21000694> — Cited on pages 2 and 22.
- [23] N. de Miguel, B. Acosta, D. Baraldi, R. Melideo, R. Ortiz Cebolla, P. Moretto, [The role of initial tank temperature on refuelling of on-board hydrogen tanks](#), *International Journal of Hydrogen Energy* 41 (20) (2016) 8606–8615. doi:
<https://doi.org/10.1016/j.ijhydene.2016.03.158>.

- URL <https://www.sciencedirect.com/science/article/pii/S0360319915315391> — Cited on pages 2 and 19.
- [24] J. Cheng, J. Xiao, P. Bénard, R. Chahine, [Estimation of final hydrogen temperatures during refueling 35mpa and 70mpa tanks](#), *Energy Procedia* 105 (2017) 1363–1369, 8th International Conference on Applied Energy, ICAE2016, 8-11 October 2016, Beijing, China. doi:<https://doi.org/10.1016/j.egypro.2017.03.505>.
URL <https://www.sciencedirect.com/science/article/pii/S1876610217305465> — Cited on page 2.
- [25] C. Dicken, W. Mérida, [Measured effects of filling time and initial mass on the temperature distribution within a hydrogen cylinder during refuelling](#), *Journal of Power Sources* 165 (1) (2007) 324–336. doi:<https://doi.org/10.1016/j.jpowsour.2006.11.077>.
URL <https://www.sciencedirect.com/science/article/pii/S0378775306024244> — Cited on pages 2, 5, 17, 18, 127, and 128.
- [26] G. Wang, J. Zhou, S. Hu, S. Dong, P. Wei, [Investigations of filling mass with the dependence of heat transfer during fast filling of hydrogen cylinders](#), *International Journal of Hydrogen Energy* 39 (9) (2014) 4380–4388. doi:<https://doi.org/10.1016/j.ijhydene.2013.12.189>.
URL <https://www.sciencedirect.com/science/article/pii/S0360319913031819> — Cited on page 5.
- [27] S. J. Oh, J. H. Yoon, K. S. Jeon, J. Choi, A study on the thermal characteristics of hydrogen storage vessel related to condition of charging, *Journal of Mechanical Science and Technology* 36 (3) (2022) 1579–1586. doi:[10.1007/s12206-022-0243-2](https://doi.org/10.1007/s12206-022-0243-2). — Cited on pages 2 and 5.
- [28] C. J. B. Dicken, [Temperature distribution within a compressed gas cylinder during filling](#), Ph.D. thesis, University of British Columbia (2006). doi:<http://dx.doi.org/10.14288/1.0080715>.
URL <https://open.library.ubc.ca/collections/ubctheses/831/items/1.0080715> — Cited on pages 5, 6, and 33.
- [29] T. Terada, H. Yoshimura, Y. Tamura, H. Mitsuishi, S. Watanabe, [Thermal behavior in hydrogen storage tank for fcv on fast filling \(2nd report\)](#) (2008) 2008–01–0463doi:[10.4271/2008-01-0463](https://doi.org/10.4271/2008-01-0463).
URL <https://www.sae.org/content/2008-01-0463/> — Cited on pages 5, 17, 18, 128, 141, 149, and 152.
- [30] European Commission, European industry and European researchers, [Hytransfer: Pre-normative research for thermodynamic optimization of fast hydrogen transfer](#), FCH JU 2012-1-325277 (2013).
URL <https://cordis.europa.eu/project/id/325277/reporting> — Cited on pages 7, 18, 19, 20, and 25.
- [31] T. Bourgeois, F. Ammouri, D. Baraldi, P. Moretto, [The temperature evolution in compressed gas filling processes: A review](#), *International Journal of Hydrogen Energy* 43 (4) (2018) 2268–2292. doi:[10.1016/j.ijhydene.2017.11.068](https://doi.org/10.1016/j.ijhydene.2017.11.068).
URL <https://linkinghub.elsevier.com/retrieve/pii/S0360319917343860> — Cited on pages 17, 93, and 149.
- [32] M. Li, Y. Bai, C. Zhang, Y. Song, S. Jiang, D. Grouset, M. Zhang, [Review on the research of hydrogen storage system fast refueling in fuel cell vehicle](#), *International Journal of Hydrogen Energy* 44 (21) (2019) 10677–10693. doi:[10.1016/j.ijhydene.2019.02.208](https://doi.org/10.1016/j.ijhydene.2019.02.208).
URL <https://linkinghub.elsevier.com/retrieve/pii/S0360319919308663> — Cited on page 17.

- [33] B. E. Launder, D. B. Spalding, *Lectures in mathematical models of turbulence*, Academic Press London, New York, 1972. — Cited on page 17.
- [34] O. Redlich, J. N. S. Kwong, *On the thermodynamics of solutions. v. an equation of state. fugacities of gaseous solutions.*, *Chemical Reviews* 44 (1) (1949) 233–244, PMID: 18125401. [arXiv:https://doi.org/10.1021/cr60137a013](https://doi.org/10.1021/cr60137a013), doi:10.1021/cr60137a013. URL <https://doi.org/10.1021/cr60137a013> — Cited on pages 17, 18, 21, and 33.
- [35] S. C. Kim, S. H. Lee, K. B. Yoon, *Thermal characteristics during hydrogen fueling process of type iv cylinder*, *International Journal of Hydrogen Energy* 35 (13) (2010) 6830–6835, iSMF-09. doi:<https://doi.org/10.1016/j.ijhydene.2010.03.130>. URL <https://www.sciencedirect.com/science/article/pii/S0360319910006476> — Cited on page 18.
- [36] R. Immel, A. Mack-Gardner, *Development and validation of a numerical thermal simulation model for compressed hydrogen gas storage tanks*, *SAE International Journal of Engines* 4 (2011) 1850–1861. doi:10.4271/2011-01-1342. — Cited on page 18.
- [37] R. H. Aungier, *A fast, accurate real gas equation of state for fluid dynamic analysis applications*, *Journal of Fluids Engineering* 117 (2) (1995) 277–281. [arXiv:https://asmedigitalcollection.asme.org/fluidsengineering/article-pdf/117/2/277/5530185/277_1.pdf](https://asmedigitalcollection.asme.org/fluidsengineering/article-pdf/117/2/277/5530185/277_1.pdf), doi:10.1115/1.2817141. URL <https://doi.org/10.1115/1.2817141> — Cited on pages 18, 21, and 33.
- [38] Y. Takagi, N. Sugie, K. Takeda, Y. Okano, T. Eguchi, K. Hirota, *Numerical investigation of the thermal behavior in a hydrogen tank during fast filling process* ASME/JSME 2011 8th Thermal Engineering Joint Conference (03 2011). doi:10.1115/AJTEC2011-44270. URL <https://doi.org/10.1115/AJTEC2011-44270> — Cited on page 18.
- [39] T. Setoguchi, M. Alam, M. Monde, H. Kim, *Characteristics of turbulent confined jets during fast filling of h2 tank at high pressure*, *International Journal of Aeroacoustics* 12 (5-6) (2013) 455–474. [arXiv:https://doi.org/10.1260/1475-472X.12.5-6.455](https://doi.org/10.1260/1475-472X.12.5-6.455), doi:10.1260/1475-472X.12.5-6.455. URL <https://doi.org/10.1260/1475-472X.12.5-6.455> — Cited on page 18.
- [40] A. Suryan, H. D. Kim, T. Setoguchi, *Three dimensional numerical computations on the fast filling of a hydrogen tank under different conditions*, *International Journal of Hydrogen Energy* 37 (9) (2012) 7600–7611, 7th Petite Workshop on the Defect Chemical Nature of Energy Materials, 14-17 March 2011, Storaas, Kongsberg, Norway. doi:<https://doi.org/10.1016/j.ijhydene.2012.02.019>. URL <https://www.sciencedirect.com/science/article/pii/S0360319912003412> — Cited on page 18.
- [41] B. Ravinel, B. Acosta, N. De Migue, P. Moretto, O.-C. Rafael, J. Goran, v. d. L. Ulrich, *D4.1 report on the experimental filling test campaign*, Tech. rep. (2017). URL https://s02291b7740b89df1.jimcontent.com/download/version/1493713659/module/11623534399/name/HyTransfer_Report%20on%20the%20experimental%20filling%20test%20campaign_public.pdf — Cited on pages 18, 21, 22, 25, 29, 30, 82, 83, 84, 128, 147, 149, 150, 152, 163, 169, 171, 176, and 186.
- [42] C. Devilliers, *D7.5 final synthesis of the project findings for the industry*. (2017). URL https://s02291b7740b89df1.jimcontent.com/download/version/1493039366/module/11623560599/name/HyTransfer_Final%20synthesis%20of%20the%20project%20findings%20for%20the%20industry_public.pdf — Cited on pages 18, 20, 170, and 187.

- [43] T. Bourgeois, T. Brachmann, F. Barth, F. Ammouri, D. Baraldi, D. Melideo, B. Acosta-Iborra, D. Zaepffel, D. Saury, D. Lemonnier, [Optimization of hydrogen vehicle refuelling requirements](#), *International Journal of Hydrogen Energy* 42 (19) (2017) 13789–13809, special Issue on The 21st World Hydrogen Energy Conference (WHEC 2016), 13-16 June 2016, Zaragoza, Spain. doi:<https://doi.org/10.1016/j.ijhydene.2017.01.165>. URL <https://www.sciencedirect.com/science/article/pii/S0360319917303312> — Cited on pages 22, 36, 81, 165, and 186.
- [44] N. de Miguel, B. Acosta, P. Moretto, R. Ortiz Cebolla, [Influence of the gas injector configuration on the temperature evolution during refueling of on-board hydrogen tanks](#), *International Journal of Hydrogen Energy* 41 (42) (2016) 19447–19454. doi:<https://doi.org/10.1016/j.ijhydene.2016.07.008>. URL <https://www.sciencedirect.com/science/article/pii/S0360319916307340> — Cited on pages 18 and 19.
- [45] E. Yamada, W. Hiraki, H. Muramatsu, [Hydrogen fast filling to a type iv tank developed for motorcycles](#), *ICHS* (2015). URL <http://www.ichs2015.com/images/papers/133.pdf> — Cited on page 18.
- [46] X. Wu, J. Liu, J. Shao, G. Deng, [Fast filling strategy of type iii on-board hydrogen tank based on time-delayed method](#), *International Journal of Hydrogen Energy* 46 (57) (2021) 29288–29296. doi:<https://doi.org/10.1016/j.ijhydene.2021.01.094>. URL <https://www.sciencedirect.com/science/article/pii/S0360319921001865> — Cited on pages 19 and 23.
- [47] M. Galassi, B. Acosta-Iborra, D. Baraldi, C. Bonato, F. Harskamp, N. Frischauf, P. Moretto, [Onboard compressed hydrogen storage: Fast filling experiments and simulations](#), *Energy Procedia* 29 (2012) 192–200, wHEC 2012 Conference Proceedings – 19th World Hydrogen Energy Conference. doi:<https://doi.org/10.1016/j.egypro.2012.09.024>. URL <https://www.sciencedirect.com/science/article/pii/S1876610212014440> — Cited on page 19.
- [48] M. C. Galassi, D. Baraldi, B. Acosta Iborra, P. Moretto, [Cfd analysis of fast filling scenarios for 70 mpa hydrogen type iv tanks](#), *International Journal of Hydrogen Energy* 37 (8) (2012) 6886–6892, iIII Iberian Symposium on Hydrogen, Fuel Cells and Advanced Batteries, HYCELTEC-2011. doi:<https://doi.org/10.1016/j.ijhydene.2012.01.041>. URL <https://www.sciencedirect.com/science/article/pii/S0360319912000912>
- [49] M. C. Galassi, E. Papanikolaou, M. Heitsch, D. Baraldi, B. A. Iborra, P. Moretto, [Assessment of cfd models for hydrogen fast filling simulations](#), *International Journal of Hydrogen Energy* 39 (11) (2014) 6252–6260. doi:<https://doi.org/10.1016/j.ijhydene.2013.03.164>. URL <https://www.sciencedirect.com/science/article/pii/S0360319913008422>
- [50] B. Acosta, P. Moretto, N. de Miguel, R. Ortiz, F. Harskamp, C. Bonato, [Jrc reference data from experiments of on-board hydrogen tanks fast filling](#), *International Journal of Hydrogen Energy* 39 (35) (2014) 20531–20537. doi:<https://doi.org/10.1016/j.ijhydene.2014.03.227>. URL <https://www.sciencedirect.com/science/article/pii/S0360319914009550>
- [51] I. Simonovski, D. Baraldi, D. Melideo, B. Acosta-Iborra, [Thermal simulations of a hydrogen storage tank during fast filling](#), *International Journal of Hydrogen Energy* 40 (36) (2015) 12560–12571. doi:<https://doi.org/10.1016/j.ijhydene.2015.09.024>

- 1016/j.ijhydene.2015.06.114.
URL <https://www.sciencedirect.com/science/article/pii/S0360319915015992>
- [52] R. Ortiz Cebolla, B. Acosta, N. de Miguel, P. Moretto, [Effect of precooled inlet gas temperature and mass flow rate on final state of charge during hydrogen vehicle refueling](#), *International Journal of Hydrogen Energy* 40 (13) (2015) 4698–4706. doi:<https://doi.org/10.1016/j.ijhydene.2015.02.035>.
URL <https://www.sciencedirect.com/science/article/pii/S036031991500364X>
- [53] N. de Miguel, B. Acosta, P. Moretto, R. O. Cebolla, [The effect of defueling rate on the temperature evolution of on-board hydrogen tanks](#), *International Journal of Hydrogen Energy* 40 (42) (2015) 14768–14774, 2nd Euro-Mediterranean Hydrogen Technologies Conference (EmHyTeC2014), 9–12 December 2014, Taormina, Italy. doi:<https://doi.org/10.1016/j.ijhydene.2015.06.038>.
URL <https://www.sciencedirect.com/science/article/pii/S0360319915015232>
- [54] D. Melideo, D. Baraldi, N. De Miguel Echevarria, B. Acosta Iborra, [Effects of the injector direction on the temperature distribution during filling of hydrogen tanks](#), 7th International Conference on Hydrogen Safety, 2017.
URL <https://www.hysafe.info/ichs2017/> — Cited on pages 19, 23, and 93.
- [55] D. Melideo, D. Baraldi, N. De Miguel Echevarria, B. Acosta Iborra, [Effects of some key-parameters on the thermal stratification in hydrogen tanks during the filling process](#), *International Journal of Hydrogen Energy* 44 (26) (2019) 13569–13582. doi:[10.1016/j.ijhydene.2019.03.187](https://doi.org/10.1016/j.ijhydene.2019.03.187).
URL <https://linkinghub.elsevier.com/retrieve/pii/S0360319919312169> — Cited on pages 19, 23, 50, 93, and 127.
- [56] R. Ortiz Cebolla, B. Acosta, P. Moretto, N. de Miguel, [GASTEF: The high pressure gas tank testing facility of the European commission joint research centre](#), *International Journal of Hydrogen Energy* 44 (16) (2019) 8601–8614. doi:<https://doi.org/10.1016/j.ijhydene.2019.01.207>.
URL <https://www.sciencedirect.com/science/article/pii/S0360319919303660> — Cited on pages 19 and 20.
- [57] F. R. Menter, R. Langtry, S. Völker, [Transition modelling for general purpose CFD codes](#) 77 (1) (2006) 277–303. doi:[10.1007/s10494-006-9047-1](https://doi.org/10.1007/s10494-006-9047-1).
URL <http://link.springer.com/10.1007/s10494-006-9047-1> — Cited on pages 19, 23, and 93.
- [58] R. B. Langtry, F. R. Menter, [Correlation-based transition modeling for unstructured parallelized computational fluid dynamics codes](#), *AIAA Journal* 47 (12) (2009) 2894–2906. doi:[10.2514/1.42362](https://doi.org/10.2514/1.42362).
URL <https://arc.aiaa.org/doi/10.2514/1.42362> — Cited on pages 19, 23, and 93.
- [59] D. Zaepffel, F. Mathey, B. Ravinel, T. Bourgeois, F. Ammouri, [CFD analysis of the different flow regimes occurring during the filling of a hydrogen vehicle tank](#), 21st World Hydrogen Energy Conferencg, 2016. — Cited on pages 19, 23, 24, and 81.
- [60] H. Li, Z. Lyu, Y. Liu, M. Han, H. Li, [The effects of infill on hydrogen tank temperature distribution during fast fill](#), *International Journal of Hydrogen Energy* 46 (17) (2021) 10396–10410. doi:<https://doi.org/10.1016/j.ijhydene.2020.12.133>.
URL <https://www.sciencedirect.com/science/article/pii/S0360319920347479> — Cited on pages 19 and 23.

-
- [61] Muto Charles J., [An experimental investigation of the effects of heat transfer during charging and blowdown of single gas receivers.](#), Tech. rep., Calhoun: Naval postgraduate school archive (1959).
URL <https://calhoun.nps.edu/handle/10945/14191> — Cited on pages 20, 21, and 135.
- [62] W. C. Reynolds, Analytical investigation of the blowdown and charging processes in a single gas receiver, including the effects of heat transfer., Tech. rep., Stanford University (1955). — Cited on pages 20 and 21.
- [63] Q. Li, J. Zhou, Q. Chang, W. Xing, Effects of geometry and inconstant mass flow rate on temperatures within a pressurized hydrogen cylinder during refueling, *International Journal of Hydrogen Energy* 37 (7) (2012) 6043–6052. doi:10.1016/j.ijhydene.2011.12.020. — Cited on page 20.
- [64] V. Ramasamy, E. Richardson, [Thermal response of high-aspect-ratio hydrogen cylinders undergoing fast-filling](#), *International Journal of Heat and Mass Transfer* 160 (2020) 120179. doi:https://doi.org/10.1016/j.ijheatmasstransfer.2020.120179.
URL <https://www.sciencedirect.com/science/article/pii/S001793102033115X> — Cited on pages 20 and 23.
- [65] W. H. McAdams, *Heat transmission*, 3rd Edition, McGraw-Hill New York, 1954. — Cited on page 21.
- [66] C. Perret, [Modelling and simulation of the filling of a gaseous hydrogen tank under very high pressure](#), Tech. rep., CEA (2003).
URL <http://www.eihp.org/> — Cited on pages 21 and 22.
- [67] G. Soave, [Equilibrium constants from a modified redlich-kwong equation of state](#), *Chemical Engineering Science* 27 (6) (1972) 1197–1203. doi:https://doi.org/10.1016/0009-2509(72)80096-4.
URL <https://www.sciencedirect.com/science/article/pii/0009250972800964> — Cited on pages 21 and 33.
- [68] D.-Y. Peng, D. B. Robinson, [A new two-constant equation of state](#), *Industrial & Engineering Chemistry Fundamentals* 15 (1) (1976) 59–64. arXiv:https://doi.org/10.1021/i160057a011, doi:10.1021/i160057a011.
URL <https://doi.org/10.1021/i160057a011> — Cited on pages 21 and 33.
- [69] P. L. Woodfield, M. Monde, Y. Mitsutake, Measurement of averaged heat transfer coefficients in high-pressure vessel during charging with hydrogen, nitrogen or argon gas, *Journal of Thermal Science and Technology* 2 (2) (2007) 180–191. doi:10.1299/jtst.2.180. — Cited on pages 22 and 36.
- [70] T. Bourgeois, F. Ammouri, M. Weber, C. Knapik, [Evaluating the temperature inside a tank during a filling with highly-pressurized gas](#), *International Journal of Hydrogen Energy* 40 (35) (2015) 11748–11755. doi:https://doi.org/10.1016/j.ijhydene.2015.01.096.
URL <https://www.sciencedirect.com/science/article/pii/S0360319915001640> — Cited on pages 22, 36, 81, and 165.
- [71] J.-Q. Li, J.-C. Li, K. Park, S.-J. Jang, J.-T. Kwon, [An analysis on the compressed hydrogen storage system for the fast-filling process of hydrogen gas at the pressure of 82 mpa](#), *Energies* 14 (9) (2021). doi:10.3390/en14092635.
URL <https://www.mdpi.com/1996-1073/14/9/2635> — Cited on page 22.
- [72] J.-Q. LI, N.-S. Myoung, J.-T. Kwon, S.-J. Jang, T. Lee, Y.-H. Lee, [A theoretical analysis of temperature rise of hydrogen in high-pressure storage cylinder during fast filling process](#), *Advances in Mechanical Engineering* 12 (12) (2020)
-

1687814020971920. [arXiv:https://doi.org/10.1177/1687814020971920](https://doi.org/10.1177/1687814020971920), doi:10.1177/1687814020971920.
URL <https://doi.org/10.1177/1687814020971920>
- [73] J. Xiao, X. Wang, X. Zhou, P. Bénard, R. Chahine, [A dual zone thermodynamic model for refueling hydrogen vehicles](#), *International Journal of Hydrogen Energy* 44 (17) (2019) 8780–8790, special issue on The 7th International Conference on Hydrogen Safety (ICHS 2017), 11-13 September 2017, Hamburg, Germany. doi:<https://doi.org/10.1016/j.ijhydene.2018.10.235>.
URL <https://www.sciencedirect.com/science/article/pii/S0360319918335183>
- [74] V. Molkov, M. Dadashzadeh, D. Makarov, [Physical model of onboard hydrogen storage tank thermal behaviour during fuelling](#), *International Journal of Hydrogen Energy* 44 (8) (2019) 4374–4384. doi:<https://doi.org/10.1016/j.ijhydene.2018.12.115>.
URL <https://www.sciencedirect.com/science/article/pii/S0360319918340837> — Cited on page 33.
- [75] T. Kuroki, N. Sakoda, K. Shinzato, M. Monde, Y. Takata, [Dynamic simulation for optimal hydrogen refueling method to fuel cell vehicle tanks](#), *International Journal of Hydrogen Energy* 43 (11) (2018) 5714–5721. doi:<https://doi.org/10.1016/j.ijhydene.2018.01.111>.
URL <https://www.sciencedirect.com/science/article/pii/S0360319918302234>
- [76] T. Kuroki, K. Nagasawa, M. Peters, D. Leighton, J. Kurtz, N. Sakoda, M. Monde, Y. Takata, [Thermodynamic modeling of hydrogen fueling process from high-pressure storage tank to vehicle tank](#), *International Journal of Hydrogen Energy* 46 (42) (2021) 22004–22017. doi:<https://doi.org/10.1016/j.ijhydene.2021.04.037>.
URL <https://www.sciencedirect.com/science/article/pii/S0360319921013410> — Cited on page 22.
- [77] C. J. B. Dicken, W. Mérida, [Modeling the transient temperature distribution within a hydrogen cylinder during refueling](#), *Numerical Heat Transfer, Part A: Applications* 53 (7) (2007) 685–708. [arXiv:https://doi.org/10.1080/10407780701634383](https://doi.org/10.1080/10407780701634383), doi:10.1080/10407780701634383.
URL <https://doi.org/10.1080/10407780701634383> — Cited on page 23.
- [78] A. Suryan, H. D. Kim, T. Setoguchi, [Comparative study of turbulence models performance for refueling of compressed hydrogen tanks](#), *International Journal of Hydrogen Energy* 38 (22) (2013) 9562–9569. doi:10.1016/j.ijhydene.2012.07.055.
URL <https://app.dimensions.ai/details/publication/pub.1025692856> — Cited on page 23.
- [79] H. Li, Z. Lyu, Y. Liu, M. Han, H. Li, [The effects of infill on hydrogen tank temperature distribution during fast fill](#), *International Journal of Hydrogen Energy* 46 (17) (2021) 10396–10410. doi:<https://doi.org/10.1016/j.ijhydene.2020.12.133>.
URL <https://www.sciencedirect.com/science/article/pii/S0360319920347479> — Cited on page 23.
- [80] T.-H. Shih, W. W. Liou, A. Shabbir, Z. Yang, J. Zhu, [A new k-epsilon eddy viscosity model for high reynolds number turbulent flows](#), *Computers & Fluids* 24 (3) (1995) 227–238. doi:[https://doi.org/10.1016/0045-7930\(94\)00032-T](https://doi.org/10.1016/0045-7930(94)00032-T).
URL <https://www.sciencedirect.com/science/article/pii/004579309400032T> — Cited on page 23.
- [81] F. Menter, T. Esch, [Element of industrial heat transfer predictions](#), 16th Brazilian congress of mechanical engineering, 2001. — Cited on page 23.

-
- [82] E. Demael, M. Weber, P. Renault, [Experimental and Numerical Evaluation of Transient Temperature Distribution inside a Cylinder during Fast Filling for H2 Applications](#), 18th World Hydrogen Energy Conference, 2010.
URL https://juser.fz-juelich.de/record/135541/files/HS1_pp_Dem_Weber_rev0610.pdf — Cited on page 23.
- [83] [Website: Joint Research Centre of the European Commission](#) (2021).
URL <https://publications.jrc.ec.europa.eu/repository/> — Cited on page 25.
- [84] H. G. Weller, G. Tabor, H. Jasak, C. Fureby, [A tensorial approach to computational continuum mechanics using object-oriented techniques](#), *Computers in Physics* 12 (6) (1998) 620–631. [arXiv:https://aip.scitation.org/doi/pdf/10.1063/1.168744](#), [doi:10.1063/1.168744](#).
URL <https://aip.scitation.org/doi/abs/10.1063/1.168744> — Cited on page 28.
- [85] G. Chen, Q. Xiong, P. Morris, E. Paterson, A. Sergeev, Y. Wang, Openfoam for computational fluid dynamics, *Notices of the American Mathematical Society* 61 (4) (2014) 354–363. [doi:10.1090/noti1095](#). — Cited on page 28.
- [86] The OpenFOAM Foundation, [C++ source code guide](#).
URL <https://cpp.openfoam.org/v9/> — Cited on page 28.
- [87] H. Nilsson (Ed.), *Conjugate heat transfer in OpenFOAM*, In *Proceedings of CFD with OpenSource Software*, 2016. — Cited on page 31.
- [88] [Paraview](#) (2022).
URL <https://www.paraview.org/> — Cited on page 28.
- [89] [Salome](#) (2022).
URL <https://docs.salome-platform.org/7/gui/SMESH/index.html> — Cited on page 28.
- [90] E. Ruffio, D. Saury, D. Petit, Thermodynamic analysis of hydrogen tank filling. effects of heat losses and filling rate optimization, *International Journal of Hydrogen Energy* 39 (2014) 12701–12714. [doi:10.1016/j.ijhydene.2014.06.069](#). — Cited on page 33.
- [91] T. Setoguchi, M. Alam, M. Monde, H. Kim, [Characteristics of turbulent confined jets during fast filling of h2 tank at high pressure](#), *International Journal of Aeroacoustics* 12 (5-6) (2013) 455–474. [arXiv:https://doi.org/10.1260/1475-472X.12.5-6.455](#), [doi:10.1260/1475-472X.12.5-6.455](#).
URL <https://doi.org/10.1260/1475-472X.12.5-6.455> — Cited on page 33.
- [92] M.-S. Kim, J.-H. Ryu, S.-J. Oh, J.-H. Yang, S.-W. Choi, [Numerical investigation on influence of gas and turbulence model for type iii hydrogen tank under discharge condition](#), *Energies* 13 (23) (2020).
URL <https://www.mdpi.com/1996-1073/13/23/6432> — Cited on page 33.
- [93] S. Shitanshu, P. Kapil, R. Rupesh, S. Pawan Kumar, [H2 refueling assessment of composite storage tank for fuel cell vehicle](#), *International Journal of Hydrogen Energy* 44 (42) (2019) 23699–23707. [doi:https://doi.org/10.1016/j.ijhydene.2019.07.044](#).
URL <https://www.sciencedirect.com/science/article/pii/S0360319919325923> — Cited on page 33.
- [94] I. A. Johnston, *The noble-abel equation of state: Thermodynamic derivations for ballistics modelling*, Tech. rep., Defence Science and Technology Organisation Edinburgh (2005). — Cited on page 33.
-

- [95] J. W. Leachman, R. T. Jacobsen, S. G. Penoncello, E. W. Lemmon, [Fundamental equations of state for parahydrogen, normal hydrogen, and orthohydrogen](#), *Journal of Physical and Chemical Reference Data* 38 (3) (2009) 721–748. [arXiv:https://doi.org/10.1063/1.3160306](#), [doi:10.1063/1.3160306](#).
URL [https://doi.org/10.1063/1.3160306](#) — Cited on page 33.
- [96] M. Deymi-Dashtebayaz, M. Farzaneh-Gord, N. Nooralipoor, H. Niazmand, The complete modelling of the filling process of hydrogen onboard vehicle cylinders, *Brazilian Journal of Chemical Engineering* 33 (2016) 391–399. [doi:10.1590/0104-6632.20160332s20140209](#). — Cited on page 33.
- [97] M. Kormann, I. Krüger, Application of a Real Gas Model by Van-der-Waals for a Hydrogen Tank Filling Process, 13th International Modelica Conference, 2019. [doi:10.3384/ecp19157665](#). — Cited on page 33.
- [98] B. H. Park, C. K. Chae, [Development of correlation equations on hydrogen properties for hydrogen refueling process by machine learning approach](#), *International Journal of Hydrogen Energy* 47 (6) (2022) 4185–4195. [doi:https://doi.org/10.1016/j.ijhydene.2021.11.053](#).
URL [https://www.sciencedirect.com/science/article/pii/S0360319921044402](#) — Cited on page 33.
- [99] E. W. Lemmon, I. Bell, M. L. Huber, M. O. McLinden, [NIST Standard Reference Database 23: Reference Fluid Thermodynamic and Transport Properties-REFPROP, Version 10.0](#), National Institute of Standards and Technology (2018). [doi:https://doi.org/10.18434/T4/1502528](#).
URL [https://www.nist.gov/srd/refprop](#) — Cited on page 33.
- [100] J.-Q. LI, N.-S. Myoung, J.-T. Kwon, S.-J. Jang, T. Lee, Y.-H. Lee, [A theoretical analysis of temperature rise of hydrogen in high-pressure storage cylinder during fast filling process](#), *Advances in Mechanical Engineering* 12 (12) (2020) 1687814020971920. [arXiv:https://doi.org/10.1177/1687814020971920](#), [doi:10.1177/1687814020971920](#).
URL [https://doi.org/10.1177/1687814020971920](#) — Cited on page 33.
- [101] E. W. Lemmon, I. Bell, M. L. Huber, M. O. McLinden, [NIST Standard Reference Database 23: Reference Fluid Thermodynamic and Transport Properties-REFPROP, Version 10.0](#), National Institute of Standards and Technology (2018). [doi:https://doi.org/10.18434/T4/1502528](#).
URL [https://www.nist.gov/srd/refprop](#) — Cited on page 33.
- [102] Yuusha, [tabulatedThermophysicalProperties](#), [https://github.com/charlespwd/project-title](#) (2019). — Cited on page 34.
- [103] I. H. Bell, J. Wronski, S. Quoilin, V. Lemort, [Pure and pseudo-pure fluid thermophysical property evaluation and the open-source thermophysical property library coolprop](#), *Industrial & Engineering Chemistry Research* 53 (6) (2014) 2498–2508. [arXiv:http://pubs.acs.org/doi/pdf/10.1021/ie4033999](#), [doi:10.1021/ie4033999](#).
URL [http://pubs.acs.org/doi/abs/10.1021/ie4033999](#) — Cited on page 34.
- [104] F. Massard, [Aide-mémoire du thermicien](#), Elsevier, 1997.
URL [https://books.google.fr/books?id=6iNRxgEACAAJ](#) — Cited on page 37.
- [105] B. Eckhardt, T. M. Schneider, B. Hof, J. Westerweel, [Turbulence transition in pipe flow](#), *Annual Review of Fluid Mechanics* 39 (1) (2007) 447–468. [doi:10.1146/annurev.fluid.39.050905.110308](#).
URL [http://www.annualreviews.org/doi/10.1146/annurev.fluid.39.050905.110308](#) — Cited on page 38.

-
- [106] D. S.-K. Ting, [Chapter 4 - turbulence scales](#), in: D. S.-K. Ting (Ed.), *Basics of Engineering Turbulence*, Academic Press, 2016, pp. 69–98. doi:<https://doi.org/10.1016/B978-0-12-803970-0.00004-0>. URL <https://www.sciencedirect.com/science/article/pii/B9780128039700000040> — Cited on page 38.
- [107] F. R. Menter, [Two-equation eddy-viscosity turbulence models for engineering applications](#), *AIAA Journal* 32 (8) (1994) 1598–1605. doi:[10.2514/3.12149](https://doi.org/10.2514/3.12149). URL <https://arc.aiaa.org/doi/10.2514/3.12149> — Cited on page 40.
- [108] F. R. Menter, M. Kuntz, R. Langtry, Ten years of industrial experience with the sst turbulence model, *Heat and Mass Transfer* 4 (01 2003). — Cited on page 40.
- [109] D. C. Wilcox, [Formulation of the k-w turbulence model revisited](#), *AIAA Journal* 46 (11) (2008) 2823–2838. arXiv: <https://doi.org/10.2514/1.36541>, doi:[10.2514/1.36541](https://doi.org/10.2514/1.36541). URL <https://doi.org/10.2514/1.36541> — Cited on page 40.
- [110] B. Launder, D. Spalding, [The numerical computation of turbulent flows](#), *Computer Methods in Applied Mechanics and Engineering* 3 (2) (1974) 269–289. doi:[https://doi.org/10.1016/0045-7825\(74\)90029-2](https://doi.org/10.1016/0045-7825(74)90029-2). URL <https://www.sciencedirect.com/science/article/pii/0045782574900292> — Cited on page 40.
- [111] F. R. Menter, A. R. Center, Improved two-equation k -omega turbulence models for aerodynamic flows, National Aeronautics and Space Administration, Ames Research Center ; National Technical Information Service, distributor Moffett Field, Calif. : [Springfield, Va, 1992. — Cited on page 40.
- [112] D. S.-K. Ting, [Chapter 6 - wall turbulence](#), in: D. S.-K. Ting (Ed.), *Basics of Engineering Turbulence*, Academic Press, 2016, pp. 119–138. doi:<https://doi.org/10.1016/B978-0-12-803970-0.00006-4>. URL <https://www.sciencedirect.com/science/article/pii/B9780128039700000064> — Cited on pages 41 and 42.
- [113] [kLowReWallFunction](#) (2021). URL <https://www.openfoam.com/documentation/guides/latest/doc/guide-bcs-wall-turbulence-kLowReWallFunction.html> — Cited on page 42.
- [114] [ChtMultiRegionFoam](#) (2021). URL <https://openfoamwiki.net/index.php/ChtMultiRegionFoam> — Cited on page 43.
- [115] A. Ashrafizadeh, [Comparison of monolithic and partitioned approaches for the solution of fluid-solid thermal interaction problems](#), *Journal Of Applied and Computational Sciences in Mechanics* 31 (1) (2020) 23–38. arXiv: https://mechanic-ferdowsi.um.ac.ir/article_33190_61e444eda6bb68e6a85e897adea64e61.pdf, doi:[10.22067/fum-mech.v31i1.84760](https://doi.org/10.22067/fum-mech.v31i1.84760). URL https://mechanic-ferdowsi.um.ac.ir/article_33190.html — Cited on page 43.
- [116] [cfmesh](#) (2022). URL <https://cfmesh.com/> — Cited on page 43.
- [117] R. Issa, [Solution of the implicitly discretised fluid flow equations by operator-splitting](#), *Journal of Computational Physics* 62 (1) (1986) 40–65. doi:[https://doi.org/10.1016/0021-9991\(86\)90099-9](https://doi.org/10.1016/0021-9991(86)90099-9). URL <https://www.sciencedirect.com/science/article/pii/0021999186900999> — Cited on page 47.
-

- [118] S. Patankar, D. Spalding, [A calculation procedure for heat, mass and momentum transfer in three-dimensional parabolic flows](#), *International Journal of Heat and Mass Transfer* 15 (10) (1972) 1787–1806. doi:[https://doi.org/10.1016/0017-9310\(72\)90054-3](https://doi.org/10.1016/0017-9310(72)90054-3).
URL <https://www.sciencedirect.com/science/article/pii/0017931072900543> — Cited on page 47.
- [119] R. Gonin, P. Horgue, R. Guibert, D. Fabre, R. Bourguet, F. Ammouri, E. Vyazmina, [A computational fluid dynamic study of the filling of a gaseous hydrogen tank under two contrasted scenarios](#), *International Journal of Hydrogen Energy* 47 (55) (2022) 23278–23292. doi:<https://doi.org/10.1016/j.ijhydene.2022.03.260>.
URL <https://www.sciencedirect.com/science/article/pii/S0360319922014100> — Cited on page 53.
- [120] B. R. Morton, G. I. Taylor, J. S. Turner, [Turbulent gravitational convection from maintained and instantaneous sources](#), *Proceedings of the Royal Society of London. Series A. Mathematical and Physical Sciences* 234 (1196) (1956) 1–23. arXiv:<https://royalsocietypublishing.org/doi/pdf/10.1098/rspa.1956.0011>, doi:[10.1098/rspa.1956.0011](https://doi.org/10.1098/rspa.1956.0011).
URL <https://royalsocietypublishing.org/doi/abs/10.1098/rspa.1956.0011> — Cited on pages 127, 132, and 133.
- [121] G. Jirka, [Integral model for turbulent buoyant jets in unbounded stratified flows. part i: Single round jet](#), *Environmental Fluid Mechanics* 4 (2004) 1–56. doi:[10.1023/A:1025583110842](https://doi.org/10.1023/A:1025583110842). — Cited on pages 127, 132, 133, 135, and 141.
- [122] J. H. W. Lee, V. H. Chu, [Turbulent Jets and Plumes: A Lagrangian Approach](#), Springer US, Boston, MA, 2003. doi:[10.1007/978-1-4615-0407-8_2](https://doi.org/10.1007/978-1-4615-0407-8_2).
URL https://doi.org/10.1007/978-1-4615-0407-8_2 — Cited on pages 127, 132, and 133.
- [123] A. Fragkou, P. Papanicolaou, [Positively and negatively round turbulent buoyant jets into homogeneous calm ambient](#), *Proceedings* 2 (11) (2018). doi:[10.3390/proceedings2110572](https://doi.org/10.3390/proceedings2110572).
URL <https://www.mdpi.com/2504-3900/2/11/572> — Cited on page 127.
- [124] G. Abraham, [Jet diffusion in stagnant ambient fluid](#), Ph.D. thesis, Civil Engineering and Geosciences, Hydraulic Engineering (1963). — Cited on page 131.
- [125] N. Rajaratnam, [Turbulent Jets](#), *Developments in water science*, Elsevier Scientific Publishing Company, 1976. — Cited on pages 131 and 132.
- [126] G. Carazzo, E. Kaminski, S. Tait, [The route to self-similarity in turbulent jets and plumes](#), *Journal of Fluid Mechanics* 547 (2006) 137–148. doi:[10.1017/S002211200500683X](https://doi.org/10.1017/S002211200500683X). — Cited on pages 133 and 141.
- [127] A. N. Tikhonov, V. Y. Arsenin, [Solutions of ill-posed problems](#), *Scripta Series in Mathematics*, V. H. Winston & Sons, 1977, 10239. — Cited on page 180.
- [128] E. Ruffio, [Estimation de paramètres et de conditions limites thermiques en conduction instationnaire pour des matériaux anisotropes. Apport des algorithmes stochastiques à la conception optimale d'expérience.](#), Theses, ISAE-ENSMA Ecole Nationale Supérieure de Mécanique et d'Aérotechnique - Poitiers (Dec. 2011).
URL <https://tel.archives-ouvertes.fr/tel-00664748> — Cited on pages 181 and 183.
- [129] H. Villinger, [Solving cylindrical geothermal problems using the gaver-stehfest inverse laplace transform](#), *GEOPHYSICS* 50 (10) (1985) 1581–1587. arXiv:<https://doi.org/10.1190/1.1441848>, doi:[10.1190/1.1441848](https://doi.org/10.1190/1.1441848).
URL <https://doi.org/10.1190/1.1441848> — Cited on page 183.

- [130] H. Stehfest, [Algorithm 368: Numerical inversion of laplace transforms \[d5\]](#), Commun. ACM 13 (1) (1970) 47–49. doi:10.1145/361953.361969. URL <https://doi.org/10.1145/361953.361969> — Cited on page 183.
- [131] F. R. de Hoog, J. H. Knight, A. N. Stokes, [An improved method for numerical inversion of laplace transforms](#), SIAM Journal on Scientific and Statistical Computing 3 (3) (1982) 357–366. arXiv:<https://doi.org/10.1137/0903022>, doi:10.1137/0903022. URL <https://doi.org/10.1137/0903022> — Cited on page 183.
- [132] K. J. Hollenbeck, [Invlap.m: A matlab function for numerical inversion of laplace transforms by the de hoog algorithm](#) (1998). URL <http://www.isva.dtu.dk/staff/karl/invlap.htm> — Cited on page 183.
- [133] Y. Jannot, [Transferts thermiques](#), Edilivre, 2012. URL <http://www.thermique55.com/principal/thermique.pdf> — Cited on page 183.
- [134] A. N. Tikhonov, V. I. Arsenin, [Solutions of ill-posed problems](#), Winston ; distributed solely by Halsted Press Washington : New York, 1977. — Cited on page 184.